Georgia State University
ScholarWorks @ Georgia State University

Physics and Astronomy Dissertations | Department of Physics and Astronomy

Spring 4-2-2012

Spectroscopy and Interferometry of the Winds of Luminous Blue Variables

Noel D. Richardson
Center for High Angular Resolution Astronomy

Follow this and additional works at: https://scholarworks.gsu.edu/phy_astr_diss

Recommended Citation
Richardson, Noel D., "Spectroscopy and Interferometry of the Winds of Luminous Blue Variables." Dissertation, Georgia State University, 2012.
https://scholarworks.gsu.edu/phy_astr_diss/52

This Dissertation is brought to you for free and open access by the Department of Physics and Astronomy at ScholarWorks @ Georgia State University. It has been accepted for inclusion in Physics and Astronomy Dissertations by an authorized administrator of ScholarWorks @ Georgia State University. For more information, please contact scholarworks@gsu.edu.

SPECTROSCOPY AND INTERFEROMETRY OF THE WINDS OF LUMINOUS BLUE VARIABLES

by

NOEL DOUGLAS RICHARDSON

Under the Direction of Douglas R. Gies

ABSTRACT

Massive stars are rare, but emit most of the light we observe in the Universe and create many of the heavy elements in the Universe. In this dissertation, I explore the winds of the massive luminous blue variable (LBV) stars. New observational approaches and long time-series are utilized in order to examine the basic observable properties of the stars and the mass lost during their lifetimes.

The mass lost through a hot star's wind impacts its long-term evolution. In order to study the winds and the long-term changes of the stars, hot stars with some of the strongest winds (the luminous blue variables or LBVs) were studied in detail with optical spectroscopy and photometry. A 25-year survey on the prototype P Cygni is presented, where the long-term changes are documented for many parameters that have not been examined before. In addition, we present a detailed study of the H-band emitting region through interferometric imaging with the CHARA Array and the MIRC beam combiner as well as spectrophotometry. A detailed study of the Hα line variability of the LBV η Carinae near its recent periastron is presented. The LBV candidate HDE 326823 is found to be a binary system with variability driven by the close binary companion and Roche lobe overflow. Finally, I present a three-year study of many LBVs in the Milky Way Galaxy and Magellanic Clouds for a statistically

significant survey of the long-term variability properties of these rare stars as a population. These results show that all the sample stars exhibit similar types of variability, although with different amplitudes. Future studies of LBV winds are outlined, as well as a short discussion of Georgia State University's Hard Labor Creek Observatory for these types of studies.

INDEX WORDS: Circumstellar matter, Stars, Emission-line, Be, Winds, Outflows, Early type, Evolution, Spectroscopic binaries

SPECTROSCOPY AND INTERFEROMETRY OF THE WINDS OF LUMINOUS BLUE VARIABLES

by

NOEL DOUGLAS RICHARDSON

A Dissertation Submitted in Partial Fulfillment of Requirements for the Degree of

Doctor of Philosophy

in the College of Arts and Sciences

Georgia State University

2012

Copyright by
Noel D. Richardson
2012

SPECTROSCOPY AND INTERFEROMETRY OF THE WINDS OF LUMINOUS BLUE VARIABLES

by

NOEL DOUGLAS RICHARDSON

Committee Chair:	Douglas R. Gies
Committee:	Harold A. McAlister
	Todd J. Henry
	Misty C. Bentz
	Brian D. Thoms
	Nancy D. Morrison

Electronic Version Approved:

Office of Graduate Studies

College of Arts and Sciences

Georgia State University

May 2012

Dedication

This dissertation is dedicated to my family, especially my wonderful wife Kristy and our newest addition, Hailey. Our next chapter is about to begin.

ACKNOWLEDGMENTS

This dissertation has taken a large effort to collect and analyze the necessary data. I could not have done this without a large amount of support. First, I would like to thank my wonderfully patient wife, Kristy. She has supported me through the large changes that have occurred over the previous six years, kept me on track when I couldn't see what to do, and listened to me as graduate school caused stress. She was incredibly understanding as I went on observing runs to the CHARA Array or Lowell Observatory, traveled to conferences, or on collaborative trips. I owe much of this work to her support, and could never thank her enough. Her dedication to the final work in this dissertation is fundamentally important, as she often cared for our daughter so I could write.

The rest of my family has also been supportive through this process. My mother encouraged me through my education, and I wish she were still here so that she would be able to see this final stage. My father has supported me in many ways, and has always listened when I needed to talk. My sisters have been there through it as well, listening to my frustrations and aspirations. During this research, I have gone to Boston twice to work on things with Dan Clemens (BU) and my aunt and uncle in Boston have graciously helped me out at those times by providing a place to stay and transportation while I was there.

Doug Gies has been an extraordinary advisor who has allowed me to shape this dissertation in my own manner from the beginning. He encouraged me to take on projects and did not ever tell me not to pursue work on LBVs, despite his lack of former experience with these stars. He has supported the projects with grants, time, dedication, and enthusiasm. I cannot thank him enough for that.

My committee has offered advice related to my career, the dissertation, and helped with acquiring telescope time. In particular, Hal McAlister has encouraged me with CHARA work, even if the PAVO project I undertook did not ever make it far off the ground (due to

software development issues). Also, Todd Henry encouraged me to apply for SMARTS time, which led to the development of Chapters 4–6 of this dissertation.

Nancy Morrison advised me with my undergraduate and M.S. research at the University of Toledo. The methods she taught me provided a solid basis for this research. Her long-term monitoring projects at Ritter Observatory allowed for the development of Chapter 2, which has interesting aspects of LBV physics from an in-depth study of the wind of P Cygni. I appreciate her advice, her time, and her travel for this dissertation.

Chapter 2 also benefited greatly by the advice and help of several people. Nevena Markova provided many useful comments, as well as her earlier published data on the star (both spectroscopy and photometry). Erica Hesselbach provided new reduced observations of the star made at Ritter Observatory. John Percy provided additional archival photometry and great advice in the early stages of the project.

CHARA observations of P Cygni are shown in Chapter 3. Early CHARA observations of this star developed my interest in LBVs, so special thanks to Peter Tuthill (University of Sydney) and Theo ten Brummelaar for that help. The MIRC observations and analysis presented in Chapter 3 began with the help of Gail Schaefer. Early analysis was performed with her assistance as well as that of John Monnier and Yamina Touhami. Rob Parks performed additional imaging tests at that time. This work continues with help from Fabien Baron. The CHARA Array relies on the additional help of Chris Farrington, P.J. Goldfinger, Sandy Land, Judit Sturmann, Laszlo Sturmann, Nils Turner, and Larry Webster.

As previously mentioned, the CTIO 1.5 m telescope operated by the SMARTS Consortium was the main facility used for Chapters 4–6 of this thesis. Time was awarded by both the SMARTS Consortium and NOAO. SMARTS time was locally allocated by Todd Henry. The last 1.5 years were allocated by the National Optical Astronomy Observatory, which is operated by the Association of Universities for Research in Astronomy, under contract with the National Science Foundation. Fred Walter managed the queue scheduling of these

observations, which was certainly difficult with the η Carinae program, and all data were masterfully scheduled.

The η Carinae project (Chapter 4) benefited from advice from Mike Corcoran, Kris Davidson, Ted Gull, Roberta Humphreys, Tom Madura, Krister Nielsen, and Julian Pittard. Roberta Humphreys was also a great help in the early stages of my LBV survey. She provided a few targets that I had overlooked and that are certainly interesting in their own respect.

Some spectra were obtained at GSU's Hard Labor Creek Observatory. This facility has come a long way over the time I have spent at GSU. Our department chairman, Dick Miller, has certainly been instrumental in these upgrades and improvements. The new 20 inch telescope was also helped along by Hal McAlister. The installation of this telescope was done with the help of Charles Hopper and Nic Scott, with some additional help from the instrument shop, John Wilson, and many other people in the department. The spectrograph saw first light last summer, which was overseen by many of the people already listed in this paragraph. Additional support for that project came from Ben Jenkins, who completed his M.S. thesis with that instrument. However, I must acknowledge Emily Aldoretta who spent her summer and fall semesters learning the instrument and telescope, the data reduction, and performing some analysis for her undergraduate thesis. Her help was instrumental in showing how much work can be done with that telescope and spectrograph.

I am grateful for permission to reproduce figures from other publications. Permissions were granted from Roberta Humphreys, Kerstin Weis, Joseph Cassinelli, Nathan Smith, and Rens Waters. This research has made use of the data archive for the HST Treasury Program on Eta Carinae (GO 9973) which is available online at http://etacar.umn.edu. The archive is supported by the University of Minnesota and the Space Telescope Science Institute under contract with NASA. This material is based upon work supported by the National Science Foundation under Grant No. AST-0606861 and AST-1009080. Support for this work was provided by NASA through grant number HST-GO-11943 from the Space Telescope Science

Institute, which is operated by the Association of Universities for Research in Astronomy, Inc., under NASA contract NAS5-26555. Institutional support has been provided from the GSU College of Arts and Sciences and from the Research Program Enhancement fund of the Board of Regents of the University System of Georgia, administered through the GSU Office of the Vice President for Research and Economic Development.

TABLE OF CONTENTS

LIST OF TABLES

LIST OF FIGURES

LIST OF ABBREVIATIONS

ASAS	All Sky Automated Survey
CCD	Charged Coupled Device
Co-I	Co-Investigator
HST	*Hubble Space Telescope*
IDL	Interactive Data Language
IR	infrared
LMC	Large Magellanic Cloud
LSST	Large Synoptic Survey Telescope
LOS	line-of-sight
LBV	Luminous Blue Variable
MAST	Multimission Archive at Space Telescope
NASA	National Aeronautics and Space Administration
NIR	near infrared
pc	parsec
PAVO	Precision Astronomical Visibilities Observatory
PI	Principal Investigator
SED	spectral energy distribution
SMC	Small Magellanic Cloud
STIS	Space Telescope Imaging Spectrograph

1
INTRODUCTION

1.1 THE IMPORTANCE OF MASSIVE STARS

The most massive stars, those with spectral types of O and B, are much hotter and more massive and luminous than the Sun. They have short lifetimes, and so they evolve quickly. This fast evolution leads to the possibility of studying stellar evolution on short time-scales. The typical luminosity of an O star is $10^6 L_\odot$ or higher, so these stars are visible over extremely large distances despite the vast amount of their luminosity being emitted in the ultraviolet and their extreme rarity. Due to the large luminosities, and the relative faintness of most nearby stars, O and B stars are a significant fraction of the stars visible to the naked eye (human) observer on our planet. These stars also provide heavy element synthesis in their stellar cores and during supernovae explosions, allowing heavy elements to be dispersed throughout the universe.

The extreme luminosities of these stars cause them to lose mass at larger rates compared to the Sun. The relationship between the mass loss rate ($\dot{M}$) and luminosity of the star (Crowther & Willis 1994) is a proportion of the form

$$\dot{M} \propto L^{1.7}.$$

This means that mass loss is a key process during the lifetimes of these stars. An O star will lose several solar masses of material through its stellar wind during the main sequence phase, and this plus subsequent post-main sequence mass loss plays a critical role in the end-point of massive stellar evolution. Uncertainties related to mass loss rates make difficult the theoretical calculation of the initial mass needed for a black hole or neutron star remnant (from the final supernova of the star). This dissertation will focus on mass loss of the massive stars after the main sequence.

1.2 STELLAR WINDS

The modern theory of stellar winds from hot stars was developed by Castor et al. (1975)(CAK). CAK showed that in both static and expanding atmospheres, the force due to a spectral line is sufficient to allow atoms and ions to escape the gravity of the star. As such, the emerging force necessary to drive a stellar wind will be a sum of the forces of all spectral lines.

A driving force then emerges from a hot star's flux due to the thousands of lines of ionized Fe III and Fe IV in the ultraviolet, as well as the famous resonance lines such as the ultraviolet C IV or Si IV lines. For an O star, with a mass above $\simeq 30 M_{\odot}$, the resulting mass-loss rate may be on the order of $-6.5 \lesssim \log(\dot{M}[M_{\odot}\mathrm{yr}^{-1}]) \lesssim -5$ (Fullerton et al. 2006). This implies that massive O stars have a strong enough wind while still on the main sequence that the course of evolution of these stars may be slightly affected. The lifetime of an O star on the main sequence is on the order of 10^6 yr, so a significant amount of mass (a few solar masses) is lost while on the main sequence. As the star evolves off the main sequence, the atmosphere expands and the luminosity increases, which increases the mass loss rate. This additional mass loss may increase the mass loss rate by orders of magnitude.

In general, two equations define the stellar wind mass loss rate. The mass conservation equation is related to the mass loss rate,

$$\dot{M} = 4\pi r^2 \rho v = \text{constant}.$$

The second equation describes the radial outflow, or the velocity law, often called the β-law,

$$v(r) \simeq v_0 + (v_\infty - v_0)(1 - \frac{R_*}{r})^{\beta}.$$

Here, v_0 represents the velocity of matter as it leaves the surface, r is the radial distance from the center of the star, and β is the velocity law exponent, which all shows that the

material expelled from the surface is accelerated as it leaves the stellar surface.

The most massive stars are thought to lose at least 60% of their mass before exploding in a supernova (Smith & Owocki 2006). The stars considered in this dissertation have some of the strongest winds observed. These winds may alter the conditions in the surrounding interstellar medium, and in some cases these winds may have triggered star formation. Indeed, the highly attenuated Galactic luminous blue variable G24.73+0.69 was recently shown to have at least seven young stellar objects in the stellar wind-created nebulosity (Petriella et al. 2011).

1.3 OBSERVABLES OF STELLAR WINDS

If there is a significant amount of matter surrounding the star and the gas is ionized by the central star, then there may be emission lines present in the spectrum. As electrons recombine with ions, recombination lines may form. In the optical portion of the electromagnetic spectrum, the hydrogen Balmer lines are the most likely to be observed in emission. The $n = 3$ to 2 transition of hydrogen will be the strongest of these lines, and will present itself as a strong red emission line (Hα) at 6562.682 Å. Other species that may be visible in emission for these hot stars include multiple transitions of He I and Fe II (Chentsov et al. 2003; Nielsen et al. 2009a).

Often these lines may appear to have a morphology called a *P Cygni profile*. This profile (see Fig. 1.1) is observed to have an emission line next to a blue-shifted absorption line. The stellar wind gas cloud surrounding the star will emit light for a certain line transition (region H in Fig. 1.1) , and we will observe a range of Doppler shifts corresponding to velocities over $\pm v_\infty$. However, in the column of gas between the star and the observer (region F in Fig. 1.1), the light may be scattered out of the line of sight by wind atoms, causing an absorption line blue shifted (negative velocity) from the central emission. This absorption component may be completely black for a resonance line.

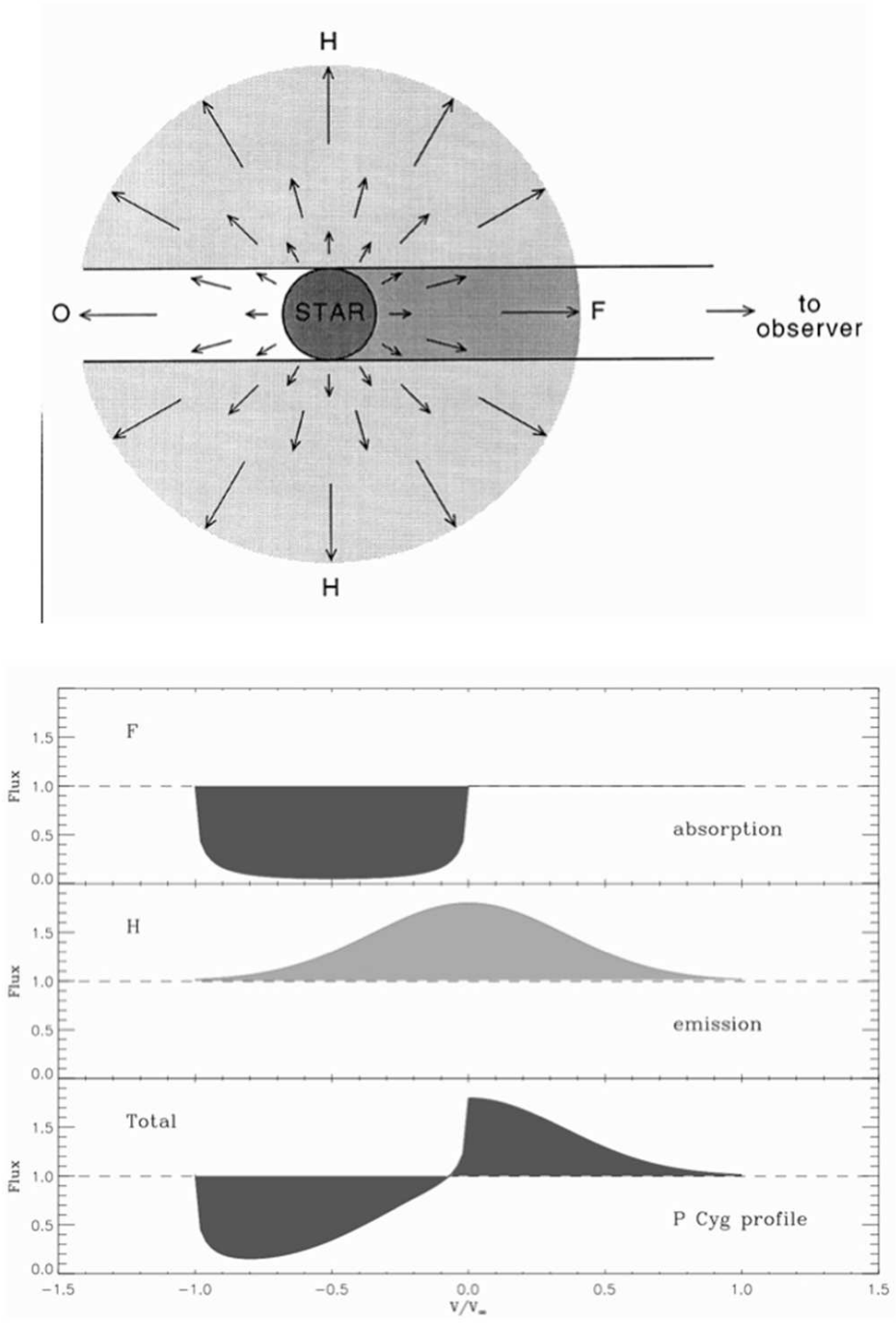

Figure 1.1 Formation of the P Cygni Profile. Reproduced with permission from Lamers & Cassinelli (1999). See text for details.

ll

Table 1.1 Types of Massive, Evolved Stars

Type	Description
LBV	See Section 1.5
Hot Supergiant	Hot star, narrow absorption lines, luminosity class I
Wolf Rayet	Hot star, strong wind, broad emission lines can be nitrogen enriched (WN) or carbon enriched (WC)
Hypergiant	Ia+ luminosity class, highly luminous supergiant ($M_V < -8$)
B[e]	large IR excess, B spectral type, allowed and forbidden em. lines

Lastly, hot stars with circumstellar environments, including winds, will show signs of an infrared excess in their spectral energy distribution. This will often show up in the NIR and is observed when the SED is compared with a typical star of similar spectral type without the excess gas. The hydrogen in this gas will be ionized from photons emitted by the star with energies greater than 13.6 eV, and the emission occurs when free electrons interact with the hydrogen nuclei through bound-free and free-free processes.

1.4 TYPES OF STARS MENTIONED IN THIS DISSERTATION

Luminous blue variables are the main star of interest in this dissertation, but several other types of stars populate the upper H-R diagram and will be occasionally used as comparison stars to the LBVs. These are tabulated in Table 1.1. In general, LBVs evolve from an O star progenitor and will evolve into either Wolf Rayet stars (more likely) or red supergiants (for the lowest initial masses that can become LBVs).

1.5 DEFINITION AND THE IMPORTANCE OF LUMINOUS BLUE VARIABLES

Very massive stars ($> 25 M_{\odot}$; Meynet & Maeder 2003) start their lives as O stars and will lose large amounts of mass as they pass through evolutionary stages such as red supergiants (RSG) and Wolf-Rayet (W-R) stars during their post-main sequence evolution (Crowther et

al. 1995). These most massive stars often go through the highly unusual stage of evolution that is observed in objects such as P Cygni and η Carinae: the Luminous Blue Variable (LBV, or S Doradus variable) stage. Some authors use the term S Doradus variable more than the term LBV. Here, I will primarily use the term LBV, as S Doradus is one of the stars mentioned, and this could cause confusion.

In the first major review paper on LBVs, Humphreys & Davidson (1994; hereafter HD94) explain the many criteria for a star to become a member of this class of objects. Here, I review these criteria based upon the work of HD94 unless otherwise noted. The "luminous" portion from the name requires that *these stars are extremely luminous*. The typical absolute magnitude for a normal LBV is $M_V < -9.5$, but there may be some related or similar objects with an $M_V \approx -8$, which corresponds to luminosities in the range of $10^{5.5-6.5} L_\odot$. These stars lie in the upper portion of the empirically determined Hertzsprung-Russell (H-R) diagram of temperature and luminosity. As a massive star runs out of H in its core and evolves beyond the main sequence, its atmosphere expands and cools. The stars that try to evolve to the red supergiant stage, but are as luminous as these LBVs, will encounter the Eddington luminosity limit (empirically, this is the Humphreys-Davidson (HD) limit; see Humphreys & Davidson 1979, 1984) and are unable to become red supergiants. Beyond the Eddington limit, the outward radiative force will exceed the inward gravitational force, causing the star to lose its outer atmosphere. An H-R Diagram of LBVs and other related stars is shown in Figure 1.2, with this empirical Humphreys-Davidson limit noted.

LBVs are subject to at least four types of *photometric variability*, which is the criterion of the "variable" part of the name. The first, the "giant eruptions" have amplitudes of ≥ 2 magnitudes in the visual. This variability is extremely rare, and has only been observed in a few stars. In the Galaxy, only P Cygni and η Carinae have been observed to exhibit such changes. The star HD 5980 in the Small Magellanic Cloud erupted in the 1990s (Koenigsberger et al. 2010), and the star R127 in the Large Magellanic Cloud recently recovered

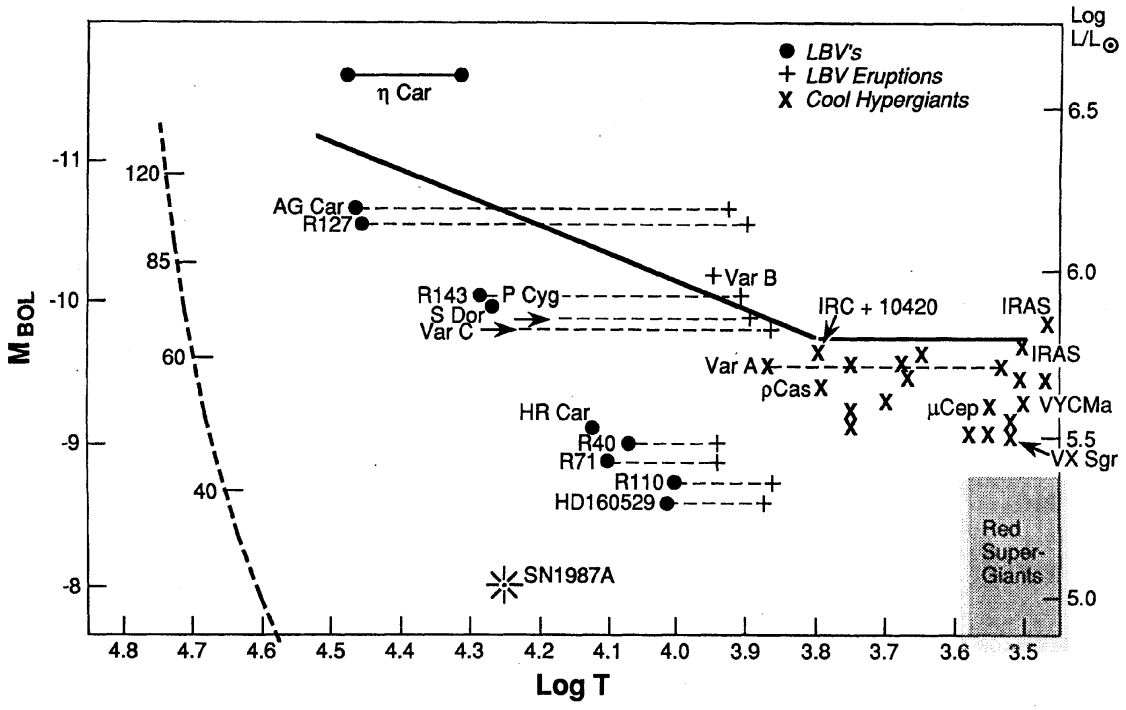

Figure 1.2 The upper H-R Diagram, showcasing the locations of famous LBVs such as S Dor and P Cyg. Horizontal lines show the observed temperature range. The classical "Humphreys-Davidson limit" is shown as a solid line (HD94), which represents the observed value for the Eddington limit. The zero-age main sequence is shown as a thick dashed line, and yellow hypergiants and red supergiants are marked as an 'X'. Diagram is reproduced with permission from HD94.

from a $\sim$ 30 year outburst (Walborn et al. 2008). Other examples are often called "supernova imposters" and are extragalactic in origin, and they are only seen in supernova surveys (Smith et al. 2011), except for both P Cygni and η Carinae in our Galaxy. This large-scale variability is not well understood, both from a theoretical standpoint and an observational perspective because of the small number of observations of such events.

On timescales of approximately 10–40 years, these stars exhibit large "eruptions" (as defined by HD94), also called long S Doradus-phases (long SD-phase; van Genderen 2001). I will refer to this as the long-SD phase or long term variability to avoid confusion with the "great eruptions." The term SD-phase originated with van Genderen et al. (1997) because

the mass loss rate is not seen to vary dramatically during these changes. These variations are typically on the order of 0.5–2 magnitudes, and the star appears redder when brighter in the optical. One of the discoveries relating to these variations is that the bolometric luminosity is roughly constant throughout this variability (see the horizontal dashed lines for LBVs in Fig 1.2). When the star brightens in the optical, the UV flux drops to keep the total integrated bolometric luminosity constant.

Similar to this is the short-SD phase (HD94 refers to these variations as "oscillations"), in which the stars display similar flux and color variations, but on timescales of less than 10 years (but usually at least 1 year in duration). It is unknown if the long SD and short SD-phases are of different underlying origin, but an LBV can exhibit both simultaneously.

These stars are also subject to microvariations that occur on timescales of a few days to about a month. These are similar to instabilities (α-Cygni variability) observed in other hot supergiants (e.g. Deneb; Richardson et al. 2011c). The amplitude is small, and these microvariations can be ignored when considering the long time scales and amplitudes of the long and short SD-phases or the great eruptions.

These stars have *strong stellar winds* that are often observed through spectroscopy. The winds show a strong thermal IR excess (e.g. P Cygni; Touhami et al. 2010) with strong emission lines from hydrogen, helium, and Fe II. These optical emission lines are usually strongest at optical minimum light due to the higher temperature at that time. At optical minimum, these stars will sometimes exhibit the spectral appearence of the unusual Of/WN9 stars (Groh et al. 2011) with temperatures ranging from 12,000–30,000 K, depending on the star. At visual maximum light, their spectrum may appear more like an A or F type supergiant (e.g. S Dor; Massey 2000), and the stellar atmospheric temperatures drop as low as 7000–8000 K. The entire temperature range lies above that of the Sun, and this is the reason for the term "blue" in the name, since they have colors bluer than the Sun.

The *typical mass loss rates that are observed for these stars are on the order of* 10^{-5} –

$10^{-3} M_\odot$ yr^{-1}, with an average around $2-3\times10^{-4} M_\odot$ yr^{-1} according to HD94. The expected lifetime for this stage is on the order of 25,000 yr, implying that the stellar wind alone (ignoring the giant eruptions for stars such as P Cygni or η Carinae) produces about 5 $M_\odot$ of ejected mass. This is comparable to the amount of mass that a massive 50–100 $M_\odot$ star must lose after burning all H in its core to become a Wolf-Rayet star (which is often the pre-SN stage for the most massive stars, HD94). Indeed, Massey, Waterhouse, & DeGioia-Eastwood (2000) found that the Magellanic Cloud clusters with LBV members have a main sequence turnoff around 85 $M_\odot$, implying an initial mass for these stars of at least 85 $M_\odot$.

The large stellar winds and great eruptions that are observed in these stars create *ejecta* around many of them (Fig. 1.3). The most famous ejection nebula is likely the Homunculus around the massive η Carinae system, which was observed several times by the Hubble Space Telescope (Davidson & Humphreys 1997) through a Treasury program that examined the spectroscopic and photometric variability for 10 years with excellent spatial resolution.

The LBVs have an interesting geometry surrounding them. The IR excess becomes visible in the optical as this excess is so large. The general schematic is shown in Figure 1.4, where the emitting regions for the $R-$, $H-$, and $K-$ bands are shown in comparison to the stellar photosphere and Hα emitting region.

LBVs provide us with the means to study the extremes of stellar wind phenomena. Studies of their high mass-loss rates, massive and large ejecta and circumstellar matter, variable temperature of the underlying stars, and changes that can happen in short timespans of a few years offer us a probe into the mass-loss physics of the most massive stars. In the interest of understanding the driving mechanisms of these winds, variability studies offer probes to the changes that are observed. Most studies to date have dealt with one (or a few) of these stars. No systematic spectroscopic study using homogeneous instrumentation for a significant fraction of the known LBVs has been performed before. This is the driving motivation for a portion of this dissertation, which also includes interesting case studies for

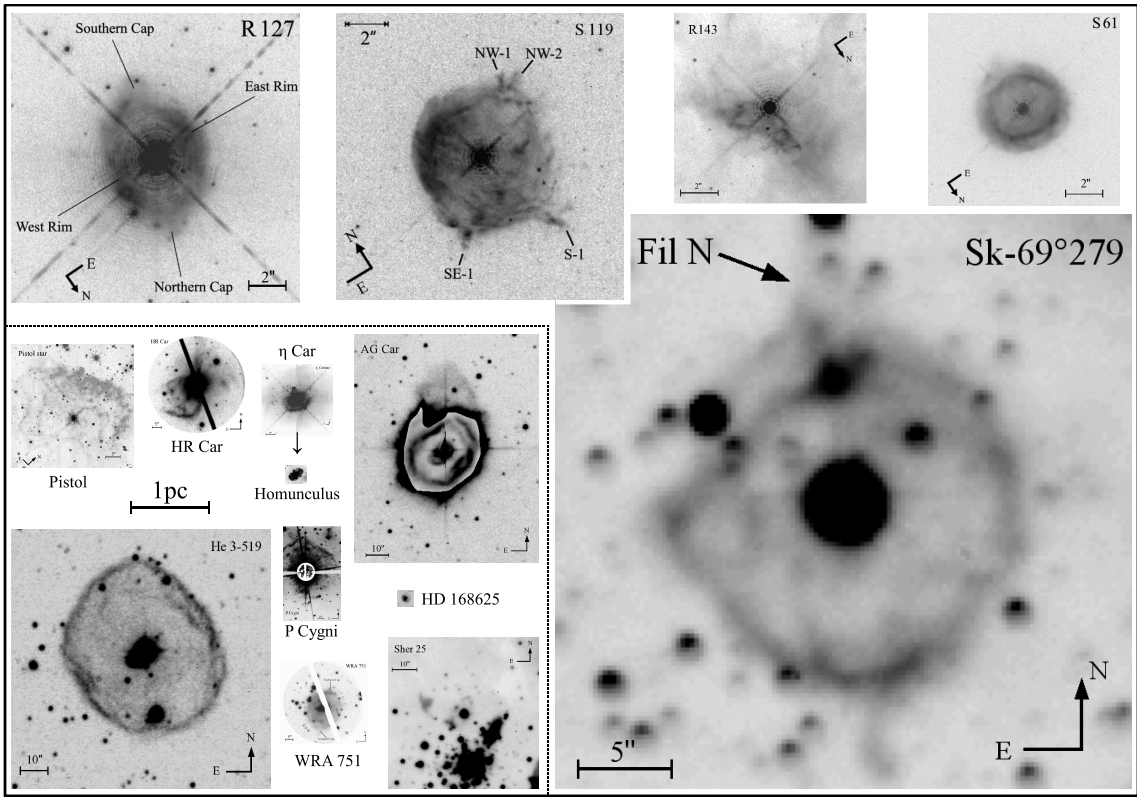

Figure 1.3 Ejecta surrounding LBVs, drawn to the same physical scale after correction for their individual distances. Diagram reproduced with permission from Weis (2011).

some of the more famous stars in this class.

1.6 BINARIES AND THE LBVS

In massive stellar systems, binaries are common, with more than 75% of O stars in associations or clusters being multiple systems (Mason et al. 2009). In favorable cases, we can measure their fundamental parameters through analysis of their spectroscopic and photometric variability. This is more complicated for LBVs. In the current literature, there are four confirmed binaries in the class, of which two are eclipsing.

The most famous of the two eclipsing binary LBVs is an unusual system in the Small Magellanic Cloud (SMC). This system, HD 5980, has a spectral appearance of a Wolf-Rayet

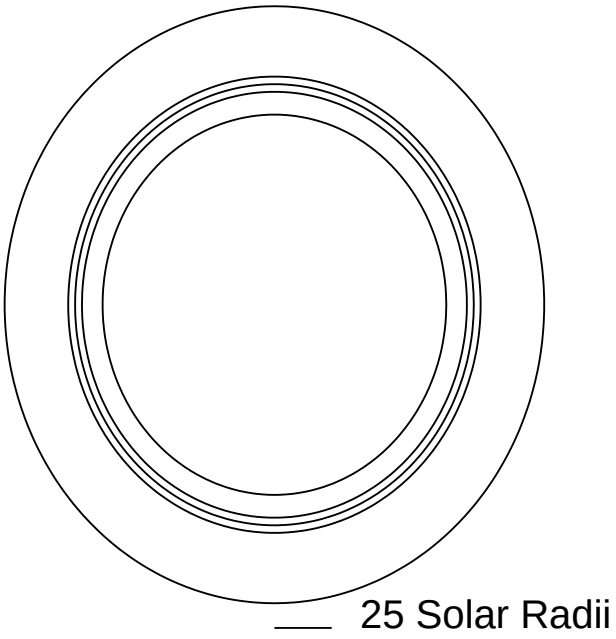

Figure 1.4 The geometry of an LBV wind. The central circle is the stellar photosphere, which is typically has a radius near 75 $R_{\odot}$. The next circles represent the expected emitting region sizes for the optical $R-$band, $H-$band, and $K-$band emitting regions, as predicted from spectroscopic models (Hillier & Miller 1998). The largest emitting region shown is for the optically bright emission line Hα. Changes in mass loss rate will make these regions become smaller or larger.

(WR) star (Koenigsberger et al. 2010, see Figure C). The system brightened suddenly in 1994, in an event similar to a giant eruption. However, this event was very short-lived in comparison to the Galactic eruptions of P Cygni or η Carinae, which was likely because of the close companion in the system that would pass through a large effective photosphere during this type of event. The central binary is a short period system (19.3 d), with a

moderate eccentricity in contrast with most orbits that become circular with time. The small semi-major axis (smaller than the derived radius of HD 5980A during the eruption) allows us a view of the interior of an LBV, as the secondary clears out material, keeping the primary's radius smaller. This makes this system crucial to modeling of the interiors of LBVs. Indeed the long-term variability (Koenigsberger et al. 2010) shows that the primary star is an LBV, and that even though the primary's spectrum appears as a W-R star (it is one of the hottest observed LBVs), the secondary has a great influence on the evolution of the system and the primary. The orbital elements and masses are shown in Table 1.2.

Table 1.2: Published Orbital Elements of HD 5980;
adapted from Koenigsberger et al. (2010)

Parameter	Value	Epoch	Reference
$P_{orbital}$	19.2654 d		Sterken & Breysacher (1997)
i	88°		Moffat et al. (1998)
a	127 $R_\odot$		Niemela et al. (1997)
	143–157 $R_\odot$		Foellmi et al. (2008)
e	0.30±0.16		Foellmi et al. (2008)
M_A	50 $M_\odot$		Niemela et al. (1997)
	58–79 $M_\odot$		Foellmi et al. (2008)
M_B	28 $M_\odot$		Niemela et al. (1997)
	51–67 $M_\odot$		Foellmi et al. (2008)
R_A	23–25 $R_\odot$	1978	Perrier et al. (2009)
	280 $R_\odot$	1994 (September)	Drissen et al. (2001)
	150 $R_\odot$	1994 (December)	Koenigsberger et al. (1998a)
R_B	16–17 $R_\odot$		Perrier et al. (2009)
L_A	$3\times10^6 L_\odot$	1994 (December)	Koenigsberger et al. (1998b)
L_A	$10^7 L_\odot$	1994 (September)	Drissen et al. (2001)
$T_{eff,A}$	21,000 K	1994 (November)	Koenigsberger et al. (1996)
$T_{eff,A}$	35,500 K	1994 (December)	Koenigsberger et al. (1998b)

The other known eclipsing system with an LBV as a component star is HDE 269128 in the Large Magellanic Cloud (LMC). The analysis of the photometric light curve and spectroscopy by Tubbesing et al. (2002) show that the system has stellar masses that are very uncertain. The derived masses have extremely large errors, but are $M_{LBV} = 14.3^{+48.7}_{-10.4} M_\odot$

and $M_2 = 3.7^{+18.7}_{-2.1} M_\odot$. During the primary eclipse, where the smaller star passes in front of the line of sight of the LBV, we observe an enhanced mass outflow in our line of sight, which is seen from large amounts of blue shifted P Cygni type absorption in all optical wind lines observed. As such, we can expect that mass-loss is larger through the Lagrangian point L_1, which is located between the LBV and the secondary.

The companions in these systems influence the system and the observations of these syetems. Binary interactions are thought to have played a role in the great eruption of η Carinae (e.g. Smith & Frew 2011). A fundamental question to ask is: *Are binary interactions a driving mechanism for the largest variability of these stars or is it a complication?* The answer can only be found by constraining the multiplicity and orbits of these stars. If binary interactions are a driving force, then we can begin to think about LBV eruption rates in relation to the multiplicity properties.

1.7 OUTLINE OF THIS DISSERTATION

Here, I will begin with an in-depth study of the first discovered LBV, P Cygni. Chapter 2 will discuss a long-term study of the Hα profile in the spectrum of P Cygni. Chapter 3 will examine interferometric observations of P Cygni made with multi-baseline $H-$band measurements made with the CHARA Array and MIRC beam combiner. This is combined with a near-infrared spectrophotometric study that was carried out simultaneously. I will also discuss future efforts that can be accomplished with the Array in the area of stellar winds. The other prototypical Galactic LBV is η Carinae, which posseses both typical LBV properties and has a binary companion star in a long period, highly eccentric orbit. In Chapter 4, I present a detailed study of η Carinae during the recent periastron passage to explore how the companion influences this LBV's wind. Chapter 5 will show how an unusual LBV candidate, HDE 326823, is a binary where Roche lobe overflow causes the observed variability and spectral appearance. In Chapter 6, I detail a long-term survey of LBVs using

optical spectroscopy. This chapter shows how the sample stars' amplitudes of variability are related to strength of their winds, and then provides a simple way of determining if other stars have this type of variability present. I conclude in Chapter 7 with thoughts on future observational efforts that can be obtained with modern instrumentation, including GSU's Hard Labor Creek Observatory, and long-term observational studies of stellar winds.

2
THE Hα VARIATIONS OF THE LUMINOUS BLUE VARIABLE P CYGNI: DISCRETE ABSORPTION COMPONENTS AND THE SHORT S DORADUS PHASE

The results portion of this thesis will begin with a detailed study of the wind of the famous star P Cygni[1]. P Cygni was discovered in the year 1600 when it experienced a great eruption and became visible in the constellation Cygnus at the time. It was one of the first variable stars discovered (along with the supernovae of Tycho and Kepler) and is considered a prototypical LBV because of this eruption.

2.1 INTRODUCTION TO P CYGNI

Luminous Blue Variables (LBVs or S Doradus variables) are evolved, massive stars. LBVs are characterized by large mass loss rates and variability on multiple timescales. The two "prototypical" Galactic LBVs are η Carinae and P Cygni, and they probably represent different extremes of mass loss rate within the scheme of LBV evolution (Israelian & de Groot 1999) as these stars likely have very different masses. One of the defining criteria of the LBVs is the observation of a large scale eruption, when the star brightens by several magnitudes. The quiescent times between these eruptions may last centuries. In addition to such rare, giant eruptions, these stars also display lesser photometric and spectroscopic variations on other timescales (e.g. Humphreys & Davidson (1994)). van Genderen (2001) defines the S Doradus (SD-) phase to be the moderate, long-term, brightening and fading phases. There are two types of these phases, short and long, with similar characteristics. The short SD-phase is typically on the order of years (< 10 years), while the longer SD-phase is on a timescale of decades. These phases are thought to originate from changes in the star's photosphere, and both may have the same physical driving mechanism. These long-

[1]Originally published as Richardson et al. (2011b).

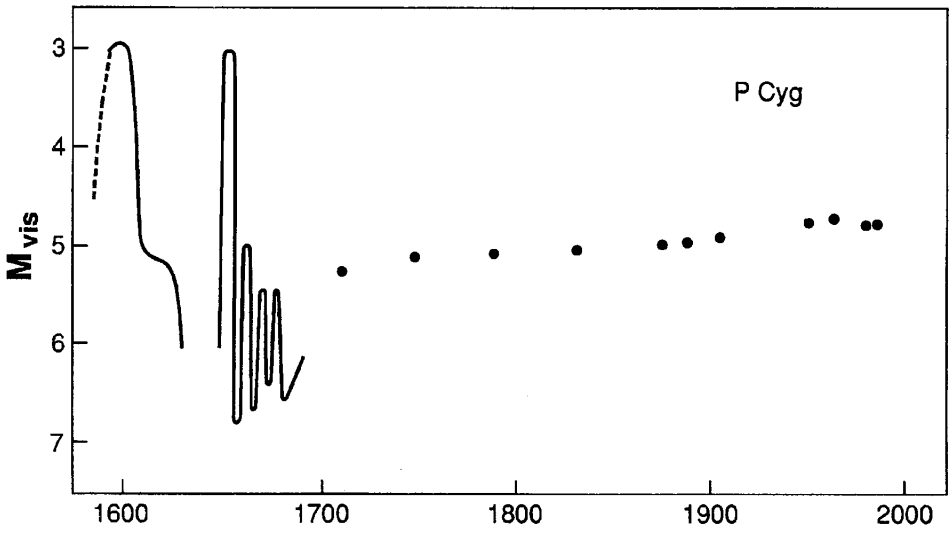

Figure 2.1 A historic light curve of P Cygni, as presented by Humphreys & Davidson (1994)

term variations are observed to differ from cycle to cycle, both in duration and amplitude (Sterken et al. 1997b).

P Cygni (HD 193237, HR 7763, Nova Cyg 1600) remains one of the most fascinating objects in the sky. It was discovered during its first recorded great eruption in 1600 by Willem Janszoon Blaeu, a Dutch chart-maker and mathematician. During this eruption, the star brightened to about 3rd magnitude for about six years, and then it faded from visibility by 1626. It rose again in 1654 to about the same maximal brightness, where it remained for five years. The star faded after this, and although its long-term variability is poorly documented, the star has been slowly brightening to its current magnitude of about 4.8 (Israelian & de Groot 1999). The slow brightening may reflect evolutionary changes (de Groot & Lamers 1992; Lamers & de Groot 1992; Langer et al. 1994). The historical light curve, including the great eruptions of the 17th century, is shown in Figure 2.1.

Long-term photometric monitoring of P Cygni began in the 1980s when Percy & Welch (1983), Percy et al. (1988), and de Groot (1990) embarked on extended observing campaigns. Their observations showed that the variations often occur on three characteristic timescales:

a short ~ 17 day variation similar to the α Cygni type variations observed in hot supergiants, a ~ 100 day "quasi-period" similar to that observed in other LBVs, and a long-term cycle (years) attributed to a short-SD phase (de Groot et al. 2001; Percy et al. 2001).

According to Israelian & de Groot (1999), comprehensive spectral monitoring of P Cygni was started by Luud (1967) and Markova (1993), among others. The first long-term spectroscopic monitoring campaign of P Cygni was presented in seminal papers by Markova et al. (2001a,b). They found evidence of co-variability of the Hα emission line strength and Johnson UBV photometry, indicating a short-SD phase with a quasi-period of $\sim$7 years, although their observations did not fully cover two cycles. The variations were attributed to inversely correlated changes in effective temperature and radius, maintaining a nearly constant luminosity. A similar cycle time was found by de Groot et al. (2001), who reported on photometric variations which were consistent with a timescale of 5.5 to 8.5 years.

In addition to the large scale variations in emission strength, Markova (2000) found that there are at least four other kinds of line profile variability in the spectrum of P Cygni. The most striking of these is the long documented appearance of blueward-migrating, absorption sub-features that are called Discrete Absorption Components (DACs: Israelian & de Groot 1999; Markova 2000). These are generally observed in low and intermediate excitation state lines in the optical (Markova 2000) and UV spectrum (Israelian et al. 1996). They are frequently detected in the upper sequence of the H Balmer lines (principal quantum number $9 \leq n \leq 15$; Markova 2000), but to our knowledge, DACs have not been reported before now for the absorption component of Hα. DACs are often (but not always) narrow (FWHM $\approx 10 - 15$ km s^{-1}) and may be unresolved in low-dispersion spectra. The DACs tend to appear over a radial velocity range of -90 to -200 km s^{-1} with an acceleration of -0.1 to -0.6 km s^{-1} d^{-1}. A recurrence timescale of ~ 200 d is sometimes observed (Markova 1986; Israelian et al. 1996; Kolka 1998). These accelerations are much slower and the timescales are much longer than those associated with DACs in the winds of O-stars (Kaper et al.

1999). The DACs in the spectrum of P Cygni may form in outward moving and dense shells (Lamers et al. (1985); Markova 1986a; Israelian et al. 1996), in spiral-shaped co-rotating interaction regions (CIRs) (Cranmer & Owocki 1996; Markova 2000), or in dense clumps in the wind (Lépine & Moffat 2008).

In this chapter, we present new high resolution Hα spectroscopy, which we combined with previous measurements by Markova et al. (2001) to explore the characteristics of P Cygni's short SD-phase. We also compare this with archival Johnson V photometry and new observations obtained by AAVSO observers. Section 2.2 describes the observations. In Section 2.3, we present the analysis of long-term variations of the continuum and the Hα equivalent width. We describe the Hα profile morphology changes and DAC propagations in Section 2.4. The discussion and conclusions are presented in Section 2.5.

2.2 OBSERVATIONS

We obtained 126 new spectroscopic observations of P Cygni using the University of Toledo's Ritter Observatory 1 m telescope and échelle spectrograph (Morrison et al. 1997) between 1999 June 7 and 2007 October 30 (PI N. D. Morrison). These high resolving power ($R = 26,000$) spectra were reduced by standard techniques with IRAF[2]. Observations collected prior to 2007 were taken using the setup described in Morrison et al. (1997). These observations record a 70 Å range in the order centered on Hα, and they typically have a signal-to-noise ratio between 50 and 100 per resolution element in the continuum. Observations made during the calendar year 2007 were taken with the same spectrograph, except the camera was a Spectral Instruments 600 Series camera, with a front-illuminated Imager Labs IL-C2004 4100×4096 pixel sensor (15×15 micron pixels). To maintain consistency with the older observations, the camera was operated with 2×2 pixel binning. The newer observa-

[2]IRAF is distributed by the National Optical Astronomy Observatory, which is operated by the Association of Universities for Research in Astronomy, Inc., under cooperative agreement with the National Science Foundation.

tions recorded a larger portion of the order centered on Hα and typically reached a signal to noise ratio between 50 and 100 per resolution element in the continuum. We trimmed these spectra so that the wavelength range was the same as in the older data. The spectra taken after 2002 September have poor wavelength calibration due to problems with the Th-Ar lamp. In order to use these spectra for kinematical measurements, the telluric H_2O lines in the vicinity of Hα were fitted to improve the solution. This worked for most cases, but the errors associated with the telluric re-calibration are roughly ± 3 km s^{-1}, compared with the errors for earlier data of ± 1 km s^{-1}.

We collected V-band photometry from three sources. The first was from Markova et al. (2001). This provided concurrent photometry for the Hα data previously published. The second set came from Percy et al. (2001)[3]. These observations also ended at nearly the same time as the first data set. Finally, we downloaded the photoelectric photometry in the V-band from the American Association of Variable Star Observers (AAVSO). The AAVSO data are helpful in understanding the long-term trends, and we only used data where measurements of the check and comparison stars differed from expected values by less than 0.05 mag. The errors in the AAVSO measurements are typically around 0.01 mag, comparable to those of Markova et al. (2001) and Percy et al. (2001). The combined set contains 3142 measurements from 1985 to 2009.

2.3 THE LONG-TERM PHOTOMETRIC AND Hα EQUIVALENT WIDTH VARIABILITY

Markova et al. (2001) found that the Hα line flux, obtained by correcting the observed equivalent widths for the changing continuum, varied in concert with the V-band flux over the period from 1989 to 1999 (see their Fig. 3). Here we extend their work by considering the long-term photometric and Hα variations through 2007. Figure 2.2 shows the large time

[3]Available for download at http://schwab.tsuniv.edu/papers/paspc/pcyg/pcyg.html

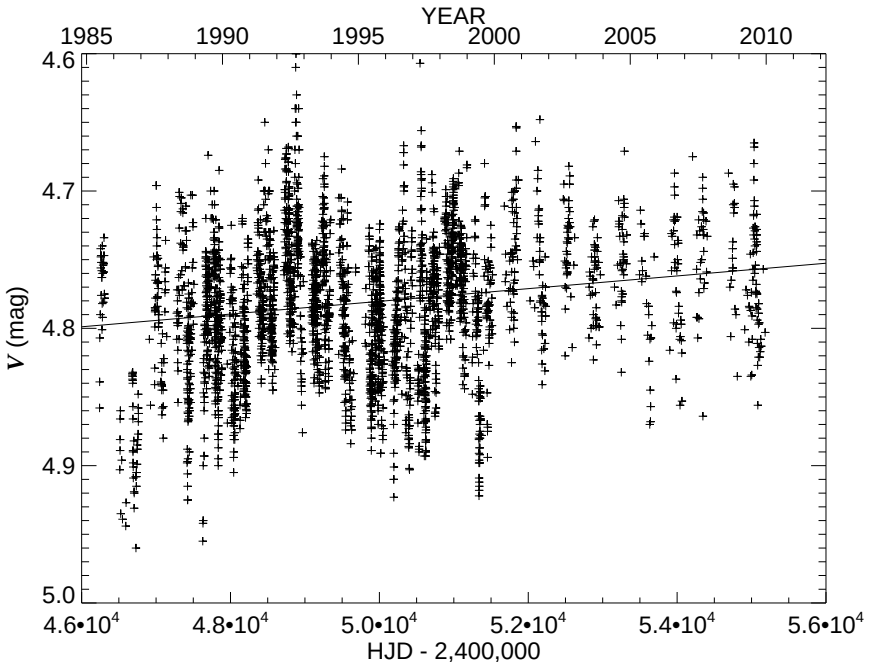

Figure 2.2 The V-band variability of P Cygni between 1985 and 2009. The long-term changes are representative of the short SD-phase. We overplotted the fit for the very-long-term brightening of the star with a solid line.

span of available photometry. The light curve over this interval shows rather modest, ± 0.1 mag variations, consistent with the star's classification by van Genderen (2001) as a "weak-active" LBV. It exhibits the kind of variability associated with a short SD-phase, similar to that reported by Markova et al. (2001). The short SD-phase is most evident in the data prior to 2000, when the star experienced two fadings of ≈ 0.1 mag (Markova et al. 2001; Percy et al. 2001). The amplitude of this long-term variability decreased in subsequent years, which indicates that the properties of the short SD-phase change with time. We made a fit of the very-long-term trend and found a brightening rate of $\approx 0.17 \pm 0.01$ mag century^{-1} (overplotted in Fig. 2.2). This rate is consistent with the very-long-term trend of 0.15 ± 0.02 mag century^{-1} documented by de Groot & Lamers (1992).

Figure 2.3 presents the "dirty" discrete Fourier Transform (Roberts et al. 1987) of the

24.5 y V-band photometry with the long-term brightening (Fig. 2.2) removed. There are no individual significant peaks in the periodogram, but there is a general tendency for more power to appear at the longer timescales (lower frequencies). Thus, the longer timescales of the short SD-phase variability tend to dominate the light curve.

We measured Hα emission strength for both the new and originally reported spectra (Markova et al. 2001) for a total of 158 measurements covering the interval from 1994 to 2007. Equivalent widths of the full Hα profile (including both the blue absorption and large emission component) were measured in the same manner as done by Markova et al. (2001) in order to keep the data sets mutually consistent. The only improvement is that telluric H_2O lines in the vicinity of Hα were removed by means of a template fitting procedure (`telluric`) in IRAF. This correction resulted in equivalent width increases of less than 2%. This is much smaller than the typical measurement error of 6% (as found by comparing equivalent widths from closely spaced observations, $\Delta t < 2$ d, where the variability of this star is minimal). Since the available wavelength range around Hα does not extend beyond the electron scattering line wings to the actual continuum levels, a multiplicative constant was used to retrieve the full equivalent width of the line. This correction, W_λ(net) = 1.096 W_λ(Ritter), accounts for unseen line wing flux and unmeasured flux lying below our continuum placement (over an integration range of 6531.5 to 6593.5Å) and is identical to that adopted by Markova et al. (2001) for the Ritter data. The heliocentric Julian dates and net adjusted equivalent widths are tabulated in columns 1 and 2 of Table B.1.

The actual line flux of Hα can be estimated by correcting the measured equivalent widths for the changing continuum. In order to make this transformation, we averaged the V-band measurements made within 20 days of each spectroscopic measurement. This time span was chosen to cancel any small but fast variations and to include enough measurements for a reliable average. We compared all the photometry measurements to a benchmark V=4.8 to remain consistent with the flux correction adopted by Markova et al. (2001). The equivalent

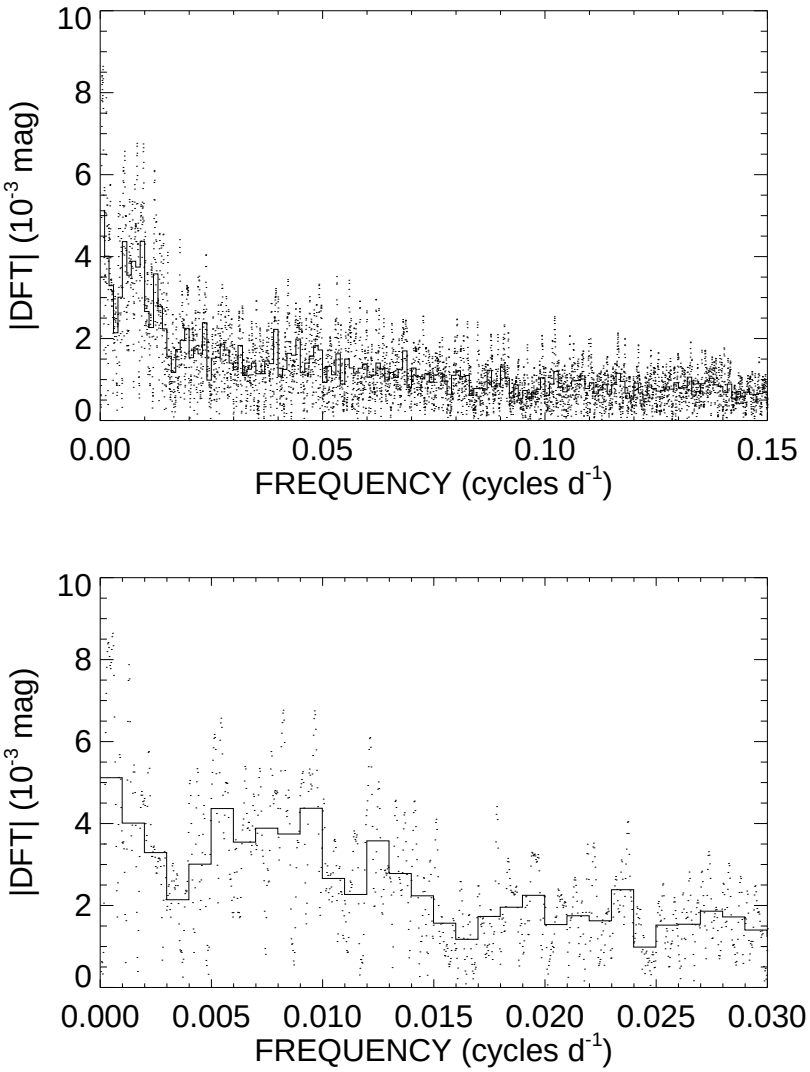

Figure 2.3 Discrete Fourier transforms of the V-band photometry. The bottom panel shows a close up of the long timescale region that is associated with the short-SD phase and 100 d timescales of variability. The overplotted stair steps show the amplitudes rebinned into increments of 0.001 cycles d^{-1}.

widths were corrected using the relationship

$$W_\lambda(\mathrm{corr}) = W_\lambda(\mathrm{net})10^{-0.4(V(t)-4.8)}.$$

The averaged V magnitudes and flux corrected equivalent widths are given in columns 3 and 4 of Table B.1. If no V magnitude was available within $\pm$20 days, then no correction was applied, which affects 18 of our measurements. These correction factors are usually small ($\approx 4\%$) and comparable to the photometric scatter within each time window.

We show the temporal variations in the flux corrected equivalent widths in Figure 2.4. The plot includes earlier measurements from Markova et al. (2001), the new measurements from Table B.1, and some additional measurements from 2005 to 2007 from Balan et al. (2010). There are two maxima (occurring around 1992 and 2002) that are separated by $\approx$ 10 years, which is longer than the reported lengths of the short SD-phase found by Markova et al. (2001), de Groot et al. (2001), or Percy et al. (2001). Furthermore, the rise and fall around the peak in 1992 are steeper than that for the 2002 peak. There is also ample evidence of faster variability within each observing season that appears to be unrelated to the longer term trends.

A visual comparison of the V-band photometry in Figure 2.2 with the flux-corrected Hα equivalent widths in Figure 2.4 immediately shows some variations in common. We found that the relative flux (from the time interpolated magnitude) is positively correlated with the corrected equivalent width. A linear fit yields a slope of $\triangle(F/ < F >)/\triangle(W_\lambda/ < W_\lambda >) = 0.16 \pm 0.01$, confirming the visual impression of co-variability. In order to compare directly the photometry and Hα equivalent widths, we removed the long-term linear trend from the photometry (Fig. 2.2), performed a running average of the photometry differences using a Gaussian weighting scheme parametrized by a Gaussian FWHM, transformed the resulting flux differences into a variation in Å units according to the correlation slope given

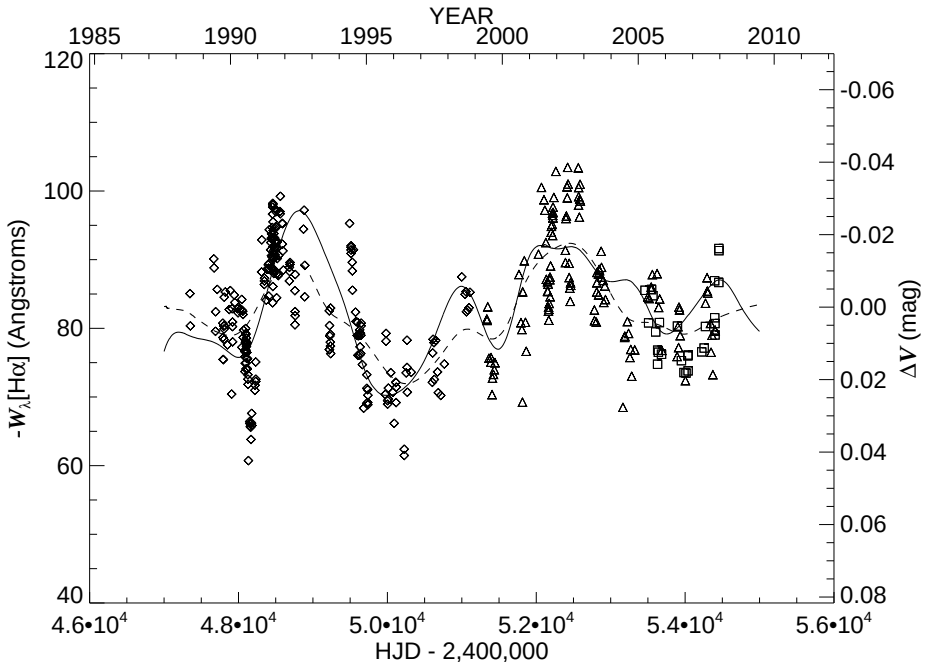

Figure 2.4 A direct comparison of the smoothed V-band photometry (solid line) and the flux corrected Hα equivalent widths. The photometric light curve is a running average of the V-band flux that was re-scaled and offset to match the equivalent width variations (see text), with the scale of the differential light curve given on the secondary y-axis. A running average of the corrected equivalent width measurements is also overplotted as a dashed line. The equivalent width measurements from Markova et al. (2001) are denoted by diamonds, our new measurements are represented as triangles, and the measurements of Balan et al. (2010) by squares. Uncertainties are comparable to the size of the points.

above, and then added the mean equivalent width to the final result. We made a number of trial comparisons by varying the adopted Gaussian FWHM to smooth the photometry, and the best fit with FWHM = 598 d is shown as a solid line in Figure 2.4. For completeness, we also plot a similar running average of the Hα equivalent widths as a dashed line. The agreement between the temporally smoothed photometric and flux corrected Hα variations is striking and it appears to confirm the positive correlation first noted by Markova et al. (2001a). The fact that smoothing parameter values smaller than 598 d yield worse fits suggests that the co-variations are less correlated on shorter timescales. Taken at face value,

this result indicates that the continuum and Hα emission fluxes sample structures in the wind in different ways (probably because of different sites of formation in the outflow). Finally, we note that the correlation also exists between the running averages of the continuum flux and the uncorrected equivalent widths W_λ(net), so the covariations are unrelated to the flux correction procedure.

2.4 Hα PROFILE MORPHOLOGY VARIABILITY

2.4.1 Emission Component Changes

The large Hα equivalent width variations described in Section 2.3 are accompanied by changes in the morphology of the profile. We present two individual spectra in Figure 2.5 that represent the extrema of the equivalent widths observed (a minimum at HJD 2,450,004, plotted with a dashed-dot line, and a maximum at HJD 2,452,070 plotted with a solid line). It is clear that the profile experiences a change in the peak emission intensity, the line width, the net profile velocity, and the shape of the blue absorption trough. For each of the spectra collected at Ritter Observatory we measured the peak intensity above continuum level, I_p, which was corrected for the changing continuum level in the same manner as the equivalent width (§3), the FWHM (profile width) of the emission portion of the profile above continuum, and a relative radial velocity $\triangle V_r$, derived by cross-correlating each profile against an unweighted average of all the spectra obtained at Ritter Observatory. We chose to use a cross-correlation technique because this method is model-free and is most sensitive to the steep emission line wings, resulting in a measure similar to a FWHM bisector velocity. The resulting measurements of FWHM and $\triangle V_r$ are shown for these two profiles in Figure 2.5 with horizontal and vertical lines, respectively.

All these measurements are given in columns 5, 6, and 7 of Table B.1, and are plotted as a function of time in the three panels of Figure 2.6. We see that times of strong emission

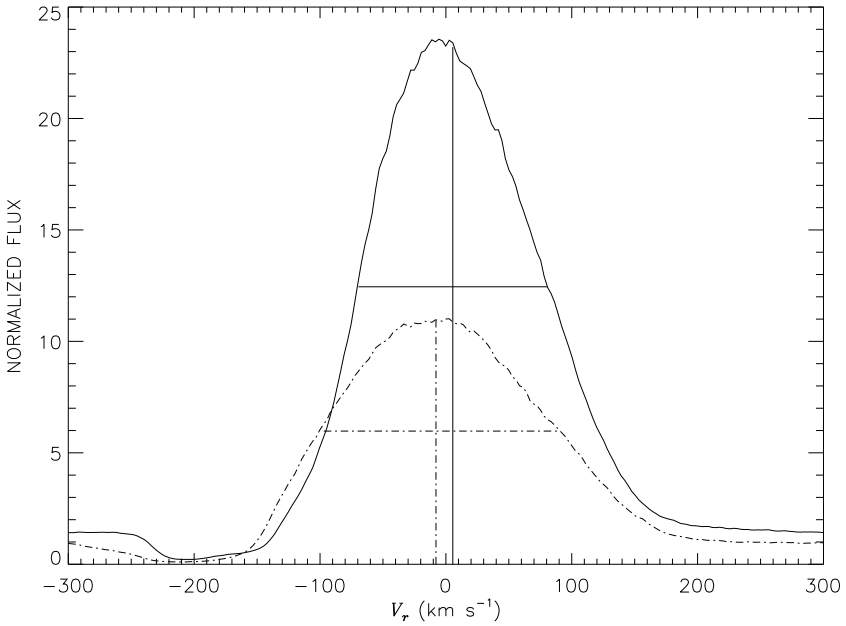

Figure 2.5 A comparison of two observed Hα profiles corresponding to extremes of the emission variability (maximum and minimum in corrected equivalent width). The spectrum plotted as a solid line is from HJD 2,452,070, while that shown as a dash-dot line is from HJD 2,450,004. Vertical and horizontal line segments show the velocity offset $\triangle V_r$ and the FWHM range, respectively.

(for example, HJD 2,452,500; see Fig. 2.4, MJD $5.25{\cdot}10^4$) correspond to profiles with the largest peak intensity and smallest FWHM. We also see a small radial velocity shift that is correlated with the long-term variations. The profile had the largest (most positive) velocity when the line flux at the position of the emission peak was strongest, which was also when the profile showed the smallest FWHM (Fig. 2.6). This is likely due to changes in the P Cygni absorption component. When the profile has the most emission, the blue absorption portion appears to shift to a more positive velocity and removes more of the blue side of the emission peak (see Fig. 2.5), and thus, the net radial velocity tends toward a larger (more positive) value at those times. We find that the measurement errors for $\triangle V_r$ and the FWHM are about 1 km s^{-1}, which adds in quadrature to the calibration errors discussed in §2, to

yield net errors of approximately ± 1.5 km s^{-1} for most of the data, and ± 3.2 km s^{-1} for data taken after 2002 September. The errors for I_p are on the order of $3-5\%$.

Kashi (2010) has suggested P Cygni is a binary system with a fainter B-type companion and that small long-term radial velocity variations due to reflex motion might be observed in extended high resolution spectroscopic observations. This cannot be the explanation for the $\triangle V_r$ changes we observe, since the Hα emission is formed over a volume that is much larger in radius than the predicted semimajor axis of the putative orbit of the P Cygni primary star. Wind gas leaving the star at any instant would have a Keplerian orbital component that decreases with distance from the center of mass. As the gas packet moves out to the radius where Hα becomes optically thin and emits the photons we observe (at $\approx 10R_\star$ and larger; see below), the radial outflow component will increase by radiative driving while the orbital motion component will drop with distance to conserve angular momentum. Thus, at the large distance of line formation, the gas motion will be almost completely radial. If the putative companion is to be found from radial velocity variations of this star, then detailed analyses of photospheric or wind lines formed very close to the star will need to be analyzed. Further, these radial velocity variations are not strictly periodic, and cannot be considered orbital motion. Lastly, given the method of measuring these velocities, the measured radial velocity is at least partially due to morphological changes in the Hα line profile.

2.4.2 Blue Absorption Changes

We used all of the Hα spectra from Ritter Observatory, including those that were measured by Markova et al. (2001), to investigate the variations in the blue absorption trough of the P Cygni profile. This portion of the profile is especially interesting as it is formed in the outflowing gas along our line of sight to the star. In order to emphasize the relative changes in line absorption, we first formed a reference, average high-intensity, minimum-absorption spectrum, as follows. At each wavelength step, we ordered the time-series by

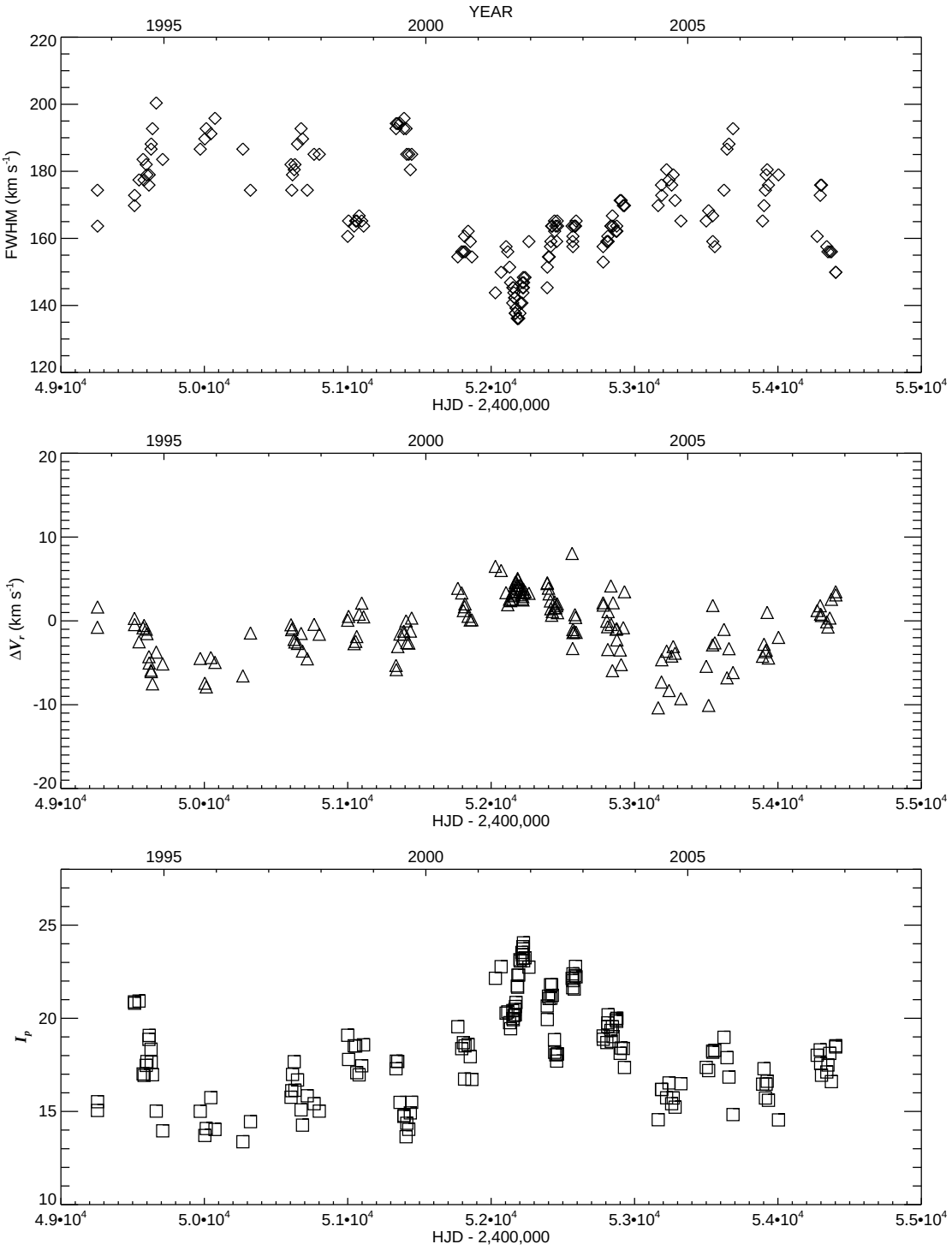

Figure 2.6 The long-term variability of the FWHM (top panel), the relative radial velocity $\triangle V_r$ (middle panel), and flux corrected peak intensity I_p (bottom panel) of the emission peak of the Hα profile. The long timescales of variability are similar to those seen in the V-band photometry and the Hα equivalent widths (Fig. 2.4). Uncertainties are comparable to the symbol sizes.

intensity and then constructed the average of all the intensities falling between the 90th and 95th percentiles at that wavelength step. This removed any spurious peaks caused by cosmic rays from contaminating the minimum absorption average. We then divided each of the spectra by this reference spectrum to form a matrix of quotient spectra. Since we are interested in the variability of the central absorption, and not that of the far wings, and because the line wings never reach the continuum in the region recorded, the quotient spectra had a depressed continuum. We then re-normalized these to a unit continuum (outside of the velocity region $\pm$500 km s^{-1}). These spectra are illustrated in a gray-scale dynamical spectrum in Figure 2.7. In this figure, we present each quotient spectrum as a function of radial velocity and time with a gray-scale intensity between the minimum value (black; 0.14 in the quotient) and maximum value (white; 1.75 in the quotient) based upon a linear time interpolation between the nearest observations (indicated by arrows). The low absorption reference spectrum is displayed for comparison in a panel below the gray-scale image. For simplicity, these quotient spectra were not corrected for the variable continuum flux since we are interested in both emission and absorption changes.

We need to bear in mind that the low absorption spectrum was formed by different subsamples at each wavelength point, and this has important consequences for the appearance of the dynamical spectrum. For example, inspection of Figure 2.5 shows that blue absorption core can extend to high negative velocities (dash-dot line) while at other times the blue absorption is limited to moderate velocities (solid line). Thus, the construction of the low absorption spectrum will be dominated by the latter examples in the vicinity of the blue absorption edge, and in our collection of Hα spectra, the more extended blue absorption occurred much more frequently. Consequently, the quotient spectra in Figure 2.7 appear to be dominated by a blue absorption feature, near $-$220 km s^{-1}, except near HJD 2,452,500 (MJD $5.25{\cdot}10^4$) when the blue edge moved to a more positive velocity. This feature is due entirely to our selection of spectra from around HJD 2,452,500 in making the low absorp-

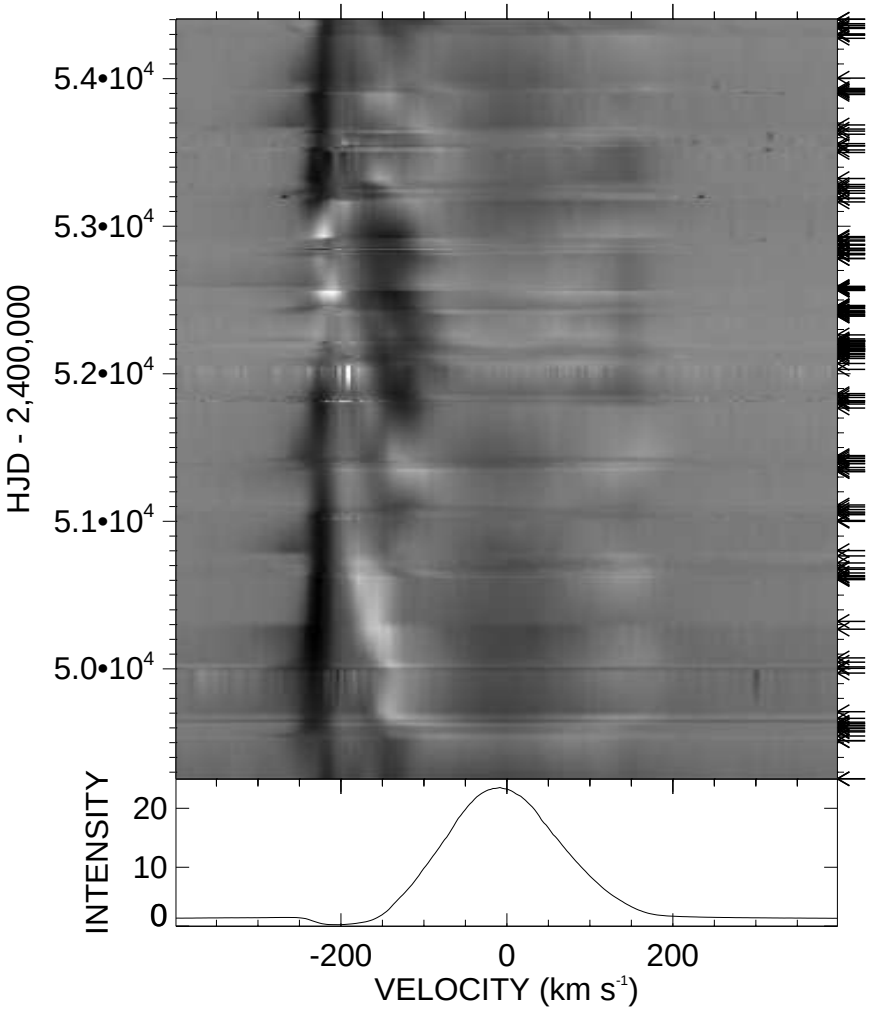

Figure 2.7 A dynamical spectrum showing the quotient of the Hα spectra and a constructed low absorption profile (shown in the lower panel) as a function of radial velocity and time. The blueward moving features are the DACs, which are almost always present in Hα. The gray-scale image is formed by a time interpolation (over 100 d in some rare cases) to fill in observational gaps in the data. Arrows on the right of the diagram indicate the dates of observation. The range of the plot is from 0.14 (black) to 1.75 (white) in intensity ratio. The original spectra, as well as the maximum intensity profile, are available in a supplementary file in the online version of Richardson et al. (2011b).

tion spectrum. We made this selection for our template so that the subfeatures appear in absorption most of the time.

We also see evidence in Figure 2.7 of several blueward moving, absorption features (in the velocity range between -100 and -200 km s^{-1}) that appear morphologically similar to the Discrete Absorption Components (DACs) observed previously in other spectral lines (Israelian & de Groot 1999; Markova 1986a, 2000). Figure 2.8 is a montage of a subset of the quotient spectra. It shows how the DAC (center) moved progressively blueward over this time span ($\approx$ 800 d). There are times where the regions between successive DACs appear bright in the dynamical spectrum, which correspond to those cases (usually sparsely sampled in time) where the flux was higher than the mean in the 90% to 95% part of the flux distribution that defined the minimum absorption spectrum. Finally, we see in the gray-scale image of Figure 2.7 the long-term variations in peak intensity (I_p) and wing extension (FWHM) that are associated with the short SD-phase, equivalent width variations (Fig. 2.6).

We measured the variability of the quotient spectra by calculating the standard deviation at each pixel of velocity space. This standard deviation spectrum is shown in Figure 2.9. There is a broad feature centered at rest velocity which is associated with the varying peak height of the profile. Another feature is present at $\sim +150$ km s^{-1}, which could be caused by either the variations in the profile width (FWHM) or red emission wing variability from traveling bumps (Markova 2000). The largest two features are from the DACs (seen as a broad peak around -140 km s^{-1}) and from the variations present near the blue edge of the absorption core (visible as a peak centered at -220 km s^{-1}).

Figures 2.5, 2.7, 2.8, and 2.9 all demonstrate that there are significant changes observed in the profile near the blue edge of the absorption core. The blue-edge velocity of a P Cygni profile is generally set by the position where the absorption core rises to intersect with the local continuum, and this velocity corresponds to the fastest moving gas projected against the disk of the star. However, in the case of Hα in the spectrum of P Cygni, this location is

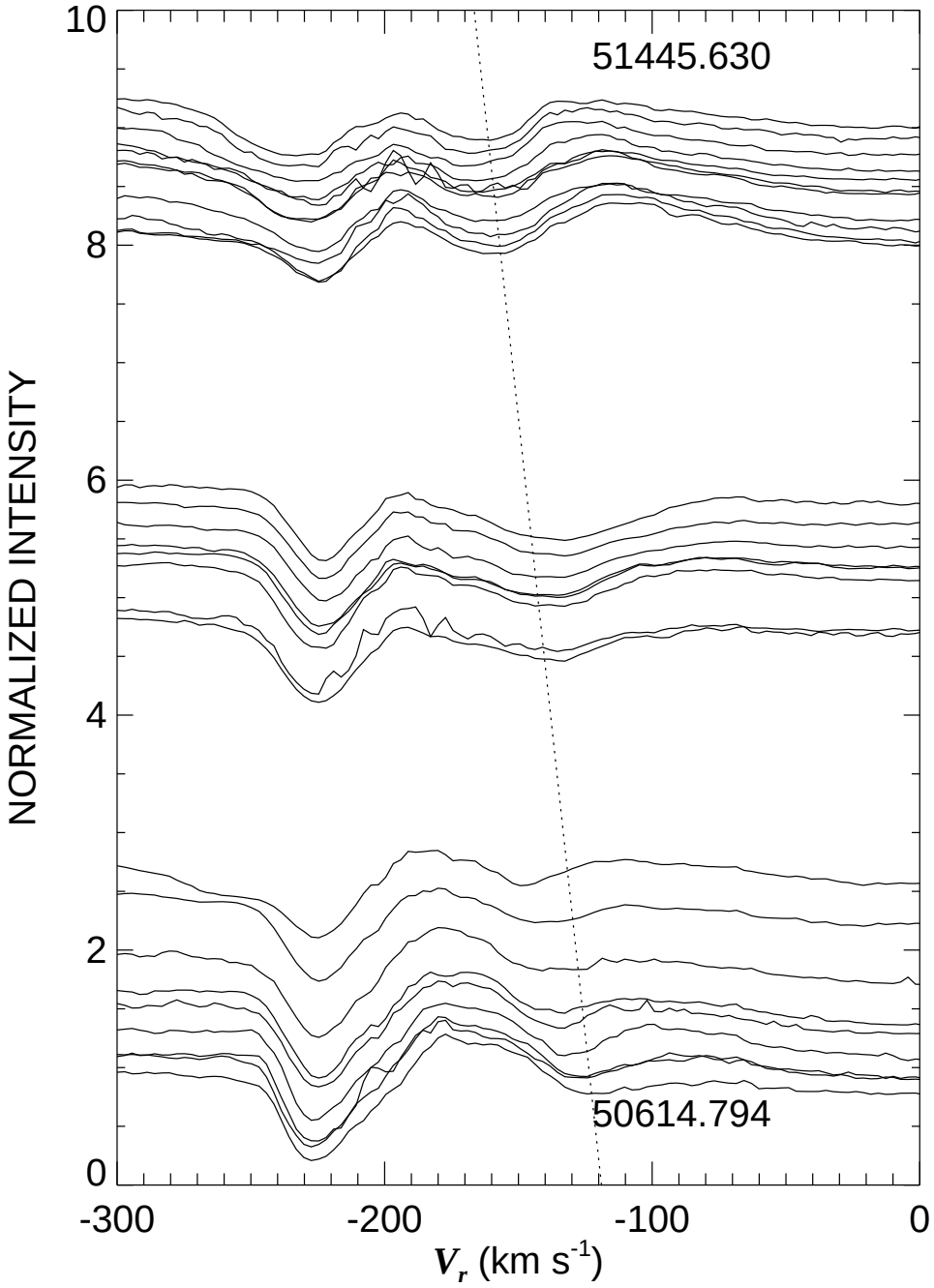

Figure 2.8 A series of quotient spectra offset according to the time of observation (HJD − 2,400,000 indicated for the first and last spectrum in this sequence). The DAC present migrated from approximately −125 km s^{-1} to −160 km s^{-1} over this interval. The dotted line represents a linear fit to the measured centroid velocities for this DAC.

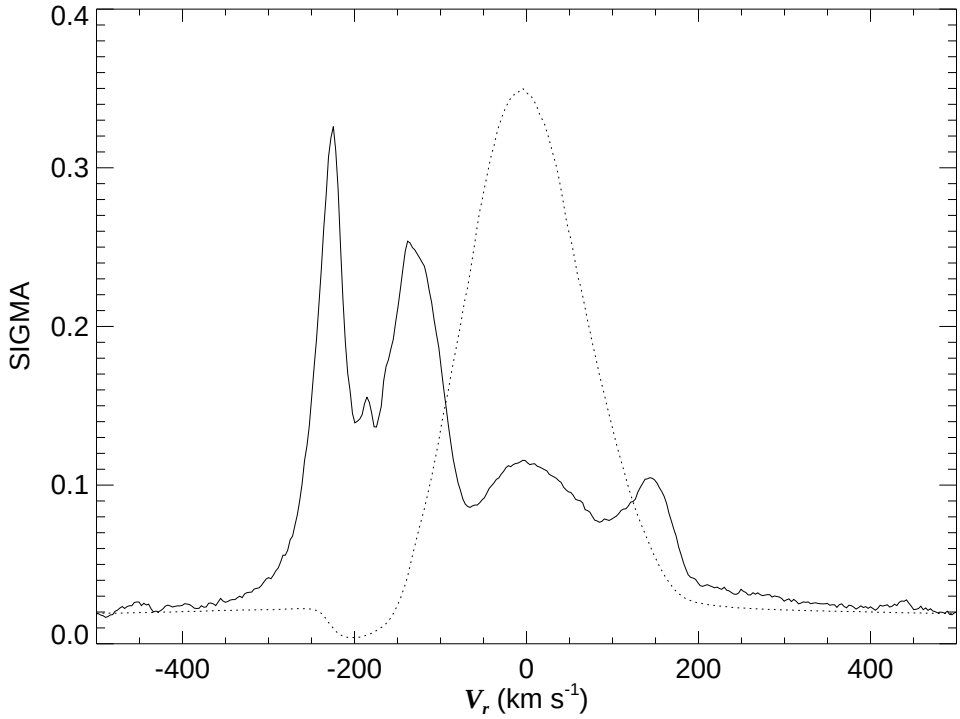

Figure 2.9 The pixel-by-pixel standard deviation of the quotient spectra (solid line). We also show the low absorption reference profile (dotted line; re-scaled to this range) to highlight those parts of the profile where the largest relative variations are occurring: near the terminal velocity blue edge (near -220 km s $^{-1}$), over the range traversed by the DACs (centered near ≈ -150 km s $^{-1}$), near the emission peak (0 km s $^{-1}$), and in the emission wings (± 150 km s $^{-1}$). The standard deviation of the quotient is larger in the absorption core because the low absorption profile is close to zero there.

often poorly constrained because absorption may extend blueward with a shallow slope (see Fig. 2.5). Thus, we decided instead to document the kinematical changes near the blue edge by measuring the position of the absorption core flux minimum, V_r(min), which is normally found near -210 km s^{-1} where the slope of the profile changes sign abruptly. We determined this position by finding the zero crossing in the numerical derivative of a smoothed version of the spectrum. The S/N ratio was sufficient in all our spectra that the zero of the derivation was always well-defined. This estimate of the minimum flux velocity V_r(min) is given in column 8 of Table B.1, and the errors in V_r(min) are comparable to the errors associated with the emission line kinematic measurements. This velocity is probably related to the

wind speed at a location in the wind where Hα ceases to be optically thick.

It is difficult to measure the radial velocities of the DACs because their morphologies vary and because the absorption may consist of multiple components. We decided to measure a centroid for the DACs wherever possible by means of the relationship

$$V_r(\mathrm{DAC}) = \frac{\int_{v_1}^{v_2} v_r(1 - Q(v_r))\ dv_r}{\int_{v_1}^{v_2} (1 - Q(v_r))\ dv_r}$$

where Q represents the quotient spectrum and v_r is the radial velocity. We adopted a velocity range of $v_1 = -200$ km s^{-1} and $v_2 = -100$ km s^{-1} based upon the strongest regions of the standard deviation spectrum plotted in Figure 2.9. Typical errors in these measurements (from the scatter in densely sampled regions of the time series) are ± 3 km s^{-1}. This approach worked for most of the spectra, but some low contrast features were not measured correctly, and are omitted from Table B.1 and our analysis. During some epochs, there were multiple DACs present, so V_r(DAC) represents a weighted average of multiple components. The DAC radial velocities V_r(DAC) are given in column 9 of Table B.1. Column 10 lists a relative equivalent width for the DAC measured by a direct numerical integration of $Q(v_r)$ between v_1 and v_2. The typical errors associated with these equivalent width measurements are on the order of 5%, which is similar to the errors associated with the equivalent widths of the profile (§3).

We show the temporal evolution of the DAC and blue-minimum flux velocities in Figure 2.10. At some epochs, a long progression of DAC velocities is present. The most well defined sequence began near HJD 2,450,700, and lasted about 800 days (Fig. 2.8). This timescale is much longer than that of a typical DAC observed in an O star, where the progression is measured in hours or days. As this particular DAC was relatively narrow and recorded in many spectra over its duration, it is an optimal feature to measure the Hα DAC acceleration. From a simple linear fit, shown overplotted in Figures 2.8 and 2.10, we mea-

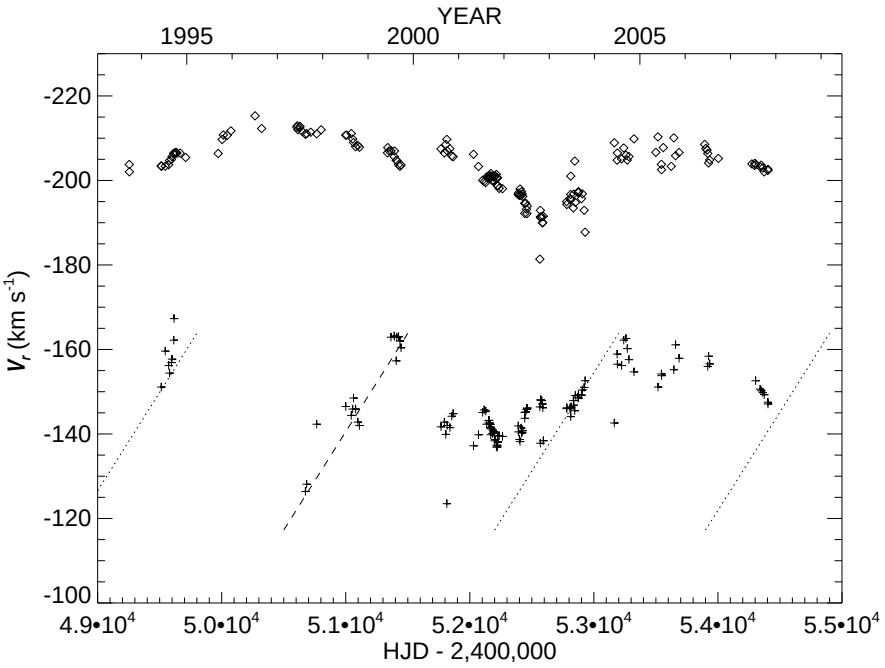

Figure 2.10 The temporal variations of the measured velocities of the DACs, V_r(DAC) (plus signs), and the minimum flux wind velocities, V_r(min) (diamonds). The dashed line represents the acceleration fit to the DAC progression near HJD 2,451,000, and the dotted lines represent the same fit translated by intervals of 1700 days, which we derived as a possible recurrence time.

sured the acceleration to be -0.047 ± 0.002 km s^{-1} d^{-1}. For comparison, the observed DACs in the spectrum of a normal hot supergiant of similar spectral type, ϵ Ori (HD 37128; B0 Ia), have an acceleration of -500 km s^{-1} d^{-1} (Prinja et al. 2002).

We used the Lomb-Scargle periodogram method (Scargle 1982) to search for a recurrence time in the appearance of the DACs, and derived a cycle time of 1700 d. This recurrence timescale is shown in Figure 2.10 where we overplot the linear acceleration of the DAC shown in Figure 2.8 for three additional epochs over the time span of the Ritter data. There is some evidence that a DAC progression is seen at each of these four epochs. The major deviations from the expected velocity trends occur when multiple components are present. For example, there were two DACs present between HJD 2,451,700 and 2,452,400, and the

velocity centroid we measured represents a blend of these components. Neither of these two DACs occurred at the expected recurrence time in the 1700 d cycle.

Our work represents the first detection of DACs in the blue absorption trough of Hα, and their properties differ from those observed in other spectral lines (Israelian et al. 1996; Markova 1986, 2000). For example, the recurrence timescale of 1700 d is much larger than the 200 d interval found in earlier work, and the acceleration measured is about a factor of 10 smaller than measured by others for ultraviolet lines of P Cygni. It is suspected that these differences are due to the large optical depth of the Hα line compared to that of other lines where DACs have been investigated. This will mean that the radius of optical depth unity is larger for Hα (Najarro et al. 1997), and consequently any wind structures formed at smaller radii will have no affect on the Hα line formation. It could be suspected that observations of other, less optically thick lines are more sensitive to the detection of DACs formed at smaller radii in the wind of P Cygni where more and faster accelerating structures may exist.

2.5 DISCUSSION

The V-band and Hα variations observed need to be interpreted in the context of current models for the star and its wind. Langer et al. (1994) discuss the atmospheric properties of P Cyg, and they argue that the star is in the LBV phase where the temperature and helium abundance are increasing, and the mass and luminosity are decreasing, as the star evolves towards the Wolf-Rayet phase. Langer et al. emphasize the earlier conclusion from Pauldrach & Puls (1990) that the atmospheric parameters are close to a bi-stability point where the mass loss rate can change by an order of magnitude with small changes in radius and/or luminosity, which may explain the great eruptions observed in prior centuries. The atmospheric parameters are well established through a detailed quantitative spectroscopic analysis by Najarro et al. (1997) and Najarro (2001), who find that He is overabundant and

that the mass loss rate is high ($\approx 2 \times 10^{-5}$ $M_\odot$ y^{-1} including wind clumping effects) and wind terminal velocity is low ($v_\infty = 185$ km s^{-1}). Najarro et al. (1997) derive a systemic velocity of $\gamma = -29$ km s^{-1}, and thus our minimum measurement of $V_{\rm min} = -215$ km s^{-1} is consistent with their estimate of $\gamma - v_\infty = -214$ km s^{-1} as this velocity measurement is related to v_∞. They estimate that the continuum forming radius is $76R_\odot$, which for a distance of 1.8 kpc implies an angular diameter of $\theta = 0.39$ mas. On the other hand, Najarro et al. (1997) predict that the emitting size of Hα will be much larger because of its greater optical depth. For example, their models show that there is a local maximum in the wind temperature distribution (presumably where the recombination processes that form Hα peak) near $r/R_\star = 11$ (see their Fig. 2.6b). The corresponding angular size for Hα of ≈ 4 mas agrees well with the range of $3 - 7$ mas from Hα interferometry by Balan et al. (2010). Thus, we need to keep in mind that the Hα variations reflect changes over a much larger spatial scale in the wind than those observed in the V-band flux.

Variations in the Hα emission equivalent width are related to changes in both the mass loss rate and the wind velocity. In a very simplified approach, it can be assumed that most of the Hα flux originates in the optically thick region projected on the sky,

$$f = \pi r_\tau^2 F(T)$$

were r_τ is the boundary separating the optically thick and thin regimes, $F(T)$ is the monochromatic surface flux, and T is the wind temperature at r_τ (Najarro et al. 1997). If we assume that the wind is approximately isothermal at this physical location (a reasonable choice: see Fig. 5b in Najarro et al. 1997), then the emission flux variations are due to changes in the projected size of the optically thick region,

$$\triangle f/f = 2\triangle r_\tau/r_\tau.$$

Thus, it is expected that the relative variations in angular size will be only half as large as the emission equivalent width variations, which is probably consistent with the lack of measurable size changes in the Hα interferometric measurements (Balan et al. 2010).

The Hα optical depth is dependent on the electron density squared since the emission is a recombination process. Thus, we expect that the optical depth unity boundary r_τ will always be defined by the location in the wind with a specific characteristic density, ρ_τ. We assume that ρ_τ has an approximately constant value so that the effective r_τ boundary will vary as fluctuations in the wind mass loss rate and velocity define the radius where the density reaches ρ_τ. According to the mass continuity equation, r_τ is related to this density by

$$r_\tau^2 = \frac{\dot{M}}{4\pi\rho_\tau v}$$

where $\dot{M}$ is the mass loss rate and v is the wind velocity at the radial distance r_τ. We can differentiate the mass continuity equation to express the radius variation in terms of the changes in $\dot{M}$ and v,

$$2r_\tau \triangle r_\tau = \frac{1}{4\pi\rho_\tau} \triangle[\dot{M}/v],$$

which we divide by r_τ^2 to obtain

$$2\frac{\triangle r_\tau}{r_\tau} = \frac{\triangle[\dot{M}/v]}{[\dot{M}/v]}.$$

Since we argued above that the flux also varies as r_τ^2, we can then use the relation above to re-write the fractional flux variation in terms of logarithmic changes in $\dot{M}$ and v,

$$\triangle \ln f = \triangle \ln \dot{M} - \triangle \ln v.$$

Since we have observational data on the variations in emission strength and wind velocity, we can rearrange this equation to solve for the mass loss variations as a function of flux

variations,

$$\triangle \ln \dot{M} / \triangle \ln f = 1 + \triangle \ln v / \triangle \ln f.$$

Puls et al. (1996) present a much more detailed analysis of the dependence of the emission equivalent width on the wind parameters of hot, massive stars. However, in the limit of high optical depth, their expression for the emission flux (their eq. 41) leads to a similar relation,

$$\triangle \ln \dot{M} / \triangle \ln f = \frac{3}{4}(1 + \triangle \ln v / \triangle \ln f).$$

We found in the previous section that the Hα equivalent width appears to vary inversely with two quantities related to wind dynamics, the Hα emission peak FWHM and the blue minimum flux velocity V_r(min). Figure 2.11 quantifies this relationship. The upper panel shows the inverse correlation between the emission peak FWHM and flux corrected Hα equivalent width, and if the FWHM is taken as a proxy for the wind speed, then a linear fit of natural logarithms of these measures gives $\triangle \ln v / \triangle \ln f = -0.66 \pm 0.12$. It is cautioned that the FWHM is also influenced by the absorption component of Hα, and we showed above (Fig. 2.5) that the absorption component moves inward towards the line core when the emission is strong. Consequently, the apparent decrease in FWHM as the emission increases probably results both from a wind speed decrease and a blue wing decline due to blending with the absorption component. The minimum flux velocity is perhaps a more direct measurement of wind speed (at least in our line of sight), and we show in the lower panel of Figure 2.11 the co-variations of the difference between V_r(min) and the systemic velocity of P Cyg, $\gamma = -29$ km s^{-1} (Najarro et al. 1997), as a function of the corrected equivalent width. A fit of the logarithmic slope here gives a smaller estimate of $\triangle \ln v / \triangle \ln f = -0.22 \pm 0.04$.

If we adopt the minimum flux co-variation result as representative of the wind velocity component of variability, then the mass loss rate variation derived from the relation above

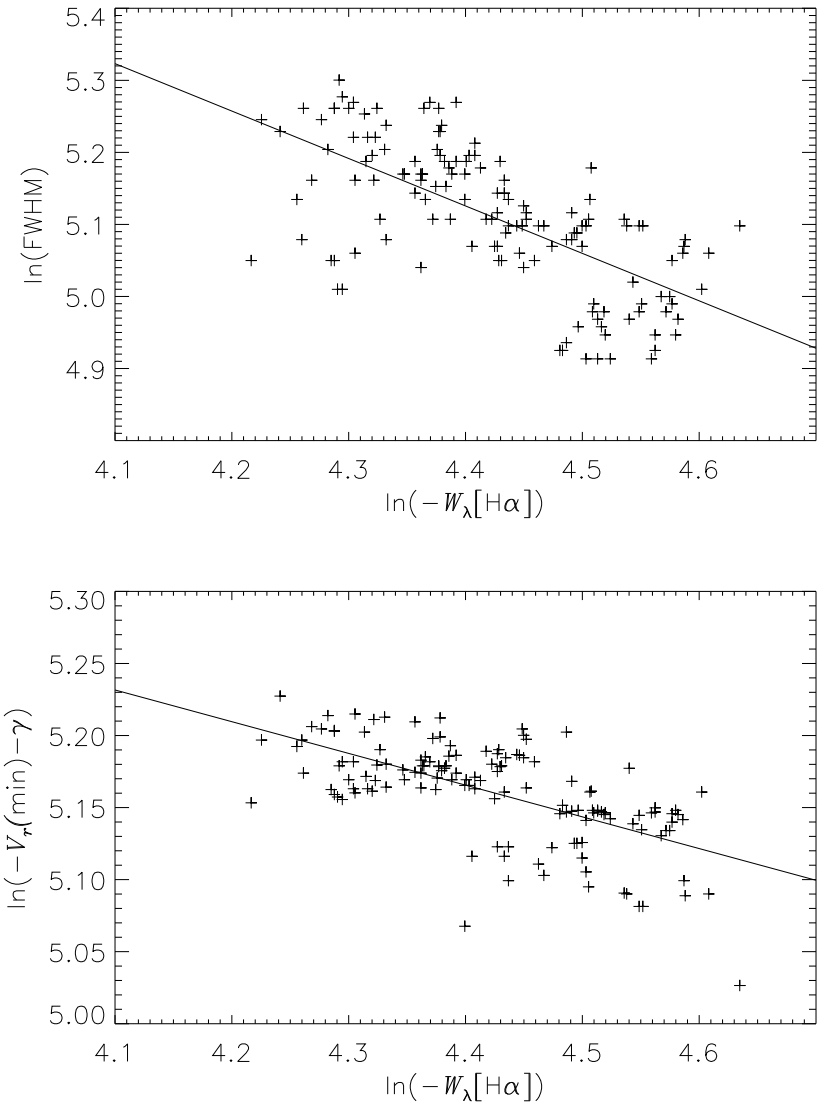

Figure 2.11 A comparison between the flux corrected equivalent width of Hα and the FWHM of the emission peak (top panel). The best fit (solid line) has a slope of -0.66. The lower panel shows a comparison between the corrected equivalent width of Hα and the difference between the minimum flux velocity V_r(min) and the systemic velocity γ of P Cyg. A linear fit yields a slope of -0.22 (solid line). All uncertainties are similar in size to the symbol size.

has an emission flux dependence of $\triangle \ln \dot{M} \approx 0.78 \triangle \ln f$. Omitting the bottom and top 10% of the distribution of W_λ(corr), the derived range in emission strength in our observations of $\pm 14\%$ probably implies mass loss rate changes of $\pm 11\%$. Markova et al. (2001a) used the optically thick relation from Puls et al. (1996) to arrive at an estimate of $\pm 9\%$ for the mass-loss variation amplitude. We showed above that the relation from Puls et al. carries a factor of 3/4 that is missing from our simple analysis, and if the Puls et al. relation is used instead, we arrive at a mass loss rate variation of $\pm 8\%$, confirming the estimate from Markova et al. (2001a). In this scenario, the Hα emission variations result from changes in the effective emission radius r_τ caused by variations in the mass loss rate and wind velocity. During episodes when the mass loss rate is higher and the wind is slower, the projected size of the emission region increases leading to larger Hα emission flux. The same process probably causes the V-band variations, but the fractional radius variations must be smaller at the continuum forming radius because we found in last section that $\triangle \ln f[V] / \triangle \ln f[\mathrm{H}\alpha] = 0.16$ so that $\triangle \ln r_{\tau V} = 0.16 \triangle \ln r_{\tau \mathrm{H}\alpha}$, i.e., the continuum size variations are only 16% as large as those in Hα. It is possible that the changes in the mass-loss rate are caused by a change in the luminosity of the star which would propagate through the wind, and be observed in both the V-band brightness and the emission line flux of Hα.

Finally we return to the relationship of the DACs to the short SD-phase variations. We found a trend with the DAC strength and the Hα emission equivalent width. We present in Figure 2.12 the temporal behavior of DAC quotient equivalent width W_λ(DAC) (Table B.1, column 10) along with scaled, running averages of the Hα equivalent width and V-band flux (Fig. 2.3). We rescaled the amplitude of the Hα flux by $\triangle W_\lambda(\mathrm{DAC}) = \triangle W_\lambda(\mathrm{corr})/20.46$ and the photometric light curve was rescaled by $\triangle W_\lambda(\mathrm{DAC}) = \triangle f_V \times 22.56$. These curves were then shifted vertically to match the W_λ(DAC) points. We see that the DAC strength variations track both the Hα and V-band flux variations, suggesting that the DACs are related in some way to the short SD-phase changes. For example, we see that some of the

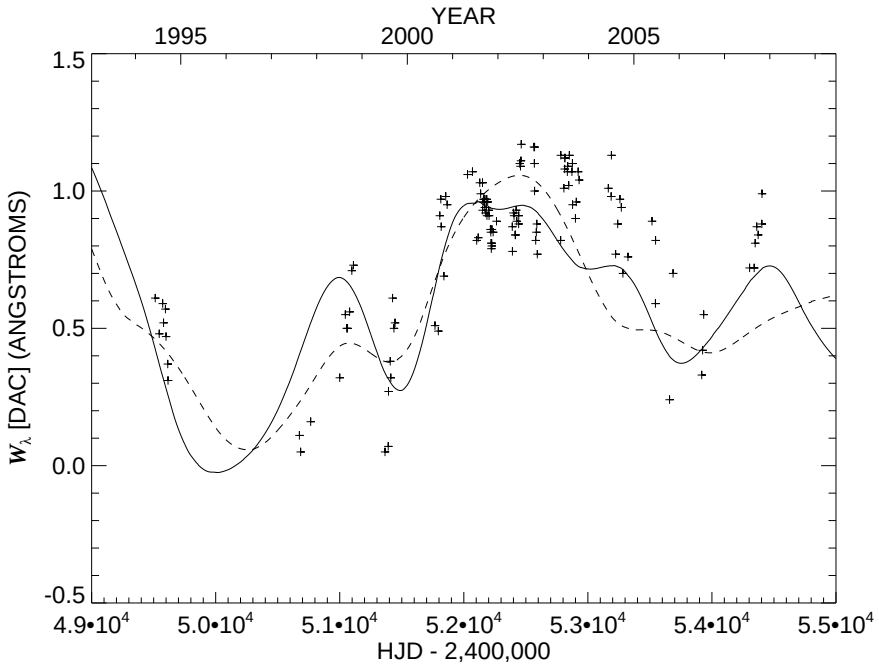

Figure 2.12 The temporal variations of the relative equivalent width of the DACs. We overplot the running average of the V-band photometry (solid line) and the Hα corrected equivalent width (dashed line) that were both rescaled and shifted to match the DAC variability (see text). The DAC strength appears to follow the variations associated with the short-SD phase.

strongest DACs were observed when the Hα emission was strong (around HJD 2,452,500; MJD $5.25{\cdot}10^4$ in our plots) and the DACs were very faint or absent when the emission was weak (around HJD 2,450,500).

The DAC phenomenon is primarily observed in the UV wind lines of hot stars (Kaper et al. 1999; Puls et al. 2008), and, in fact, DACs have only been observed once in the Hα profile where wind-related variations are usually due to changes in the dense and slower moving wind close to the star (Kaper et al. 1997; Markova et al. 2005). The only DAC ever observed in Hα was in HD 92207 (Kaufer et al. 1996) with a lifetime of $\sim$ 150 d and only one DAC observed, so the recurrence time is unknown. This star is cooler than P Cygni and is a "normal" supergiant, compared to the luminous blue variable nature of P Cyg. The

DACs observed in the UV wind lines of O-stars are first seen at velocities of 0.2 to 0.4 v_∞ and then they migrate blueward to v_∞ on time scales of a day or so, exhibiting accelerations that are much slower than expected for the wind velocity law (Kaper et al. 1999). Many of these same features are seen in the DACs in Hα for P Cygni, although they occur on vastly longer time scales. For example, the wind flow time scales as $R_\star/v_\infty$, and while the wind gas will accelerate from $0.1v_\infty$ to $0.9v_\infty$ in 0.5 d for an O-star like ξ Per (Kaper et al. 1999), it will take some 43 d for the wind of P Cygni. However, this flow time is very short compared to the longevity of the DACs (10^3 d), so we are led to the same conclusion found for the O-stars, namely that the DACs represent some kind of perturbation in the wind through which the gas flows. Changes in wind velocity and/or mass loss rate can cause shocks and create structure in the wind, and these structures produce density enhancements and/or velocity plateaus that imprint DACs in the wind lines (Fullerton & Owocki 1992; Runacres & Owocki 2002; Puls et al. 2008).

Current theory suggests that the DACs are related to large scale spiral features in the wind known as co-rotating interaction regions that are formed at the intersection of fast and slower outflows, which develop from some inhomogeneity in the stellar photosphere (for example, pulsation or spots; Cranmer & Owocki (1996); Lobel & Blomme 2008). In these models, it is the slow transit of these equatorially centered regions across the photosphere that creates the DACs in the absorption cores but has little influence on the emission parts of the wind line (Dessart (2004); Lobel & Blomme 2008). However, in the case of P Cygni, we find that emission parts do appear to strengthen when DACs are prominent (Fig. 2.11), and this indicates that the wind perturbation profoundly affects both wind gas surrounding the star and the wind gas projected against the photosphere. Thus, it is suggested that the structures causing the DACs in P Cygni may be more spherically symmetric than assumed in the geometry of the co-rotating interaction regions. In some models the seed perturbation occurs at a fixed longitude on the star, so that a new wind structure appears each time the

star rotates (although for the best studied case of HD 64760, Lobel & Blomme (2008) argue that the originating spots must rotate some five times slower than the star in order to fit models to the observations). If this is the case for P Cygni, then the 1700 d DAC recurrence time may be related to the star's rotational period. Markova (2000) found an upper limit of 100 d for the rotational period based upon estimates of the stellar radius and the projected rotational velocity. However, the line broadening in early supergiants may be dominated by turbulence rather than rotation (Howarth et al. 1997, 2007; Markova & Puls 2008), so a longer rotational period remains a possibility. However, regardless of the origin of the DACs, their close relation with the emission line and continuum flux variations (Fig. 2.12) suggests that much of the short-SD variability is caused by propagating structural perturbations in the outer atmosphere of the star.

The discovery of the short SD-phase variations in P Cygni and its relationship to the wind velocity and DAC occurrence in the wind is a new observational result that warrants future investigation both for this star and other LBVs. The changing characteristics over these long timescales may eventually lead to a better understanding of the LBV stage of evolution and the underlying physics of their winds and circumstellar environments. In a later chapter, we present results from a three year, spectroscopic monitoring program of Galactic and Magellanic Cloud LBVs. Such long-term observations will reveal much of the underlying physics will show whether the variations found in P Cygni are a general phenomena among LBVs.

3
THE ANGULARLY RESOLVED WIND OF P CYGNI

In this portion of the dissertation, I present a more detailed wind study of P Cygni accomplished through near-infrared interferometry and spectrophotometry. Some initial thoughts comparing the large scale structures from the great eruption and the wind geometry are also presented.

3.1 INTRODUCTION AND BASIC THEORY

The observations of massive stellar winds have been largely achieved without high angular resolution techniques (e.g., spectroscopy of wind sensitive lines such as Hα), but in some cases spatially resolved techniques have provided a basis for understanding the complicated wind structures. For example, Smith et al. (2003) found evidence that the polar wind of the prototype LBV η Car has higher velocities than the equatorial wind. Basic stellar wind theory predicts that the angular size observed at different wavelengths is dependent on the parameters of the star and its wind. The following derivation (adapted from Lamers & Cassinelli 1999) paints the basic picture of how wavelength dependent observations of a stellar diameter for hot stars with winds will place strong constraints on the temperature and density of stellar winds.

The frequency dependent flux for a star with a wind is given approximately by

$$L_\nu \simeq 4\pi r^2(\tau_\nu = \tau_{\rm eff})\pi B_\nu(T(\tau_\nu = \tau_{\rm eff}))$$

where L_ν is the monochromatic flux in erg s^{-1} Hz^{-1} and B_ν is the Planck function (blackbody) for a temperature at an effective optical depth ($\tau_{\rm eff}$) where the emerging light is emitted at radius r. Lamers & Cassinelli (1999) state that the effective optical depth, $\tau_{\rm eff}$ is about 2/3 for a plane-parallel atmosphere and about 1/3 for an extended stellar wind.

Free-free opacity, κ_ν, is inversely dependent on frequency cubed (ν^{-3}), or dependent on wavelength cubed (λ^3) in the near infrared. This is the main dependency for the optical depth of the star and its wind, so that the radius where $\tau_\nu = \tau_{\rm eff}$ will increase with wavelength. If we were able to resolve the angular diameter of a star with a significant wind, we would observe that the star's apparent diameter is dependent on the wavelength observed, and for instance, we may observe an excess of $\sim 5 - 10\%$ in radius between the optical ($\sim V$-band) and near infrared ($\sim H$ or K-band).

A good example of the wind flux excess is found in the spectral energy distribution (SED) of the famous luminous blue variable P Cygni (Waters & Wesselius 1986). They modeled the spectral energy distribution to find the gaseous and dusty components of the strong wind being emitted by this star. They find that the flux is dominated by the star in the optical and by the wind in the mid-infrared ($\sim 10\mu$m). Their SED is shown in Figure 3.1.

The frequency dependent flux for a "normal" star without a wind is similar to that for the wind,

$$L_\nu^* \simeq 4\pi R_*^2 \pi B_\nu(T_{\rm eff}).$$

Comparing the two flux expressions (both with and without a wind), we see that

$$\frac{L_\nu}{L_\nu^*} \simeq \frac{r^2(\tau_\nu = \tau_{\rm eff})}{R_*^2} \cdot \frac{B_{\nu,\rm wind}(T(\tau_\nu = \tau_{\rm eff}))}{B_\nu(T_{\rm eff})}.$$

The winds of hot stars are ionized by the stellar radiation, and to first order, we can consider the wind to be isothermal with $T_{\rm wind}$ roughly equivalent to the temperature of the stellar photosphere, $T_{\rm eff}$. Then the ratio of wind to stellar flux is approximately the same as the ratio of projected areas on the sky. This is illustrated in Figure 3.2 (Lamers & Cassinelli 1999).

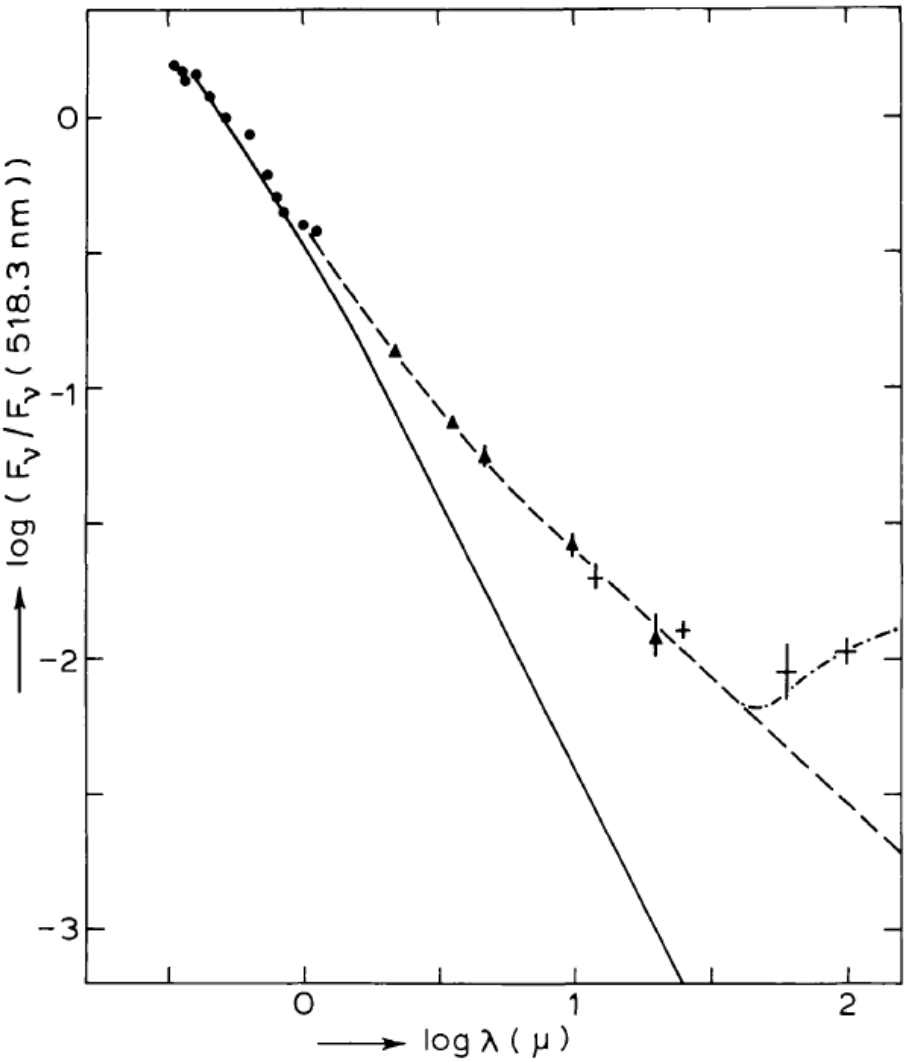

Figure 3.1 Modeled spectrophotometry of a star with a strong wind (P Cygni), reproduced with permission from Waters & Wesselius (1986). The solid curve is the predicted photospheric contribution, while the dashed line is the addition of free-free and bound-free emission in the wind. The dashed-dot line is a contribution from cool dust.

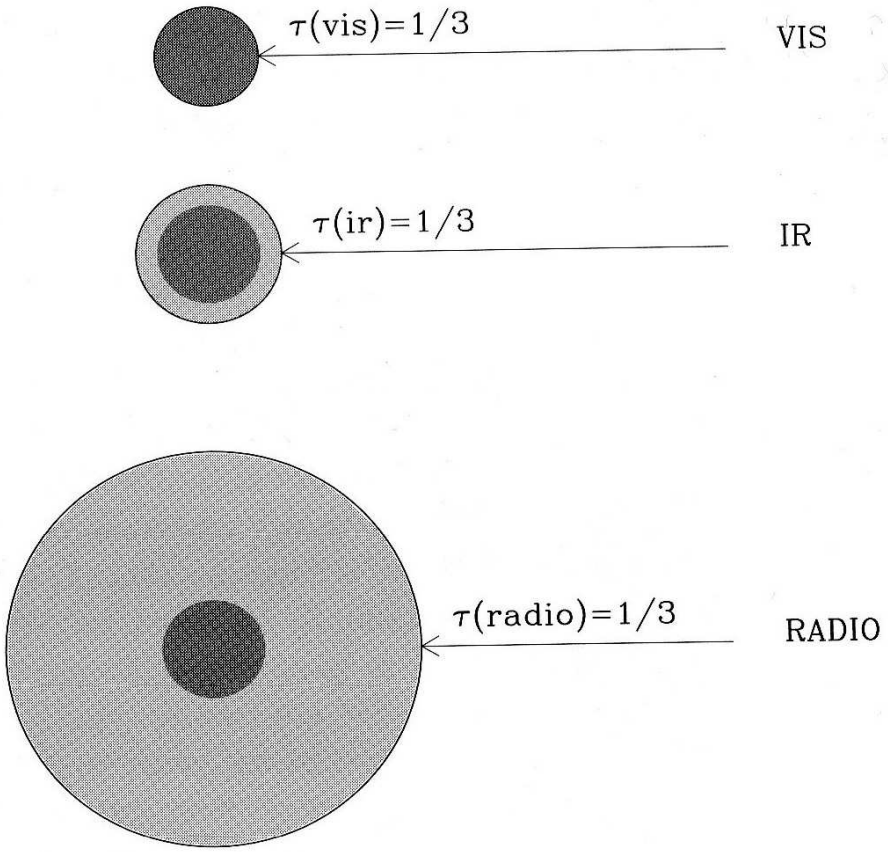

Figure 3.2 As the wavelength is increased, the observed radius of a star with a wind is increased, as described in Section 3.1. This figure is adapted from Lamers & Cassinelli (1999).

With the advent of optical (and near-infrared) long baseline interferometry, it is now possible to measure the wind extent of relatively nearby hot stars (i.e., diameter measurements at multiple wavelengths). Such observations can be made in conjunction with spectral energy distribution measurements for an independent assessment of the envelope flux contribution. The best examples of such stars are hot supergiants and LBVs such as P Cygni.

3.2 *H*-BAND MEASUREMENTS of P CYGNI AND ITS WIND WITH THE CHARA ARRAY

P Cygni was the subject of an early study with the CHARA Array (Tuthill et al. 2006) and the Classic beam combiner (ten Brummelaar et al. 2005). Tuthill et al. (2006) used the Classic beam combiner and two narrow band filters to attempt to disentangle the Brγ emission line forming region from the K' continuum emitting region with their method of Double-Fourier, spatio-spectral decoding. The end results of this study were somewhat inconclusive, probably in part due to the assumption that the flux recorded in a narrow band K'-continuum filter was being emitted at the stellar photosphere. The IR excess is a well known feature for this star, but the size of the spatial emitting region recorded by the K'-continuum filter was unknown. Nevertheless, the experiment showed that the Brγ emission line forming region is much larger than the continuum forming region.

The results of Chapter 2 (Richardson et al. 2011b) demonstrate that substructures (DACs) in the Hα profile of P Cygni co-vary with photometric and spectroscopic changes observed in the star. We found that the emission portion of the Hα line strengthens when DACs are prominent (Fig. 2.11). This indicates that the wind perturbation that causes the DACs profoundly affects both wind gas surrounding the star and the wind gas projected against the photosphere. It suggests that the structures causing the DACs in P Cygni may be caused by small perturbations in a wind that is spherically symmetric. This is not necessarily the case for most LBVs and supergiants, but a nearly spherically symmetric wind provides an excellent case study for a first interferometric study of stellar winds.

On UT 2010 August 23, P Cygni was observed with the MIRC beam combiner (Monnier et al. 2007) and the CHARA Array using telescopes S2, E2, W1, and W2. MIRC recorded two sets of fringes for interference between four telescopes (six baselines, four closure phases) across eight wavelength channels, resulting in 96 measurements of the squared visibility, V^2, and 64 closure phase measurements. There were two independent observations of P Cygni on

that night, and they were calibrated using the calibrator star σ Cygni, which was estimated to have a uniform disk diameter of $\theta_{UD} = 0.57 \pm 0.02$ mas from a fit to the spectral energy distribution. The (u, v) coverage for these observations is shown in Figure 3.3, and Table B.4 lists the squared visibility (and associated error), wavelength channel, and baseline for each of the 96 measurements.

Recall that the visibility of a star is related to the minimum and maximum observed fringe intensities by

$$V = \frac{I_{max} - I_{min}}{I_{max} + I_{min}}$$

which was defined by Michelson & Pease (1921), in the first paper to show the application of interferometry to resolving the angular diameter of a star (Betelgeuse) other than the Sun. This visibility is a measure of the fringe contrast. If $V = 1$, a star is entirely unresolved, whereas if $V = 0$, the star is completely resolved. The second measured quantity that can be made with an interferometer (if there are three or more telescopes used) is a closure phase (Lawson 2000). There is a slight phase shift observed at any telescope of an interferometer, such that, for telescopes 1 and 2

$$\Phi(1-2) = \Phi_0(1-2) + [\phi(2) - \phi(1)].$$

Φ represents the observed phase difference, with Φ_0 being intrinsic to the source, and the $[\phi(2)-\phi(1)]$ being an atmospheric term for the difference introduced for different atmospheric properties between telescopes 2 and 1. If these phases are added for three telescopes, the atmospheric terms cancel out and we can observe the phase difference from an astrophysical source. This allows us to capture the asymmetries that are intrinsic to the spatial flux distribution of the target.

Najarro et al. (1997) constructed the best spectroscopic model of P Cygni to date, which

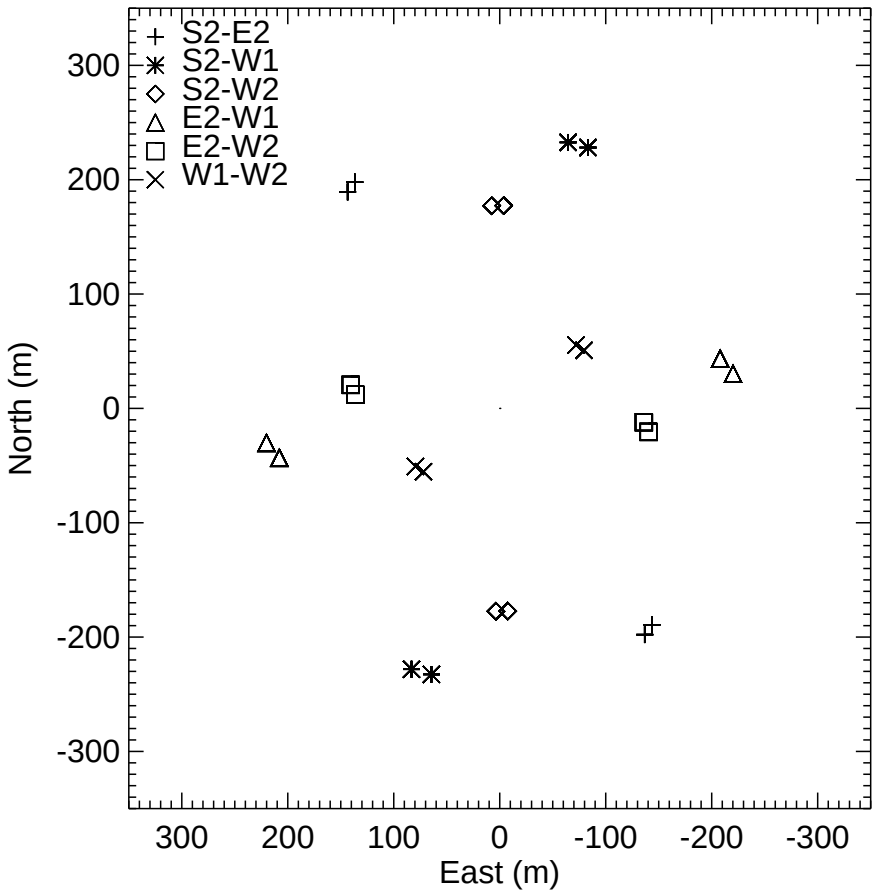

Figure 3.3 (u, v) Coverage for MIRC observations of P Cygni. The units of meters are physical units for the projected baseline. The broad coverage allows us to have sensitivity to large and small structures and to explore asymmetries in the region surrounding P Cygni.

was built with the non-LTE code CMFGEN to model both the star and the wind, and they estimate that the stellar radius is $75R_{\odot}$ with a distance of 1.7 ± 0.1 kpc. At that distance, the angular diameter of the star is 0.39 ± 0.02 mas. We first fit the MIRC V^2 data with a uniform disk model, which is given for a single star by

$$V(b) = |\frac{2J_1(\frac{\pi\theta b}{\lambda})}{(\frac{\pi\theta b}{\lambda})}|$$

where V is the visibility, J_1 is a first order Bessel function, θ is the angular diameter of the source in radians, b is the baseline, and λ is the observed wavelength. Note that the baseline and the wavelength need to be in the same units. The projected baseline may be expressed in units of $\frac{\text{Baseline}}{\text{Wavelength}} \times 10^{-6}[M\lambda]$ in order to include multi-wavelength data in the fit. Our uniform disk diameter fit for P Cygni in the H-band makes a poor fit to the data (Figure 3.4), and yields a much higher value than predicted for the angular diameter, $\theta_{UD} = 0.93 \pm 0.02$ mas. The uniform disk model under-predicts the values of V^2 at large values of $M\lambda$ and over-predicts those at small values of $M\lambda$. The reduced χ^2_ν is 8.3, much larger than unity, as expected for a good fit of the data.

We proceeded to add a second component to create another model for P Cygni. We held the stellar diameter (hence, angular diameter) constant at 0.39 mas (based upon estimates from the models of Najarro et al.; the small angular size is not resolved by these baselines, and so reasonable changes in the stellar diameter will not effect these measurements), and allowed a spherical Gaussian profile to contribute a portion of the flux. The width and intensity of this Gaussian were allowed to vary, and model and observed differences were minimized using a Levenberg-Marquardt least-squares fit to the resulting visibility[1] in a manner similar to that done by Schaefer et al. (2010). This created an excellent fit to the data. The resulting model image is shown in Figure 3.5, and the fit to the visibility curve is shown in Figure 3.4. Our simple model has a reduced $\chi^2_\nu = 0.32$, meaning that the model residuals are smaller than the errors associated with the measurements. It provides estimates of the relative flux contributions of the star (0.600 ± 0.007) and a Gaussian smoothed wind (0.400 ± 0.007), as well as the angular size of the wind (1.150 ± 0.026 mas FWHM). We also tried to fit only a Gaussian component (with no contribution from a stellar photosphere), and the results provided a similar χ^2_ν as the uniform disk model, so this model is also not

[1]The Levenberg-Marquardt least-squares fit IDL code is available from http://cow.physics.wisc.edu/∼craigm/idl/idl.html

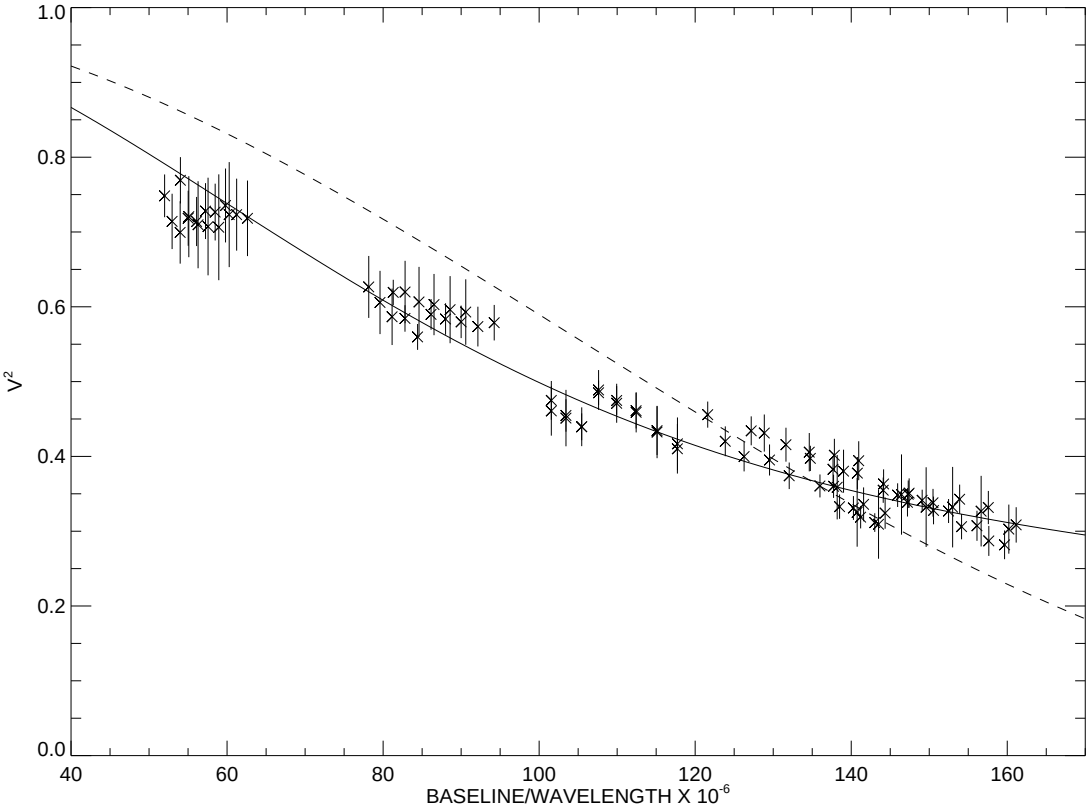

Figure 3.4 The uniform disk fit to the MIRC observations of P Cygni is shown in a dashed line. This is not an adequate representation of the observed visibilities. The best fit model, using a Gaussian distributed wind and a uniform disk star, is shown as a solid line.

realistic.

There may be a degeneracy between the stellar photospheric contribution and the angular size of the shell in cases of limited baseline coverage. The best way to solve this degeneracy and to ensure that the interferometric model is correct is to obtain simultaneous measurements of the infrared flux excess (see, e.g. Touhami 2012). This will be discussed in Section 3.4.

Another benefit of the MIRC beam combiner is that it produces accurate closure phases. The measured closure phases (given for both observations and all four combinations of three telescopes in Fig. 3.6) are small, but are non-zero, implying that the source is not quite

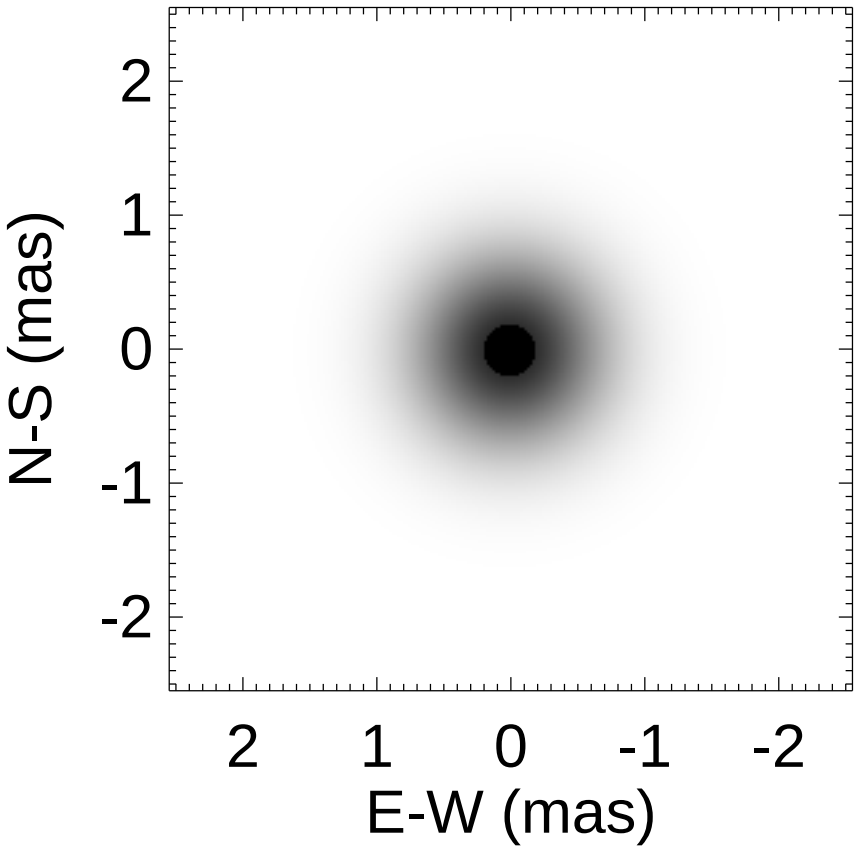

Figure 3.5 Best fit star and Gaussian wind model flux distribution for the MIRC data of P Cygni.

symmetric. The small values of closure phase can be hard to model, but the spherically symmetric model can be used as an input to reconstruct an image of the environment surrounding P Cygni to see if the asymmetries have astrophysical consequences.

The MArkov Chain Imager (MACIM) is a publically-available Monte Carlo imaging algorithm (Ireland et al. 2006) that can use an input image, such as the one shown in Figure 3.5 to reconstruct an image from interferometric data that includes information on visibility and closure phase. We used this algorithm and the model image (uniform disk star

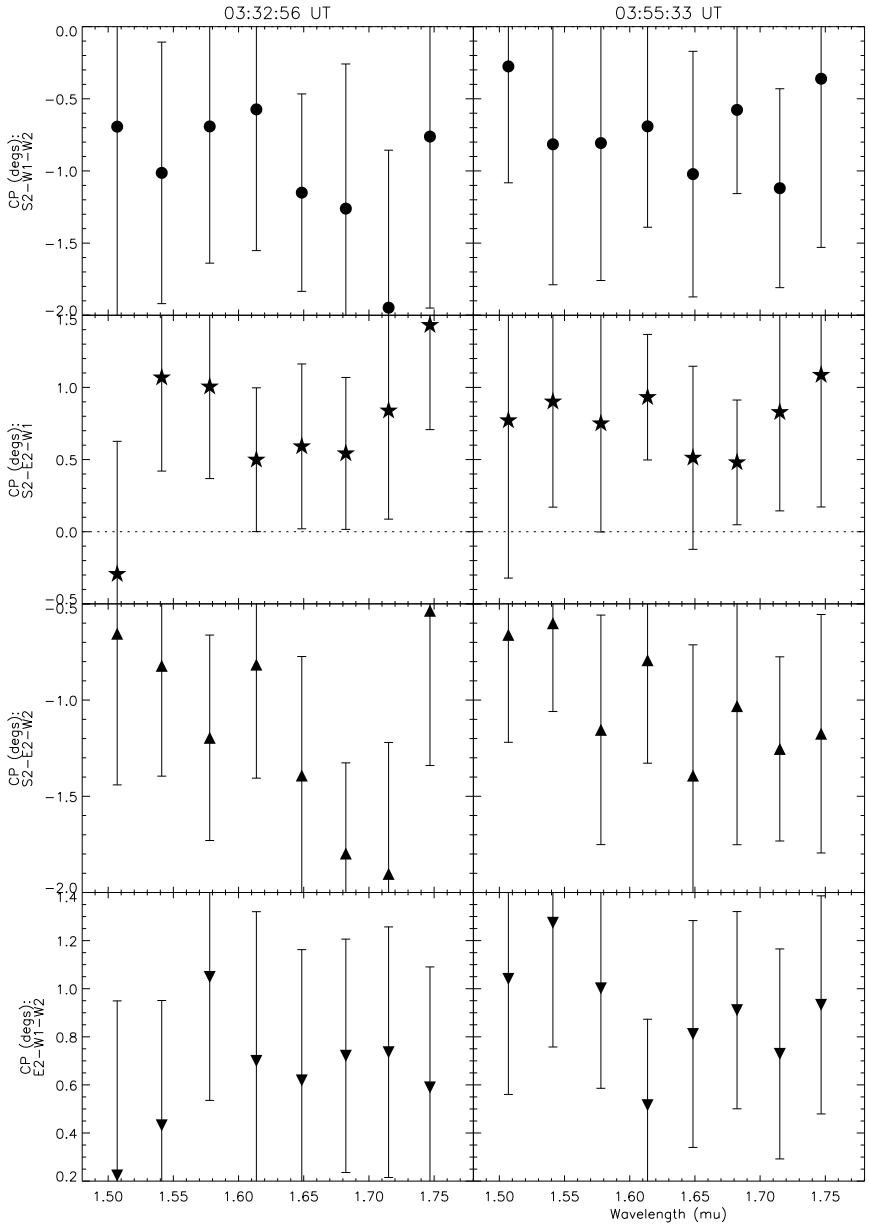

Figure 3.6 Closure phases observed for P Cygni for different telescope triangles and spectral channels.

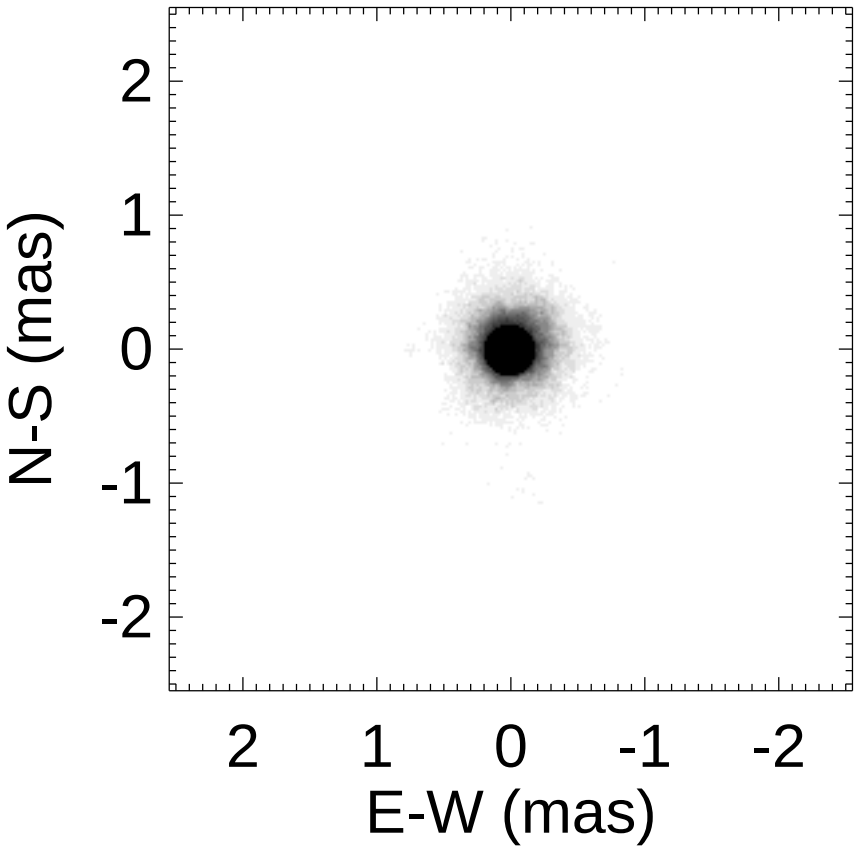

Figure 3.7 MACIM image reconstruction of the MIRC data of P Cygni. Note the slight asymmetry of excess flux to the north-west of the central star.

and a Gaussian distributed wind) to construct an image of the environment surrounding P Cygni. The resulting image from the MACIM reconstruction is shown in Figure 3.7.

The image constructed from the MIRC observations (Fig. 3.7) has several features, some of which are real, and some of which are artifacts. The artifacts of image reconstruction include a "snowflake" like pattern in the faint outskirts of the light of the wind (which is not seen in the intensity levels depicted in Fig. 3.7). A look at the (u, v) coverage plot (Figure 3.3) shows that these extended regions are aligned in the direction with the longest baselines

we used for these observations. The star has sharp edges due to the assumption of a uniform disk. In reality, the star would have limb darkening, but MIRC is not sensitive enough to measure the limb darkening for such a small uniform disk. The wind likely is clumped, but we would likely need a resolution that is three orders of magnitude more sensitive to find the clumps in the wind. There is one feature that is likely real and that causes the closure phases to be non-zero (Fig. 3.6). There is a density enhancement in the wind on the north-west side of the star, close to the star's limb. If this feature is real, it has some interesting consequences for the wind of P Cygni and other LBVs.

In Figure 3.8, we show a representation of the MACIM reconstruction, where the flux of the star and the wind projected against the star have been removed. We also removed the low-lying flux that caused the snowflake pattern in the large scale representation of the wind. The remaining features seen in the image reconstruction probably offer us the best representation of the inner stellar wind. The slight asymmetry was measured to have a position angle of $314^\circ \pm 10^\circ$, when measured from north towards east, indicating a NW enhancement in the stellar wind. This measurement was made by estimating the center of light of the remaining wind light in Figure 3.8, and comparing it to the position of the center of the star.

We examined the radial distribution of the light in the image reconstruction, which is shown in Figure 3.9. We compare this distribution to that of the Gaussian distributed wind and uniform disk star, and find that the Gaussian underestimates the inner flux of the wind.

3.3 IMPLICATIONS OF THE MIRC OBSERVATIONS AND THE LARGE SCALE STRUCTURE OF P CYGNI'S EJECTA

The Hα emitting region surrounding P Cygni was investigated interferometrically by Balon et al. (2010). They used a similar model as ours to investigate the region, but they assumed a stellar angular diameter of 0.2 mas. There was likely a missing factor of two to convert from

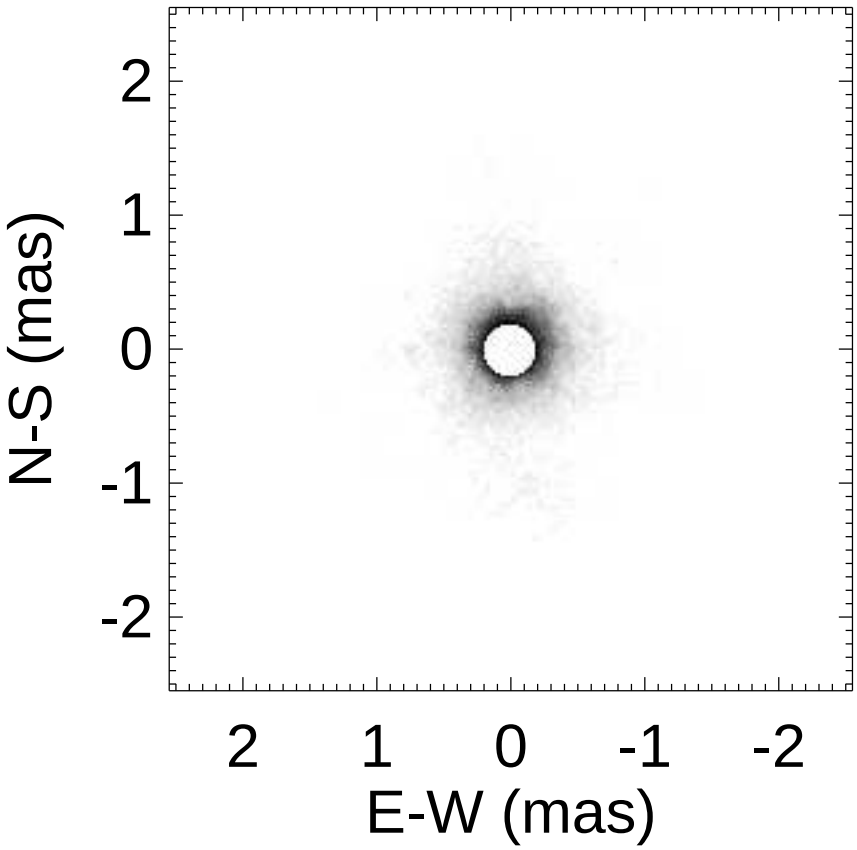

Figure 3.8 MACIM image reconstruction of the MIRC data of P Cygni, with the star and wind flux in front of the star removed, as well as low-level artifacts removed. Note the slight asymmetry to the north-west of the central star.

radius to diameter in these measurements, but as the baselines of the Naval Prototype Optical Interferometer (NPOI) that were used were small, this conversion error does not greatly affect their results. They derived a Gaussian wind of diameter $3-7$ mas FWHM, with a flux contribution from the stellar photosphere around 70% (compared to our $H-$band results of 1.15 mas FWHM for the wind emitting region and the stellar photosphere contributing 60% of the flux). The large optical depth of Hα in a wind like that of P Cygni will naturally contribute a significant portion of the observed flux over a large area of the sky (around 11

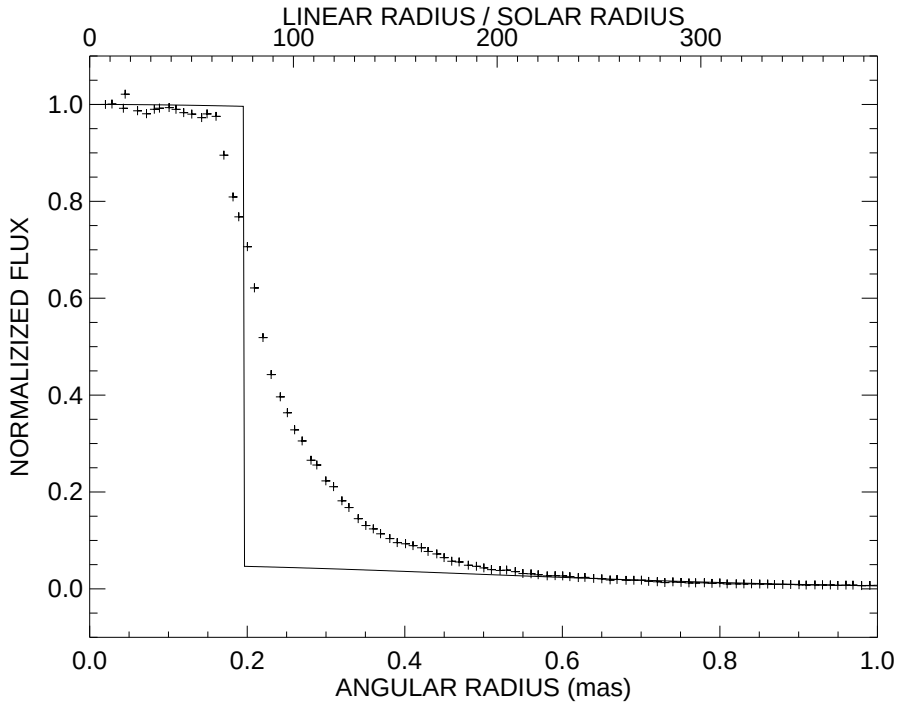

Figure 3.9 Radial distribution of the light from the MACIM image reconstruction of the MIRC data of P Cygni, shown as plus signs. The Gaussian wind model is also shown as a solid line.

R_*, Chapter 2), so these results are not surprising. The central portion of the Hα emission can be up to 75$\times$ brighter than the continuum, which corresponds to an emitting region that could be 11 stellar radii, depending on the density distribution and actual line flux at the time. The optical depth at the longer wavelength of H-band is smaller than that of Hα, so we would expect to find a smaller envelope. In the less massive B stars that have gaseous equatorial disks, the near-infrared observations with interferometry often show that the hydrogen free-free emission that causes the IR excess comes from a region smaller than the recombination emission from Hα (Gies et al. 2007).

An interesting comparison can be made between the H-band MIRC observations, which record the small structures in the current wind, and those of the large scale ejecta from the great eruptions of the seventeenth century. This allows a comparison of the wind at epochs

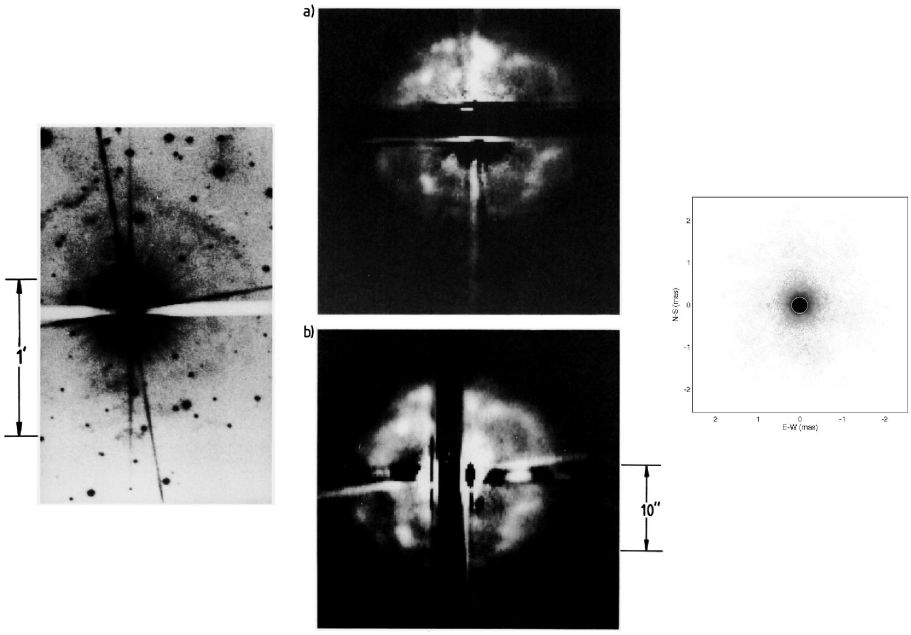

Figure 3.10 The wind and ejected matter of P Cygni imaged by Barlow et al. (1994) and by MIRC. Left panel: Large scale [N II] emission seen several arcminutes from the star; Middle panels: [N II] emission seen surrounding P Cygni at a few arcseconds with the occulting bar at perpendicular projections on the sky; Right: Model for MIRC observations. In all images, north is up and east is left.

separated by about 400 years. Barlow et al. (1994) imaged the ejecta of P Cygni at the arcsecond and arcminute scales using a narrow-band filter centered on the [N II] 6384 Å line. Their images used an occulting bar to block the large amount of light from the star. Their results are compared to the MACIM image of the H-band continuum in Figure 3.10.

The circumstellar environment of P Cygni presents a rich and complex set of features. On the largest scale, there is evidence of a giant lobe of line emission that extends 12 arcmin to the east of the star (Meaburn et al. 2004). The star itself is centered on an outer shell of 1.6 arcmin diameter and an inner shell of 22 arcsec diameter (Boumis et al. 2006). These outer and inner shells are illustrated in the left and central panels of Figure 3.10 (from the work of Barlow et al. 1994). The inner shell contains a number of knots or clumps that are particularly located in the north-western sector (Nota et al. 1995). Smith & Hartigan

(2006) present a kinematical study of the line emission from the inner shell that they argue corresponds to mass ejected in the great eruption of 1600. Smith & Hartigan point out that the clumps tend to be blue-shifted in the northern part and red-shifted in the southern part, which they argue may result from outflow organized around a symmetry axis seen at an intermediate angle. Very close to the star the wind emission itself can be resolved. Chesneau et al. (2000) used adaptive optics observations of the Hα emission to reconstruct the emission flux on sub-arcsec scales. They found a very clumpy appearance with a central elongation along a north-east to south-west axis. This same sense of elongation was observed in radio continuum observations from the VLA (Contreras et al. 2004). Some of the highest angular resolution measurements come from radio interferometry of the wind emission. Exter et al. (2002) show that the emission from the inner 400 mas is clumpy and time variable. In this context, it may be that the asymmetry we find in the wind emission is related to clump formation close to the star. However, on the other hand, if the asymmetry is a consistent feature in future observations, then it may be related to the axial geometry of the outflow. For example, if there is an enhanced polar outflow, then the polar region in our direction may appear brighter than the foreshortened (and possible obscured) counter flow, and it may create the asymmetry in the light distribution. New high angular resolution observations will be key to understanding the origin of the asymmetry.

3.4 *H*-BAND VARIATIONS OF P CYGNI, AND IMPLICATIONS ON THE EMITTING REGION SIZE

3.4.1 Spectroscopic *H*-band Observations

We observed P Cygni in the infrared at seven epochs spanning 2006–2010. Six of these observations are spectrophotometric, with one epoch being a narrow slit observation. Five of these observations were made with the Lowell Observatory Perkins Telescope and Mimir instrument capable of NIR imaging, polarimetry, and spectroscopy (Clemens et al. 2007).

The first two epochs were obtained with the NASA IRTF telescope and the SpeX instrument (Rayner et al. 2003).

The SpeX data were reduced using the SpeXtool package (Vacca et al. 2003). The Mimir reductions were performed with custom software designed for the Mimir instrument[2]. These reductions corrected the raw frames by use of dark frames (which include both the bias and the dark current) to remove background counts and by flat fields to remove fringing and pixel-to-pixel variations. These frames were all taken either immediately before or directly after the science exposures. In addition, the Mimir observations were further calibrated for non-linearity by a set of flat fields that were made with multiple exposure lengths. These exposures calibrated the linearity function for each pixel. Wavelength calibration was performed using an Argon lamp taken at the same location in the sky, and the star was dithered along the slit to remove bad pixels. A typical observation of P Cygni includes at least 10 exposures of the star (with different locations along the slit), several calibration lamps, dome flats at the same location (by rotating the dome in front of the star) with lights both on and off (so that the real pixel-to-pixel variations can be found using a difference image), and several zero second bias frames along with dark frames of the same exposure length. This is accompanied by a set of observations of a nearby A0 V star, HD 192538. The A0V star was used to fit a telluric spectrum at the same sky location. The atmospheric transmission is then divided out to ensure that the actual flux and stellar emission line profiles are free of its instrumental and atmospheric signatures.

3.4.2 *H*-band Variability

Touhami et al. (2010) found that the NIR continuum of P Cygni is variable, which is probably due to changes in the stellar wind and circumstellar environment. Here, we examine the reality of the NIR variability from 2006–2010, as Touhami et al. had only observed P Cygni

[2]available for download at http://people.bu.edu/clemens/mimir/

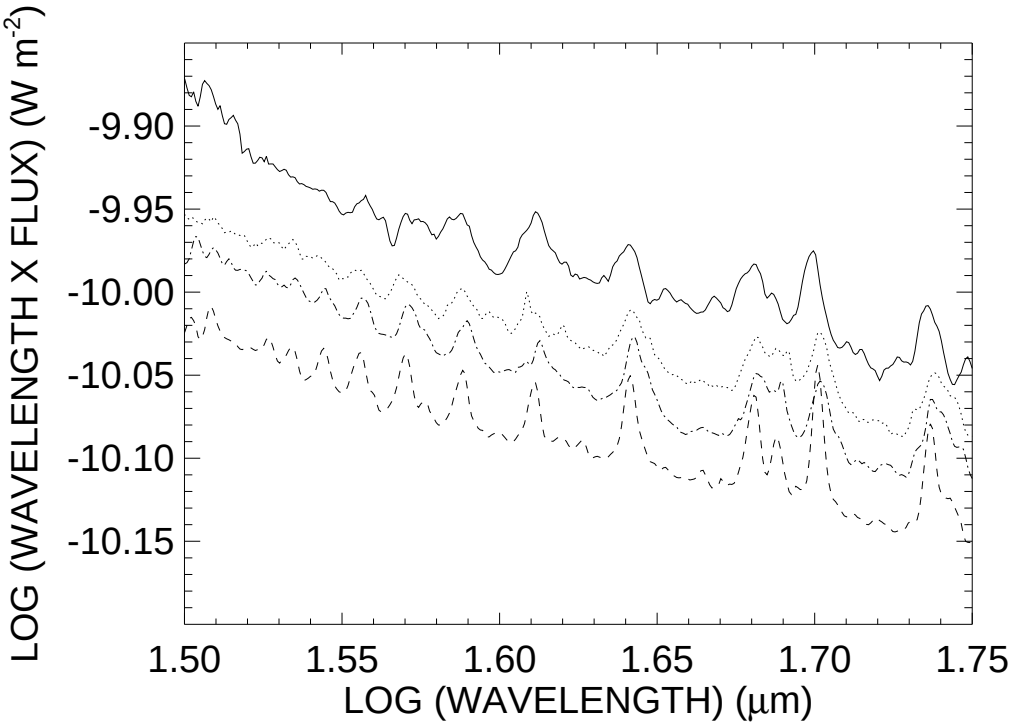

Figure 3.11 H-band spectrophotometry of P Cygni 2008–2010. Data from 2008 Oct 20 is a solid line, 2009 Jul 13 is a dashed dotted line, 2009 Nov 06 is a dashed line, and 2010 Jul 03 is a dotted line.

two times. Over this 2006–2010, the Hα profile did not vary over its full range (Chapter 2 results and the results of Balan et al. 2010), so the NIR variability should be smaller than the full range of fluxes possible for the stellar wind.

The H-band spectrophotometry of P Cyg spans 2008 October – 2010 July. The spectra are shown in Figure 3.11. Overall, the continuum is variable by about 0.10 dex, consistent with the lack of Hα variability mentioned previously. These spectra imply that the star and its environs remained relatively stable throughout this time period. Flux values for a wavelength of 1.6μm are listed in Table 3.1. The K band spectrophotometry (Figure 3.12) shows a similar range for the variability during 2006–2010.

The results obtained with the Mimir instrument suggest that the continuum is only slightly variable in the near-infrared, by up to $\sim$ 20%. The errors associated with the H-

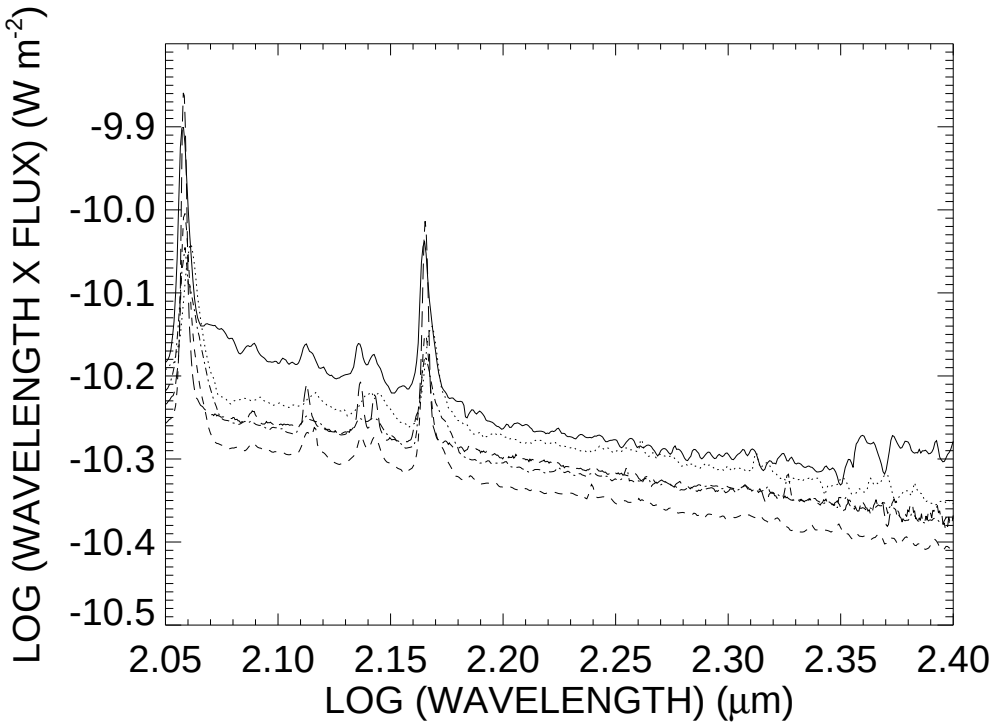

Figure 3.12 K-band spectrophotometry of P Cygni 2006–2010. Data from 2006 Sep 16 is a long-dashed line, 2008 Oct 20 is a solid line, 2009 Jul 13 is a dashed dotted line, 2009 Nov 06 is a dashed line, and 2010 Jul 03 is a dotted line.

Table 3.1 Infrared Flux Measurements of P Cyg

Date (UT)	Telescope/ Instrument	H (1.6μm) (ergs s^{-1} cm^{-2} Å^{-1})	K (2.3μm) (ergs s^{-1} cm^{-2} Å^{-1})
2006 Sep 16	IRTF/SpeX	...	1.97×10^{-12}
2008 Oct 20	Lowell/Mimir	6.41×10^{-12}	2.21×10^{-12}
2009 Jul 13	Lowell/Mimir	5.59×10^{-12}	2.03×10^{-12}
2009 Nov 06	Lowell/Mimir	5.14×10^{-12}	1.85×10^{-12}
2010 Jul 03	Lowell/Mimir	6.03×10^{-12}	2.15×10^{-12}

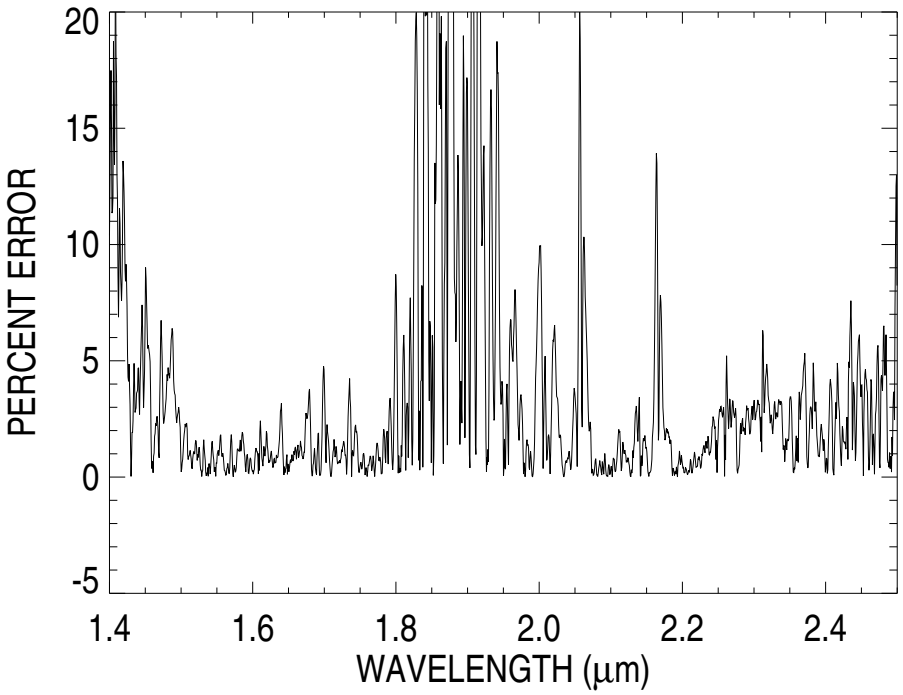

Figure 3.13 Flux errors for Mimir observations as a function of wavelength. The large errors in the central part of this region is due to the low transparency in the region between H and K band. In K-band, the average error is on the order of 3–5%, while the error is $\sim 2\%$ in the H-band.

band flux measurements are on the order of 1–2%. We estimated this property of the Mimir data by comparing multiple observations of P Cygni made on the same observing run. The standard deviation as a function of wavelength is shown in Figure 3.13. As the typical errors are on the order of a few percent, we can conclude that these measurements signify real variability of the H-band continuum of P Cygni.

Touhami et al. (2010) compared the SED of P Cygni in the optical and near infrared with a Kurucz model atmosphere for a star with the same $T_{\rm eff}$, $\log g$, and reddening as reported by Najarro et al. (1997). They find that the near-infrared flux excess is 0.26 ± 0.03 dex in the H-band (see Fig. 3.14 for the 2008 Mimir data reported here), which corresponds to a stellar contribution of $(55 \pm 4)\%$ of the flux and a wind contribution of $(45 \pm 4)\%$ of the flux

in H-band. This agrees with our star plus Gaussian fit of the interferometric observations, where we derived 60% and 40% for these contributions, respectively.

The general agreement about the relative flux contributions from spectrophotometry and the interferometry offers support for the simple models of the wind flux. We note, however, that the actual flux distribution from the wind may differ significantly from this Gaussian model. The small asymmetry we found suggests that the wind is mostly spherical near the star, as postulated from the Hα DAC analysis in Chapter 2. However, a non-zero asymmetry raises the question about the nature of the wind geometry over time. The ejecta around P Cygni may show similar asymmetries, and if so, the wind of P Cygni might have a long-lived structure (perhaps superimposed upon the clumping variations).

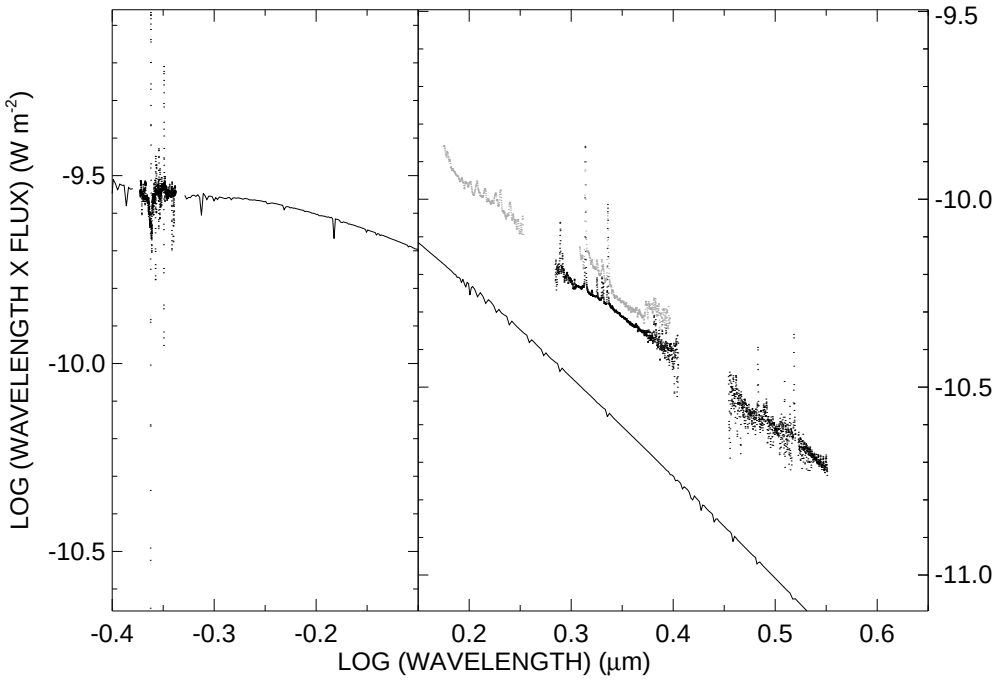

Figure 3.14 Spectrophotometry of P Cygni compared with a model atmosphere, as reported by Touhami et al. (2010). The optical B-band spectrophotometry is used for determining the model spectrum, and then the H-band excess can be determined. The model curve is for a star with no wind, fixed to the observed flux in the $B-$ band, allowing for a determination of the flux excess in the H, K, and L bands.

4
THE Hα VARIATIONS OF η CARINAE DURING THE 2009.0 SPECTROSCOPIC EVENT

The second prototype of the LBVs is the enigmatic (binary) star η Carinae. The binary companion is in a long 5.5 year period in a highly eccentric orbit. During the most recent periastron passage, I arranged an intense monitoring effort using the CTIO 1.5 m telescope and the new echelle spectrograph that was mounted on the telescope at the time. This chapter details the changing Hα profile during that time period[1].

4.1 INTRODUCTION TO η CARINAE

The star η Carinae (HD 93308) is one of the most massive and luminous objects in the local region of the Galaxy. It experienced a great eruption (Figure 4.1) in the mid-nineteenth century that led to the formation of the surrounding Homunculus Nebula (Figure 4.2, Davidson & Humphreys (1997)). The high-excitation, forbidden lines in the spectrum disappear and reappear in a 5.54 y cyclic manner (Damineli et al. 2000). This same periodicity is observed in the star's photometric (van Genderen et al. 2003; Fernández Lajús et al. 2003; Whitelock et al. 2004) and X-ray light curves (Corcoran 2005). Daminelli et al. (1997) and others proposed that this period corresponds to the orbital period of a binary companion in a very eccentric orbit, in which the spectroscopic event (as well as photometric and X-ray minima) occurs near periastron. Detection of the companion has eluded observers so far, but a fit of the spectrum from the *Chandra X-ray Observatory* with models of the X-rays generated in the wind - wind collision indicates that the companion has a powerful stellar wind and is probably also a massive star (Pittard & Corcoran 2002). X-rays from the wind - wind collision region will encounter a varying column density of gas along our line of sight with the changing binary orientation. The X-ray maximum occurs shortly before periastron when our sight line cuts through the rarefied wind of the secondary (bounded by a Coriolis-deflected,

[1]Previously published as Richardson et al. (2010)

bow shock where the winds collide), while the X-ray minimum occurs close to periastron when the collision region is blocked by obscuring, dense gas of the primary's wind. Numerical models of the wind - wind collision by Okazaki et al. (2008) and Parkin et al. (2009) can reproduce many of the features of the X-ray light curve, but they also reveal discrepancies from observations made during the intense interaction at closest approach. Although the details of wind collision need further investigation, the basic geometry of the models helps explain the spatial variations of the emission spectrum from the resolved, extended wind region surrounding the central binary (Gull et al. 2009).

The strong stellar wind and surrounding ejecta of η Car produce a very strong Hα λ6563 line. It is one of strongest emission features in the spectrum and is formed over a large volume (Hillier & Allen 1992; Hillier et al. 2001). The main emission component is formed in the wind of the primary (Hillier et al. 2001; Davidson et al. 2005; Gull et al. 2009), but there are other components formed in nearby circumstellar gas, especially the Weigelt blobs (Weigelt & Ebersberger 1986; Davidson et al. 2005; Gull et al. 2009). Dust in the Homunculus Nebula scatters the starlight of the primary star so that the spatial variations in the emission profile can be used to sample the wind as seen from different orientations. Such investigations indicate that the star has a strong and fast polar wind and a slow and dense equatorial outflow (Smith et al. 2003; Stahl et al. 2005). During the 2003.5 event Davidson et al. (2005) observed a decrease in Hα emission strength and the development of a P Cygni absorption component. However, astronomers have not observed enough periastron events to know if these developments occur every time.

We collected high dispersion Hα spectroscopy of η Car during the recent 2009.0 event through the Small and Moderate Aperture Research Telescope System (SMARTS) program with the Cerro Tololo Interamerican Observatory (CTIO) 1.5 m telescope. We present in Section 4.2 the spectroscopic observations made before, during, and after the minimum. In Section 4.3, we discuss the observed variations and compare them to those observed by

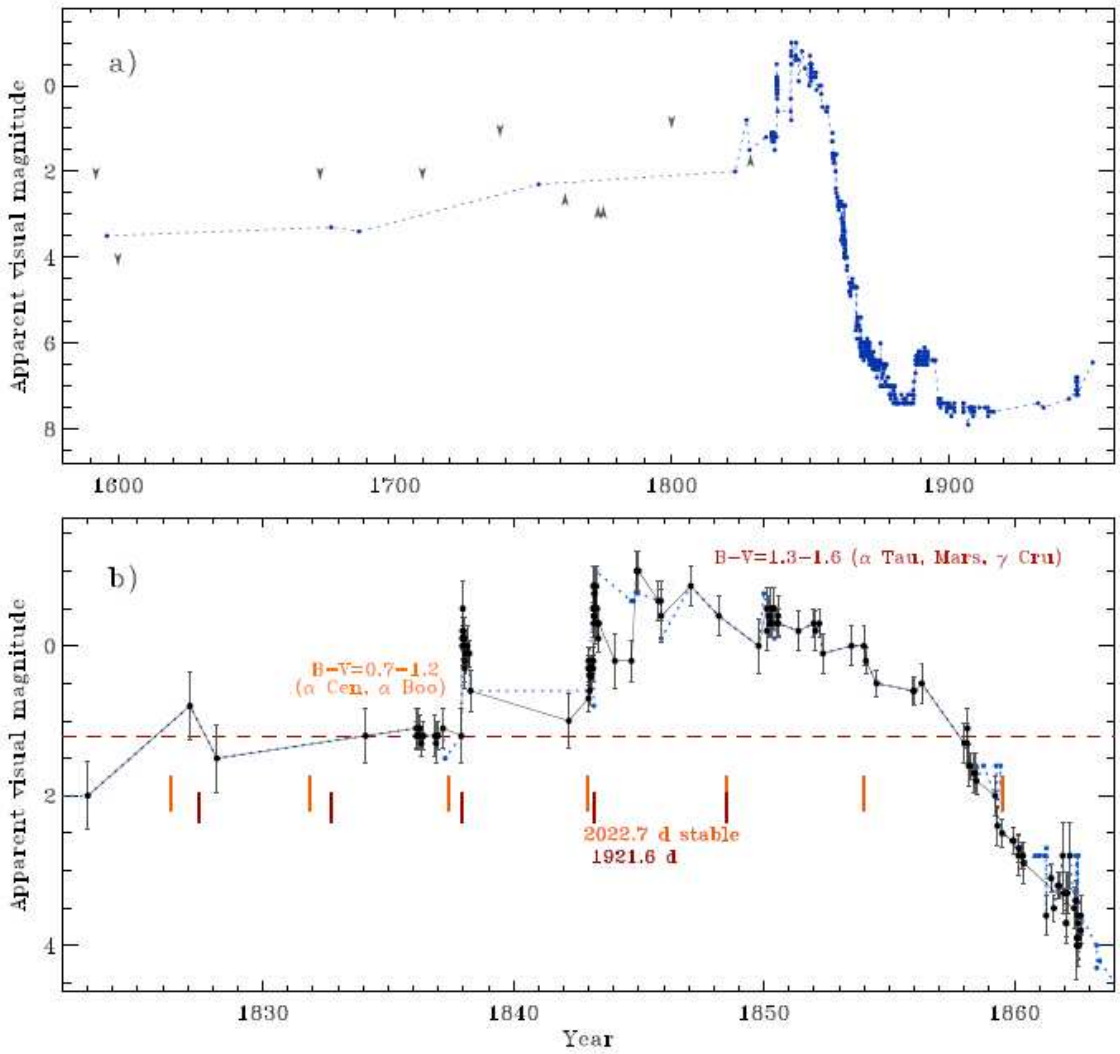

Figure 4.1 A historic light curve of η Car, as presented by Smith & Frew (2011). The bottom panel shows recently re-discovered estimates of the brightness during the eruption, and overlays the interpretation of Smith & Frew (2011) of orbital changes during the great eruption. Color version available in electronic version.

Davidson et al. (2005) during the last (2003.5) event. In Section 4.4, we argue that many of the observed changes are consistent with qualitative predictions of the wind - wind collision model.

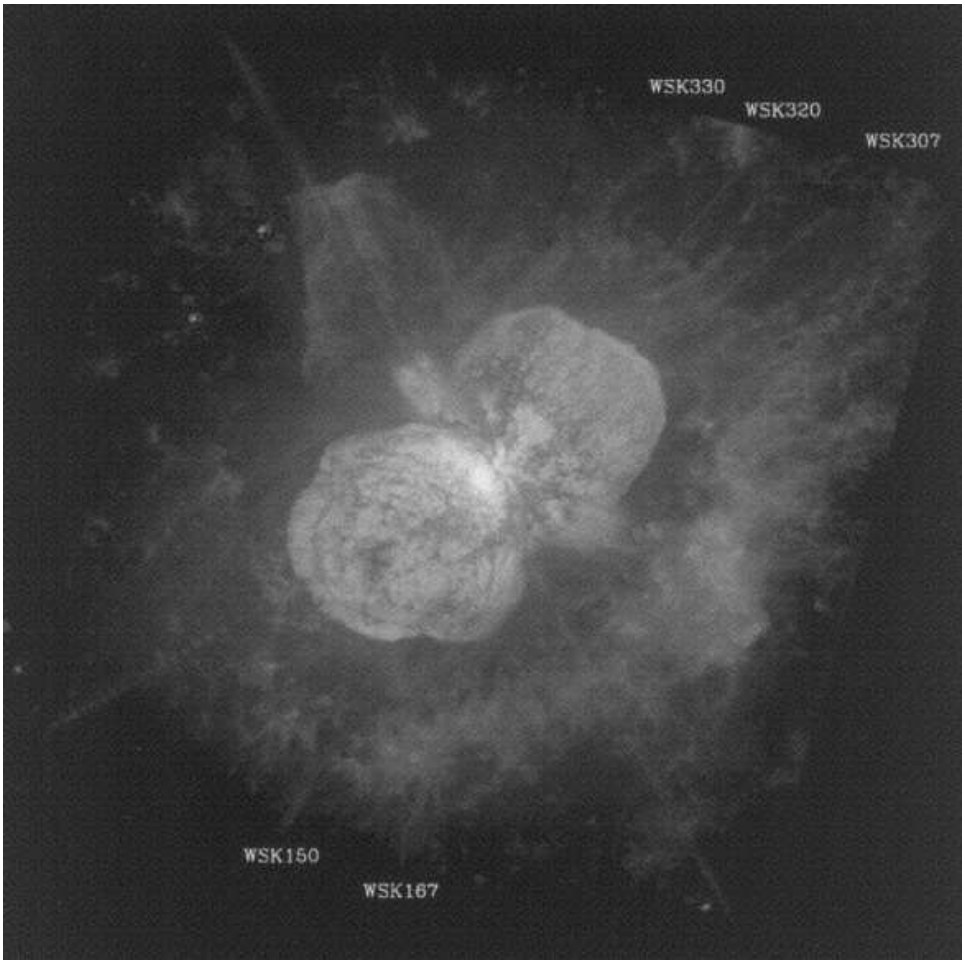

Figure 4.2 The large S Doradus eruption of η Car, observed in the year 1837 created the expanding nebulosity surrounding the central source, which is now called the Homunculus Nebula. Image from *HST*/WFPC2 in a narrow band Hα filter (Morse et al. 1999).

4.2 OBSERVATIONS

We obtained high resolution ($R \simeq 40000$; 0.16Å FWHM) echelle spectra of η Car with the 1.5 m telescope at CTIO. The Fiber Echelle Spectrograph[2] is connected to the telescope by a fiber that collects flux over a circular aperture of diameter 2.7 arcseconds on the sky. The resulting spectra will include flux contributions from the central binary, extended wind, Weigelt blobs, and some scattered light from dust in the Homunculus Nebula (Smith et al.

[2]http://www.ctio.noao.edu/~atokovin/echelle/index.html

2003; Gull et al. 2009). These observations have a good signal-to-noise ratio (between 40 and 100 per pixel in the continuum, depending on the order) and continuous coverage in the spectral region $4800 - 7400$Å. We collected the first echelle spectrum on 2008 Nov 14, and then began obtaining approximately one spectrum per night over the period from 2008 Dec 18 to 2009 Feb 19 (UT). We typically obtained three 30 s exposures, short enough to avoid saturation at Hα, the brightest feature in this spectral region. We also made longer exposure (120 s) spectra to obtain higher signal-to-noise for transitions weaker than Hα, and will be discussed in a future publication. The observations were recorded on a 2048×2048 SITe chip with 24 μm pixels. The chip is read out using two amplifiers, and images are recorded with an overscan region in the central part of the chip. All the spectra were bias-subtracted, trimmed, flat fielded, and wavelength calibrated using standard IRAF techniques for echelle spectroscopy. Wavelength calibration was achieved by means of a ThAr lamp, and the typical residuals of the solution were approximately 0.0035 Å. We extracted 46 orders from each spectrum, ranging from 50 Å to 150 Å of usable data in each order. The Hα spectra were normalized to a unit continuum after large scale sensitivity variations were removed using flat field images, and the final spectra were transformed to a uniform, heliocentric wavelength grid.

We also collected some lower resolution Cassegrain spectra using the CTIO 1.5 m telescope and R-C Spectrograph with the standard 47/Ib setup (Howell et al. 2006), which records the range from 5630 Å to 6950 Å. These spectra have a resolution of 2.2 Å FHWM ($R \simeq 3000$). The spectrograph slit was 1.5 arcseconds wide and 300 arcseconds in height and was oriented in an east - west direction. The spectra were recorded on a Loral 1200×800 CCD detector and were reduced using standard IRAF techniques. Exposures were only 0.2 s long in order to avoid saturation at Hα. Typically, we made two integrations per visit and performed the wavelength calibration using a Ne lamp. The flux standard stars Feige 110 and LTT 4364 were also observed to flux calibrate the spectra, but the spectra were subsequently

normalized to a unit continuum and transformed to a standard, heliocentric wavelength grid.

Table B.2 presents the dates of these observations. Using the period of 2022.7 d and epoch of minimum of HJD 2452819.8 derived by Damineli et al. (2008a), the data is phased to the orbital cycle of the system. Damineli et al. define phase 0.0 to be the time when the narrow emission component of the optical He I lines disappears. They count the 2003.5 event as the eleventh one since the first event noted in 1947 by Gaviola (1953). The predicted time of the 2009.0 event of HJD 2454842.5 was confirmed in recent observations by Damineli et al. (2009). Note that the beginning of the X-ray minimum occurred about 4 d after this[3] and the V-band minimum occurred $\approx$ 16 d after phase 0.0 (Fernández Lajús et al. 2010).

4.3 Hα OBSERVATIONS AND VARIABILITY DURING THE 2009.0 SPECTROSCOPIC EVENT

Figure 4.3 displays the line profiles observed with the echelle spectrograph. The main feature is a large broad emission structure that is probably formed in the wind of the primary star (Davidson et al. 2005; Gull et al. 2009). There are no large scale changes in line position visible, but we measured the radial velocity in the sensitive line wings using a line bisector method (Shafter et al. 1986). This method samples the line wings using oppositely signed Gaussian functions and determines the mid-point position between the wings by cross-correlating these Gaussians with the profile. We used Gaussian functions with FWHM = 20 km s^{-1} at sample positions in the wings of $\pm$300 km s^{-1}, and the resulting bisector velocities V_b are given in column 6 of Table B.2. These measurements (discussed in the next section) show that the broad emission shifted slightly from blue to the red near periastron (in the same sense as expected for the orbital motion of the primary star; Nielsen et al. 2007). There is a narrow emission line in the central part of the profile that originates in the nearby Weigelt blobs (Davidson et al. 2005; Gull et al. 2009). We made no attempt to remove this feature

[3]http://asd.gsfc.nasa.gov/Michael.Corcoran/eta_car/etacar_rxte_lightcurve/index.html

because spatially resolved spectra (Gull et al. 2009) show that the nebular emission extends over the full emission profile and because this nebular component probably varies near phase 0.0. The spectral sequence also shows the development of a narrow absorption line near a radial velocity of -144 km s^{-1}. This feature appeared in earlier spectra (Melnick et al. 1982; Damineli et al. 1998; Davidson et al. 2005; Johansson et al. 2005) and was referred to as the "anomalous absorption" by Humphreys et al. (2002). Several other stationary, narrow, but weaker absorption features are also seen that also appear. The blue side of the profile displayed a bumpy appearance just prior to the minimum in a manner reminiscent of the emission lines of W-R stars (Lépine et al. 1996), and these may result from structure and clumping in the outflow of the primary (Hillier et al. 2001).

Figure 4.4 shows a plot of the logarithmic intensity of the normalized spectra in a gray scale depiction as a function of radial velocity and time. The benefit of this representation is that fainter features in the wings are more readily visible. Figure 4.4 shows how the anomalous absorption feature near -144 km s^{-1} and a second, P Cygni type, absorption feature near -500 km s^{-1} both appear in the Hα profile between observations made on HJD 2454832 and HJD 2454837 (just prior to phase 0.0 at HJD 2454842.5). The P Cygni absorption shows a slight blueward progression as it becomes stronger, reaching a minimum velocity approximately 7 d after its first appearance. At about this time, there is evidence of a flat absorption plateau that extends blueward to -1000 km s^{-1} and lasts for over 10 d. This velocity range of absorption is similar to that inferred for the polar wind of the primary star from observations of scattered light spectra in the Homunculus Nebula (Smith et al. 2003). A similar development of P Cygni absorption was also observed in the 2003.5 event in both Hα and higher members of the Balmer sequence (Davidson et al. 2005; Nielsen et al. 2007). The N[II] λ6583 emission (near $+900$ km s^{-1} in the Hα frame) is seen throughout the sequence, although its strength is very weak after phase 0.0.

We compare in Figure 4.5 the variations observed in 2009.0 with those from the prior

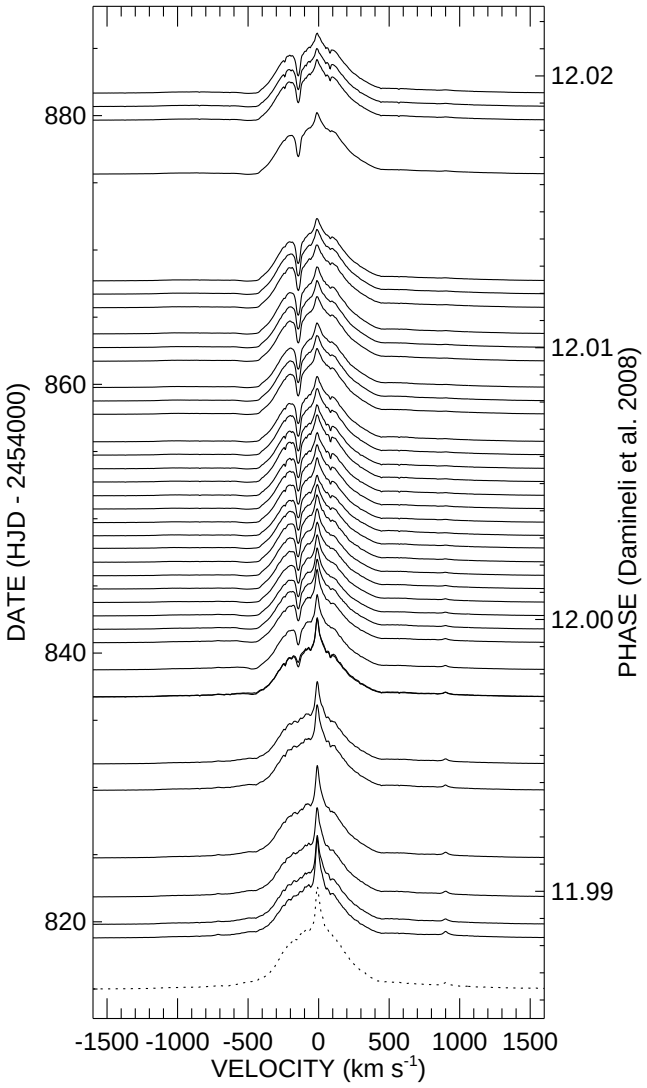

Figure 4.3 A montage of Hα profiles of η Car plotted as a function of time and heliocentric radial velocity. Each profile is placed so that the continuum level is set at the heliocentric Julian date (*left*) or orbital phase (*right*) of observation (Damineli et al. 2008a), with the exception of the first spectrum (*dotted line*) which was made on HJD 2454784.9 (phase 11.972). The line intensity is scaled such that 10× the continuum strength equals one day of time.

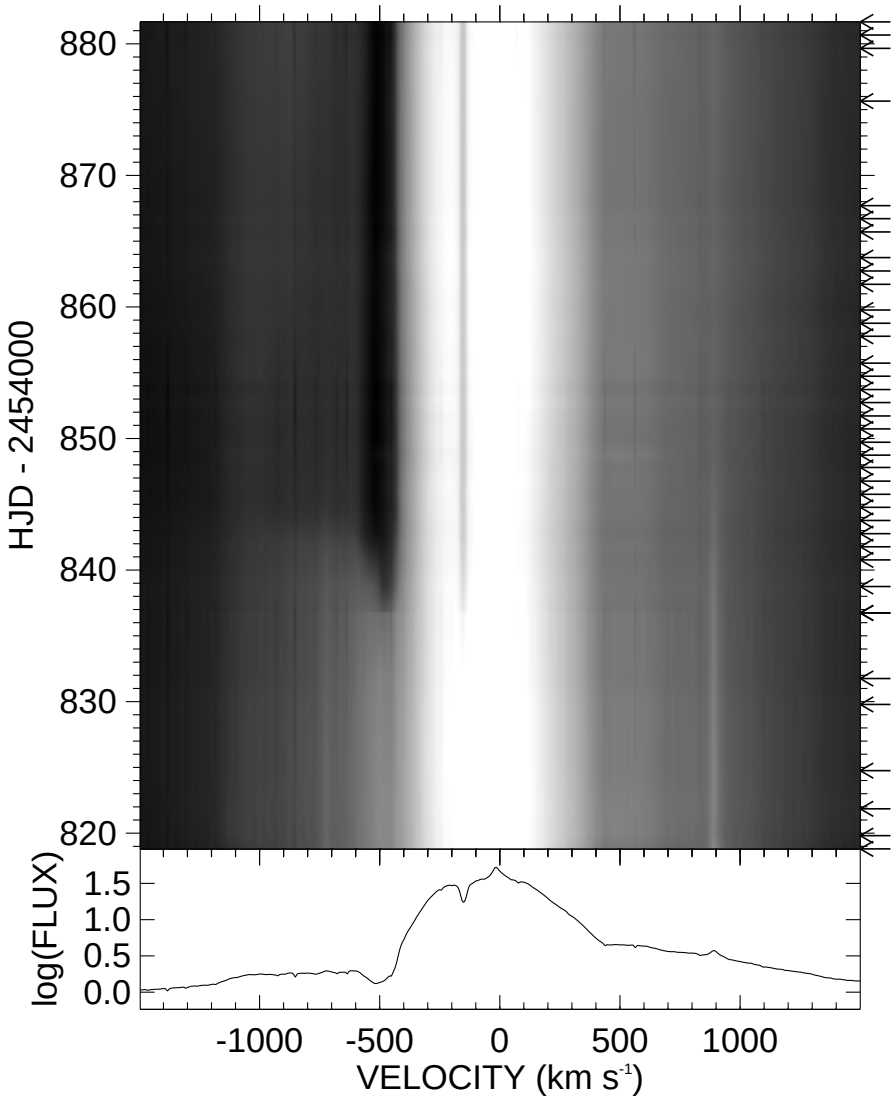

Figure 4.4 A gray scale representation of the Hα profiles, where the intensity is scaled to the logarithm of the normalized flux. The bottom panel represents the average logarithmic profile. Arrows along the right note the times of observations. The narrow absorption at -144 km s^{-1} and the P Cygni absorption at -500 km s^{-1} both appear to strengthen near HJD 2454837, just prior to phase 0.0.

2003.5 event. The Hα spectra from the 2003.5 minimum are *Hubble Space Telescope* Space Telescope Imaging Spectrograph (STIS) observations made available at the HST Treasury Program on Eta Carinae archive site[4]. The STIS spectra were summed across the entire slit to include some of the surrounding nebulosity and to make them more comparable to these ground-based data. We show the STIS spectra (*left panel*) together with the extended set of low resolution R-C spectra augmented with several echelle spectra (*right panel*), and the STIS and echelle spectra are smoothed to the lower resolution of the R-C spectra for ease of comparison. The Hα profiles are different between these two events (partly because the space- and ground-based observations sample different parts of the inner nebula and possibly due to the clumpy nature of the primary's wind; Hillier et al. 2001), but they do appear to show similar trends. They both exhibited minimum strength near phase 0.0 and showed the development of the P Cygni absorption near -500 km s^{-1} around this time (see Fig. 3 in Davidson et al. 2005). Furthermore, the anomalous absorption near -144 km s^{-1} appears to strengthen around phase 0.0 in both data sets. This suggests that these features are modulated on the orbital cycle.

We measured the Hα equivalent width W_λ by integrating the line intensity over a range corresponding to Doppler shifts of $\pm$2500 km s^{-1}. The measurements are listed in column 4 of Table B.2 and are plotted as a function of time in the top panel of Figure 4.6. The typical equivalent width error is $\pm$1%. We transformed these equivalent width measurements to a relative line flux using the $\triangle V$-band light curve of Fernández Lajús et al. (2010) (and subsequent photometry; see lower panel of Fig. 4.6) and the relation

$$W_{\lambda,corr} = W_\lambda \; 10^{-0.4(\triangle V(t) - \triangle V(t_0))}$$

where the fiducial time was set for that of the first echelle spectrum, t_0 = HJD 2454784.9.

[4]http://etacar.umn.edu/archive/

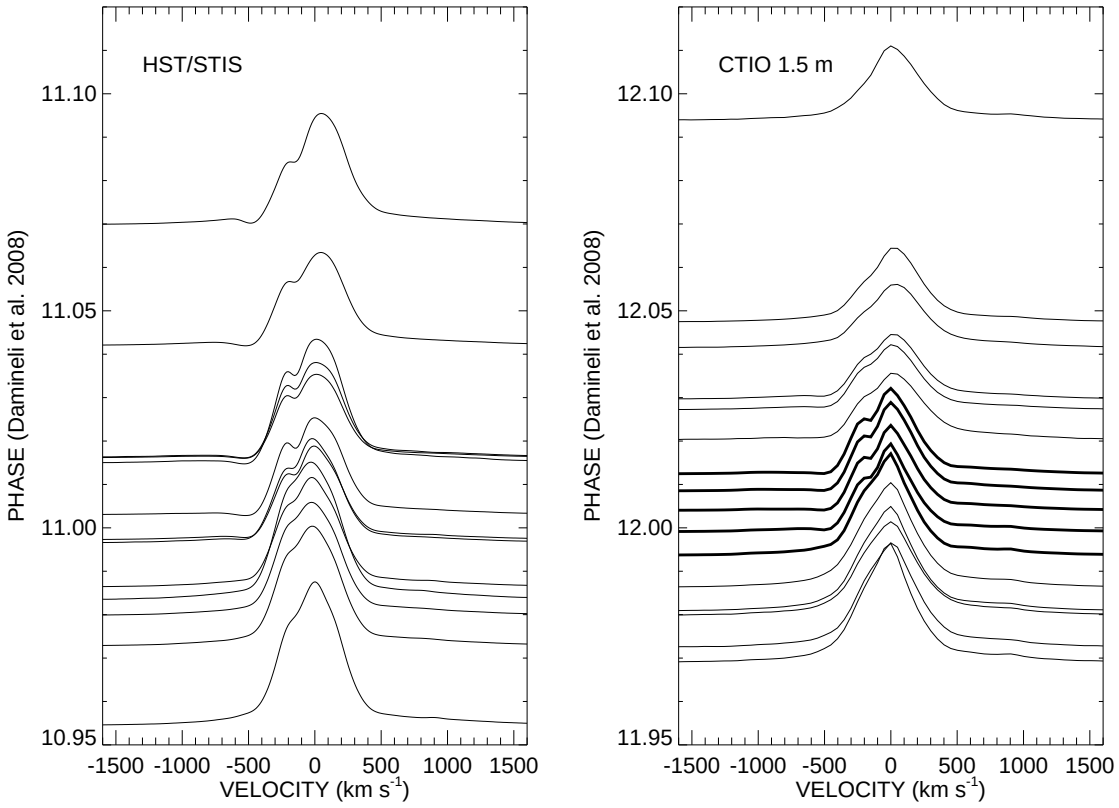

Figure 4.5 A montage of Hα profiles of η Car as it progressed through the last two spectroscopic events. The 2003.5 event spectra (*left*) are from a summation along the slit of the *HST* STIS spectra. The 2009.0 event spectra (*right*) are from CTIO (all the R-C spectra plus five representative spectra from the echelle set (*thick lines*) at mid-event). The STIS and echelle spectra were smoothed to the resolution of the R-C spectra for ease of comparison. The line intensity is scaled such that 10$\times$ the continuum strength equals 0.005 in phase.

When the equivalent widths are corrected for the changing continuum (given in column 5 of Table B.2), the minimum of the Hα flux occurs about 11 d after phase 0.0 (see middle panel of Fig. 4.6). This time lag is similar to that observed in 2003.5 (see Fig. 4 in Davidson et al. 2005). The Hα strength (Davidson et al. 2005) and V-band flux (Fernández Lajús et al. 2010) are generally stronger at other orbital phases and are subject to irregular and long term fluctuations.

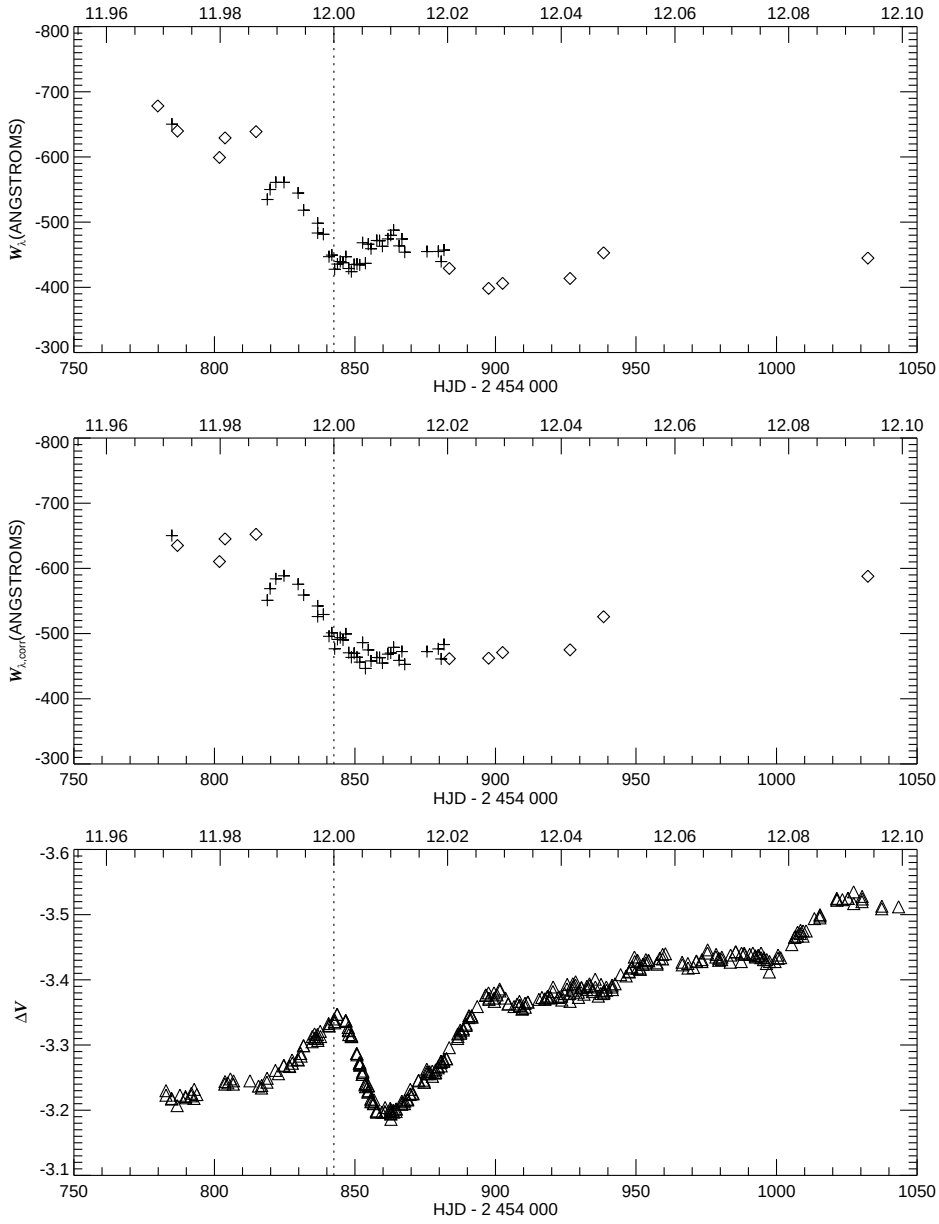

Figure 4.6 The temporal variations of Hα strength and V-band magnitude. In each plot the abscissa represents the date (*bottom*) or phase (*top*). Phase 0.0 from Damineli et al. (2008a) is marked in each plot with a vertical dotted line. The top plot shows the equivalent width derived from spectra obtained with the R-C spectrograph ($\diamond$) and with the echelle spectrograph (+). The middle plot shows the equivalent width corrected for the changing continuum flux that is documented by the differential V-band photometry in the lower plot (Fernández Lajús et al. 2010). The V-band photometry shows that an eclipse-like event began shortly after phase zero and was followed by a general increase in brightness. The typical uncertainties are smaller than the symbol sizes.

4.4 DISCUSSION

These observations show that some of the Hα variations are repeatable from event to event, and consequently it is interesting to consider what aspects of the binary interaction might be the cause. Several of the important variations can be explained in the context of the wind - wind collision model (Okazaki et al. 2008; Parkin et al. 2009; Madura et al. 2010). Okazaki et al. (2008) present a hydrodynamical simulation of the gas dynamics of the wind - wind collision in η Car that they use to model the X-ray light curve. They assume the binary consists of a $90M_{\odot}$ primary with a slow dense wind and a $30M_{\odot}$ secondary with a fast rarefied wind. The orbital eccentricity is set to a large value of $e = 0.90$, and the best fit of the X-ray light curve occurs for a longitude of periastron of the primary of $\omega = 243^{\circ}$ and orbital inclination of $i = 45^{\circ}$. In this configuration, the companion spends most of the time near its apastron position in the foreground along our line of sight (with a separation of roughly 29 AU). As periastron approaches (and the separation drops to 1.5 AU), the secondary passes beyond the plane of the sky, so that closest approach occurs when the secondary lies beyond the primary from our point of view. In Figure 4.7, we show three frames from an animation of one simulation[5]. This portrays the wind density in the orbital plane for an isothermal model. The left frame shows a time near apastron when the secondary (*right*) is well separated from the primary (*left*) and a well-defined bow shock occurs at the wind - wind collision boundary. The dark line in the panel shows the direction of viewing (which lies 45° below the plane of the diagram). The middle panel shows the configuration 21 d before periastron when the stars are much closer and the bow shock is situated very close to the primary. Finally the right panel shows the situation after periastron (a brief 42 d later) when the companion has moved 188° counter-clockwise around the primary.

[5]http://harmas.arc.hokkai-s-u.ac.jp/~okazaki/cwb/eta_car/index.html

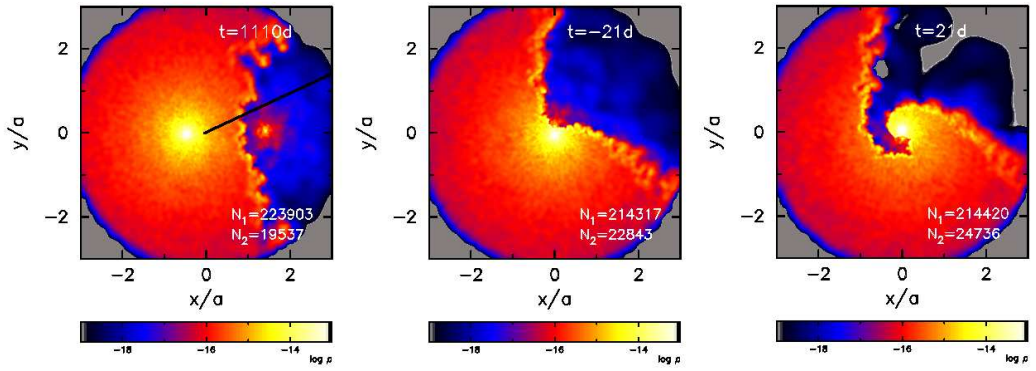

Figure 4.7 Isothermal models of the colliding winds in the binary system from the simulations by Okazaki et al. (2008). Each panel shows a density map in the orbital plane (in spatial units of the semi-major axis). The left panel shows the primary (surrounded by its wind; left side) and the secondary (dot on right side) at maximal orbital separation. The Hα flux is expected to form mainly in the densest regions of the wind. The assumed line of sight is indicated by the black line in the left panel (inclined by 45° from below the plane of the figure). The time in days relative to periastron is given in the upper right of each panel, and the diagrams show how the colliding winds change the density distribution from the usual situation near apastron (*left*) to that at times just before (*middle*) and after (*right*) periastron. Full color version available in electronic edition.

Madura et al. (2009) used similar hydrodynamical simulations to explore how the interaction affects the continuum light of the system when the stars are closest at periastron. They find that the fast wind of the secondary excavates a region of the dense wind of the primary. This "bore hole" effect first exposes to view the hotter and deeper wind layers and results in an episode of brightening. However, as the secondary progresses past periastron towards superior conjunction, the cavity region turns away from us and the system fades. The drop in flux continues past superior conjunction as the cavity reduces the effective volume of wind gas, and the system slowly returns to its original flux as the stars separate and wind material refills the cavity.

Now reconsider the Hα orbital variations in the context of these wind - wind collision models. The Hα emission forms in dense regions of wind (because the emission process is dependent on density squared) that are mainly found relatively close to the primary star

(Hillier et al. 2001). As the companion approaches periastron, the bow shock from the colliding winds gets closer to the primary, and the developing cavity reduces the effective volume of the wind emission from the primary. The resulting Hα emitting volume will reach a minimum at periastron, but will then increase again as the binary separation increases and the wind is restored to the cavity region. Hillier et al. (2001) present a model for the wind of the primary star alone in which the continuum forming radius is approximately 3 AU (where the Rosseland optical depth is one) and the Hα formation peaks near a radius of 18 AU (see their Fig. 15). Based upon the momentum balance of the colliding winds, the wind - wind collision zone will occur at a distance from the primary of $0.67a(t)$, where $a(t)$ is the binary separation at time t, and this reaches a minimum of 1 AU in the binary model (Okazaki et al. 2008). Thus, the colliding winds cavity should significantly reduce the volume of both the continuum and Hα emitting regions close to periastron. The fact that both the length and relative amplitude of the periastron variation is larger for Hα than for the continuum (Fig. 4.6) is consistent with the larger formation radius of the Hα emission. Assuming that periastron occurred when the Hα flux was a minimum at HJD 2,454,854 $\pm$2 (the same periastron time within errors assumed by Madura et al. 2009 based on a fit of the continuum light curve), then the Hα flux began to decrease about 39 d before periastron (Fig. 4.6) when the model distance from the primary to the wind-wind shock was 3 AU. This is closer than the 18 AU Hα formation radius given by Hillier et al. (2001), but it is suspected that a marked Hα reduction will only be observed once a significant fraction of the wind volume is carved out by the colliding winds (i.e., after the bow shock apex reaches to relatively deep within the wind). After periastron, as the colliding winds zone moves outward, the primary's wind will re-occupy the volume opened by the fleeing cavity. Hillier et al. (2001) note that the wind flow time to the Hα formation region is about 100 d, which is comparable to the Hα flux recovery time that was observed (Fig. 4.6).

It is probable that the periastron interaction is also the cause of the Hα radial velocity

variations observed at that time. In Figure 4.8 the measured Hα bisector radial velocity V_b (Table B.2) is shown together with the expected Keplerian orbital velocity curve for the primary. Although there is a superficial resemblance, the observed curve has a much lower semiamplitude than expected. A similar change from blue-shift to red-shift around periastron has been reported for other lines but usually with a much larger amplitude than the orbital value (Nielsen et al. 2007; Damineli et al. 2008b). It is doubtful that the velocity shift observed in Hα is related to Keplerian motion, because the formation radius of the Hα flux is so large that any orbital motion vanishes due to conservation of angular momentum (i.e., all the motion becomes radial). However, the close interaction at periastron may have a tidal influence on the wind of the primary causing the wind to become locally denser and slower along the instantaneous axis between the stars (a "focused wind"; Friend & Castor 1982). Since the Hα flux varies as density squared, this wind density enhancement would result in a slight excess in blue-shifted flux while the companion approaches from the near side of the plane of the sky and then a red-shifted excess around periastron as the companion moves beyond the plane of the sky. A full radiative transfer calculation will be required to test whether or not such a tidal enhancement can explain the timing and amplitude of the observed radial velocity variation.

The development of a P Cygni type absorption feature near a radial velocity of -500 km s^{-1} around the time of periastron (Fig. 4.4) was also observed by Davidson et al. (2005) during the last two events, so it is probably related to the binary interaction. We suggest that the emergence of this absorption component results from a change in illumination by the hot companion. In the binary model, the hot companion resides in the foreground during most of the orbit, and the radiation from the companion probably tends to overionize the outer layers of the hemisphere facing us. However, as the binary approaches periastron, the companion will appear to set below the optically thick horizon as seen from a position in the outer layers of the wind facing our direction. The subsequent gas cooling will result in

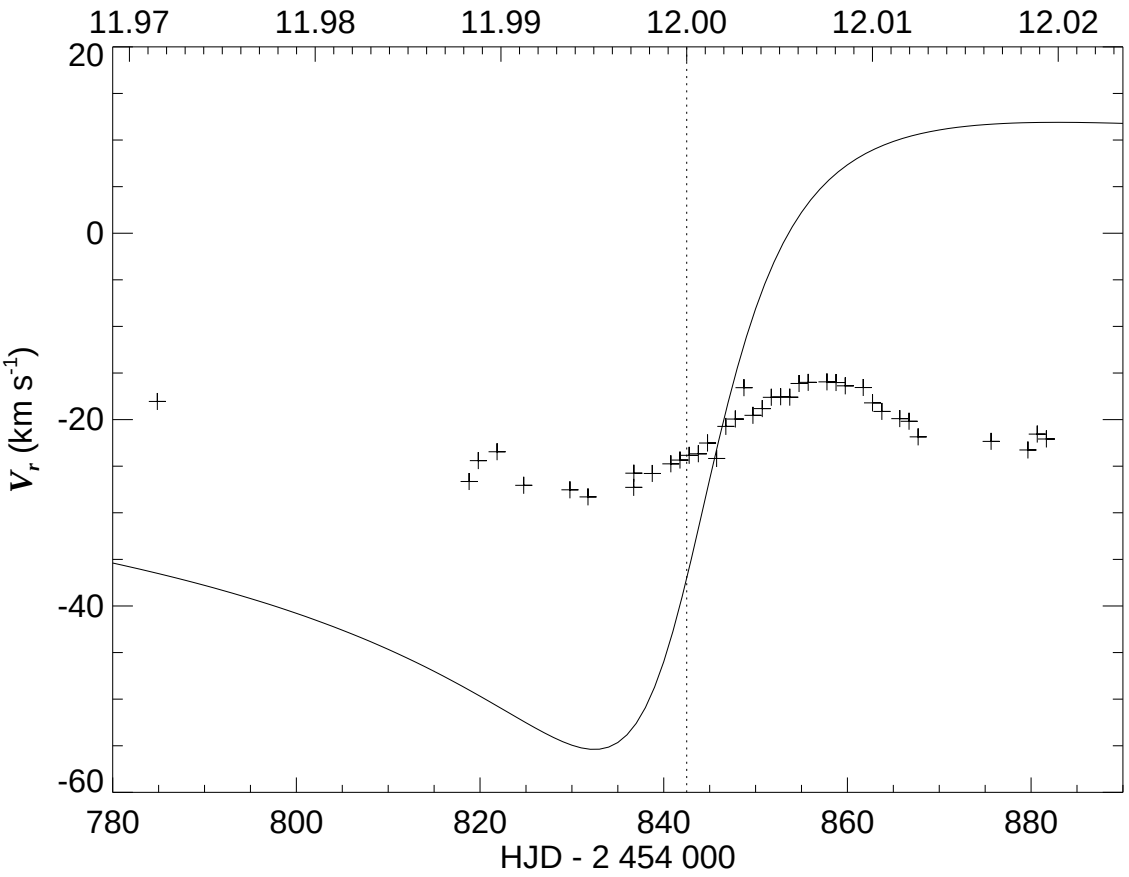

Figure 4.8 The Hα bisector velocities V_b (*plus signs*) plotted against heliocentric Julian date (*bottom*) and orbital phase (*top*). Phase 0.0 is marked with a vertical dotted line. The symbol sizes are comparable to the velocity measurement errors (≈ 1.0 km s^{-1}). The solid line shows the predicted Keplerian orbital velocity curve for the primary star according to the elements adopted by Okazaki et al. (2008), epoch of periastron from Damineli et al. (2008a); assumed identical to their phase 0.0, and the systemic velocity from Smith (2004).

greater absorption by this wind material seen projected against the primary and will cause an increase in the blue absorption of the P Cygni line. Ironically, it is then during this brief time around periastron that the undisturbed, "normal" wind of the primary is observed (at least in the sector directed towards us) with blue-shifted absorption lines that are more similar to the model predictions (Hillier et al. 2001) than observed at the other orbital phases when the hemisphere facing us is illuminated by the secondary star. Through scattered light

spectroscopic studies of the Homunculus Nebula, Smith et al. (2003) found that the polar wind of the primary star exhibits a broad absorption plateau on the blue wing of the P Cygni profile. We see this same behavior in these data (Fig. 4.4), which suggests that we observe a less obstructed view of parts of the primary star's wind during the spectroscopic event.

This same change in secondary illumination is the cause of the sudden appearance of the anomalous, narrow absorption feature just prior to periastron (Fig. 4.4). This same increase in absorption strength was first observed during the 1981.5 event by Melnick et al. (1982), then again during the 1992.5 event by Damineli et al. (1998), and finally during the 2003.5 event (Fig. 4.5) by Davidson et al. (2005), so the phenomenon is clearly linked to the binary clock. This narrow absorption feature is probably formed farther out from the central binary because the feature appears in the spatially resolved, extended emission (see Fig. 15 of Gull et al. 2009) where the gas may be cooler (consistent with the fact that the anomalous absorption is weak or absent in the profiles of the upper Balmer lines; Weis et al. (2005); Nielsen et al. 2007). The feature has the same width and radial velocity as nebular absorption lines that are observed in the far-ultraviolet spectrum and that form in the Little Homunculus, an ionized gas cloud deep within the larger Homunculus Nebula (Ishibashi et al. 2003; Smith 2005; Gull et al. 2009). Since our view to central binary passes through the nearby wall of the Little Homunculus (see Fig. 2 of Nielsen et al. 2009b), it is probable that the Hα anomalous absorption forms there. In the weeks prior to periastron, this part of the Little Homunculus is probably exposed to the ionizing radiation that escapes through the rarefied gas of the secondary star's wind and surrounding bow shock that is oriented in our direction at that time. This ionizing flux leads to a net reduction in the Hα absorption then because the hydrogen gas in the part of the Little Homunculus along our line of sight becomes over-ionized. However, as the secondary progresses towards periastron and the bow shock surface passes beyond our view to the primary, this source of ionizing flux would decrease suddenly (effectively blocked by the wind of the primary), and the net

H absorption would then become much more effective. Such a decrease in the far ultraviolet flux was observed during the 2003.5 event by Iping et al. (2005), who argued that the flux decline resulted from an atmospheric eclipse of a hot companion. The fact that the Hα absorption features at velocities of -500 km s^{-1} and -144 km s^{-1} both appear at about the same time (Fig. 4.4) strongly supports the idea that both result from cooling associated with the temporary disappearance of the ionizing flux of the companion star. Although the wall of the Little Homunculus where the absorption forms lies about 16 light days closer to us than the primary star (Nielsen et al. 2009b), the wall gas would "see" the drop in ionizing flux at about the same time that light arrives from the outer layers of the primary, so the increased absorption from the Little Homunculus will appear to us to occur at about the same time as that from the primary's wind as long as the cooling timescale in the Little Homunculus is short (less than a day). This change in illumination probably also explains the apparent temperature drop in the excitation/ionization properties of iron-group element absorption lines from the Little Homunculus around the time of periastron (Gull et al. 2006).

These arguments suggest that the primary features of the Hα emission form in the extended wind of the primary that becomes truncated and asymmetrical around periastron. The reality is certainly more complicated, and, in particular, the wind collision models predict that high gas densities should occur in the vicinity of the bow shock near periastron. Given the density squared dependence of the Hα emission, it is somewhat surprising that there is no clear evidence of Hα emission from the bow shock region itself (where it might be expected to find a component with a large radial velocity excursion as the bow shock quickly rotates around the primary at periastron). The absence of a bow shock emission component may be due to the higher gas temperatures there (which would cause a decrease in emissivity; Ferland 1980) and/or the presence of intervening, dense gas of the primary star's stellar wind that is too optically thick for the embedded bow shock flux to escape in our direction.

These results support qualitatively the colliding winds model and, in particular, the predicted changes in the primary's emitting wind structure that occur around periastron. A detailed comparison of the model predictions will require a 3D radiative transfer calculation of the Hα line intensities, a very computationally challenging task. Observations around periastron of other emission lines that form closer to the primary will also provide a good test of the validity of the basic picture of the system and its colliding winds. The 2009.0 event of η Car has offered the means to begin this kind of promising investigation.

5
A BINARY ORBIT FOR THE MASSIVE, EVOLVED STAR HDE 326823, A WR+O SYSTEM PROGENITO

During the study of southern LBVs with the CTIO 1.5 m telescope, I found a short $\sim$ 6 d period in the ASAS light curve of HDE 326823, a candidate LBV. I obtained followup echelle spectroscopy and present these results here[1].

5.1 INTRODUCTION

Mass loss plays a key role in the evolution of the most massive stars, where, for example, a 60 $M_{\odot}$ star may lose 65% of its mass before exploding as a supernova (Smith & Owocki 2006). Very massive stars ($> 25M_{\odot}$; Meynet & Maeder 2003) start their lives as O stars and will lose large amounts of mass as they pass through stages such as the red supergiant (RSG) and Wolf-Rayet (WR) phases during their post-main sequence evolution. The most massive stars may experience the rare, luminous blue variable (LBV) stage that is observed in objects such as P Cyg and η Car. During the LBV phase, a star is subject to possible great eruptions, variations on timescales from days to decades, and extremely high mass loss rates (Smith et al. 2011).

The loss of a star's envelope to become a WR star may occur entirely by winds (Massey et al. 1981) or it may be aided by Roche lobe overflow in a close binary to form WR+O systems like γ^2 Vel (North et al. 2007). The prototypical examples of the active mass-transfer objects are β Lyr (Zhao et al. 2008) and the more massive RY Sct (Grundstrom et al. 2007). In both of these cases, we observe the less massive donor star while the more massive gainer star is hidden within an optically thick, accretion torus. Such H-deficient, donor stars will likely explode in Type Ib/c supernovae (Smith et al. 2011), and understanding their pre-SN evolution is critical to the interpretation and modeling of these supernovae.

[1]Previously published as Richardson et al. (2011a)

HDE 326823 (Hen 3-1330; V1104 Sco; ALS 3918; ASAS J170654-4236.6) is a Galactic example of an unusual transition-phase object. van Genderen (2001) places this object in the category of ex-/dormant LBVs, and the star may be entering the WN (nitrogen-enriched WR) stage of evolution from either the LBV or RSG stage (Lopes et al. 1992; Sterken et al. 1995; Marcolino et al. 2007). Sterken et al. (1995a) found some changes in Strömgren photometry over long timescales from data taken three years apart, and they presented some examples of line profile variations in the optical spectrum. Analysis of the more recent photometric variations from the All Sky Automated Survey[2] (ASAS) by Pojmanski & Maciejewski (2004) indicates a short period of 6.123 d and an amplitude of 0.17 mag in V.

The far-UV spectrum of HDE 326823 resembles that of an early B-supergiant (Shore et al. 1990). However, the optical spectrum of HDE 326823 was described as "the most bizarre in the OB Zoo" by Walborn & Fitzpatrick (2000), who discussed the weak H lines, the strong Fe II emission, and several other subtle features. They placed this star in the category of an "iron star" from the presence of the Fe II emission, a group that includes only four other high luminosity objects in their study. The unusual spectrum of HDE 326823 was further examined in two key studies. Borges Fernandes et al. (2001) presented a spectral atlas for the region between 3800 and 9200 Å. They found very strong helium emission lines while the hydrogen Balmer emission lines were relatively weak. The He I, H I, and Ca II emission lines all exhibited double-peaked profiles. Marcolino et al. (2007) performed detailed modeling of the spectrum from the ultraviolet through the optical with the non-LTE radiative transfer code, CMFGEN (Hillier & Miller 1999). They found that the star's wind parameters are similar to those of low luminosity LBVs. Most importantly, they found that the mass fractions are $X_H \sim 3\%$ and $X_{He} \sim 96\%$, and their analysis supports the interpretation that the object is a pre-WN star. Their CMFGEN model fits the spectral

[2]http://www.astrouw.edu.pl/asas

energy distribution and most emission lines, but does not account for the double-peaked profiles.

In this paper, we present in Section 5.2 a re-analysis of the photometry from ASAS, and we show that the complex ASAS light curve is consistent with the earlier photometric variations observed by Sterken et al. (1995). In Section 5.3, we present new, moderate and high resolution, spectroscopic observations, use radial velocity measurements of weak N II absorption features to derive orbital elements based upon the photometric period, and show how the emission profiles vary with this period. We develop in Section 5.4 a binary scenario to explain the observational properties. We summarize our results in Section 5.5.

5.2 PHOTOMETRIC VARIATIONS

We re-analyzed the light curve by first collecting V-band measurements from ASAS (Pojmanski 2002) and removing points deemed lower quality by the ASAS data reduction pipeline. We performed a time-series analysis on the remaining 479 V-band measurements spanning 3155 d using the Lomb-Scargle periodogram (Scargle 1982). In the period domain of 2–40 d, we find strong peaks around periods 3 and 6 d. However, the 3 d period is a sub-multiple of the main period of photometric variability of 6.1228±0.0053 d (Fig. 5.1, top), confirming the 6.123 d period listed in the ASAS Catalog of Variable Stars (Pojmański & Maciejewski 2004). We see two minima and maxima in the phased light curve (maxima near phase 0.35 and 0.9 and minima around phase 0.1 and 0.8, when phased to an epoch of HJD 2454622.4312, introduced in Section 5.3). Pojmański & Maciejewski (2004) classify the light curve as a DCEP-FU type, i.e., that of a Cepheid pulsating in the fundamental mode. However, this star is so far removed from the Cepheid instability strip due to its temperature and expected luminosity that we must seek other explanations (Section 5.4).

We also examined the archival measurements of the Long-term Photometry of Variables (LTPV) program of Strömgren y magnitudes (Sterken et al. 1993; Manfroid et al. 1995;

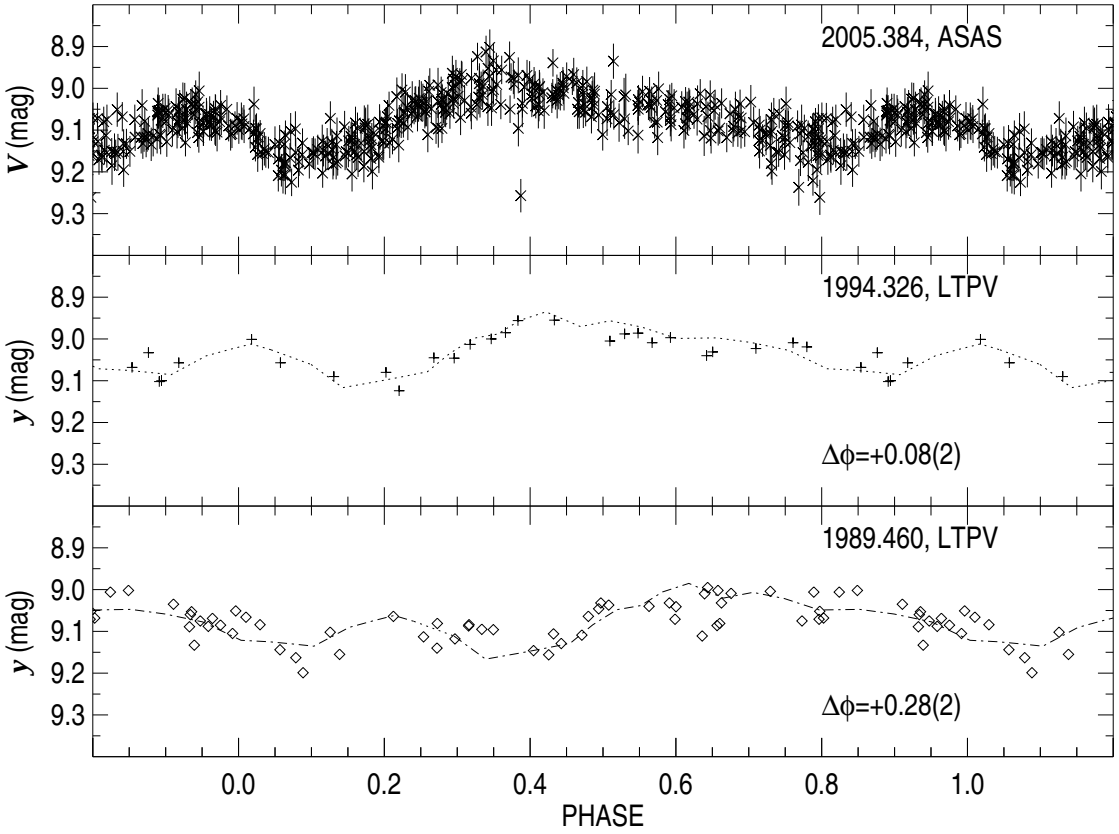

Figure 5.1 The ASAS V-band photometry is shown in the top panel according to the phasing described in the text. The middle and bottom panels illustrate the y-band measurements of Sterken et al. (1995a). Plus signs show data taken in 1994, while small diamonds represent data from 1988 to 1991. The mean date of each set is given in upper right part of each panel. The phase-averaged (and shifted) ASAS light curve is overplotted for comparison (see text). The phase shift applied to the ASAS light curve is listed in the lower right part of the middle and lower panels (with error estimates in the last digit quoted given in parentheses).

Sterken et al. 1995). Sterken et al. (1995a) analyzed these data and found a systematic brightening between data collected from 1988 and 1991 and data collected in 1994. We show their y-band measurements in the second and third panels of Figure 6.1, where the 1994 data are plotted in the middle panel and the earlier measurements are shown in the bottom panel. These light curves are qualitatively similar to the ASAS light curve, but appear shifted in phase. The appropriate phase shift was found by cross-correlating in phase the observed set

with a phase-binned, averaged light curve from ASAS. The shifted ASAS light curve is shown in the middle and bottom panels of Figure 6.1 for phase shifts of $\Delta\phi = +0.08 \pm 0.02$ and $\Delta\phi = +0.28 \pm 0.02$, respectively. These shifts indicate that the actual period may be slightly smaller and/or was smaller in the past compared to the period derived from ASAS, and we encourage continued photometric observations. Nevertheless, the reasonable agreement between the shifted ASAS light curve and the LTPV data sets indicates that the complex, cyclic, light variations have likely been present over the last two decades.

5.3 SPECTROSCOPIC VARIATIONS

5.3.1 Observations

We obtained 21, low dispersion, red spectra of HDE 326823 with the CTIO 1.5 m telescope and Cassegrain R-C spectrograph (SMARTS Consortium setup 47/Ib; described by Howell et al. 2006). These spectra have a resolution of 2.2 Å FWHM ($R \simeq 3000$). The spectra were recorded on a Loral 1200×800 CCD detector and were reduced using standard techniques. We typically made two 120 s integrations per visit and performed the wavelength calibration using a Ne lamp, with resulting residuals typically of 0.02 Å.

We also obtained high resolution spectroscopy ($R \sim 40000$) with the CTIO 1.5 m telescope and the fiber-fed, echelle spectrograph[3]. We typically made two 900 s integrations per visit. The resulting echelle spectra are of good quality in the red-green region, where we typically obtained a signal-to-noise ratio of 50–75 per pixel in the continuum. These spectra were reduced using standard echelle spectroscopy techniques with IRAF[4], but the spectra were flat-fielded after extraction with custom IDL software in order to remove residual jumps in the intensity across the center of the dual-readout chip. The wavelength solution was de-

[3]http://www.ctio.noao.edu/∼atokovin/echelle/FECH-overview.html

[4]IRAF is distributed by the National Optical Astronomy Observatory, which is operated by the Association of Universities for Research in Astronomy, Inc., under cooperative agreement with the National Science Foundation.

termined by means of a Th-Ar lamp spectrum that was made at the same sky location just prior to the science exposure. Typical residuals to the fit are on the order of 0.006 Å. We obtained spectra over five nights during the commissioning period for the spectrograph (2008 Jun 5–9) and over 15 additional nights during 2010. The commissioning period spectra cover a range 4780–6450 Å, while the more recent spectra were collected with the full chip being read out and cover a range of 4200–7350 Å. Note that all of these data suffer from very low signal-to-noise at regions blueward of ~ 5500 Å. A few of these spectra were omitted in the analysis, because of their low signal-to-noise ratio.

5.3.2 Absorption Line Variability

Very few absorption lines are present in the red part of the spectrum of HDE 326823 (Borges Fernandes et al. 2001), but there are a few N II lines in the region of 5667–5710 Å that are recorded in our echelle observations (see Fig. 1b in the paper by Borges Fernandes et al. 2001). In Figure 5.2 we show a two panel plot of these features as a function of photometric phase, both as line plots (top panel) and as a gray scale that is interpolated in phase to fill in observational gaps (lower panel). There is a subtle, double-peaked, emission feature blueward of these N II lines that is identified as Fe II $\lambda\lambda 5657, 5659$ by Borges Fernandes et al. (2001). The N II absorption lines show large radial velocity shifts as a function of photometric phase, while the Fe II emission remains kinematically stationary.

These N II features are typically observed in the spectra of B-type supergiants. We computed a reference spectrum by using the values of $T_{\rm eff} = 22,280$ K and $\log g = 2.9$ from the spectral modeling of Marcolino et al. (2007) and by interpolating within the BSTAR2006 grid of model spectra (Lanz & Hubeny 2007). This reference spectrum is shown in the top panel of Figure 5.2 with the continuum placed at phase 1.1. The N II lines in the model match reasonably well with those in the observed spectrum in most cases, but there are at least four epochs where these lines weaken or disappear entirely.

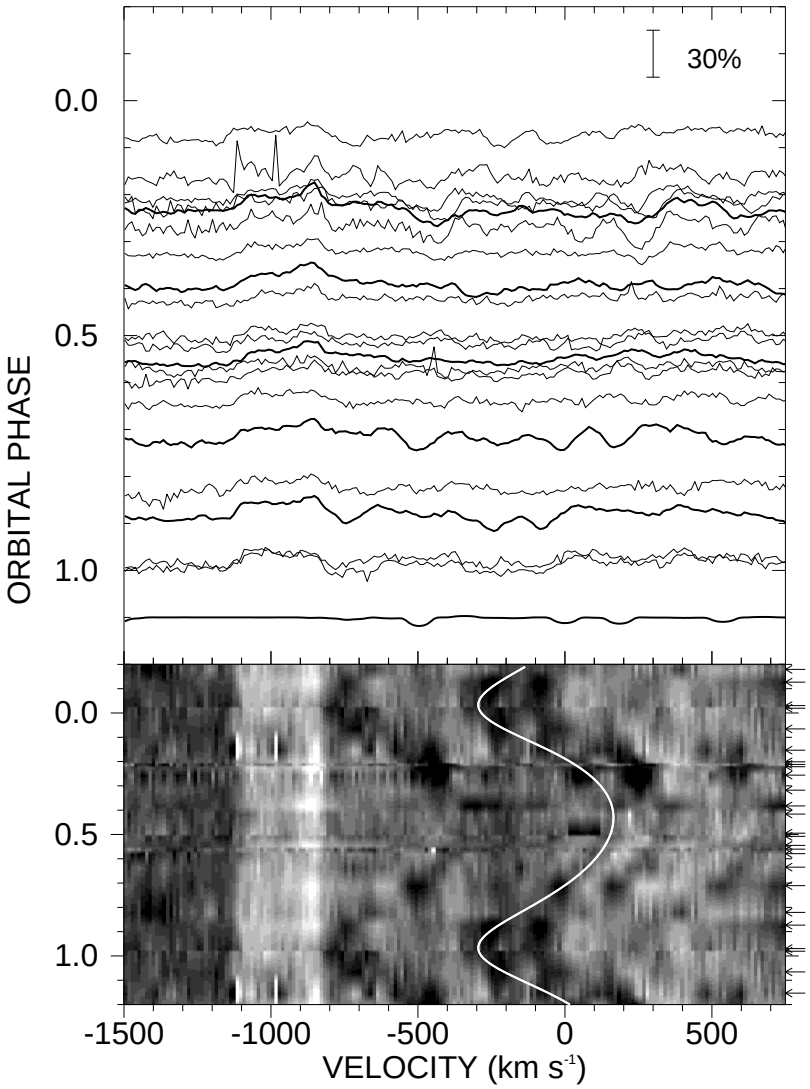

Figure 5.2 Spectra in the range 5648 – 5690 Å plotted as a function of heliocentric radial velocity (for $\lambda_0 = 5676.02$ Å) and orbital phase. This region includes Fe II λ5673 emission and N II $\lambda\lambda 5666, 5676, 5679, 5686$ absorption lines. The top panel shows individual spectrum plots with the continuum set at the phase of observation. The continuum scale is indicated with the vertical bar at the top. Also depicted is a model reference spectrum (thick line; set with the continuum placed at phase 1.1). Spectra collected in 2008 are shown by thicker lines and those from 2010 by the thinner lines. The bottom panel shows a phase-interpolated, grayscale representation of the spectra. Arrows indicate phases of observations, and the white line shows the derived radial velocity curve in the reference frame for N II λ5676.

Table 5.1 N II Radial Velocities

Date (HJD−2,450,000)	Orbital Phase	V_r (km s^{-1})	$\sigma(V_r)$ (km s^{-1})
4623.8538	0.2323	+59.5	5.7
4624.8424	0.3938	+184.6	5.9
4626.8519	0.7220	−6.7	4.0
4627.8460	0.8844	−252.9	4.2
5327.8527	0.2122	+31.6	3.6
5339.8048	0.1643	−40.2	8.5
5348.8753	0.6457	+63.0	5.8
5377.5490	0.3288	+68.8	20.0
5387.6646	0.9810	−276.3	4.7
5406.6203	0.0769	−216.8	4.6
5409.6502	0.5717	+110.8	8.0
5413.6381	0.2231	+87.2	3.3
5429.6113	0.8319	−166.1	10.0
5430.5901	0.9917	−262.7	7.8
5444.5214	0.2670	+57.2	3.4
5446.5006	0.5903	+108.7	6.1

5.3.3 A Single-Lined Spectroscopic Orbit

We measured radial velocities for the NII lines by means of cross-correlation with the reference spectrum computed above. Our results produced reliable velocities for all but four observations where the N II lines were too weak to measure. The average statistical error of the cross-correlation velocities is 6.6 km s^{-1} according to the method of Zucker (2003), but the individual errors are much larger in those cases where the N II lines are weak. We used these measurements and the derived photometric period of 6.1228 d to make an error-weighted fit of the remaining orbital elements using the program of Morbey & Brosterhus (1974). The measurements are given in Table 5.1, and the derived, single-lined, orbital elements are shown in Table 5.2 (where T is the epoch of periastron that we adopted in Section 5.2 for the light curve). We plot in Figure 5.3 the radial velocities as a function of orbital phase, together with the derived orbital velocity curve.

Our derived orbit has two features that are striking. The first is that an eccentric orbit fits the data much better than a circular orbit. When we fit a circular orbit, the rms of the residuals from the fit increased by more than a factor of two. A significant eccentricity is unusual for a short period binary because strong tidal forces should act to circularize the

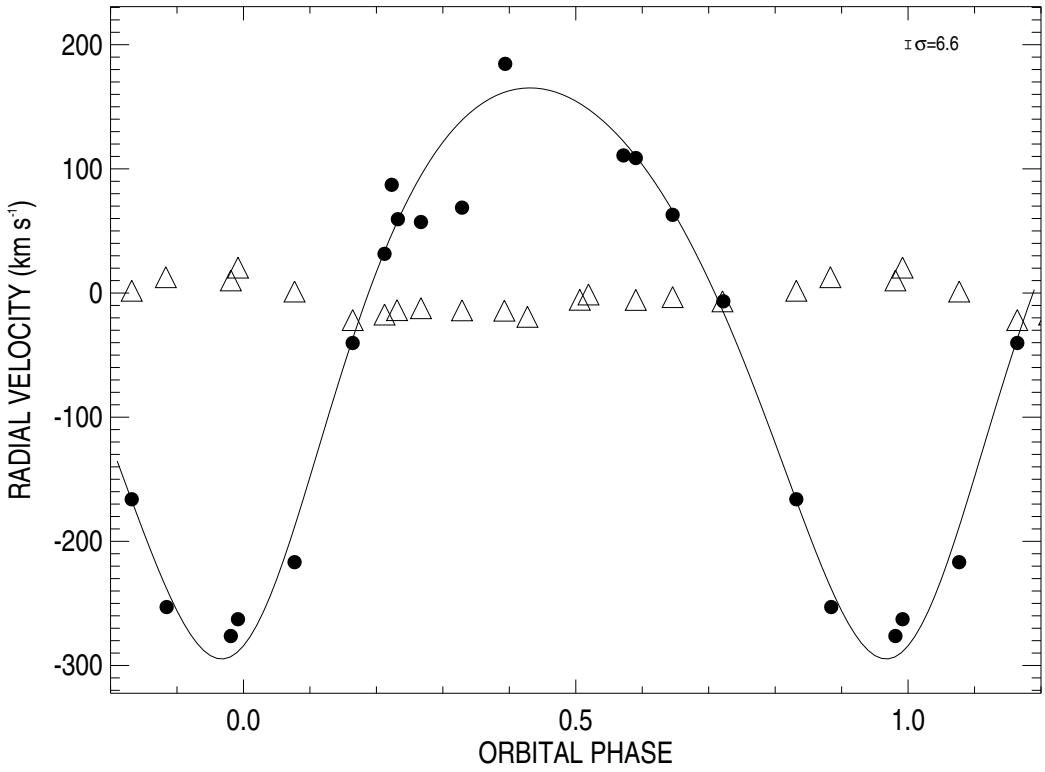

Figure 5.3 The orbital radial velocity curve (solid line) based upon the observed N II velocities (filled circles). Overplotted as triangles are the radial velocities of the He I λ5876 emission line bisector. A typical statistical uncertainty for the N II velocities (6.6 km s^{-1}) is shown in top right portion of the plot.

Table 5.2 A Single-Lined Spectroscopic Orbit

Element	Value
P (d)	6.1228 (Fixed)
T (HJD – 2,400,000)	54622.43 ± 0.25
e	0.19 ± 0.06
ω (deg)	197 ± 14
K_1 (km s^{-1})	230.0 ± 12.7
V_0 (km s^{-1})	-23.9 ± 8.4
$a_1 \sin i$ ($R_\odot$)	27.3 ± 1.5
$f(M)$ ($M_\odot$)	7.3 ± 1.2
r.m.s. (km s^{-1})	29.3

orbit. The second notable aspect of this orbit is that the mass function is large, with a value of $7.3 M_{\odot}$. This suggests that the companion is a massive star, yet there is no clear evidence of spectral features with Doppler shifts corresponding to those of the companion. We will discuss the nature of the companion star in Section 5.4.

5.3.4 Emission Line Variability

5.3.4.1 *He I Lines*

Some of the strongest emission features in the optical spectrum of HDE 326823 are the He I $\lambda\lambda 5876, 6678, 7065$ lines (Borges Fernandes et al. 2001). We show the He I $\lambda 5876$ profiles in Figure 5.4 as a function of radial velocity and orbital phase. The emission line appears relatively constant and is always double-peaked, similar to those observed in the spectra of Be stars where the flux originates in a circumstellar disk (Porter & Rivinius 2003). However, to emphasize the subtle variations related to phase, we subtracted the average profile from the observations to produce a phase-interpolated, grayscale depiction of the difference spectra that appears in the lower panel of Figure 5.4. The difference spectra exhibit an absorption subfeature that moves in the same way as found for the N II absorption lines (the N II radial velocity curve is overplotted as a white line). We interpret this as the photospheric He I $\lambda 5876$ absorption line of the visible star. In Section 5.4 we discuss several other subtle, phase-related variations, such as the well-defined, red edge of the emission that first appears near phase 0.7 and progresses linearly blueward until near phase 0.4. Similar line and grayscale difference plots for He I $\lambda\lambda 6678, 7065$ are shown in Figures 5.5 and 5.6, respectively, and these show variations similar to the case of He I $\lambda 5876$.

Remarkably, the bulk of the emission in He I $\lambda 5876$ shows no evidence of the orbital Doppler shifts we found for the N II absorption lines (Section 5.3.3). We checked this absence of motion by measuring the radial velocity of the steep line wings of He I $\lambda 5876$ using a line bisector method (Shafter et al. 1986). The bisector velocities are determined by

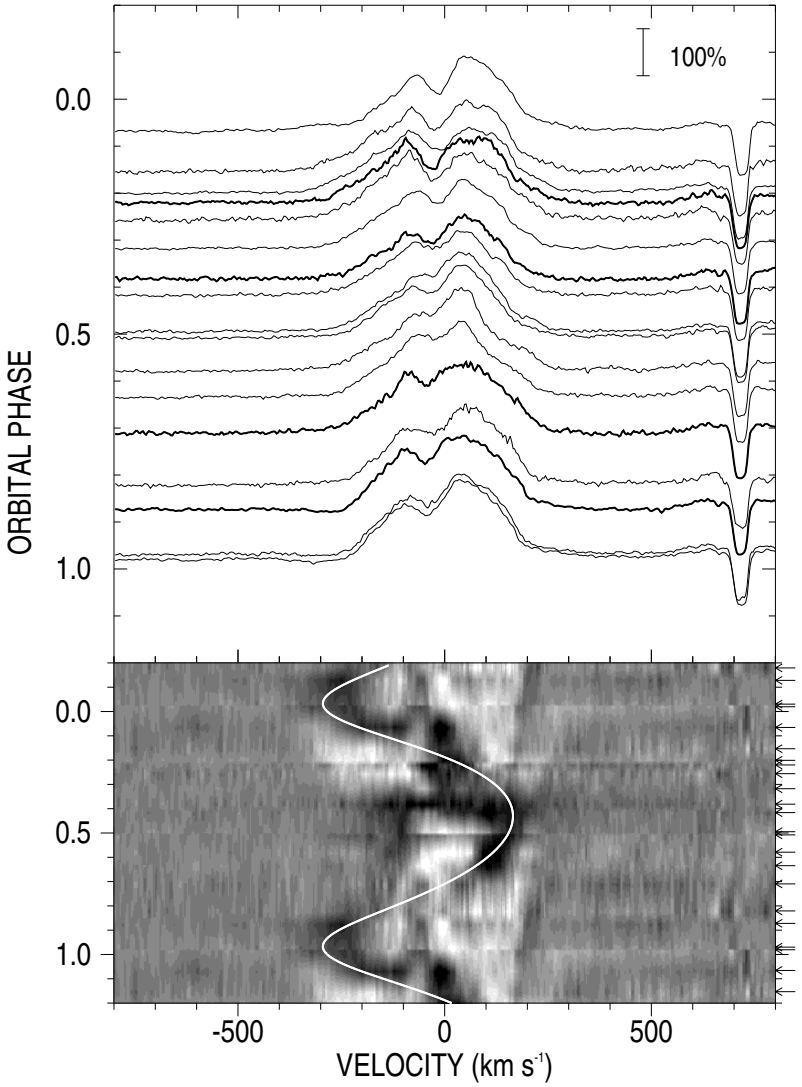

Figure 5.4 He I λ5876 echelle spectra shown as a function of heliocentric radial velocity and orbital phase in a similar manner as Fig. 5.2. The spectra from 2008 are shown as thicker line plots to show the long-lived phase dependent behavior. The bottom panel shows a grayscale depiction of the difference spectra, formed by subtracting the average profile from each individual spectrum. Arrows indicate times of observations, and the thick white line shows the derived orbital radial velocity curve from the N II absorption lines. The variable absorption component appears to follow this velocity curve.

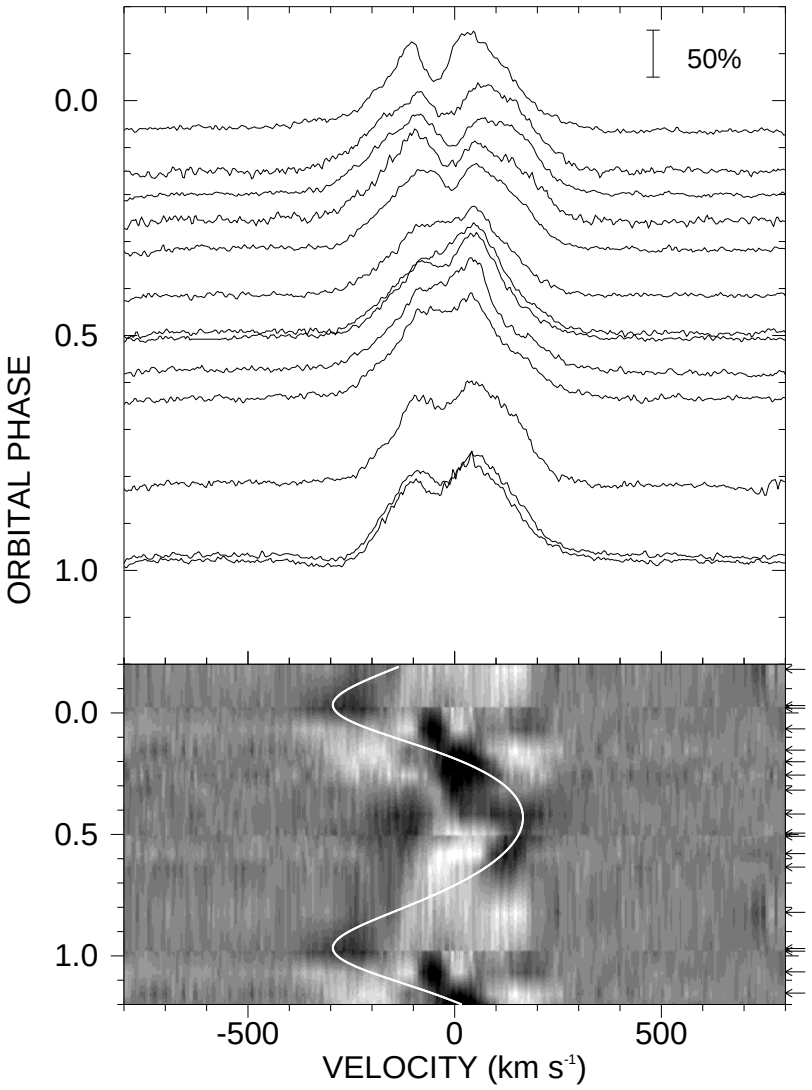

Figure 5.5 He I λ6678 echelle spectra (top) and difference spectra (bottom) presented in the same format as Fig. 5.4.

cross-correlating the observed profile with a template formed of oppositely signed Gaussian functions with FWHM = 75 km s^{-1} at offset positions of $\pm$150 km s^{-1}. The zero-crossing of the resulting cross-correlation function yields the bisector velocities V_r that are listed in Table 5.3 and plotted as plus signs in Figure 5.3. Typical uncertainties for these velocities are $\pm$3 km s^{-1} for the echelle data and $\pm$24 km s^{-1} for the lower resolution Cassegrain spectra as

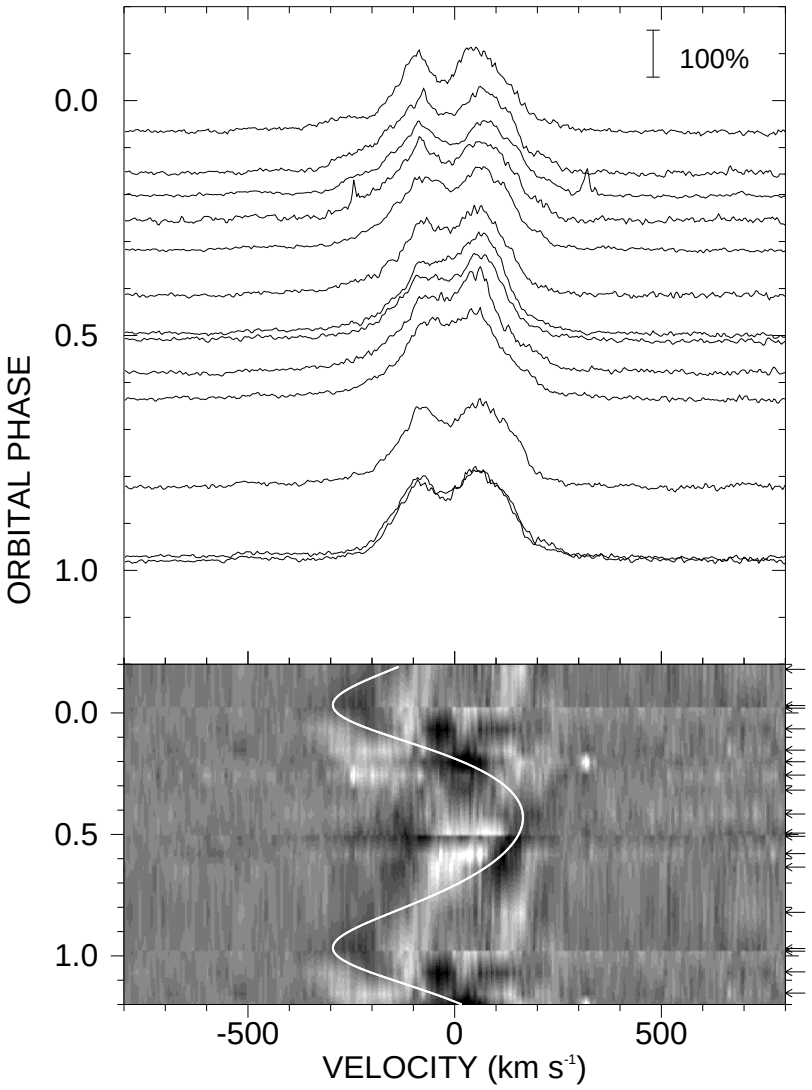

Figure 5.6 He I λ7065 echelle spectra (top) and difference spectra (bottom) presented in the same format as Fig. 5.4.

measured from variability in the velocities of the interstellar Na D absorption lines. We see a small amplitude variation in the opposite sense to that of the N II absorption lines that we attribute to the influence of the weak He I absorption component that causes an apparent reduction in the emission wing flux at the Doppler shift extrema. Thus, we conclude that the He I λ5876 feature is well explained by the superposition of a kinematically static emission

Table 5.3 He I λ5876 Measurements

HJD −2,400,000	Phase	Spectrograph	W_λ (Å)	V_r (km s^{-1})
54552.698	0.611	R-C	−9.06	−31.3
54587.861	0.354	R-C	−8.20	−36.0
54600.788	0.465	R-C	−9.70	+2.2
54623.846	0.231	echelle	−8.13	−13.8
54624.835	0.392	echelle	−6.23	−14.2
54626.844	0.721	echelle	−8.40	−6.7
54627.838	0.883	echelle	−8.39	+12.7
54638.821	0.677	R-C	−10.02	−4.5
54642.773	0.322	R-C	−8.91	+8.9
54647.788	0.141	R-C	−10.50	−22.5
54652.770	0.955	R-C	−9.27	−5.6
54682.716	0.846	R-C	−10.97	+4.0
54690.703	0.150	R-C	−10.40	−30.3
54902.828	0.795	R-C	−10.48	−6.1
54926.868	0.722	R-C	−11.42	−12.6
54984.862	0.194	R-C	−9.91	−38.8
54991.812	0.329	R-C	−8.28	−17.6
55020.802	0.063	R-C	−9.95	−2.3
55070.652	0.205	R-C	−10.08	−24.6
55111.530	0.882	R-C	−9.59	+10.6
55124.516	0.002	R-C	−9.05	+2.3
55325.864	0.887	R-C	−9.51	+9.2
55327.853	0.212	echelle	−9.76	−17.3
55335.854	0.519	echelle	−8.03	−1.2
55339.805	0.164	echelle	−9.60	−21.8
55346.866	0.317	R-C	−9.48	−23.9
55348.875	0.646	echelle	−8.77	−3.3
55358.505	0.218	R-C	−9.72	−17.6
55377.549	0.329	echelle	−7.89	−14.0
55378.634	0.506	echelle	−8.81	−5.4
55387.665	0.981	echelle	−9.37	+1.2
55385.828	0.681	R-C	−10.27	−12.3
55406.620	0.077	echelle	−8.01	+1.2
55429.611	0.832	echelle	−9.37	+1.8
55430.590	0.992	echelle	−9.36	+20.5
55444.521	0.267	echelle	−9.14	−12.3
55445.502	0.427	echelle	−6.92	−19.2
55446.501	0.590	echelle	−9.10	−5.6

line and an orbitally-modulated absorption component from the visible supergiant.

The other remarkable fact is the near constancy of the He I λ5876 emission strength indicating the emission source is never substantially occulted by the stars over the course of the orbit. We measured the net equivalent width of the feature by a numerical integration from −500 to +1200 km s^{-1} across the profile. The larger, positive boundary necessarily includes the Na I λ5890 line because the resolution of the R-C spectrograph blends the red

wing of He I λ5876 with the blue emission wing of Na I λ5890. The entire Na D component remains approximately constant and makes a negligible contribution to the variability of He I λ5876 (see Fig. 5.4). The formal errors associated with these equivalent width measurements are $\pm$2% for all of these data, primarily set by lower signal-to-noise in the echelle data and by uncertain continuum placement in the Cassegrain spectra (due to the large number of unresolved emission lines). These measurements are listed in Table 5.3 and are plotted in Figure 5.7. There is a systematic 1.1 Å difference in the average equivalent width for the two data sets that is due to differences in continuum placement. If the absolute emission flux remains constant throughout the orbit, then we would expect to observe an apparent change that varies as the inverse of the continuum flux. We overplot in Figure 5.7 scaled versions of the inverse of the flux from the smoothed ASAS V-band light curve, and we see that the equivalent width variations are similar to those expected for a constant emission line flux relative to a changing continuum. This indicates that the emission source remains clearly visible throughout the orbit.

5.3.4.2 *Hα*

HDE 326823 is extremely hydrogen deficient with a H mass fraction of 3% (Marcolino et al. 2007), and the only hydrogen lines observed in the optical spectrum are Hα and Hβ (Borges Fernandes et al. 2001). We show in Figure 5.8 the phase-related behavior of Hα observed in echelle spectroscopy from 2010. The feature appears more or less constant throughout the orbit, a property confirmed in the set of Cassegrain spectra.

5.3.4.3 *Metal Lines*

There are several Fe II emission lines in our spectra of HDE 326823 that are weak, double-peaked features. In general, the S/N ratio of our data is too low to investigate the orbital-related variations in these lines, but we show one example in Figure 5.9. This emission

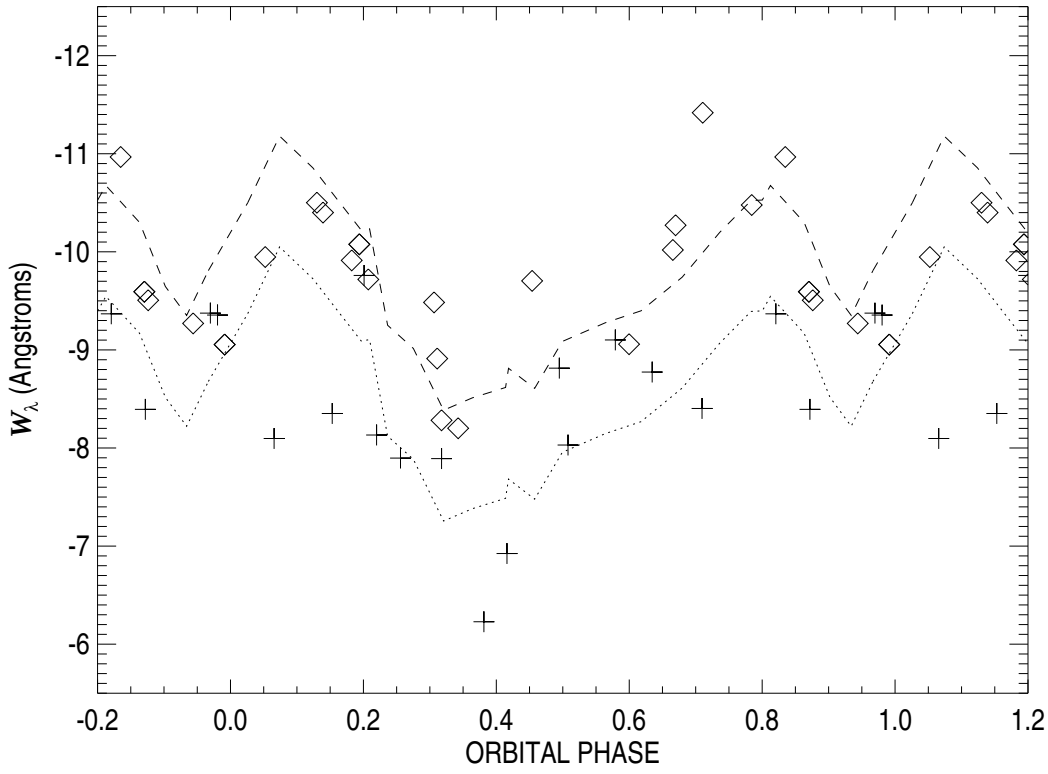

Figure 5.7 He I λ5876 equivalent width as a function of orbital phase. Measurements from the echelle spectroscopy are shown with + symbols, and the Cassegrain spectra measurements are shown with $\diamond$ symbols. The dashed and dotted lines are predictions of the variations caused by the changing continuum flux, and they represent the inverse of the flux from the phase-averaged ASAS light curve that is scaled to the average equivalent width of each data set, with the dashed line corresponding to the Cassegrain measurements and the dotted line corresponding to the echelle measurements. Uncertainties are on the order of 2–3%.

feature is identified by Borges Fernandes et al. (2001) as a blend of Fe II λ6345, Si II λ6347, and Ni II λ6347. We see some evidence of changes in the blue and red emission peak strength, and the difference profiles shown in the lower panel suggest a progressive flux shift from the red to blue emission extremes between orbital phases 0.3 and 0.9. Our interpretation will be discussed in §5.4.

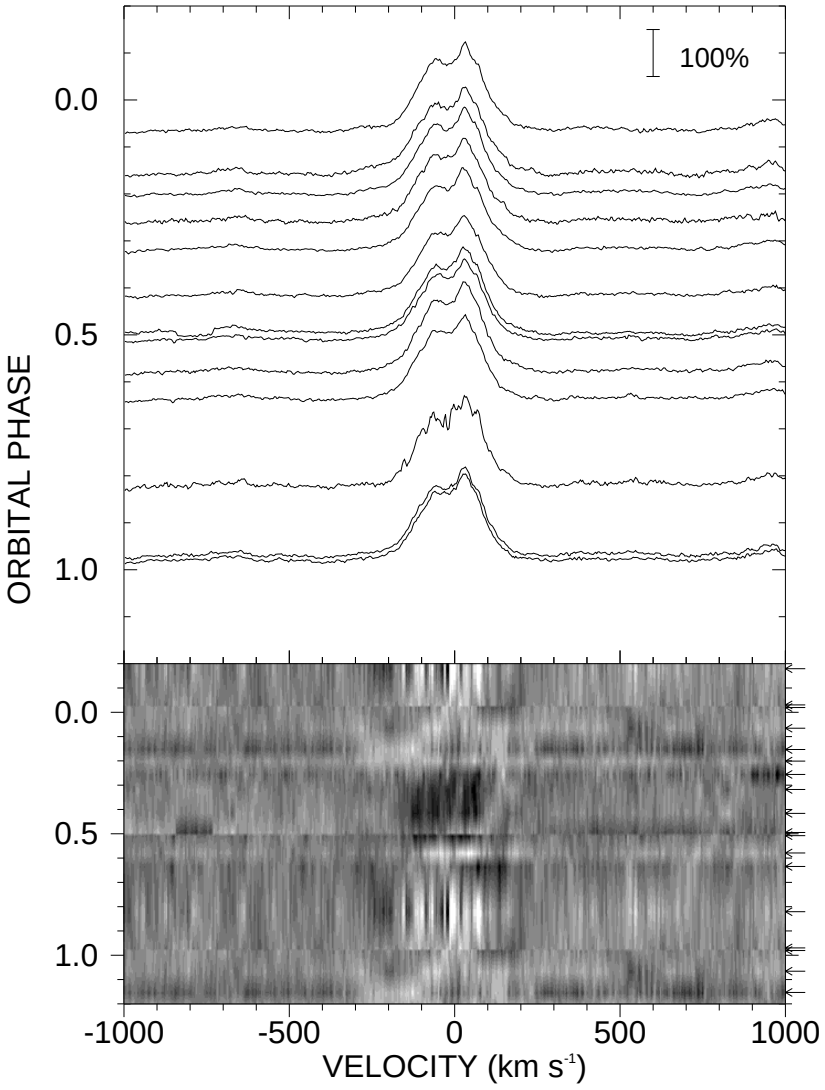

Figure 5.8 Echelle spectra of Hα as a function of orbital phase and heliocentric radial velocity. The line plots (top panel) and grayscale representation of the difference spectra (bottom panel) are in the same format as Fig. 5.4. No radial velocity curve is shown, as no photospheric component is observed.

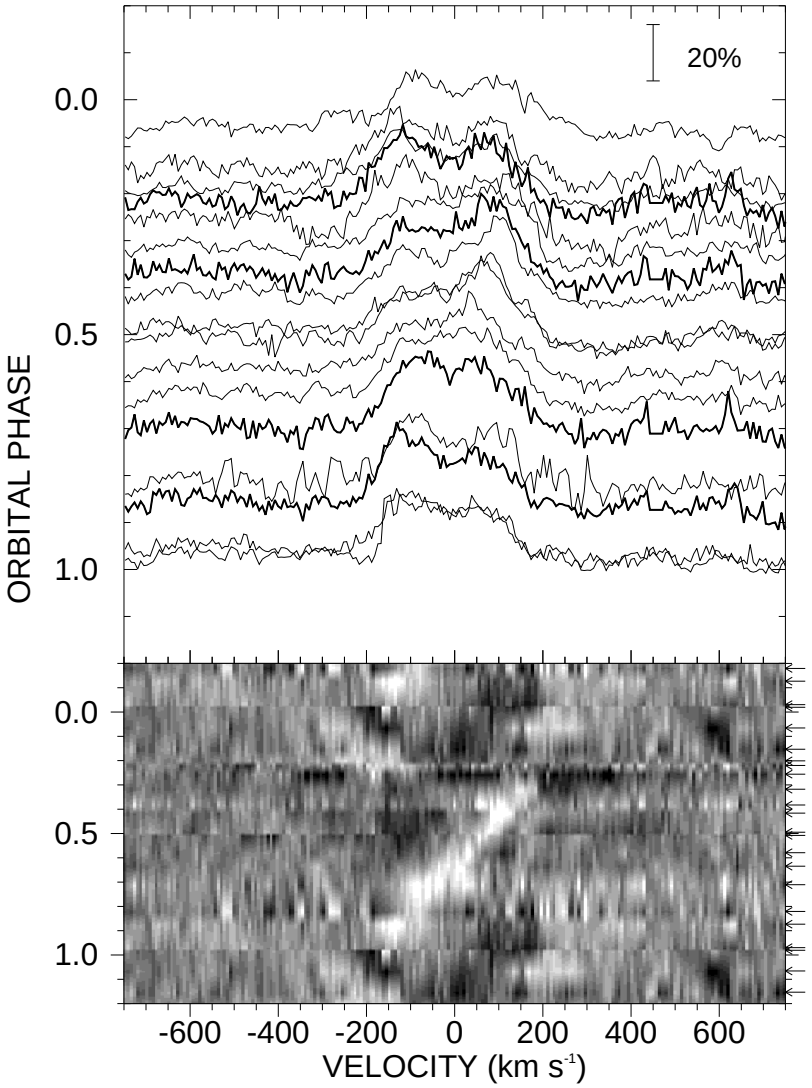

Figure 5.9 Echelle spectra of the Fe II λ6345, Si II λ6347, and Ni II λ6347 blend as a function of orbital phase and heliocentric radial velocity (in the reference frame of Si II λ6347.11). The line plots (top panel) and grayscale representation of the difference spectra (bottom panel) are in the same format as Fig. 5.4. No radial velocity curve is shown, as no photospheric component is observed.

5.4 DISCUSSION

The facts that have emerged from our spectroscopic analysis are striking and challenging. HDE 326823 is a short period binary with a massive, yet unseen companion. The low H abundance of the visible star (Marcolino et al. 2007) indicates that it has lost a significant fraction of its outer envelope, and the presence of strong emission lines indicates the presence of circumstellar gas from ongoing mass loss. All these properties suggest that HDE 326823 is an interacting binary which is experiencing active mass transfer. Here we propose that HDE 326823 is related to the W Serpentis class of massive binaries (Tarasov 2000), systems in which the mass donor appears as the visible, lower mass component and the more massive, mass gainer is hidden behind a thick accretion torus (Nazarenko & Glazunova 2006).

The mass function $f(M)$ (Table 5.2) indicates that the total mass of the system is large,

$$M_1 + M_2 = 7.3 M_\odot \left(1 + \frac{1}{q}\right)^3 \sin^{-3} i$$

where the mass ratio is $q = M_2/M_1$ and the subscripts 1 and 2 denote the visible and unseen companion star, respectively. Both the terms involving q and i on the right hand side of the expression are greater than unity, so the total mass is potentially very large. On the other hand, Marcolino et al. (2007) found that the total luminosity of HDE 326823 corresponds to that of a single star with an initial mass of $25 M_\odot$, and this suggests that the mass ratio term should be relatively small or, equivalently, $q > 1$. This agrees with our expectation that the visible mass donor has lost most of its mass to the gainer and that the mass ratio has reversed. We can make an initial estimate of the mass ratio by comparing the projected rotational velocity $V \sin i$ to the orbital semiamplitude K_1 (Gies & Bolton 1986),

$$\frac{V \sin i}{K_1} = \rho \, \Omega \left(1 + \frac{1}{q}\right) \Phi(q).$$

This expression relates the size of the visible star to the Roche radius $\Phi(q)$ (Eggleton 1983) through a fill-out factor ρ (= 1 for a Roche filling star), and the angular rotational rate is expressed relative to the synchronous rate through factor Ω. Based upon the absorption line profiles published by Borges Fernandes et al. (2001; see their Fig. 5), we estimate that $V \sin i = 83 \pm 15$ km s^{-1} (or smaller if the line broadening is significantly influenced by macroturbulence) from a visual estimate of the FWHM of the profile. We assume that the visible star fills its Roche lobe at periastron (based upon evidence of mass transfer and mass loss), so that the average fill-out factor is $\rho = (1 - e) = 0.81 \pm 0.06$. Furthermore, we imagine that tidal forces have acted to force the star into the synchronous rotation rate that occurs at periastron (when tides peak), and therefore, $\Omega = (1 - e)^{-2} = 1.51 \pm 0.22$. Then the expression above can be solved for the mass ratio, $q = 5.3^{+3.9}_{-1.8}$, which is again consistent with the mass ratio reversal expected for the advanced stage of evolution of this binary. The eccentric nature of the orbit is surprising, but it could be that episodic mass loss in the system causes the orbit to be non-circular.

We present a graphic representation of the system geometry in Figure 5.10 that shows the binary as viewed from above the orbital plane. For the purposes of this diagram, we adopt $q = 5.3$ and $i = 45°$, which leads to masses of $M_1 = 5.5 M_\odot$ and $M_2 = 29.1 M_\odot$. The central binary is drawn to a scale for the time of minimum separation at periastron. The visible star (left) is assumed to fill its Roche surface at periastron, and the companion star (right) is shown with a radius of $10 R_\odot$, appropriate for a main sequence star with the adopted mass (Martins et al. 2005). Arrows centered in each star represent their orbital velocity about the center of mass (indicated by a tick mark within the figure of the companion), and the numbers in each quadrant surrounding the binary give the orbital phase corresponding to the direction to the observer.

We suggest that many of the properties of HDE 326823 can be understood in the context of the mass transfer and mass loss processes observed in other W Ser systems such as β Lyr

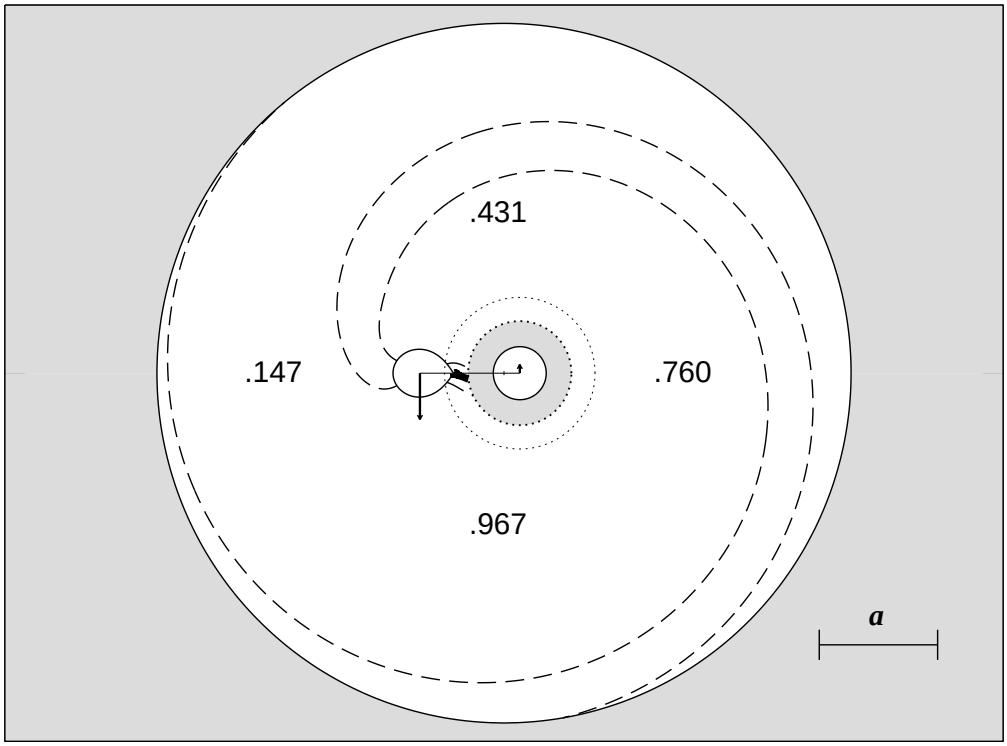

Figure 5.10 Graphic depiction of the binary system and circumbinary disk, as seen from above the orbital plane. See text for details.

(Zhao et al. 2008) and RY Sct (Grundstrom et al. 2007). The visible star in such systems is losing mass by Roche lobe overflow (RLOF) to the companion. Mass transfer is accompanied by angular momentum transfer that can spin-up the companion to the critical speed where it can no longer easily accrete additional gas. The gas then accumulates in a thick torus that surrounds and obscures the companion star. The RLOF is indicated in Figure 5.10 by thick and thin stream lines between the stars, while the torus is shown as a shaded region surrounding the companion (out to an assumed radius of 80% of the companion's Roche lobe). The large optical depth of the torus gas is the probable explanation for the absence of the companion's spectral features in the observed spectrum.

Hydrodynamical models by Nazarenko & Glazunova (2006) suggest that mass loss from the binary can occur through the loss of torus gas through the L3 region and through the lower gravitational potential region around L2 on the far side of the mass donor. We show in Figure 6.10 example trajectories of the gas leaving the donor through the L2 region (left of mass donor). These were calculated in the restricted three-body approximation ignoring the small eccentricity of the orbit. This mass stream feeds a circumbinary disk (outer shaded region in Fig. 6.10) with an inner radius of $2.83a$ (where a is the semimajor axis) that corresponds to the innermost stable orbit according to the calculations of Pichardo et al. (2008).

We suspect that the emission lines in the spectrum of HDE 326823 form in the circumbinary disk of the system. This location is consistent with the lack of observed binary orbital motion, the large volume of formation, cooler gas conditions, and rotational motion that are required to explain the double-peaked emission profiles of Hα and the He I and Fe II lines. The projected Keplerian rotational velocity of circumbinary disk gas as a function of distance r from the binary is given by

$$V_K \sin i = \frac{2\pi a \sin i}{P} \left(\frac{r}{a}\right)^{-1/2} = 226 \text{ km s}^{-1} \left(1 + \frac{1}{q}\right) \left(\frac{r}{a}\right)^{-1/2}.$$

Thus, the highest emission speed we would expect in the model for circumbinary gas would occur for the inner disk boundary at $r/a = 2.83$, or $V_K \sin i = 160$ km s^{-1} (for $q = 5.3$). This is consistent with the He I λ5876 profiles that have an average half-width at half-maximum of 146 km s^{-1} (see Fig. 5.4).

A circumbinary disk being fed through the L2 point would explain two observed features in the He I profiles. We see an excess of blue-shifted emission near phase 0.2 (Fig. 5.4). From our depiction of the binary (Fig. 5.10), this phase corresponds to times where the mass stream that is ejected from L2 appears in the foreground with negative radial velocity. As

the gas stream moves away from L2 and lags behind the binary motion, the velocities within the outward spiral will become closer to the Keplerian speeds given above. Thus, the fastest motions we observe at any given orbital phase will correspond to the projected gas speed in the part of spiral with the largest projected separation from the central binary. Since this separation will increase and the associated Keplerian velocity decrease with advancing phase, we might expect to observe a gradual decline in the wing velocity that is similar to what we observe after phase 0.0 in the blue wing and especially after phase 0.5 in the red wing of He I λ5876 (see Fig. 5.4).

The binary scenario may also explain the lack of Hα variability (§5.3.4.2) and the orbital phase-dependent behavior of the metal lines (§5.3.4.3). We suggest that all these emission lines form in the circumbinary disk, since they are generally constant in radial velocity. Unlike the He I emission lines, there is no apparent photospheric component crossing Hα (Fig. 6.8), and this may be due to the low H abundance in the atmosphere of the mass donor. We suspect that Fe II formation is favored in the somewhat cooler and dense gas conditions of the circumbinary disk, and the donor star's atmosphere may be too hot to produce any photospheric Fe II absorption lines. Indeed, Marcolino et al. (2007) found that models for the star alone were characterized by higher ionization states in the atmosphere (Fe III and Fe IV), so the presence of a somewhat cooler circumbinary disk offers a reasonable explanation for the presence of the Fe II emission lines. The moving emission peak observed in Fe II (Fig. 5.9) may result from a gas density enhancement that occurs where the spiral stream from L2 meets the inner boundary of the circumbinary disk (lower, left part of the boundary in Fig. 5.10). If the disk thickness and inclination act to restrict our view to the far side of the inner cavity, then we would expect to observe this over-dense part of the boundary with maximum redshift near phase 0.4 and maximum blueshift near phase 0.9, more or less in agreement with the emission shift observed in the Fe II difference profiles (Fig. 6.9).

We think that the binary model can also explain qualitatively the main features of the

V-band light curve (Fig. 6.1). Since the visible star fills or nearly fills its Roche surface, it will be tidally distorted and will display a characteristic ellipsoidal flux variation as we view the wide and narrow dimensions of the star with changing orbital phase. According to the binary geometry shown in Figure 6.10, we expect to observe maxima near phases 0.97 and 0.43 and minima near phases 0.15 and 0.76, and these phases correspond to the observed extrema in the light curve. Furthermore, if the accretion torus is a significant contributor to the continuum flux, then changes in the torus size with the elliptical orbit may affect the light curve. For example, increased mass transfer at periastron followed by increasing binary separation to apastron may allow the optically thick torus to increase in size (to a radius shown by the dotted line in Fig. 6.10), and consequently the torus flux contribution would increase over the interval from phase 0.0 to 0.5. This may explain why the maximum at phase 0.43 is brighter than the maximum at phase 0.97. A detailed model of these flux variations should provide an estimate of the binary inclination, since the amplitude of the ellipsoidal variation varies as $\sin i$ while the amplitude of the torus size variation varies as $\cos i$ (in the thin disk limit).

We explored three other explanations of the periodic variations, but none of these were satisfactory in the end. First, suppose that HDE 326823 is a triple system consisting of a single LBV star with a distant 6 d binary. This picture agrees with the radial velocity constancy of the emission lines, but it is inconsistent with the observed changes in the emission line wing morphology with orbital phase (Figs. 5.4, 6.5, and 6.6). Second, perhaps the emission lines originate in the accretion torus surrounding the mass gainer star and the mass ratio is so extreme that the gainer's orbital motion is negligible. However, in this case the Keplerian gas motion in the torus would be very large because the gas is so close to the massive gainer star, and we would expect the emission line widths to exceed the semiamplitude of the binary companion. This is opposite to our results that show that the binary semiamplitude K_1 (230 km s^{-1}) is much larger than the characteristic half-width at

half-maximum of the emission lines (146 km s^{-1} for He I 5876, with similar values for other species). Lastly, consider the possibility that HDE 326823 is a single star with a magnetically channeled wind that is observed at different orientations as the star rotates (Townsend & Owocki 2005; Ud-Doula et al. 2009). Suppose that the magnetic and spin axes are slightly misaligned (the oblique rotator model; Shore & Brown 1990) and that the outflow is observed in spectral lines as the magnetic pole transits the visible hemisphere. However, in the spectral lines of magnetically active massive stars, the wind material appears in absorption when its projected velocity falls within $\pm V \sin i$ and in emission at larger velocities. This is not the case in the spectrum of HDE 326823 where the N II absorption features are Doppler shifted far beyond their characteristic line width.

5.5 SUMMARY

Our spectroscopic results demonstrate that HDE 326823 is a close, interacting binary with a 6.123 d orbital period that was originally found in ASAS light curve. We propose that the visible star (which has a spectrum similar to that of a B-supergiant) is the mass donor, and it is transferring mass to a more massive gainer star that is enshrouded in a thick accretion torus. In addition, mass loss is occurring through both the L2 and L3 Lagrangian points into a large, circumbinary disk that is the source of the stationary emission lines. The complex light curve probably results from a combination of the tidal distortion of the mass donor and variations in the size of the accretion torus related to the elliptical orbit.

HDE 326823 bears many similarities to other W Serpentis interacting binaries that are experiencing a phase of dramatic mass transfer. However, its orbital period is shorter than that of most W Serpentis binaries (with the possible exception of BD+36°4063 with P = 4.8 d; Williams et al. (2009)), and because mass transfer leads to an increasing period after mass ratio reversal, HDE 326823 may have emerged from its closest, most intense interaction. Further analysis of a long term light curve could yield a value for a changing period and yield

an estimate of the mass transfer rate. The spectral properties of HDE 326823 are perhaps most closely matched in the massive LBV MWC 314 that is also a binary with a 60.85 d period (Muratorio et al. 2008, ; Lobel et al. 2012). Lobel et al. (2012) find radial velocity variations in one set of absorption lines, while the double-peaked emission lines are constant in velocity, again suggesting a RLOF binary surrounded by a circumbinary disk.

There are other known examples of luminous stars that are LBV candidates and that display prominent Fe II emission lines in their spectra (Walborn & Fitzpatrick 2000; Massey et al. 2007), and some of these may in fact be binaries with circumbinary disks like HDE 326823. However, we caution that the appearance of Fe II emission only signifies the presence of relatively cool, dense, circumstellar gas, and such an environment might be attained in a dense stellar wind rather than in a circumbinary disk. Verification of the similar binary nature of such targets will require high resolution, multiple-epoch spectroscopy to search for evidence of orbital Doppler shifts and to check for the presence of double-peaked and stationary emission lines.

These new spectroscopic observations of HDE 326823 support the idea that some WR stars can be formed in a binary system through envelope loss by mass transfer. In this picture, the initially more massive star will expand to fill its Roche Lobe and begin mass transfer onto the smaller star. The mass donor will lose its hydrogen envelope and develop a WR spectrum. The mass gainer will emerge as an O-type star, with a large mass and high effective temperature. HDE 326823 may evolve into a system like γ^2 Vel (North et al. 2008), where the mass donor is now observed as a hydrogen stripped WR star, that is orbiting a more massive O star. Assuming that this binary history is correct, it is unlikely that the donor star in HDE 326823 experienced a RSG or LBV episode in the past since both kinds of objects have radii much larger than the current binary separation. HDE 326823 is likely experiencing a short, late stage of binary evolution, and it represents an important opportunity to explore the mass loss processes that occur at this juncture.

6
A THREE YEAR SPECTROSCOPIC SURVEY ON THE VARIABILITY OF GALACTIC AND MAGELLANIC LUMINOUS BLUE VARIABLES

In this chapter, I discuss early results from a spectroscopic survey of a large sample of LBVs that are observable with small telescopes. The results on individual stars are compared, and I present a discussion on which stars are or are not actual LBVs, as well as how the mass loss rate influences the observed spectrum.

6.1 INTRODUCTION

LBVs present a number of challenges to our understanding of the physics of mass loss. We think that these stars are post-main sequence massive stars experiencing extreme mass-loss through strong stellar winds and occasional episodic ejections such as the eruptions of P Cygni (Fig. 2.1) and η Carinae (Fig. 4.1). Such large mass loss transforms these stars into Wolf-Rayet stars that will eventually explode as supernovae.

Humphreys & Davidson (1994; HD94) estimate that the typical mass-loss rate, $\dot{M}$, of an LBV is of the order of $10^{-5} - 10^{-3} M_{\odot}$ yr^{-1}, with an average around $2 - 3 \times 10^{-4} M_{\odot}$ yr^{-1}. Furthermore, they postulate that the typical lifetime in the LBV phase is of the order of 25,000 years. This implies that an LBV will lose $\sim 5 M_{\odot}$ during its lifetime.

The variability of LBVs is crucial to understanding their evolutionary status and the driving mechanisms for these stars, as well as the overall amount of mass lost during this stage of evolution. This chapter details the variability of several stars included in the CTIO and HLCO spectroscopy datasets. P Cygni, η Carinae, and HDE 326823 were already discussed in detail, so they will be excluded in this chapter. A spectral atlas for the region observed is shown for the entire sample in Appendix C.

In general, for each star I will discuss Hα variability, and if the He I profiles are easily detected, I will show the He I 5876 and the He I 6678 profile variability. As mentioned in

Chapter 5, the He I 5876 feature recorded by the RC Spectrograph may be partially blended with the nearby Na D lines. In the LBVs with the highest mass loss rates, Na D is a complex of absorption (both stellar/circumstellar and interstellar in origin) and emission (from the circumstellar gas). Consequently, the other available He I line, He I 6678 presents a much "cleaner" profile, that is only contaminated in the η Carinae system where [Ni II] is present from the dense knots in the ejecta.

This chapter will begin with a discussion of the spectroscopic observations and a general description of the properties of the spectra. We continue with a discussion of previous results on the target stars. We then show the spectroscopic results in context of contemporaneous photometry from the All Sky Automated Survey (Pojmanski 2002). We will discuss the variability properties of the population, and note other physical processes that influence the appearance of the spectra. Three targets will be left for analysis at a later date (HD 5980, HDE 269128, and MWC 314) because their variability is related to the presence of a binary companion (for example, wind-wind collisions and Roche lobe overflow). Furthermore, HDE 316285 is left for later analysis due to the small number of spectra with an un-saturated Hα profile. The order of presentation of the individual targets in this section is arranged by the right ascension of the stars, so we consider in turn targets in the Small Magellanic Cloud (SMC), the Large Magellanic Cloud (LMC), and finally our southern Galactic targets.

6.2 OBSERVATIONS AND TARGET STARS

We collected moderate resolution Cassegrain spectra using the Cerro Tololo Interamerican Observatory (CTIO) 1.5 m telescope and R-C spectrograph with the standard 47/Ib setup (Howell et al. 2006), which records the range from 5630 Å to 6950 Å. These spectra have a resolution of 2.2 Å FHWM ($R \simeq 3000$). The spectrograph slit was 1.5 arcseconds wide and 300 arcseconds in height and was oriented in an east - west direction. The spectra were recorded on a Loral 1200×800 CCD detector with 15μm pixels and were reduced using

standard IRAF techniques. Typically, we made two or three exposures per visit per target and performed the wavelength calibration using a Ne lamp. The flux standard stars Feige 110 and LTT 4364 were also observed to flux calibrate the spectra for most epochs, but the spectra were subsequently normalized to a unit continuum and transformed to a standard, heliocentric wavelength grid. In Table 6.1, I present the observations by target, number of spectra obtained, and some basic parameters of the target (including a SIMBAD spectral type, coordinates, and if it is an LBV or candidate LBV).

Table 6.1 Observations collected with SMARTS (RCspec)

Target	HD	*N*	Spec. Type	RA(2000.0)	DEC(2000.0)	Status	Galaxy
R 14	5980	44	WN p	00:59:26.6	-72:09:54	Eclipsing Binary LBV+WR	SMC
R 40	6884	37	B9 Iae	01:07:18.2	-72:28:04	Candidate	SMC
R 81	269128	35	B2.5 Iabe	05:10:22.8	-68:46:24	Eclipsing Binary LBV+...	LMC
R 85	269321	27	B5 Iae	05:17:56.1	-69:16:03	Confirmed	LMC
S Dor	35343	39	A0 e	05:18:14.3	-69:14:59	Confirmed	LMC
R 110	269662	26	B9 Iabe...	05:30:51.5	-69:02:59	Candidate	LMC
R 127	269858	26	WN 11	05:36:43.7	-69:29:48	Confirmed	LMC
HR Car	90177	38	B2 ev	10:22:53.8	-59:37:28	Confirmed	MW
AG Car	94910	39	B2 pe	10:56:11.6	-60:27:13	Confirmed	MW
Wra 751	V432 Car	33	WR	11:08:40.1	-60:42:52	Confirmed	MW
ζ^1 Sco	152236	25	B1 Iape	16:53:59.7	-42:21:43	Candidate	MW
HD 326823	326823	24	O+	17:06:53.9	-42:36:40	Binary	MW
HD 160529	160529	23	A3 Iae	17:41:59.0	-33:30:14	Confirmed	MW
HD 316285	316285	13	Be* D	17:48:14.0	-28:00:53	Candidate	MW
HD 168607	168607	24	B9 Ia	18:21:14.9	-16:22:32	Confirmed	MW
HD 168625	168625	20	B6 Ia	18:21:19.6	-16:22:26	Candidate	MW
AS 314	V452 Sct	13	A3 Ia	18:39:26.1	-13:50:47	Candidate	MW
MWC 314	V1429 Aql	7	LBV(c)	19:21:34.0	+14:52:57	Binary	MW

In addition, a few spectra were obtained at the GSU Hard Labor Creek Observatory with the 20-inch telescope and a LHIRES III spectrograph. These spectra were recorded on an electronically cooled SBIG ST-8XME CCD chip. The light was dispersed with a 600 grooves mm^{-1} grating, resulting in similar resolution and wavelength coverage as the CTIO data. We obtained a few spectra of HD 160529, HDE 316285, and MWC 314. In addition, we obtained a high quality spectrum of P Cygni (see Chapters 2 and 3) in this region which will be shown for comparative purposes.

Overall, there were 35 confirmed or candidate LBVs in our Galaxy reported by Clark et al. (2005). Since that paper, additional Galactic LBVs have been newly discovered candidate LBVs in the Galaxy discovered through infrared surveys of the Galactic Plane (Wachter et al. 2010), with more being discovered through other infrared surveys such as WISE. These numbers are extremely uncertain, as Wachter et al. (2010) show how the LBV spectra resemble that of the Be stars. Further, LBVs in the hottest state resemble WR stars or O stars, which may cause misclassification without at least 2 epochs of spectroscopy. With sufficient observational effort, the entire Galactic population may be revealed in the near future. There are 3 candidate or confirmed in the SMC and 24 confirmed or candidate LBVs in the LMC (van Genderen 2001). These stars are also visible in other Local Group galaxies, and the connection between S Doradus and the Hubble-Sandage Variables (Hubble & Sandage 1953) has been established. Currently, Massey et al. (2007) have found that the known number of LBVs and candidate LBVs in the local group total 24 in M 31, 37 in M 33, 1 in NGC 6822, and 3 in IC 10.

This survey sample is based mainly on relatively bright targets that are easily observed (short exposures) with the CTIO 1.5 m telescope. However, this likely means that our survey is volume limited to a distance closer than 3 kpc in the direction of the Galactic Center and closer than 8 kpc in the direction of the constellation Carina where dust attenuation is not as strong as towards the Galactic Center. Our sample includes a limited but very significant

portion of the LBVs in the Galaxy (roughly 40% when including P Cygni, η Carinae, and HDE 326823 from previous chapters) and can be considered as a representative sample of the entire population. The LBVs in the SMC and LMC are among the brightest stars in those galaxies and the sample probably includes most of their LBV population (66% of the SMC population, and 21% of the LMC sample).

We collected some contemporary V-band photometry from the All Sky Automated Survey (ASAS; Pojmanski 2002), which we compare to the equivalent width of the Hα emission for each target star. Our equivalent widths were measured over a kinematic range of $\pm$1500 km s^{-1} from the systemic rest velocity, which was assumed to be +250 km s^{-1} for the SMC/LMC targets, and 0 km s^{-1} for the Galactic targets. These values are tabulated in Appendix B.3.

6.3 DESCRIPTION OF THE SPECTRA OF LBVS

The strongest emission line in the optical portion of the electromagnetic spectrum of an LBV is Hα. In Figure 6.1, we present the average CTIO 1.5 m spectra for Galactic LBVs along with the data collected at HLCO for P Cygni. We have organized these spectra by increasing Hα strength.

Figure 6.1 shows that as Hα strengthens, certain features strengthen or appear. For example, some stars show Fe II emission lines that become prominent in the upper half of the plot between 6200 and 6500 Å (see spectral atlases in Appendix C for line identifications). The He I 5876 and He I 6678 lines go from (mostly) absorption at the bottom to emission or P Cygni profiles as Hα strengthens. Seven of these stars have previously determined values for the mass loss rate, $\dot{M}$ (Table 6.2), and the Hα strength correlates approximately with the mass loss rate.

It is clear that the Galactic targets show trends relating to mass loss rate in their spectra, with increasing Hα line strength, He I profile changes, and Fe II emission becoming prominent with higher mass loss rates. Similar trends are seen in the LMC and SMC stars, which are

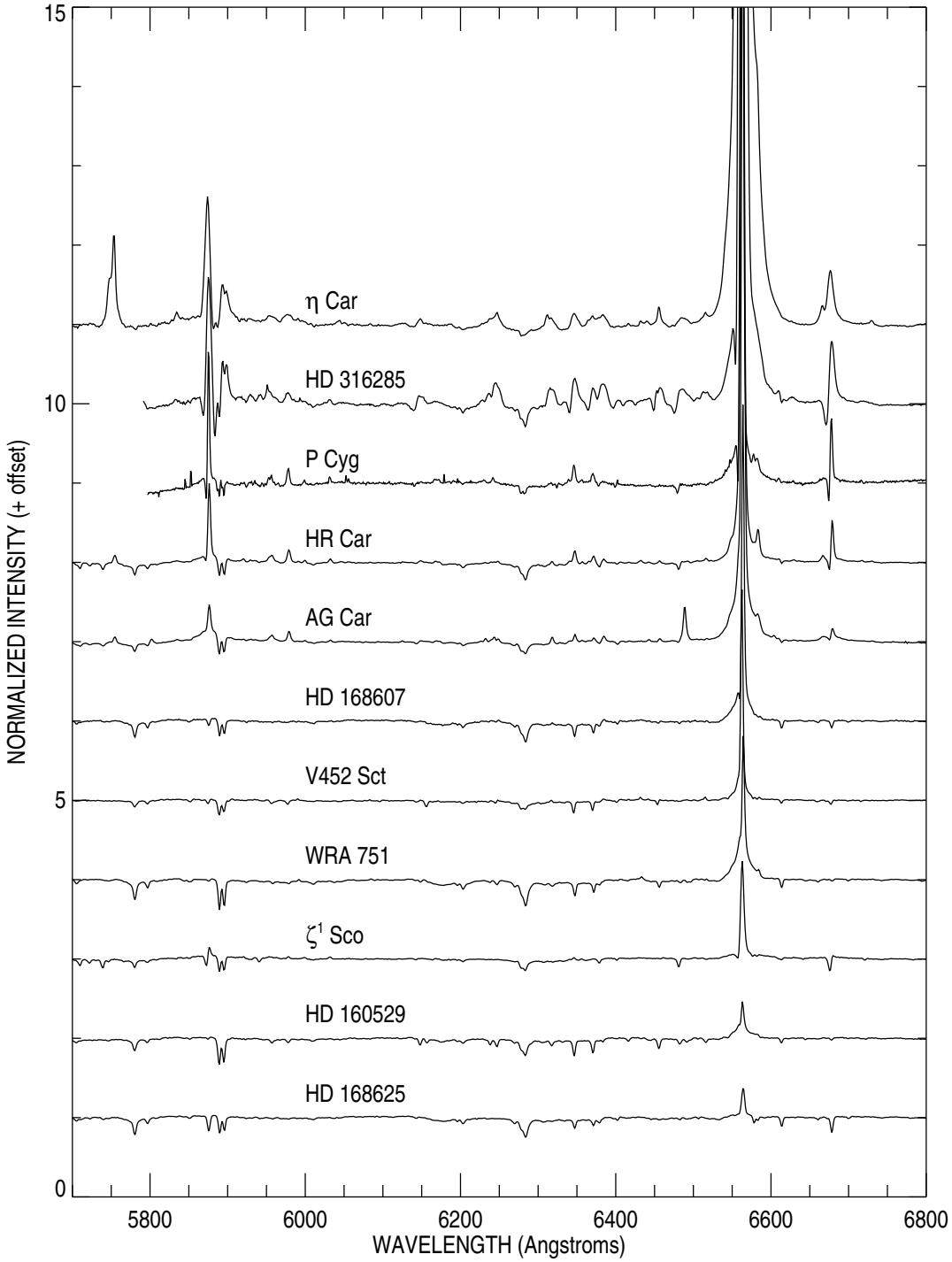

Figure 6.1 Red spectra of Galactic LBVs and candidates observed with the CTIO 1.5 m. P Cygni was observed at HLCO. Targets are sorted by increasing peak Hα height.

Table 6.2 Previously Determined Mass-loss rates of Galactic LBVs

Target	$\dot{M}$	Method	Reference
HD 168625	$(1.46 \pm 0.15) \times 10^{-6}$	Radio	Umana et al. (2010)
HD 160529	$7 \times 10^{-6} - 1 \times 10^{-5}$	Hα, CMFGEN	Stahl et al. (2003)
ζ^1 Scorpii	1.8×10^{-6}	Hα	Sterken & Wolf (1978)
HD 168607	2.2×10^{-6}	Radio	Leitherer et al. (1995)
P Cygni	3×10^{-5}	CMFGEN	Najarro et al. (1997)
HD 316285	2.2×10^{-4}	CMFGEN	Hillier et al. (1998)
η Carinae	10^{-3}	CMFGEN	Hillier et al. (2001)

sorted in a similar manner in Figure 6.2.

6.4 BACKGROUND AND RESULTS ON TARGET STARS

6.4.1 R 40

R 40 (HD 6884) is a neglected LBV in the literature, with very few publications relating to its properties and variability. Szeifert et al. (1993) demonstrated that this star was the first star in the SMC discovered to show the LBV-type variability. Over a seven year span of photometric (and some spectroscopic) data, Szeifert et al. (1993) found that the star varied by about 0.5 magnitudes, and that the star became redder while brighter, with a spectral classification near A3 I at optical maximum and B8 I at optical minimum. IUE data taken at similar epochs demonstrated that the UV flux was minimum during the optical maximum and that the UV flux was a maximum when the star was optically faint. These criteria placed the star in the LBV class. HD94 did not know of any other candidate LBVs in the SMC at the time of their publication. The SMC metallicity is extremely low with a value of [Fe/H]=-1.25 (Cioni 2009), making this an interesting target to examine how variability

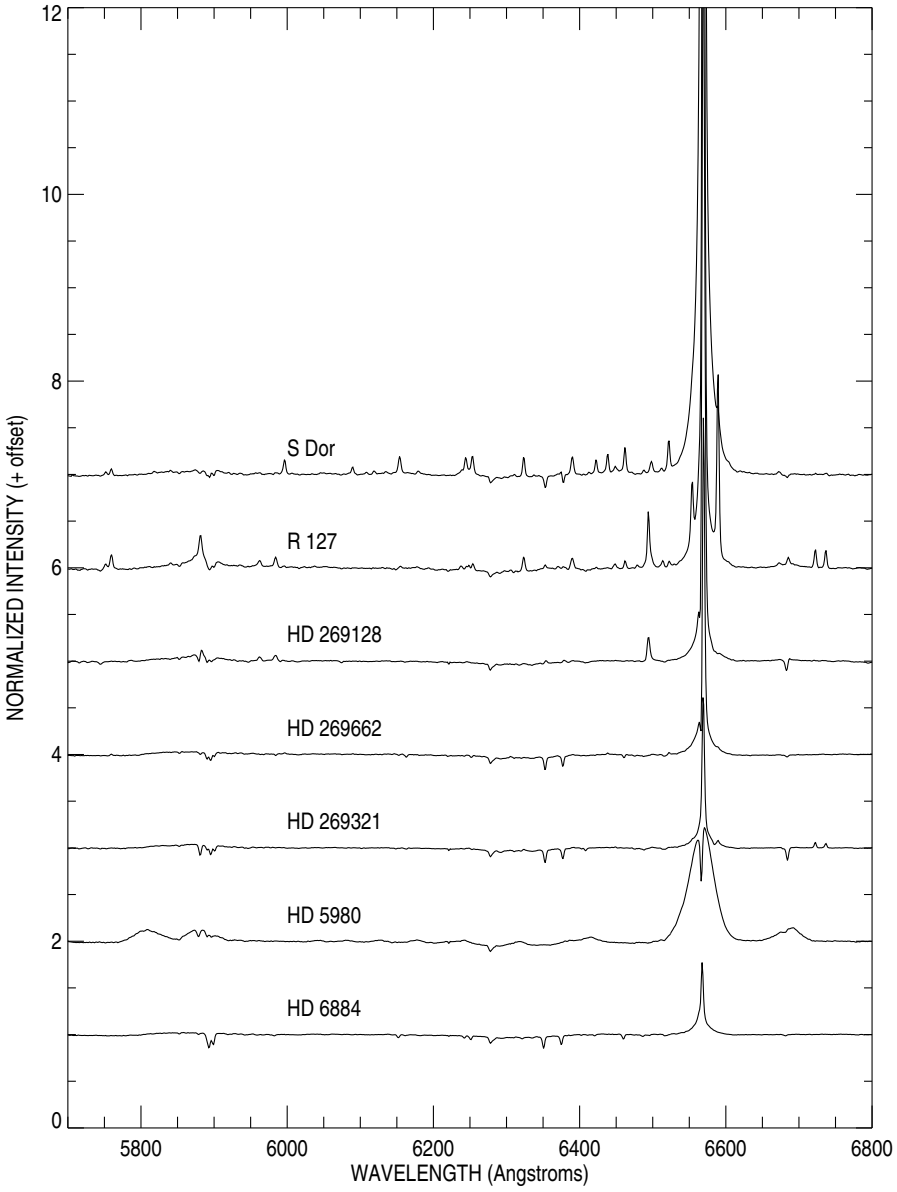

Figure 6.2 Red spectra of Magellanic LBVs and candidates observed with the CTIO 1.5m. Targets are sorted by increasing peak Hα height. The unusual spectrum of HD 5980 is due to the binary nature of the star.

differs at low metallicity.

The star had a photometric minimum in $\sim$ 1959 ($V = 10.7$) and a maximum ($V = 9.9$) in 1996 (Feast et al. 1960a; Sterken et al. 1998). The long term trends presented by Sterken et al. (1998) show possible cyclic variations with periods of $P = 1300$ d and a shorter 99.4 d. These cyclic variations could represent a short-SD phase superimposed on a long-SD phase with a timescale of > 30 y. These photometric properties led van Genderen (2001) to classify R 40 as a strong-active LBV.

Our data span three full years, which is comparable to the entire span of the short-SD phase found by Sterken et al. (1998). In Figure 6.3, we show a dynamical spectrum of the variability of the Hα profiles observed. The first observations show an obvious P Cygni absorption that then becomes a pure emission profile. Sterken et al. (1998) presented an Hα spectrum with a deeper P Cygni absorption than we observed at any epoch, which may be due to spectral resolution or due to physical changes in the star.

The three years of spectroscopy coincide with the peak height of Hα decreasing nearly monotonically (as seen in the line plots of Fig. 6.4), and the P Cygni type profile observed early in the data set changes into a pure emission profile at our resolution. The equivalent width (Fig. 6.5) decreases almost monotonically with a small amount of variability seen as scatter superimposed on the trend.

The variability exhibited by R 40 warrants further investigations to cover the entire long-SD phase both spectroscopically and photometrically. Models need to be developed to constrain the fundamental parameters of this star at the extremes of its variability. The He I 6678 and 5876 lines are very weak and are not examined here. The Hα profile varies by about a factor of 3 (minimum of $-W_\lambda = 2.95$ Å; maximum of $-W_\lambda = 10.11$ Å), which is consistent with its classification as a "strong-active" LBV (van Genderen 2001).

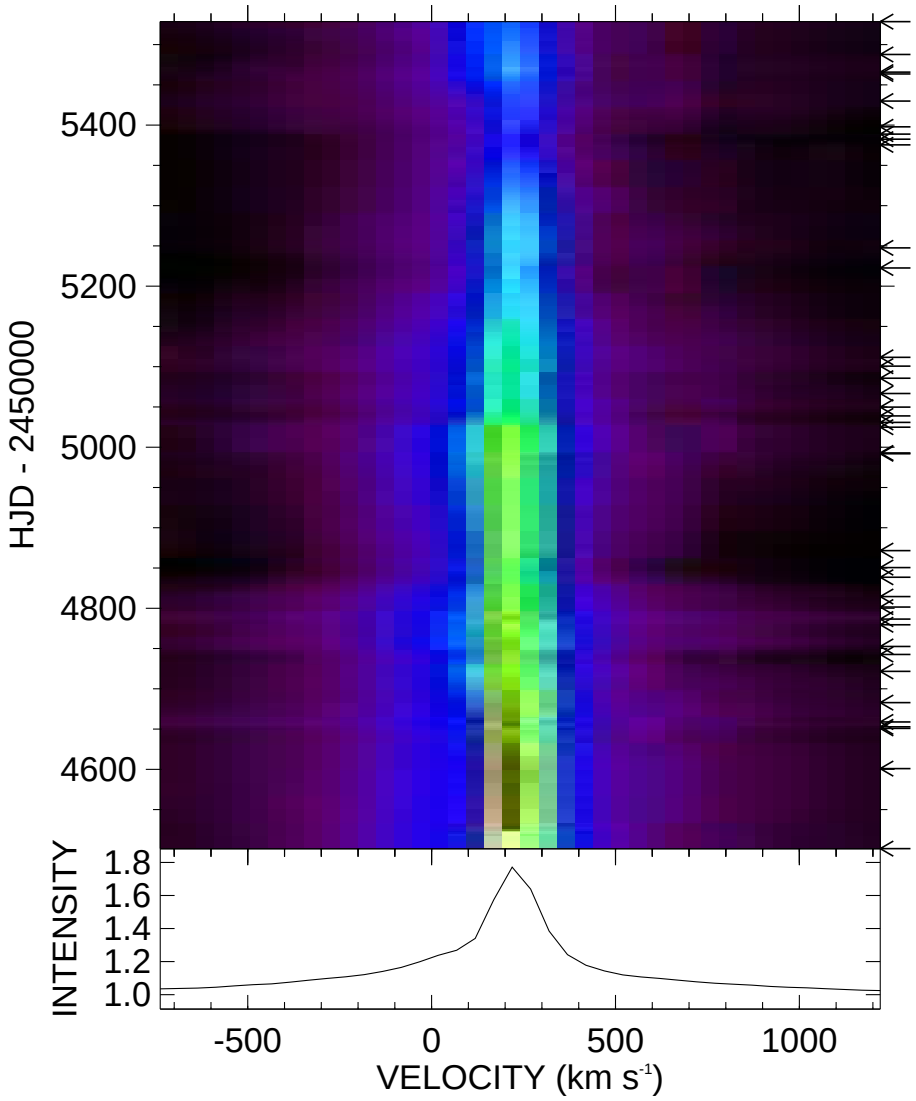

Figure 6.3 Dynamical representation of the Hα observations of R 40. The bottom plot shows the average spectrum observed, while the top shows an intensity of the spectra interpolated over time where observations were not made. Arrows indicate the actual times of observations. Color version available in electronic edition. Note that in the color version, increasing flux is scaled from blue to yellow to red, and in the gray scale version the lower intensity red should not be confused with lower intensity flux.

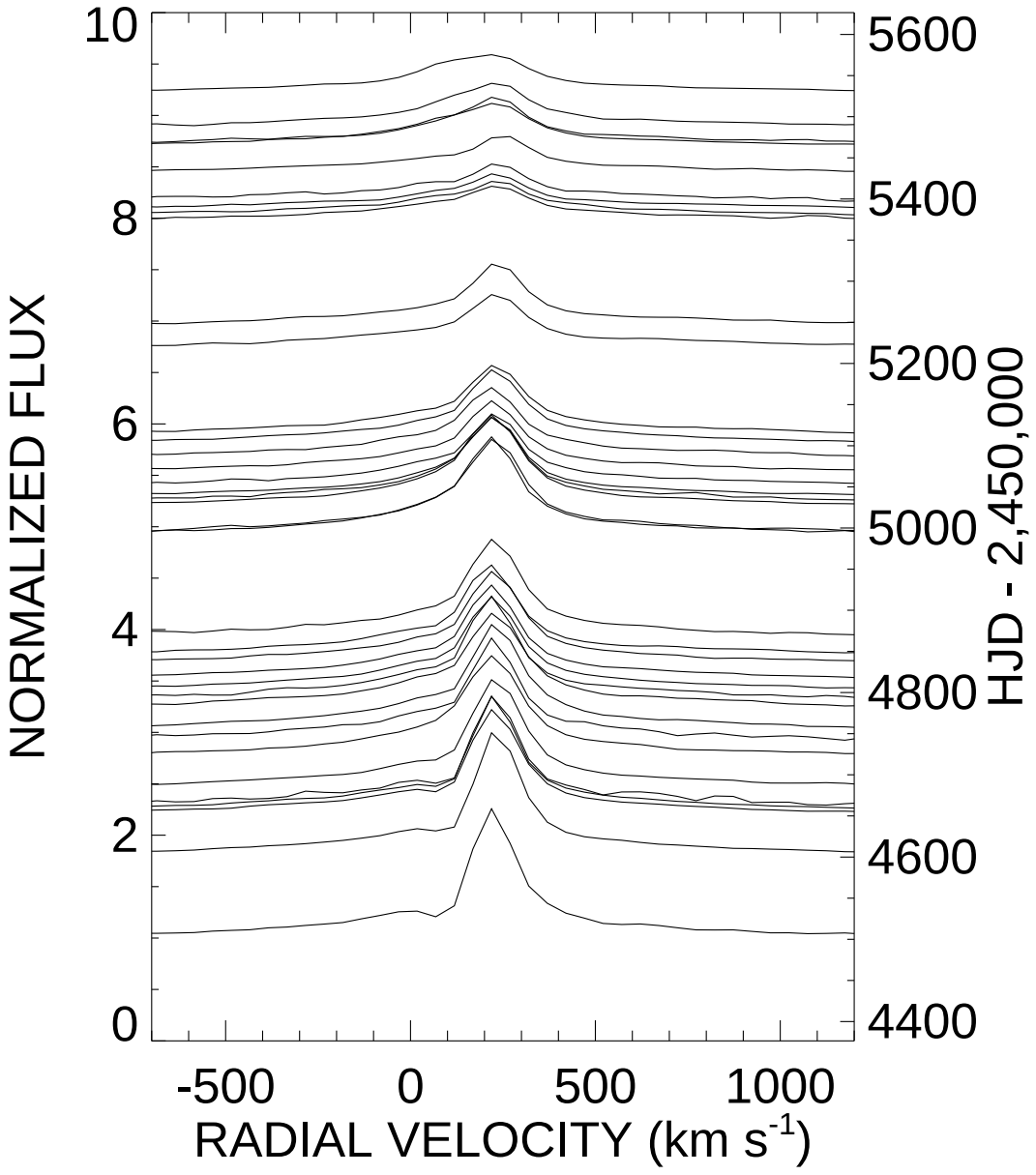

Figure 6.4 Line plots of the Hα observations of R 40. The vertical spacing is set so that the continuum corresponds to the time of the observation (right hand axis).

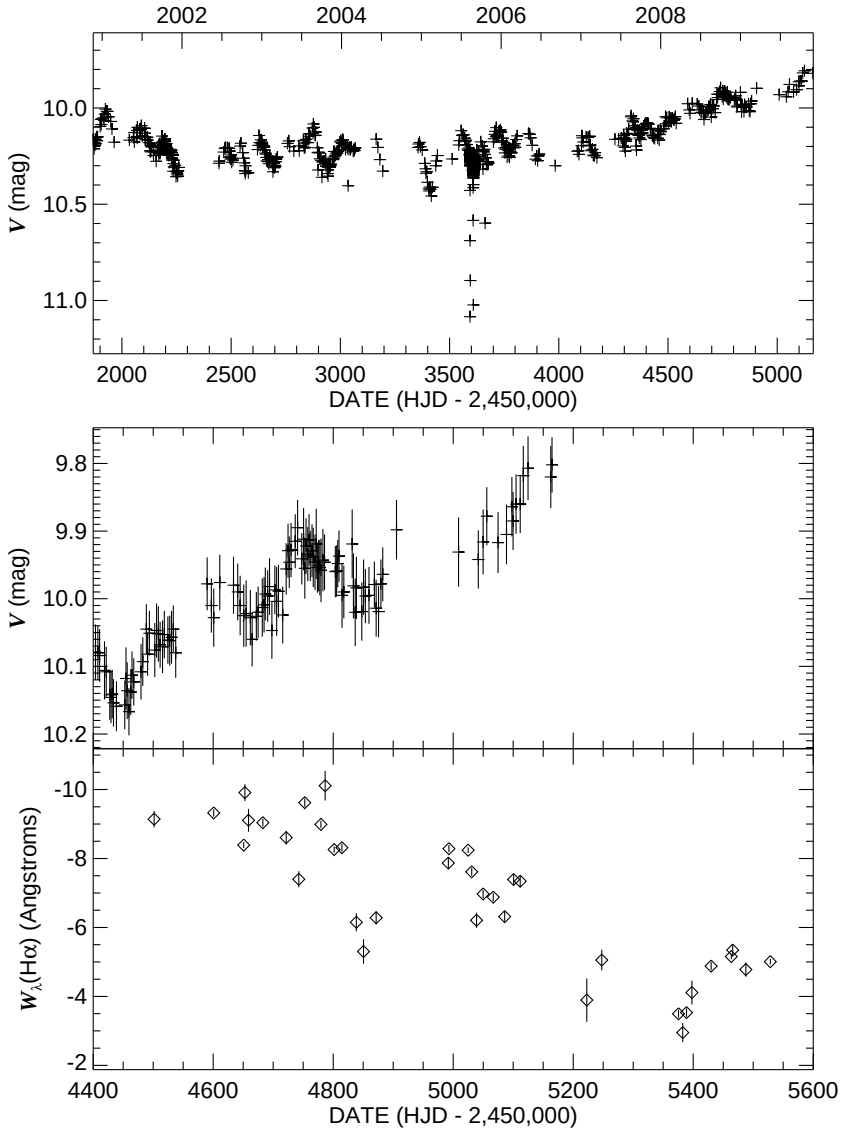

Figure 6.5 Photometry and Hα equivalent width variability of R 40. The top panel shows a historical V-band light curve, as observed by the All Sky Automated Survey (ASAS-3 Pojmanski 2002), while the bottom two panels show the photometry and Hα equivalent width behavior during the course of the survey.

6.4.2 R 85

R 85, or HDE 269231, is another neglected LBV in the literature. There are two papers describing investigations of the star. These studies were both photometric variability studies conducted in the 1980s and 1990s. The first study confirmed that the star became bluer when fainter and showed that there was long-term variability. This study (Stahl et al. 1984) also included blue spectra taken at two different epochs. Between these two times (1982 January and 1983 February) the star's flux changed by 0.3 mag in the visible. The visibly brighter time (1983) shows less emission in Hβ and increased P Cygni type absorption in Hγ and Hδ. This star was one of the six confirmed LBVs in HD94, which is surprising given the small number of studies of R 85.

Stahl et al. (1984) claimed that R 85 was similar to LBVs, but displayed too small an amplitude to be considered as an LBV. The current definitions would place this star in the "weak-active" category of LBVs. van Genderen et al. (1998) also studied this star photometrically and found that there were both $\sim$ 400 d and $\sim$ 90 d cyclic variations on the light curve (both with an amplitude near 0.1 mag). There was also some evidence of a long-SD phase with a timescale near 4 decades and an amplitude of 0.3 magnitudes. They confirmed the "bluer when fainter" nature of the star and LBV nature. van Genderen (2001) presented a long-term light curve of the object (from 1960-2000) and claims that the spectral type varied between a B5 I and an A-type supergiant.

The 27 spectra we obtained during the course of our survey are the first to document the variations over a long time scale. Our data include the stellar line transitions of Hα, He I 5876, 6678, and Si II 6347, 6371. There is also [N II] and [S II] emission from the nebulosity that is present in the vicinity of R 85.

The Hα profile of R 85 (Fig. 6.6 and 6.7) changed morphology from pure emission to a P Cygni profile and then back to pure emission over the course of the three year time span

of observations. The strength of the profile was relatively constant and varied by less than a factor of 1.3 over the course of the survey (Fig. 6.8). There are long-term trends in the light curve (Fig. 6.8), but the variability is only moderate in strength, so R 85 should be considered a member of the "weak-active" LBVs (van Genderen 2001).

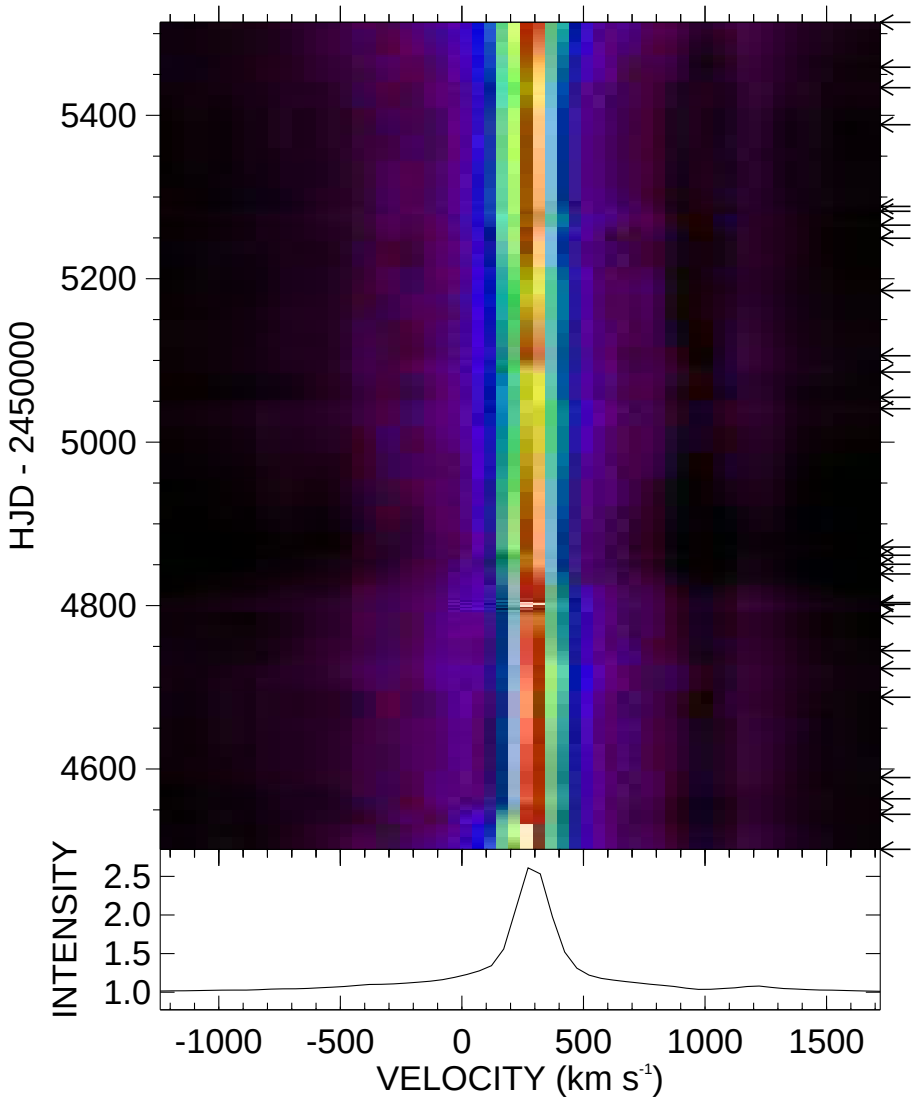

Figure 6.6 Dynamical representation of the Hα observations of R 85. Color version available in electronic edition.

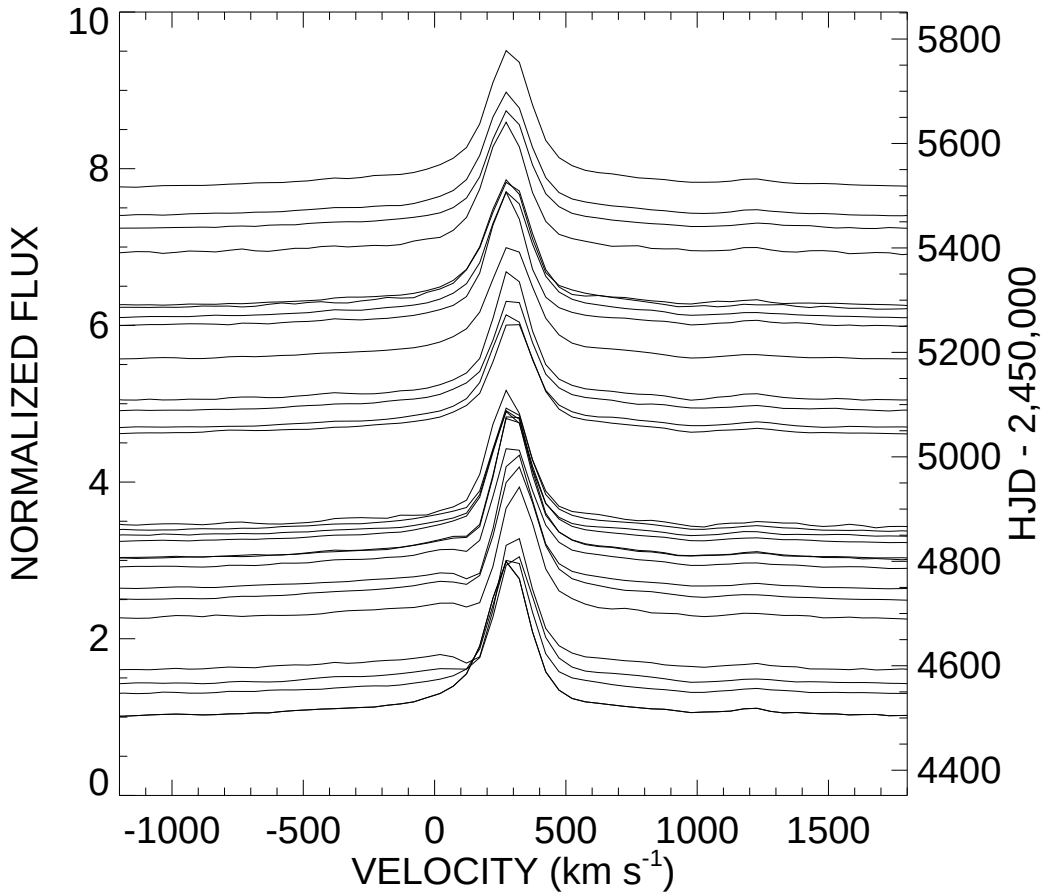

Figure 6.7 Line plots of the Hα profiles of R 85.

The He I profiles in HD 269321 (R 85) appear in pure absorption, although the profile may have a steeper slope on the red wing caused by a small amount of P Cygni type emission. The He I profile was fairly constant over the survey time span (Fig. 6.9).

The Hα profile was only moderately variable, but the photometric and spectroscopic study of Stahl et al. (1984) suggests that the higher order Balmer lines, that form closer to the star are more likely to show stronger variability. A future study of this star in the blue would be useful to understand the spectral changes.

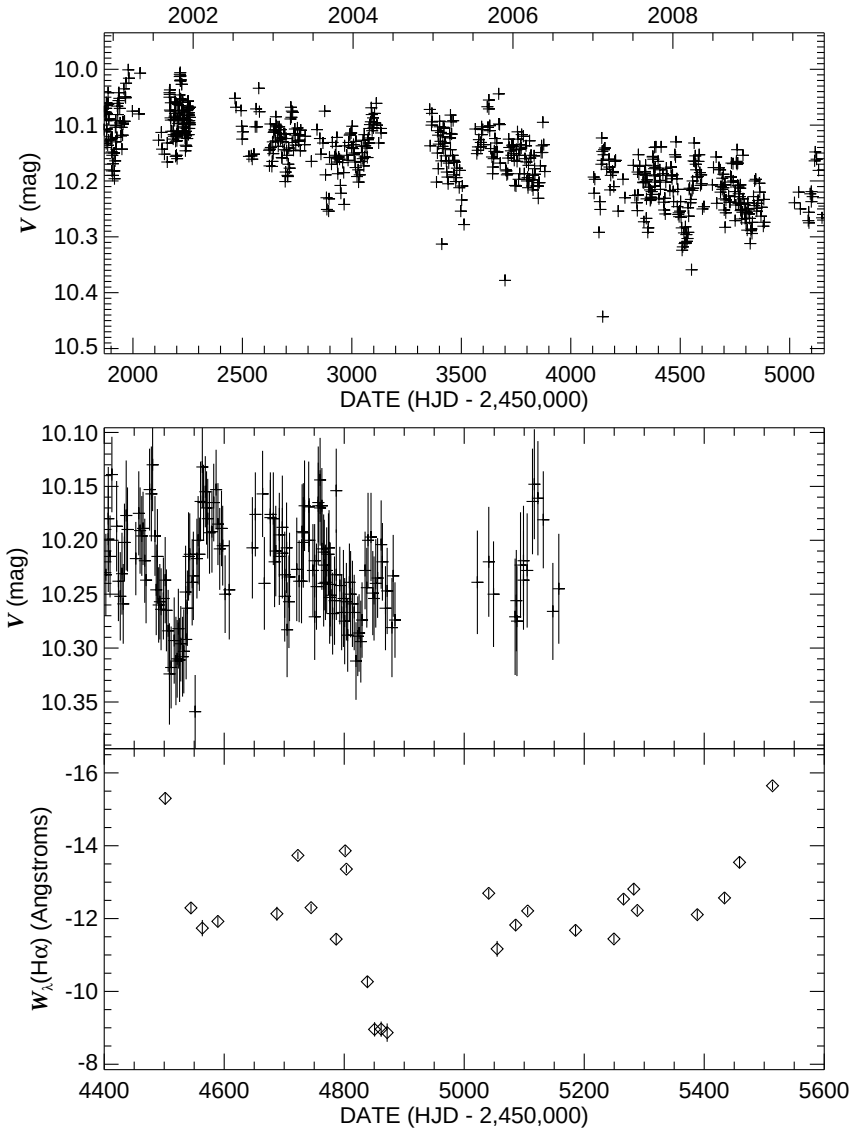

Figure 6.8 Photometry and Hα equivalent width variability of R 85. The top panel shows a historical V-band light curve, as observed by the All Sky Automated Survey (Pojmanski 2002), while the bottom two panels show the photometry and Hα equivalent width behavior during the course of our survey.

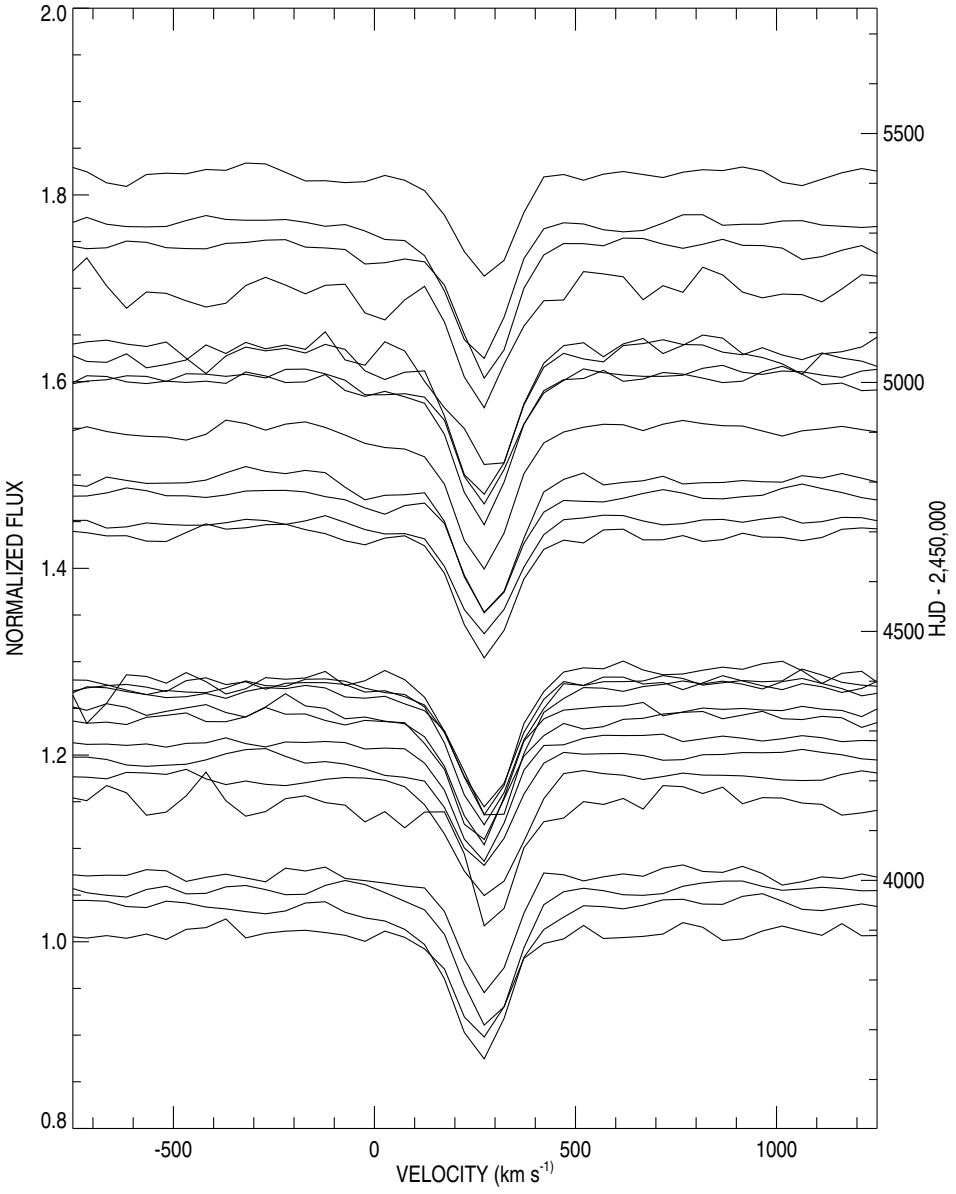

Figure 6.9 Line plots of the He I 6678 observations of R 85.

6.4.3 S Doradus

This star is a prototype whose variability has been documented for the last 120 years. The optical light curve (Figure 6.10) shows that the extremes over the last 50 years range from $V \sim 11.5$ to $V \sim 8.8$, corresponding to $L = 10^{5.96} L_{\odot}, T_{\rm eff} = 10^{3.93} K$ at optical maximum and to $L = 10^{6.30} L_{\odot}, T_{\rm eff} = 10^{4.54} K$ at optical minimum (van Genderen 2001). During the last optical maximum, Massey (2000) presented a paper entitled "An Unprecedented Change in the Spectrum of S Doradus: As Cool as It Gets." He found that the star exhibited the coolest recorded spectral type (an F supergiant) at that time. If the bolometric luminosity was roughly constant, then the ultraviolet flux was at a minimum then.

S Doradus at optical minimum is situated in the H-R diagram at the maximum observed luminosity of the LBV-minimum strip. van Genderen (2001) showed that the bolometric luminosity of S Doradus is slightly variable, with the highest luminosity occurring at minimum optical light. An accurate measurement of the ultraviolet flux at the current deep visual minimum (Fig. 6.10) would establish the high luminosity limit for S Dor and set the position of the high end of this strip for LBVs in general. Our current luminosity estimate for this stage was made from data from the 1965 minimum, when UV data were not available.

The dramatic variability of this prototype allows us to examine the SED in different states and gain further insights into the LBV phenomenon. In Figure 6.11, we show the SED of S Doradus in an optically high and low ultraviolet state (top left panel) as well as in an optically low and high ultraviolet state (bottom left panel). The UV data were collected by the International Ultraviolet Explorer satellite, and the optical spectra were from similar phases in visual magnitude from our program at CTIO. Also in this figure, we present comparisons of wind lines at these states. In a UV-high state (solid lines), the wind lines of Hα and Mg II $\lambda\lambda$ 2795,2803 are strongest in their emission and absorption strength, respectively, whereas the resonance lines of Si IV $\lambda\lambda$ 1394,1403 and C IV $\lambda\lambda$ 1548,1551

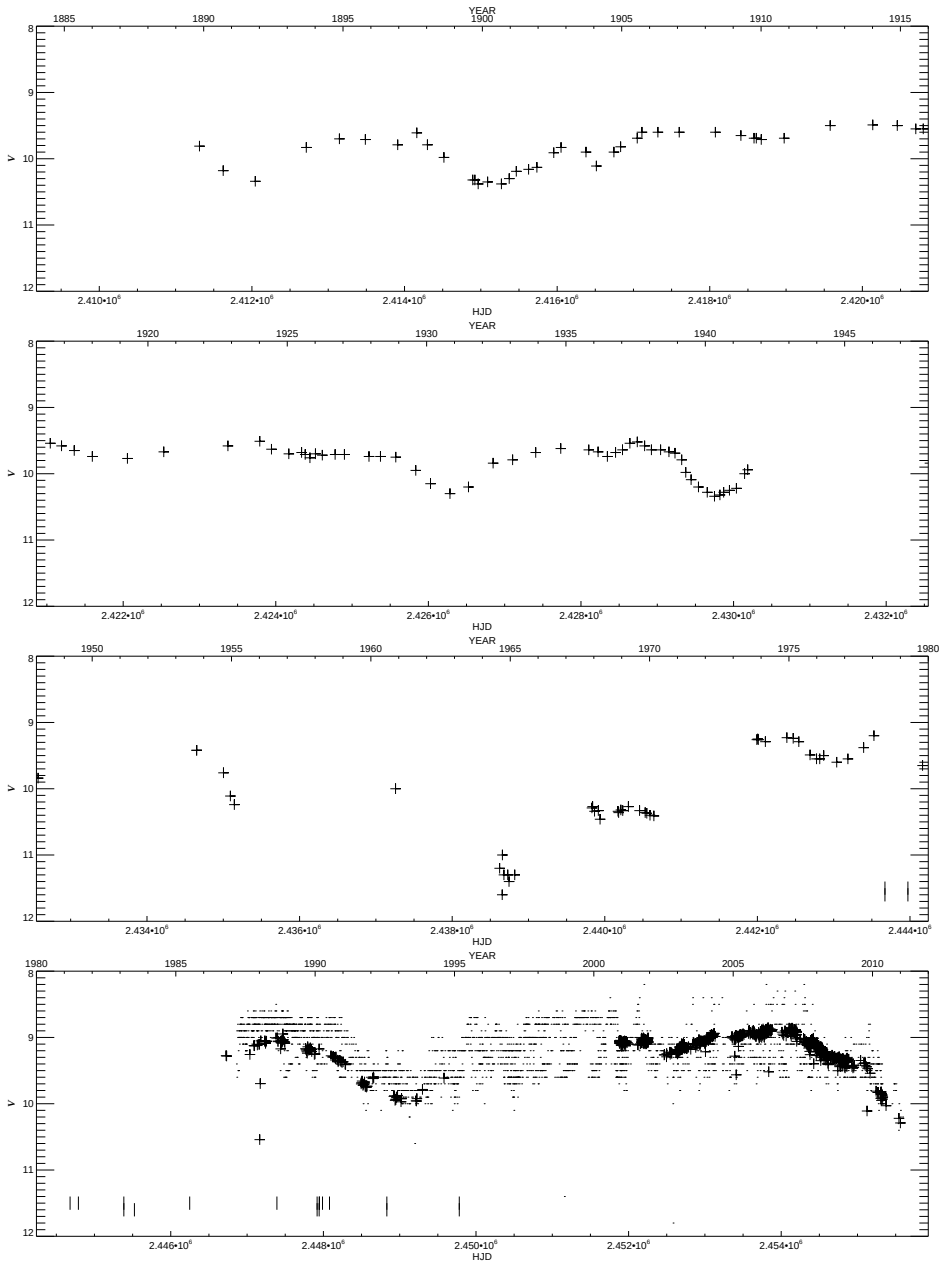

Figure 6.10 Photometry of S Doradus, 1889–present, from archival measurements and modern photometric surveys. A + symbol represents a photometric measurement while a dot represents a visual estimate. Note the deep minimum near 1965 and a new, emerging minimum at current epochs.

appear stronger during a weaker UV state.

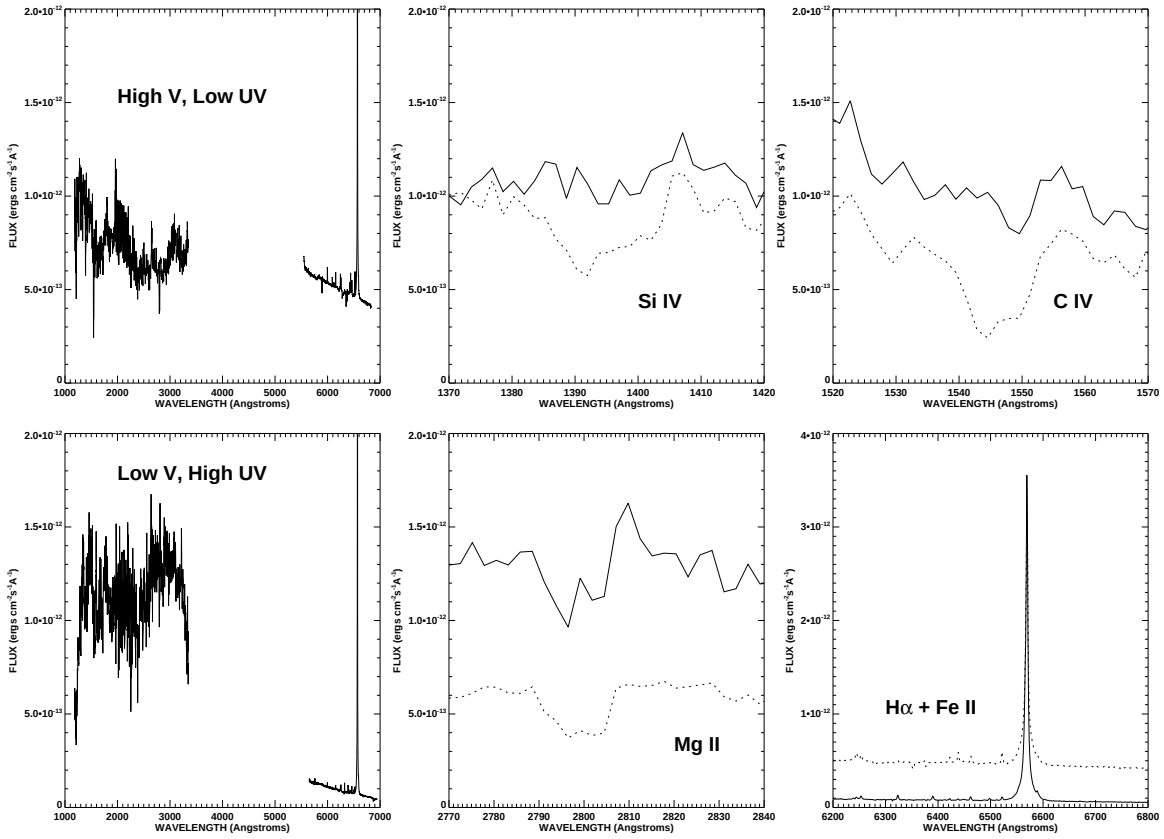

Figure 6.11 These plots show the spectra of S Dor in different optical phases. The left panels represent S Doradus in a visual high state / UV low state (top left; UV data from 1990, optical from 2007) and the opposite (bottom left; UV data from 1992, optical from 2010). The middle and right panels show how the wind lines differ at these phases, where solid lines correspond to a visual minimum and dotted lines to a visual maximum.

The wind of S Dor was studied by Leitherer et al. (1985) using both optical as well as IUE data collected at times of high optical flux. They derived a velocity law and demonstrated that the wind is driven by radiation pressure when at maximum optical light. The results for the radiation driven wind were derived from high resolution IUE data made with the LWR camera. During the optical maximum near 1988, Stahl (1990) found that several wind lines exhibited inverse P Cygni profiles, which has never been observed for any other LBV,

indicating *infall* back onto the stellar photosphere due to the line-of-sight absorption having greater positive velocity than photospheric velocities.

Our recent observations of the Hα profile show that the emission line strength is growing rapidly (Richardson & Gies 2010, Fig. 6.12, 6.13, and 6.14), and complementary photometry from both the All Sky Automated Survey (ASAS; Pojmanski 2002; Fig. 6.15) and the AAVSO show that the star is approaching a new optical minimum.

This is clearly a critical moment to explore the ultraviolet spectrum of S Dor with HST, and we were awarded time to examine this in the upcoming months with HST/STIS. The variability observed is remarkable and the strongest of any LBV observed during the three year campaign. The Hα equivalent width (uncorrected for a changing continuum) varied by more than a factor of 8 (Fig. 6.15). During the UV-strong/optical weak epochs like the present, we may have a clearer view towards the stellar photosphere in the ultraviolet, which we will examine in planned HST/STIS observations that will be made in 2012 May. Past models for this star were based on data from the optically high/UV low state. The new UV observations we will obtain will place S Doradus on the HRD at a position corresponding to its highest temperature in recent history.

This star has shown remarkable variability and shows the extreme variability possible from the LBVs. I do not show any plots for the He I 5876 and 6678 lines, as these lines remained weak throughout the observations. The overall analysis requires more work and spectral modeling, which will be accomplished with the planned HST observations.

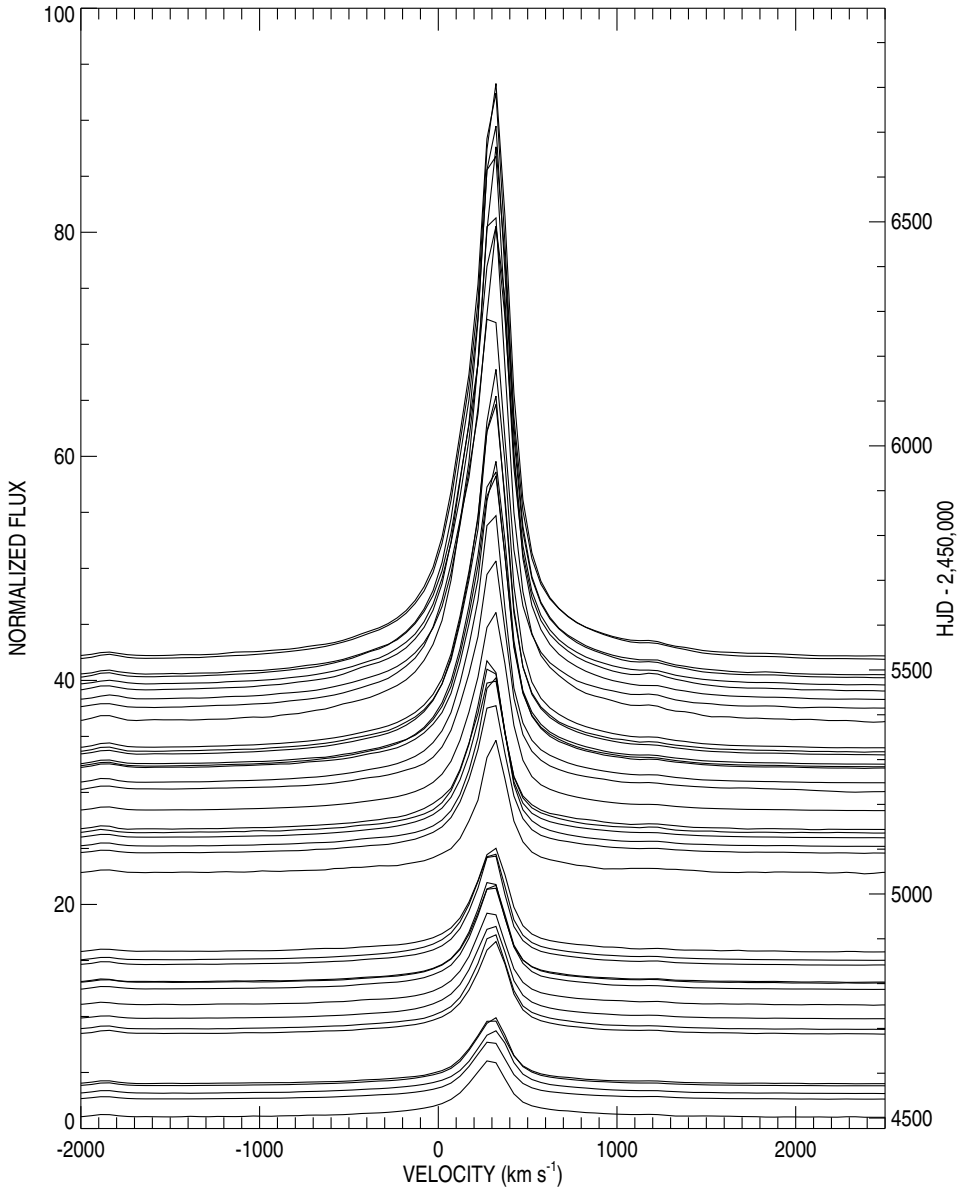

Figure 6.12 Observed Hα profiles of S Doradus from the CTIO 1.5 m telescope and R-C spectrograph. Time increases in the positive vertical direction, with the distance between the continuum normalized spectra being registered with the time of observation (right axis). Note the large increase in the line width and strength over the course of these observations.

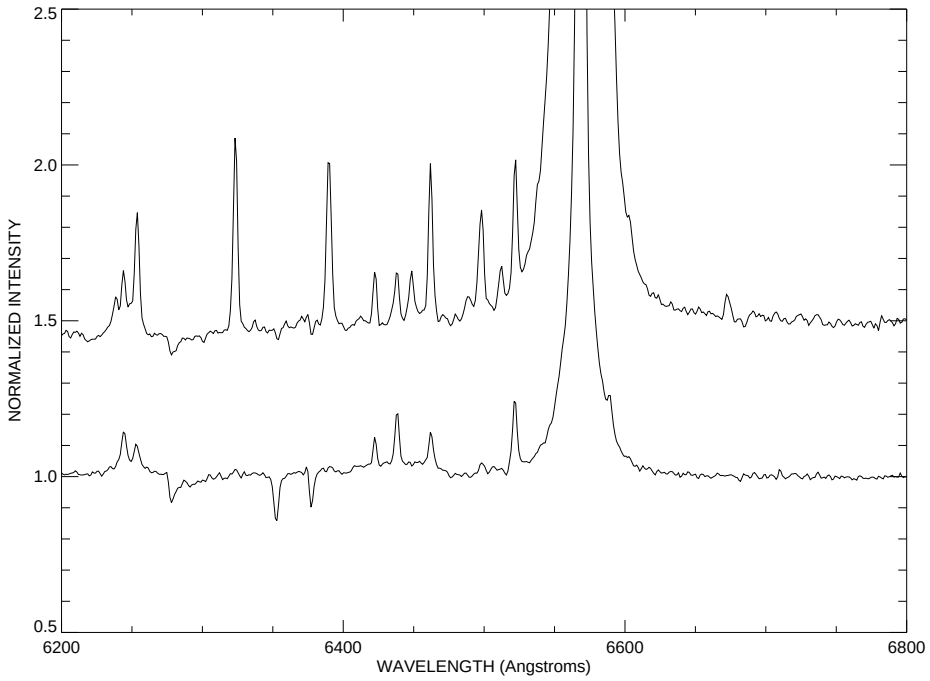

Figure 6.13 Two red spectra of S Dor taken near the beginning and end of our data set from CTIO. The first spectrum (bottom) shows a few weak emission lines in the vicinity of Hα, while the last spectrum (top) shows many more. These new emission lines are mostly Fe II lines, indicative of the larger amount of UV flux ionizing the wind when the visual flux reaches a new minimum (Fig. 6.10). Also note that the absorption lines of Si II $\lambda\lambda$ 6347, 6371 Å have gone from strong to extremely weak over the course of these observations.

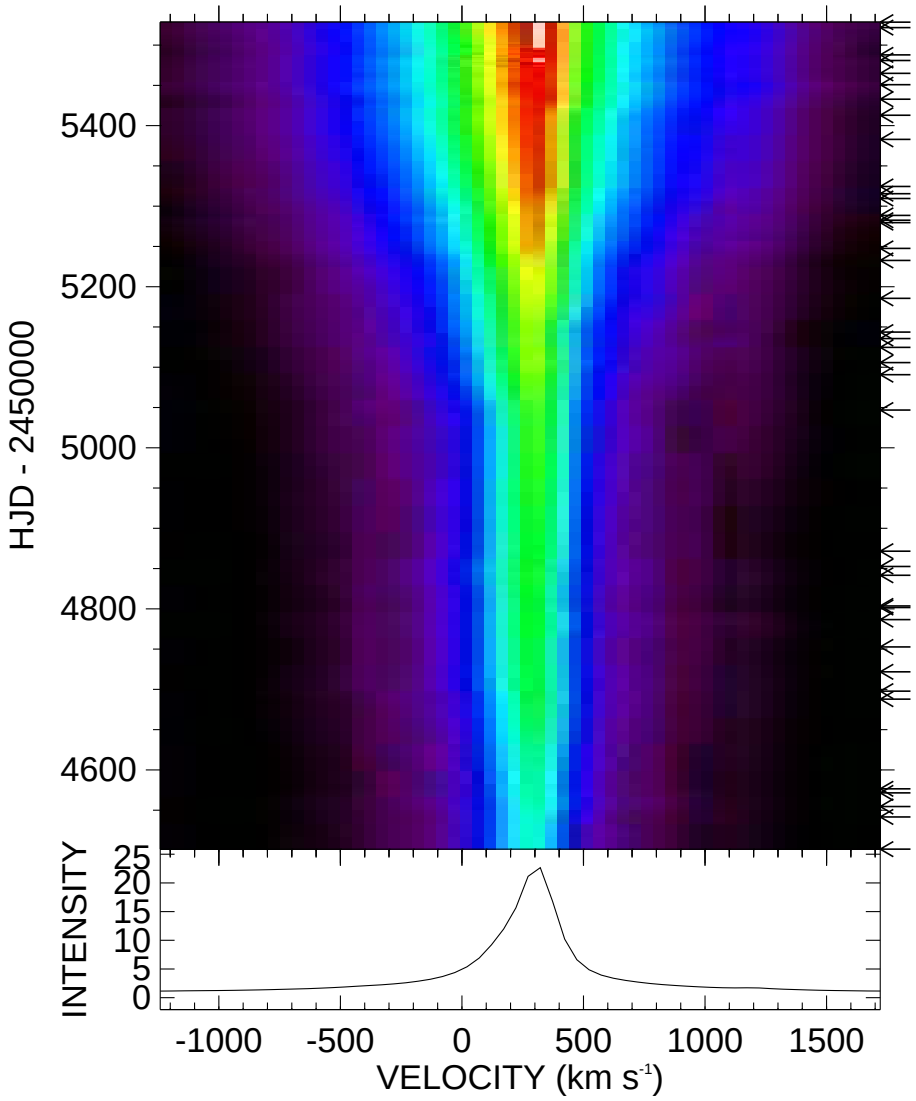

Figure 6.14 Logarithmic representation of the observed Hα profiles of S Doradus from the CTIO 1.5 m telescope and R-C spectrograph. Time increases in the positive vertical direction, with the dates of observations indicated with arrows. Note the increase in line intensity and the width of the emission. Color version available in electronic edition.

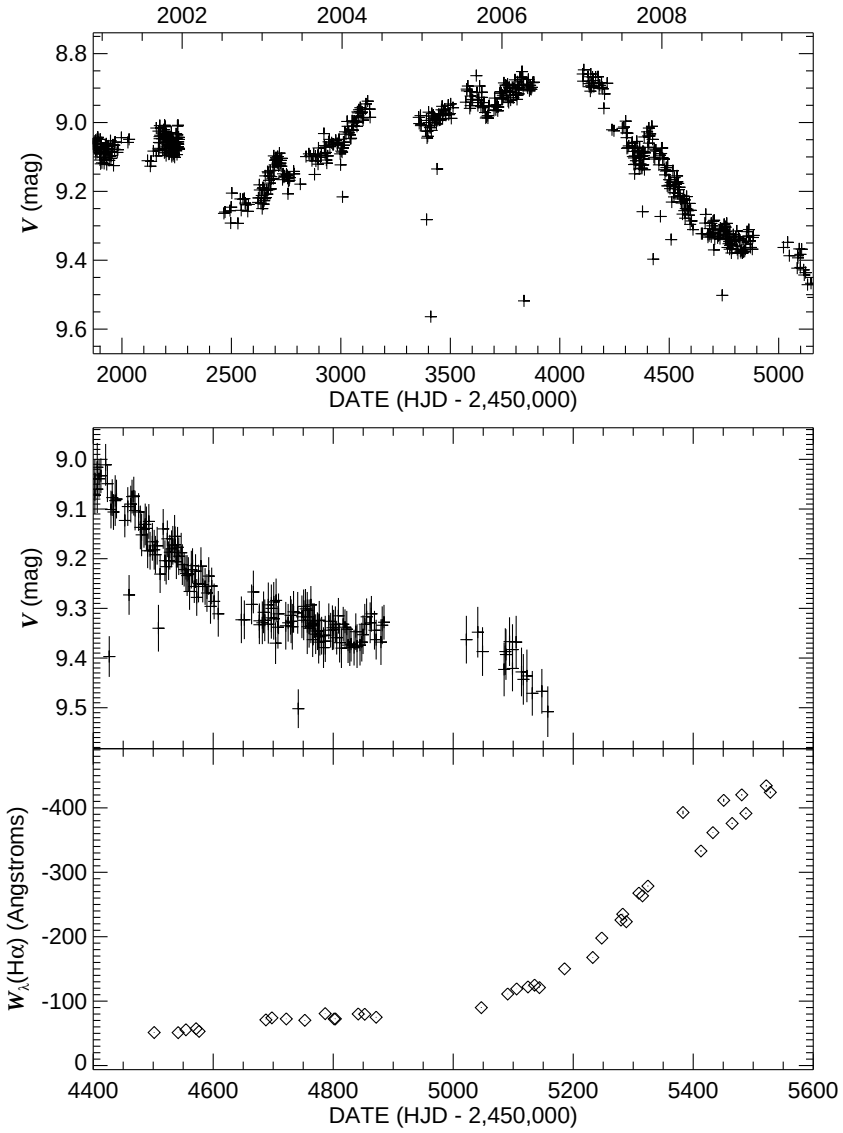

Figure 6.15 Photometry and Hα equivalent width variability of S Doradus. The top panel shows a historical V-band light curve, as observed by the All Sky Automated Survey (Pojmanski 2002), while the bottom two panels show the photometry and Hα equivalent width behavior during the course of the survey.

6.4.4 R 110

R 110 is a peculiar hypergiant in the LMC, and the fifth discovered LBV in the LMC. Its LBV nature was discovered by Stahl et al. (1990) who noted that the earlier determined spectral types were estimated as B6 I by Sanduleak (1970) and B9 I by Feast et al. (1960b). Stahl et al. (1990) found that the spectrum resembled an F0 I supergiant in 1989 January, when the star was optically bright ($V = 9.99$) and had resembled an A-type supergiant while fainter in the optical (Stahl et al. 1985) in 1971, 1974, and 1982. It was noted by Stahl et al. (1985) that the spectrum was variable between those three epochs.

The star was first found to be a photometric variable by Stahl et al. (1984), who noted the $\triangle V$ of ~ 0.3 mag over a long time scale (1970–1983). A photometric campaign on R 110 was discussed by van Genderen et al. (1997), who found that between 1957 and 1994 the star varied in V by ≈ 0.9 mag. They also noted that some microvariability had been observed, but not enough data had been collected to give reliable time scales. However, the corresponding spectroscopy noted in the literature and by Stahl et al. (1990) make this a bona fide LBV with spectral types varying from B to F (or G as noted by van Genderen et al. 1997).

During our observations, the star showed little spectroscopic variability. The only strong lines in our data were Hα and the Si II doublet at 6347, 6371 Å absorption lines. The Hα profile is always observed to have a P Cygni type profile, but the depth of the absorption is moderately variable (see Fig. 6.16 and 6.17).

The equivalent width of the Hα profile experienced some minor changes in the line strength (Fig. 6.18). There were some clear changes observed, such as the quasi-sinusoidal variation between HJD 2,455,000 and HJD 2,455,400, but there is not many data points in that region. However, this type of moderate-amplitude variability is similar to that of P Cygni (Chapter 2). The large amplitude, long-term spectroscopic changes may be observed

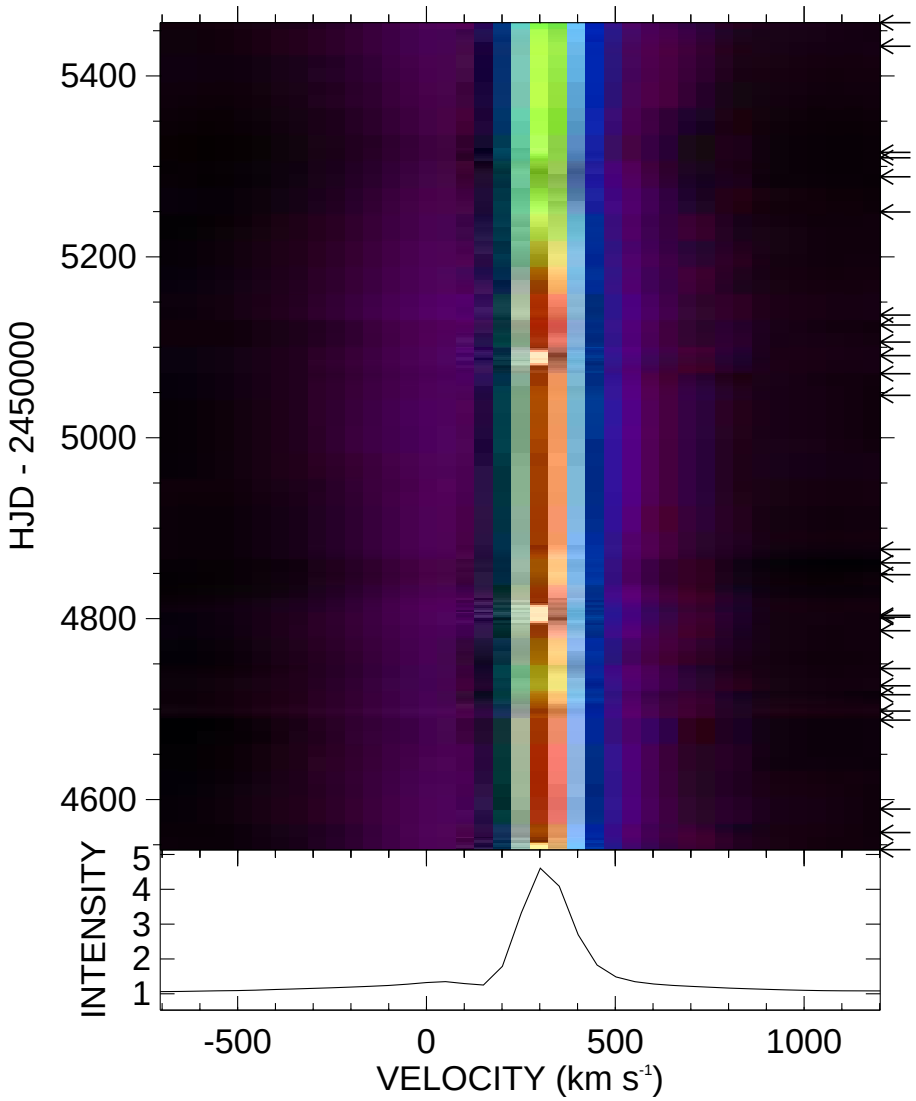

Figure 6.16 Dynamical representation of the observed Hα profiles of R 110 from the CTIO 1.5 m telescope and R-C spectrograph. Color version available in electronic edition.

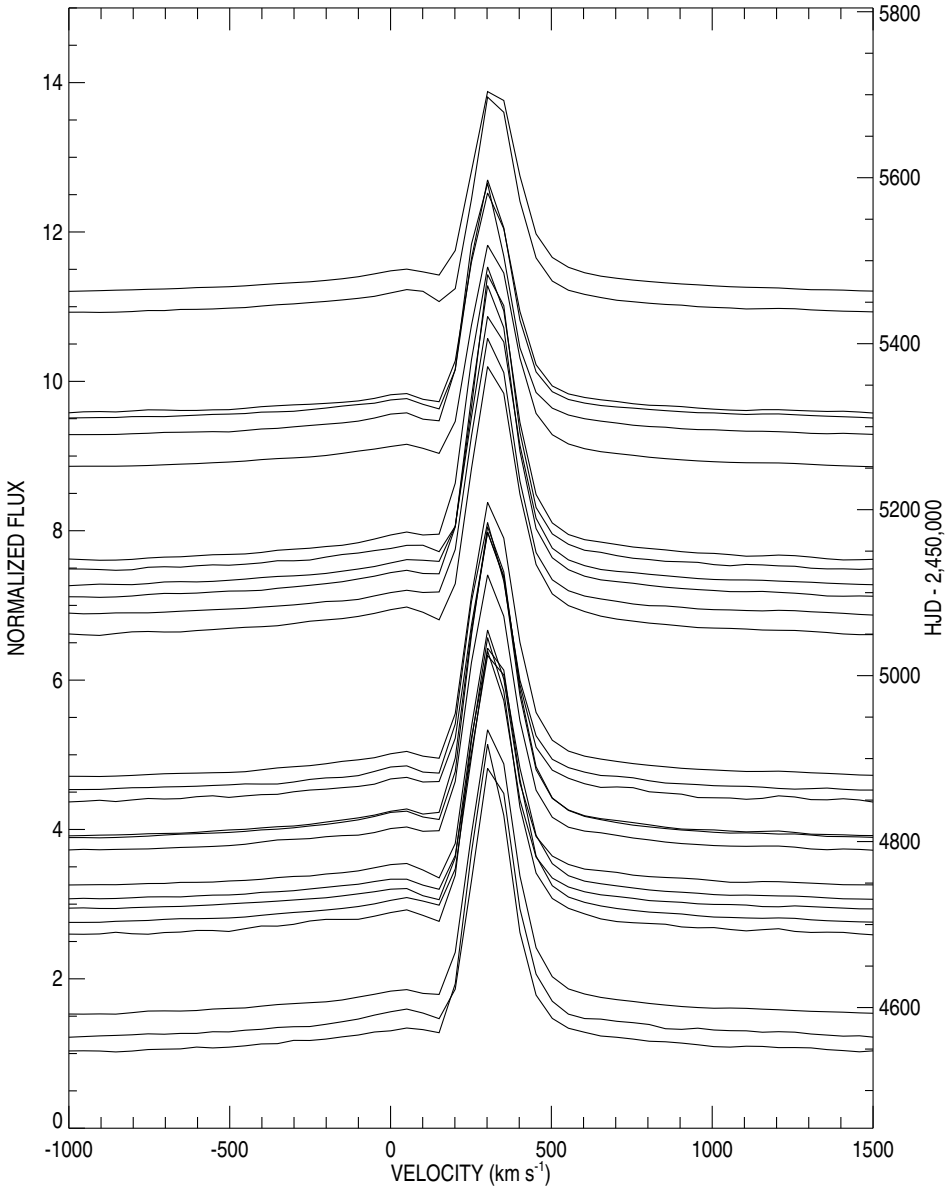

Figure 6.17 Line plots of the observed Hα profiles of R 110 from the CTIO 1.5 m telescope and R-C spectrograph.

if the star acts as it did between 1970 and 1984, as mentioned previously.

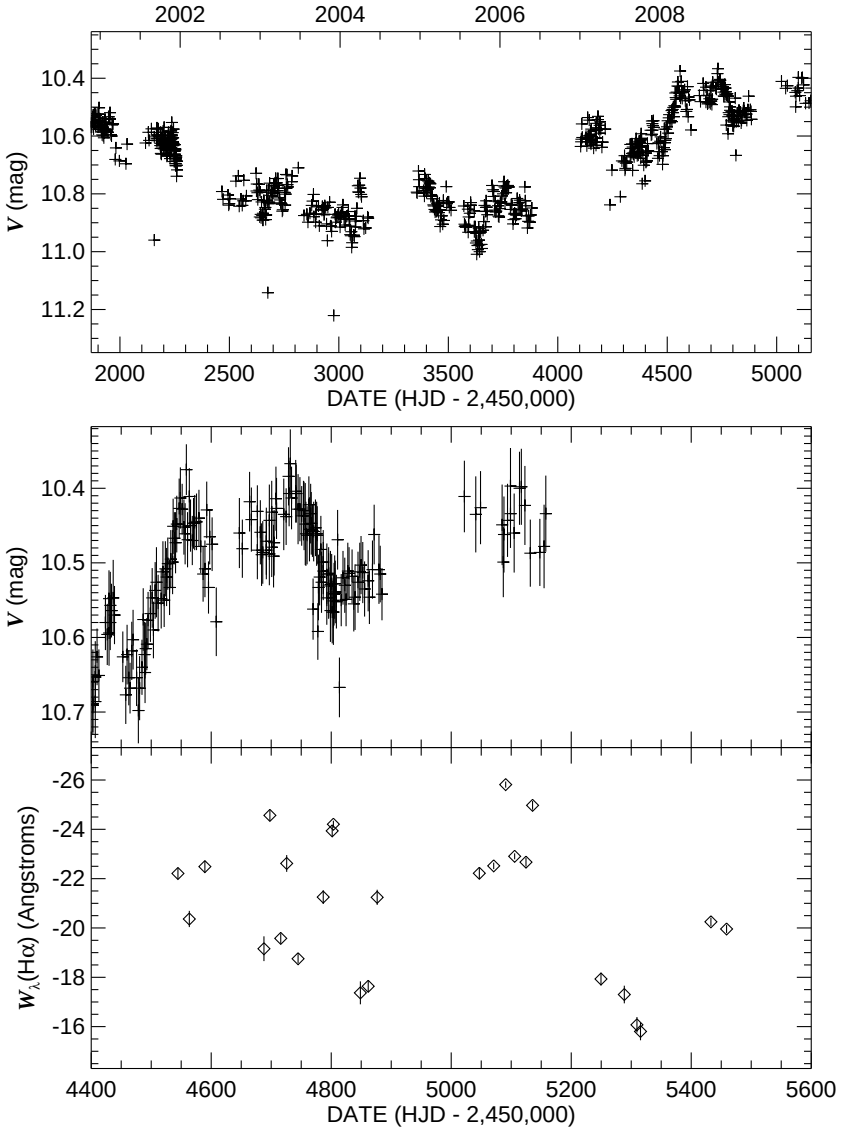

Figure 6.18 Photometry and Hα equivalent width variability of R110. The top panel shows a historical V-band light curve, as observed by the All Sky Automated Survey (Pojmanski 2002), while the bottom two panels show the photometry and Hα equivalent width behavior during the course of the survey.

6.4.5 R 127

The last LBV I will discuss in the LMC is R 127 (HDE 269858). R 127 had a recent SD-type excursion that began in about 1978 (Walborn et al. 2008). During this time, the star began a steep rise to become the optically brightest star in the LMC ($V \sim 8.7$ in 1989). The spectral type varies from OIafpe at optical minimum to an A-type supergiant at optical maximum. The spectral appearance during the subsequent decline was discussed by Walborn et al. (2008), who note that we are entering an age where the spectrum will appear as hot as possible for this star. However, Nolan Walborn (private comm.) has recently noted that the star rebrightened to an A supergiant, and began another visual decline to the hot state, which agrees with our current observations. They also claim that this star "is arguably the most important typical LBV. In fact, taking into account this report, it is not an overstatement that it is comparable to η Car and even SN 1987A, with regard to what it may teach us about late massive stellar evolution" due to its remarkable variability and position in the H-R Diagram.

Our observations covered the years 2009-2010 (the amount of telescope time increased at this time with a larger NOAO allocation), with fortunate timing during a potential decline of the optical brightness[1]. Our Hα observations also contain the forbidden [N II] emission, due to the enormous nebulosity surrounding the star (see Figure 1.3). The spectroscopic variations show a remarkable similarity to those of S Doradus. For instance, we show the first and last spectra obtained in Figure 6.19, which show a remarkable similarity to S Doradus (Fig. 6.13) due to the increase in Hα strength and the appearance of the Fe II emission lines in the red portion of the spectrum.

Our Hα observations are shown in Figures 6.20 and 6.21. The profile always has a pure emission morphology, and it is accompanied by [N II] emission on both the red and the blue

[1]Photometric magnitudes from ASAS or other surveys have not been released yet.

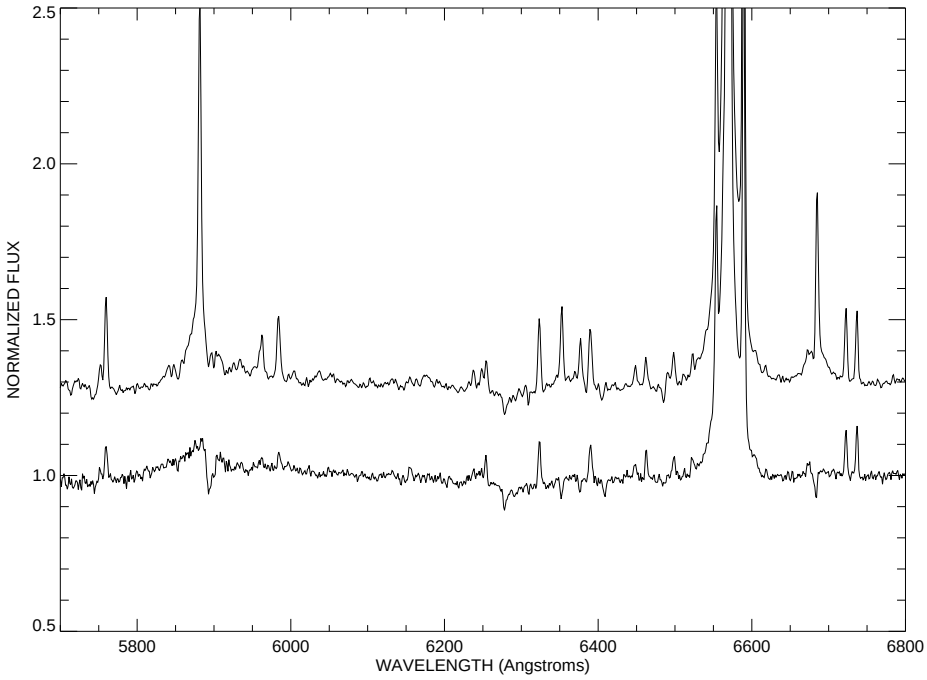

Figure 6.19 Two red spectra of R 127 taken near the beginning and end of our data set from CTIO. The first spectrum (bottom) shows a few small emission lines in the vicinity of Hα (mainly from nebular emission), while the last spectrum (top) shows many more. These new emission lines are mostly Fe II lines, indicative of the larger amount of UV flux ionizing the wind when the visual flux reaches a new minimum (Walborn, private comm.).

wings. The Hα profile is narrow (potentially due to nebular contributions), especially when compared to that in the spectra of stars such as S Doradus.

The strength of the Hα profile increased dramatically over the course of these observations. The equivalent width variations are shown in Figure 6.22. The strengthening of the profile is easily seen over the course of the observations, although some structure is seen in the trends, possibly associated with shorter timescale variability.

A striking difference between the observed spectrum of R 127 and those of S Doradus is that the spectrum of S Doradus has almost no He I 6678 or He I 5876 features. In the spectrum of R 127, these features are conspicuous and highly variable. The profiles changed from absorption to emission over the course of the the observations (Fig. 6.23).

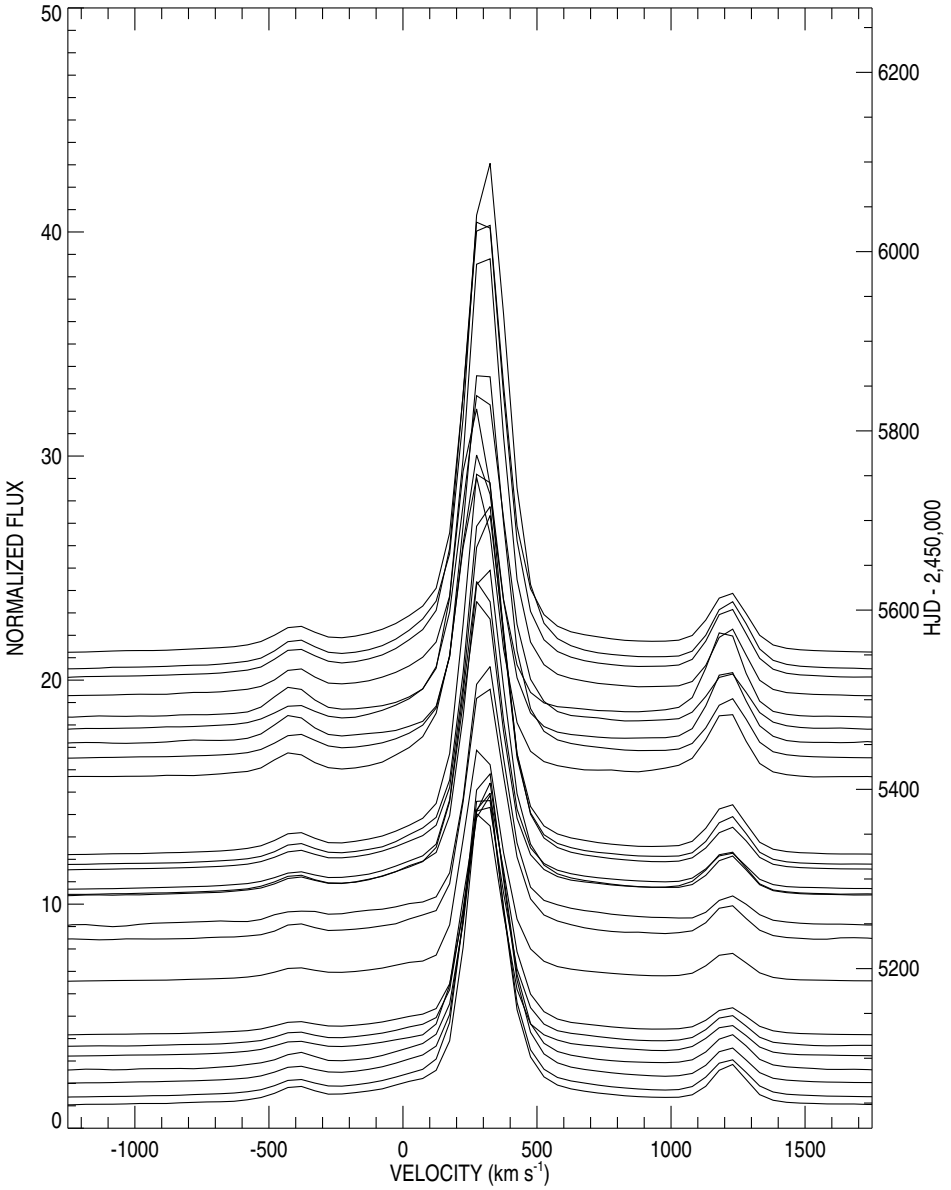

Figure 6.20 Observed Hα profiles of R 127 from the CTIO 1.5 m telescope and R-C spectrograph.

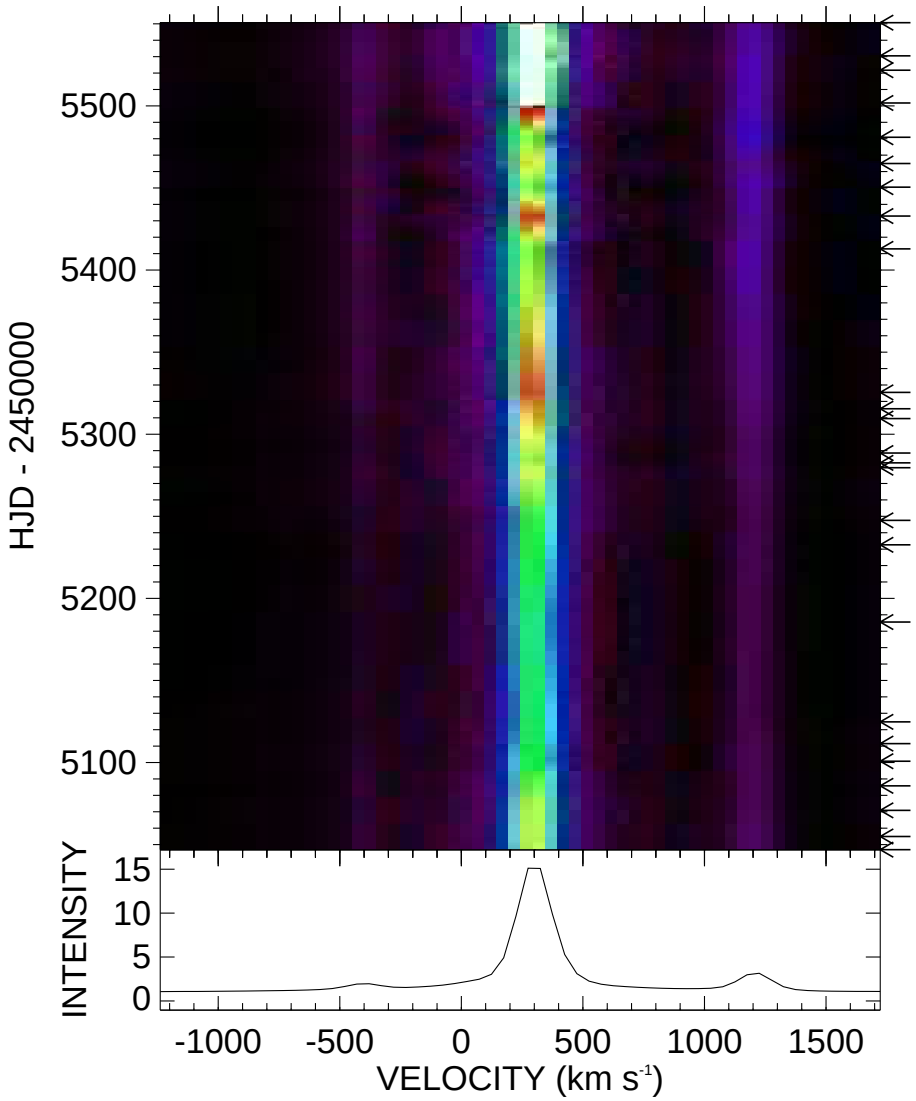

Figure 6.21 Dynamical representation of the observed Hα profiles of R 127 from the CTIO 1.5 m telescope and R-C spectrograph. Color version available in electronic edition.

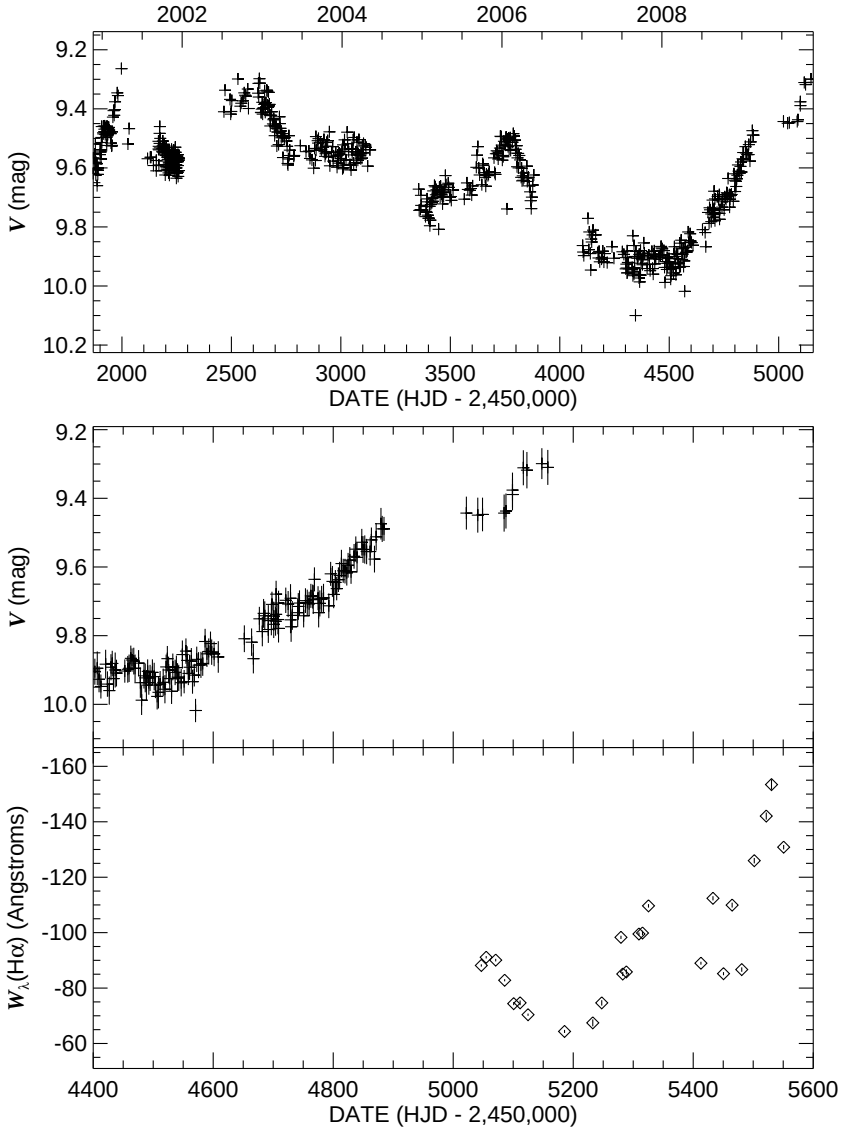

Figure 6.22 Photometry and Hα equivalent width variability of R 127. The top panel shows a historical V-band light curve, as observed by the All Sky Automated Survey (Pojmanski 2002), while the bottom two panels show the photometry and Hα equivalent width behavior during the course of the survey. The star has begun another optical decline since the time of the last ASAS observations that have been released.

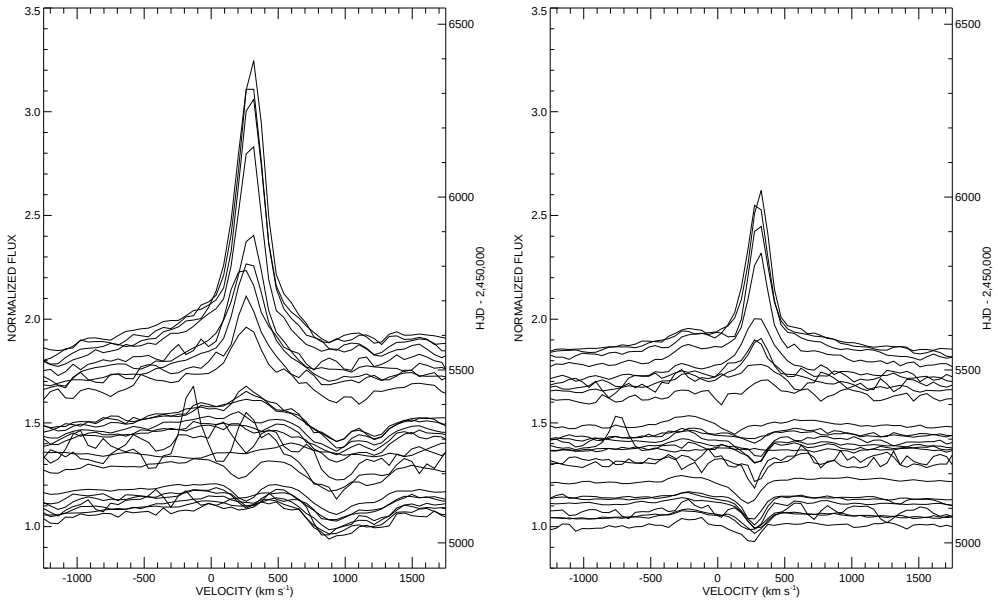

Figure 6.23 Line profiles for He I λ 5876 (left) and He I λ 6678 (right) in R 127.

These observations show that the state of R 127 is similar to that of S Doradus at the current time, but with some differences like He I. It would be worthwhile to continue studying this object and to obtain ultraviolet spectroscopy of R 127 in order to fully characterize this star in a hot state. The light curve shown in Figure 6.22 shows a maximum near the beginning of our spectral time series, but other observers have noted its recent decline in visible light.

6.4.6 HR Carinae

HR Carinae (HD 90177) is an extremely active LBV residing in the Carina spiral arm of the Galaxy. It has a rich observational record from as early as the 1960s (Bond & Landolt 1970) through the present (Groh et al. 2009a). The light variations are seen to be typical of active LBVs (Bond & Landolt 1970; Wisse & Wisse 1971; van Genderen et al. 1990; Groh et al. 2009a). The effective temperature ranges from 10,000 K at optical maximum to 18,000 K at optical minimum (Groh et al. 2009a).

The spectral variability (in the blue region) of HR Car has been observed over two S Doradus phases by Szeifert et al. (2003). These authors observe that the metallic lines change from absorption profiles at optical maximum to P Cygni type profiles at optical minimum making the overall appearance of the spectrum change dramatically across these SD-phases. Machado et al. (2002) reported on a high resolution spectrum of HR Carinae that showed P Cygni profiles for the Balmer lines with the absorption troughs exhibiting two components.

Our Hα observations (Figures 6.24 and 6.25) show a localized maximum in the Hα intensity. The profile morphology (at our spectral resolution) was always a pure emission profile. Definitive trends have been observed in the strengths of spectral lines have been observed for other optical line transitions (Szeifert et al. 2003) that are similar to those in Hα. The definitive trends are likely typical of this star, although little has been documented for its Hα profile.

The equivalent width variations of Hα are shown in Figure 6.26. It shows the same trends as Figures 6.24 and 6.25. The star reached its faintest (hottest) optical (V-band) state near HJD 2,454,700 (see Fig. 6.26), near the epoch of observations studied by Groh et al. (2009a).

Our observations of He I 6678 show some changes in the line profile morphology (Fig. 6.27 and 6.28). This line probes a portion of the wind closer to the star than Hα, and shows the

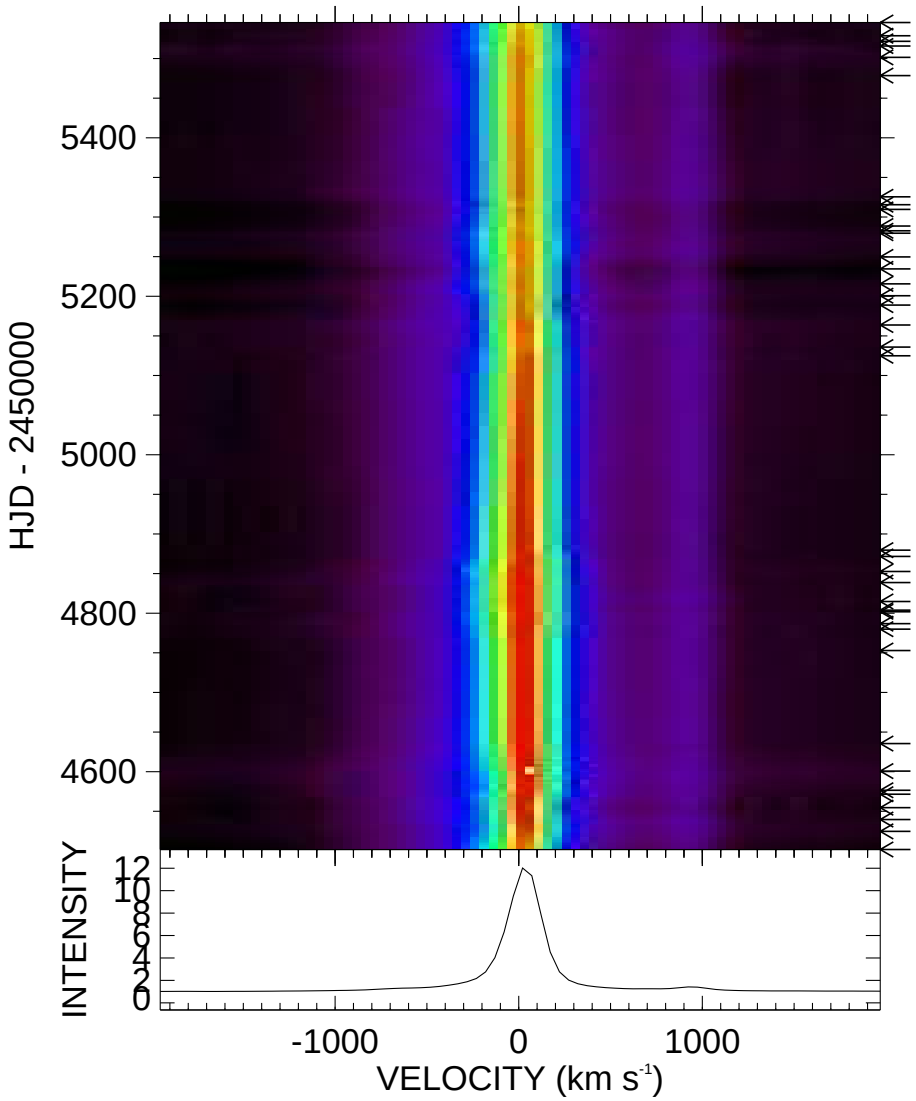

Figure 6.24 Dynamical Representation of the logarithm of the observed Hα profiles of HR Carinae from the CTIO 1.5 m telescope and R-C spectrograph. Color version available in electronic edition.

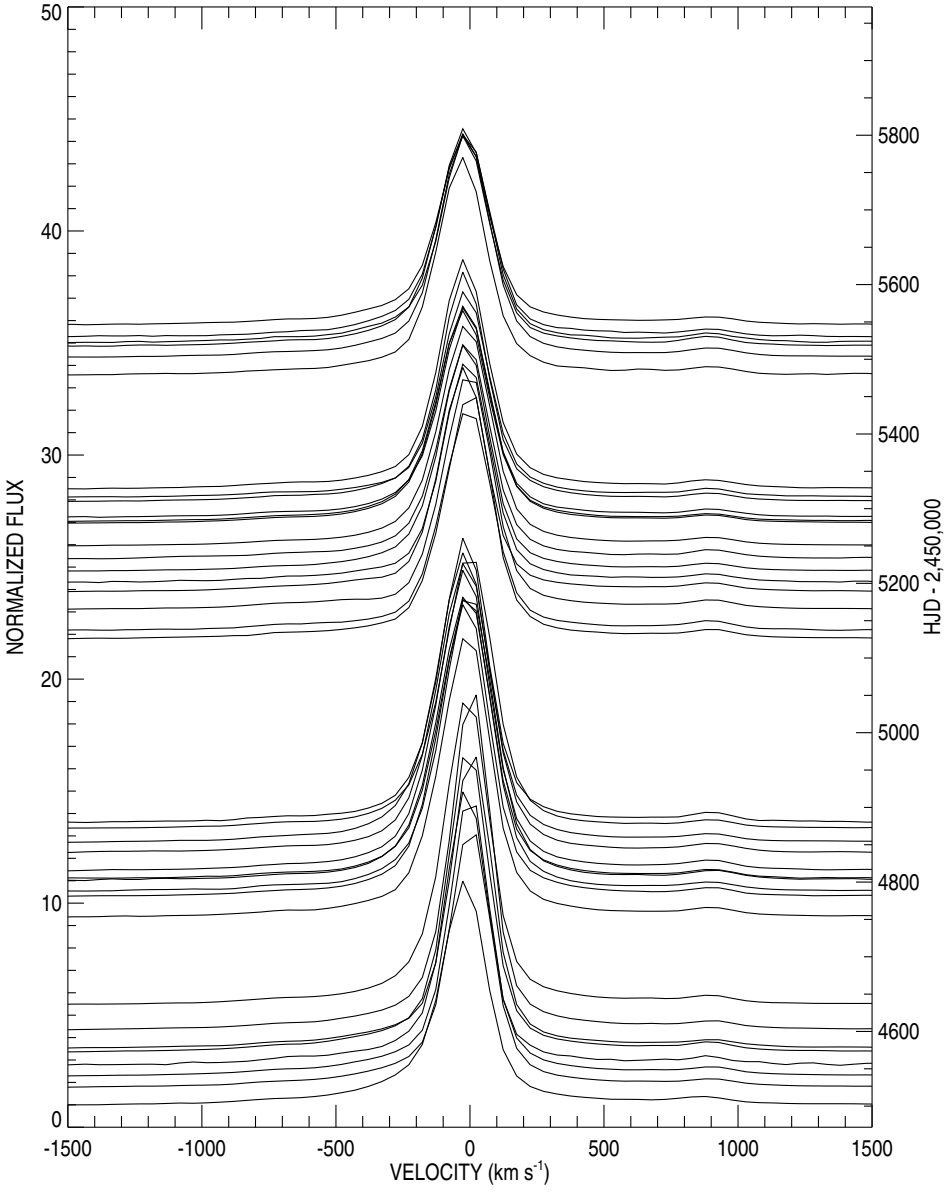

Figure 6.25 Observed line spectra of the Hα profiles of HR Carinae from the CTIO 1.5 m telescope and R-C spectrograph.

possible variability close to the star near optical minimum.

Groh et al. (2009a) study found an important clue to LBV physics during this hot state of HR Car. During the optical minimum when the star has the highest effective temperature, the star rotates at a near critical rate, as measured by the broadening of Si IV $\lambda\lambda$ 4088–4116. The calculation is based on an estimate of the Eddington parameter Γ, the stellar mass, luminosity, and radius from stellar atmosphere and wind models produced by the code CMFGEN. When the star is near maximum optical flux, the radius increases and the star is no longer a rapid rotator. The Eddington parameter is the ratio of the radiative acceleration to the local gravitational acceleration.

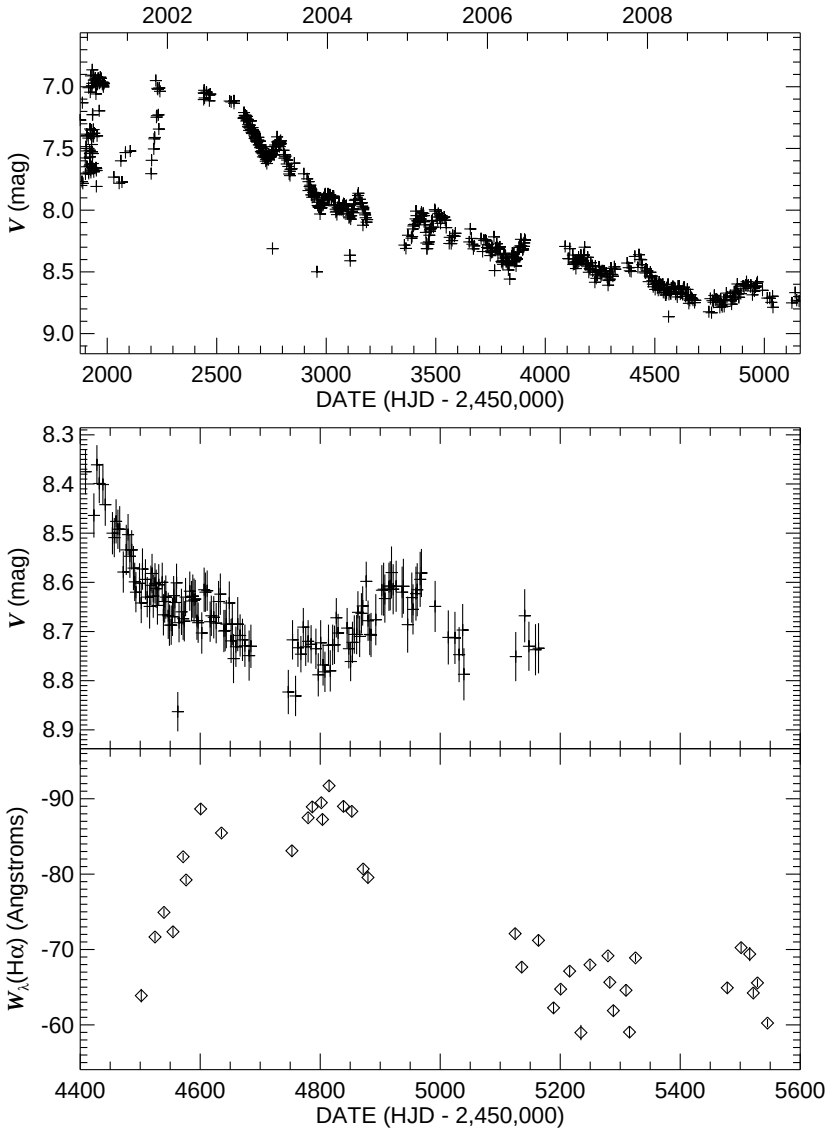

Figure 6.26 Photometry and Hα equivalent width variability of HR Car. The top panel shows a historical V-band light curve, as observed by the All Sky Automated Survey (Pojmanski 2002), while the bottom two panels show the photometry and Hα equivalent width behavior during the course of the survey.

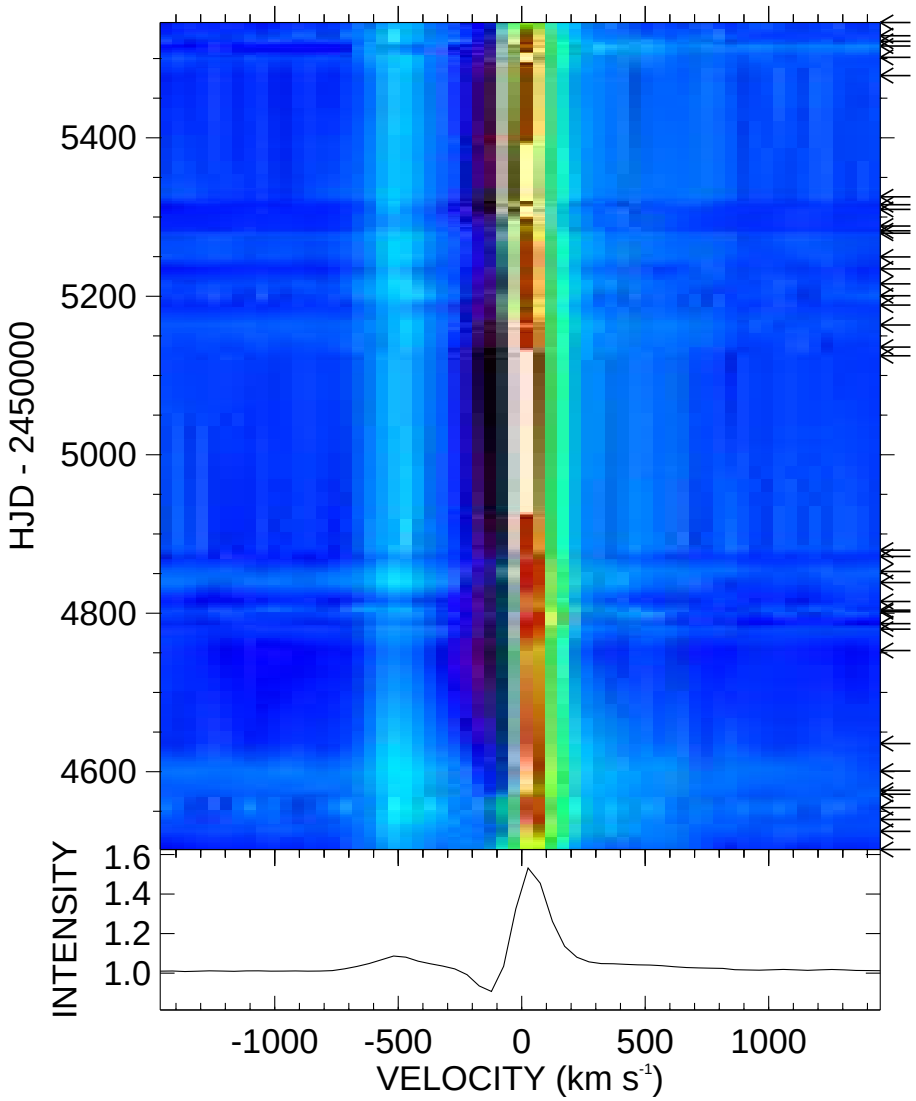

Figure 6.27 Dynamical Representation of the observed He I 6678 profiles of HR Carinae from the CTIO 1.5 m telescope and R-C spectrograph. Color version available in electronic edition.

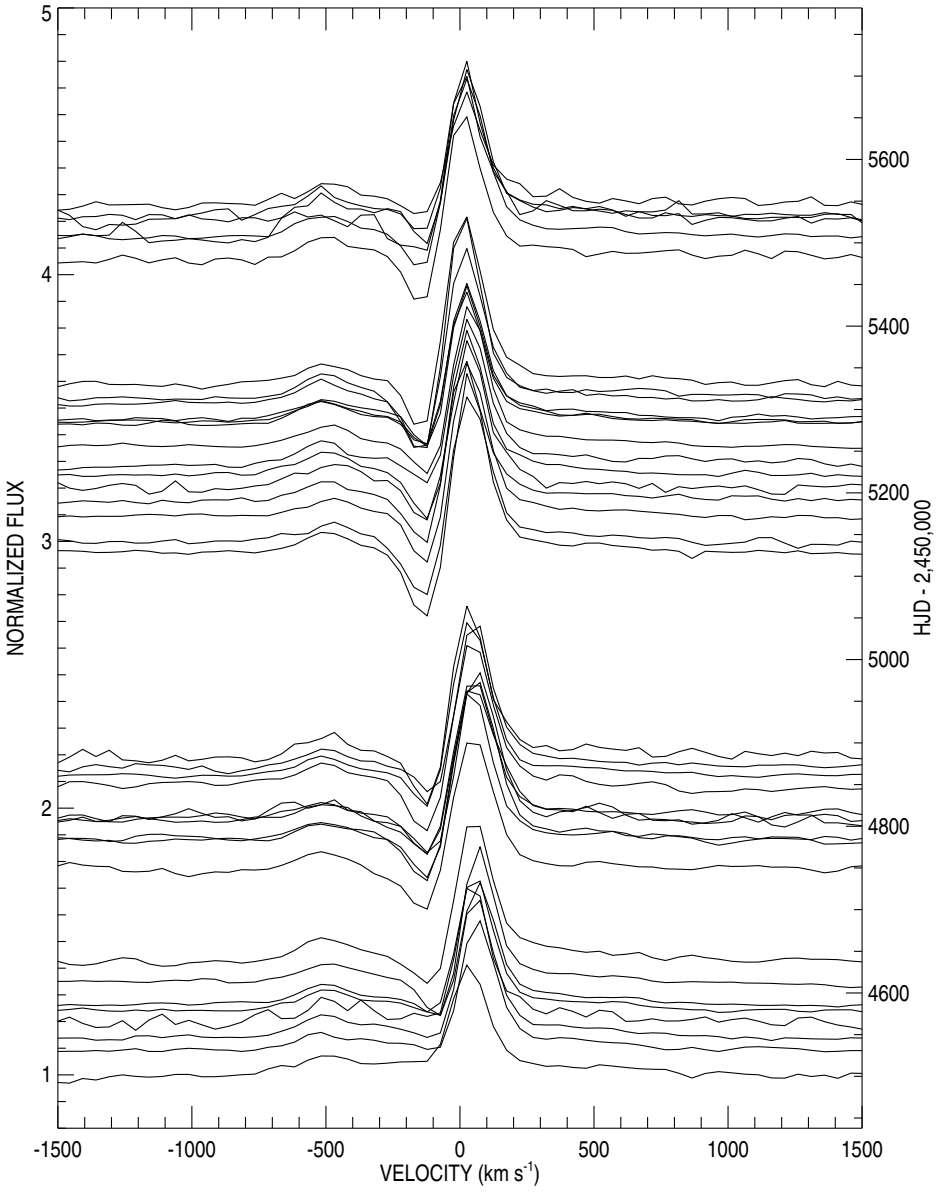

Figure 6.28 Observed line spectra of the He I 6678 profiles of HR Carinae from the CTIO 1.5 m telescope and R-C spectrograph.

6.4.7 AG Carinae

AG Carinae is another LBV that resides in the Carina spiral arm of our Galaxy. The star's photometric behavior is often considered prototypical for very active Galactic LBVs. The long term photometric behavior has been examined in several key studies by Bond & Landolt (1970), Wisse & Wisse (1971), van Genderen et al. (1990) and Groh et al. (2009b). The visual (V) magnitudes vary by about 2 mag, and the variability is similar in the K band. The long term SD-phase type variability has a timescale on the order of 15–20 years, with a short SD-phase having timescales of a few years.

A large ring nebula surrounds AG Carinae (Nota et al. 1992). Nota et al. (1992) show that the nebula is axisymmetric and aspherical, implying that it was not likely formed by a spherically symmetric wind. They suspect that the bipolar nature was due to either an equatorial excretion disk such as found in the Be stars (Porter & Rivinius 2003) or a binary companion. There is now supporting evidence that rapid rotation, also found in the Be stars, is present with AG Car. Groh et al. (2006) found that AG Carinae rotates at near critical ($v/v_{crit} = 0.86$ on 2001 Apr 12), similar to their findings on HR Carinae. Rapid rotation may have caused this bipolar outflow from differing flux contributions as a function of stellar latitude.

The spectrum of AG Carinae has been studied several times. The kinematics of the lines suggests that the star is located at a distance of ≈ 6 kpc (Humphreys et al. 1989). Groh et al. (2009b) found that the star had significantly different wind parameters during the last two visual minima, where the star has the highest effective temperature. Their study involved in-depth spectral modeling. During the deep minimum that lasted from 1985–1990, the star had $T_{\rm eff} = 22,800$ K with a mass loss rate of $\dot{M} \sim 1.5 \times 10^{-5} M_{\odot}$ yr^{-1}, while the star cooled to $T_{\rm eff} = 17,000$ K and had a higher mass loss rate of $\dot{M} \sim 3.7 \times 10^{-5} M_{\odot}$yr^{-1} during the subsequent minimum in 2000–2001. The bolometric luminosity decreased as the

star went to maximum visual flux. Furthermore, the study found the wind is very clumped (10–20% of the matter located in the clumps), and these clumps originate deep in the wind.

Our observations of AG Car show a downward and subsequent upward trend in the Hα equivalent width, indicating that we observed the star near an overarching optical maximum (Fig. 6.31), but with a localized optical minimum. The profiles are shown in Figures 6.29 and 6.30. The Hα profile is always a pure emission profile at our resolution. The strength of the profile (Figure 6.31) reflects the visual impressions and verifies the local maximum in visual light, reaching a local minimum with a cooler temperature in the middle of the time series as supported by the work of Groh et al. (2009b).

The He I 6678 profile was typically an absorption profile (Fig. 6.32 and 6.33). However, the last spectra in our time series show a remarkable increase in the emission strength. Furthermore, there is a dramatic P Cygni profile that emerges for this line transition.

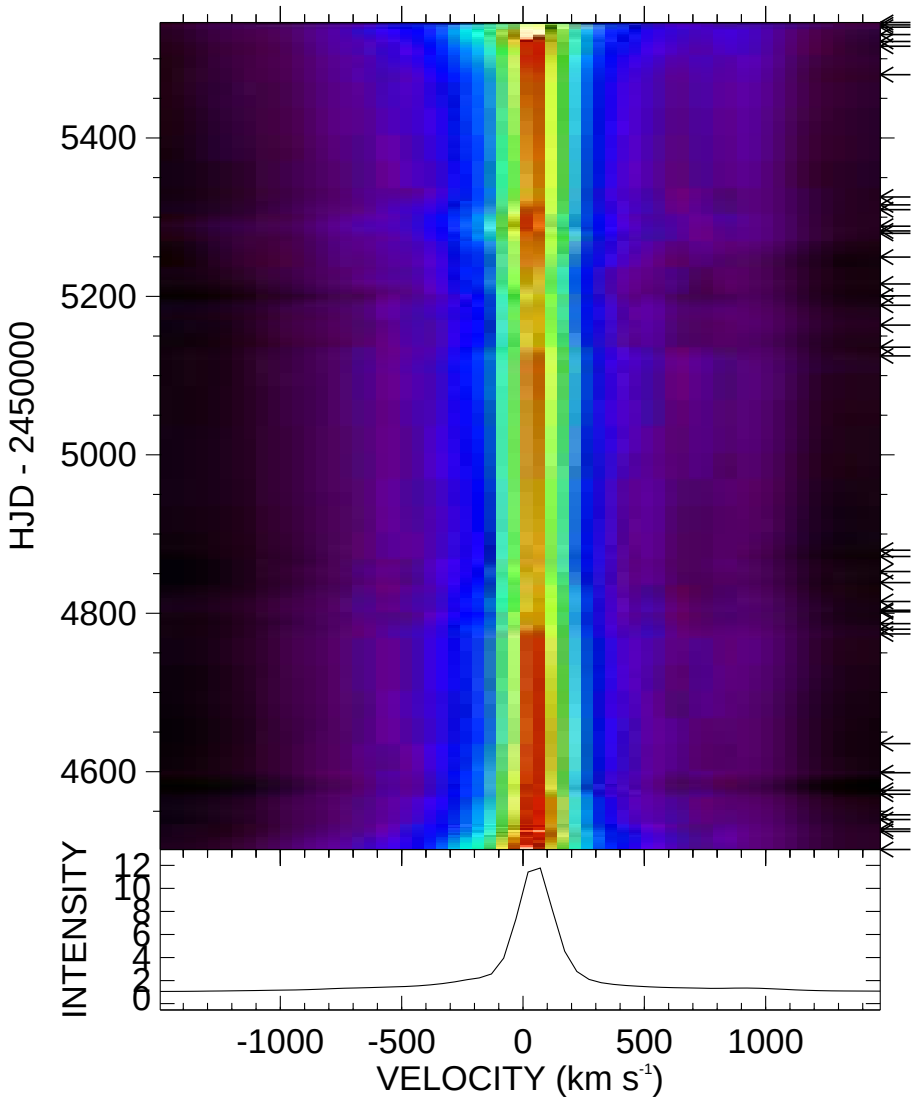

Figure 6.29 Dynamical representation of the logarithm of the observed Hα profiles of AG Carinae from the CTIO 1.5 m telescope and R-C spectrograph. Color version available in electronic edition.

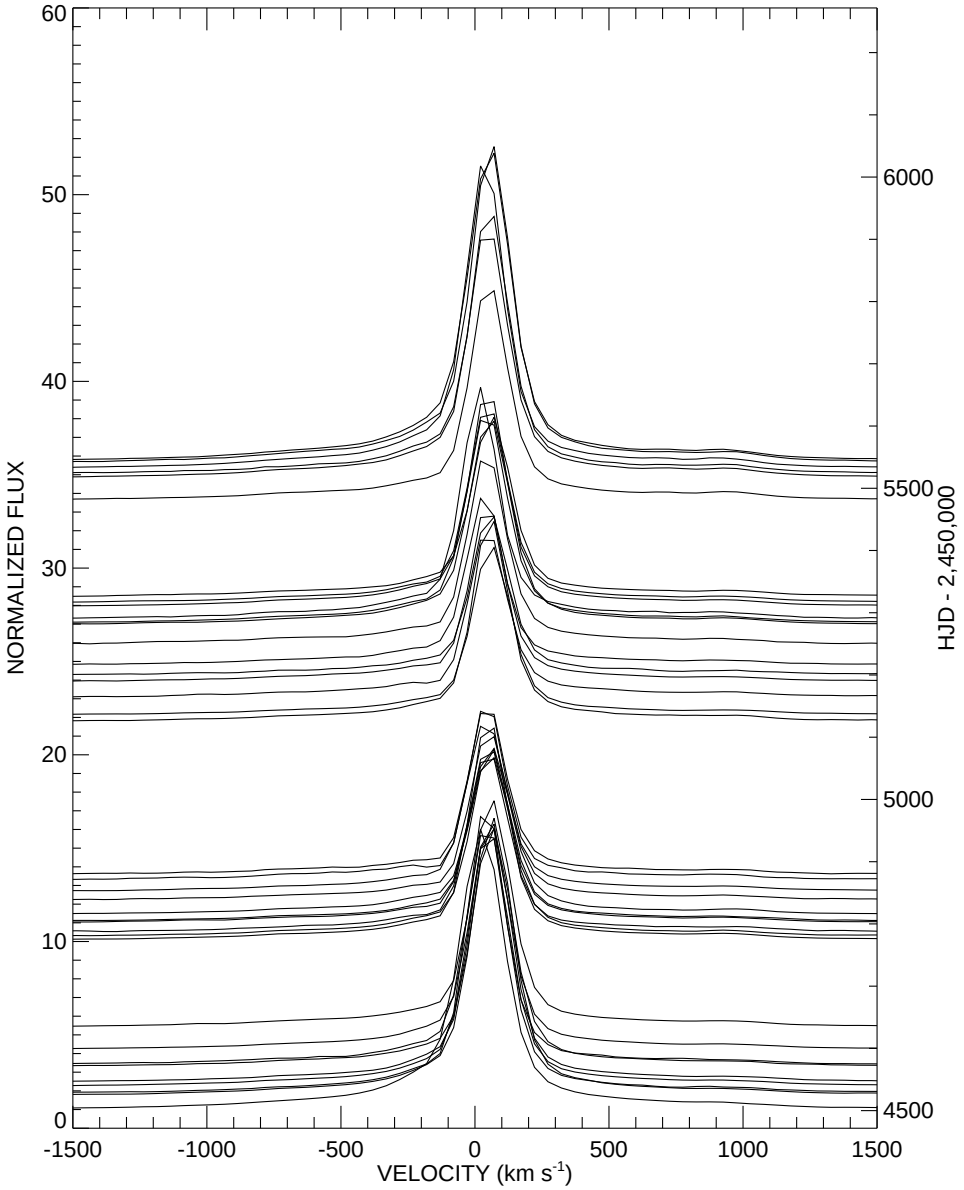

Figure 6.30 Observed line spectra of the Hα profiles of AG Carinae from the CTIO 1.5 m telescope and R-C spectrograph.

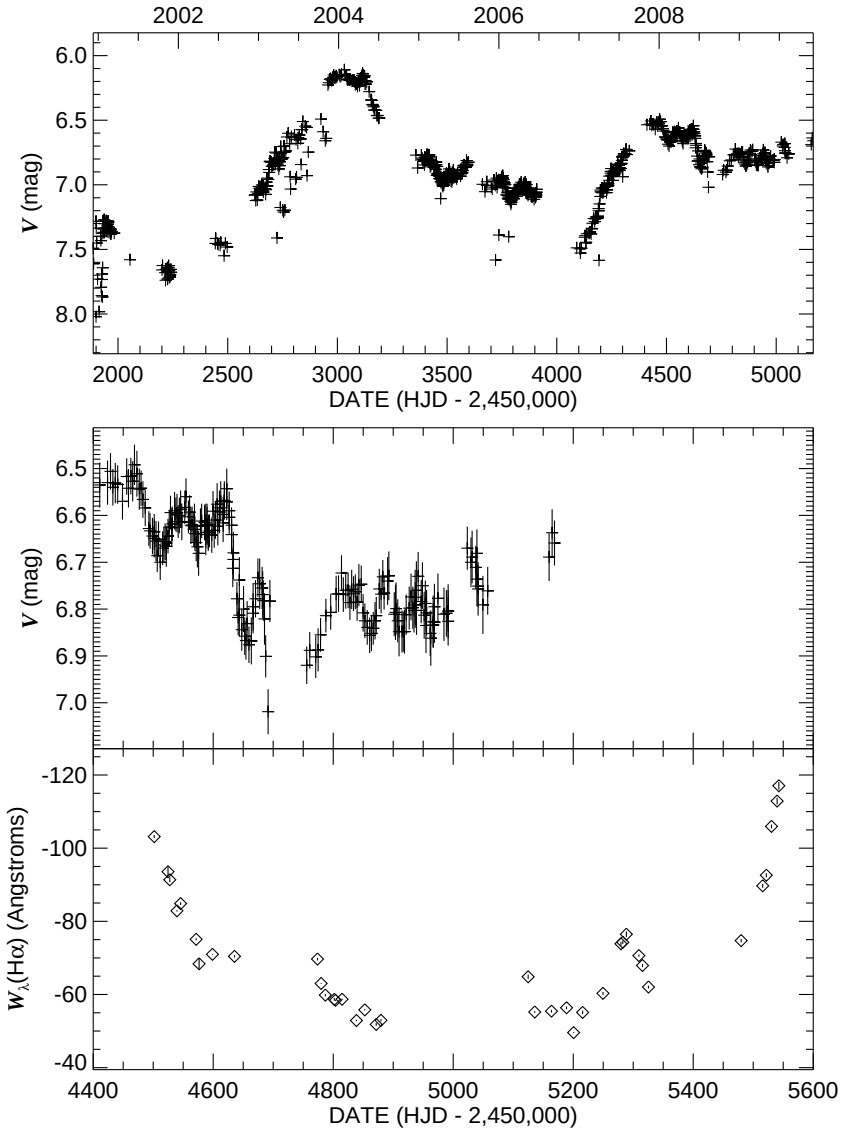

Figure 6.31 Photometry and Hα equivalent width variability of AG Car. The top panel shows a historical V-band light curve, as observed by the All Sky Automated Survey (Pojmanski 2002), while the bottom two panels show the photometry and Hα equivalent width behavior during the course of the survey.

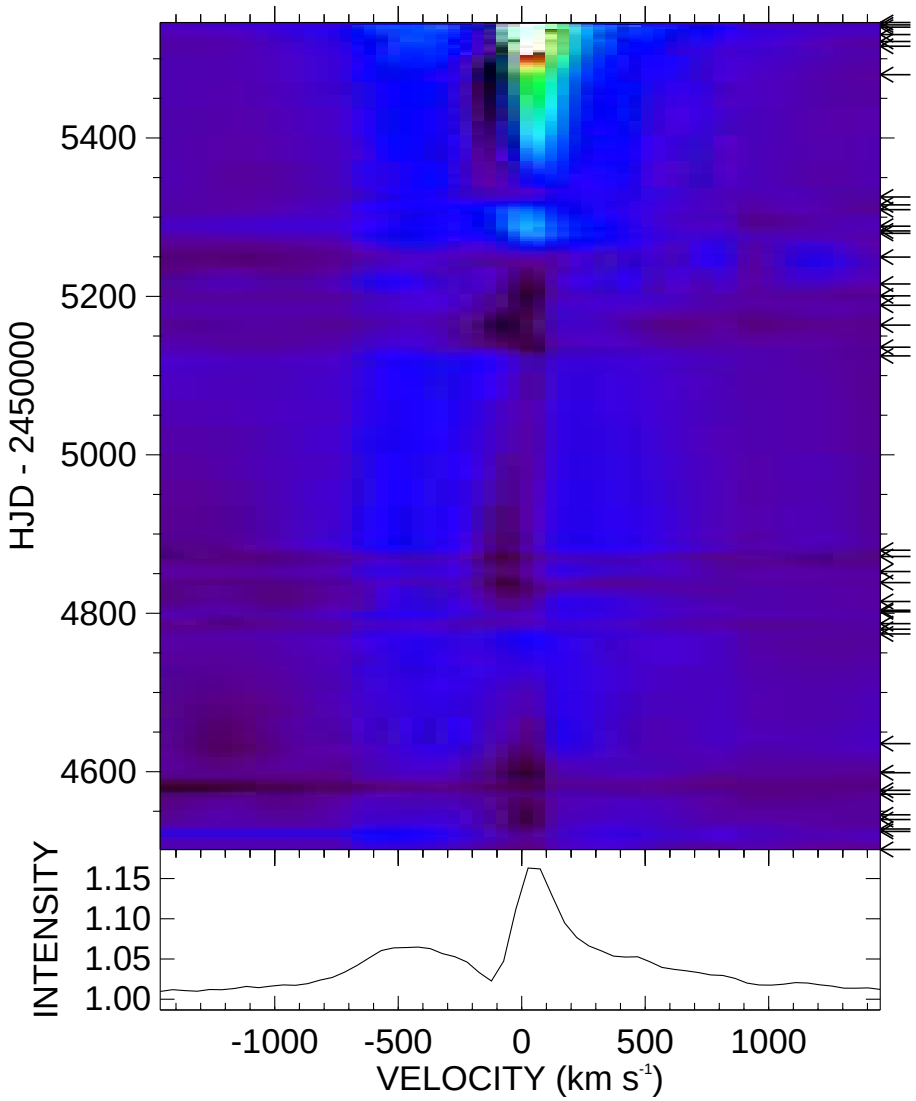

Figure 6.32 Dynamical representation of the observed He I 6678 profiles of AG Carinae from the CTIO 1.5 m telescope and R-C spectrograph. Color version available in electronic edition.

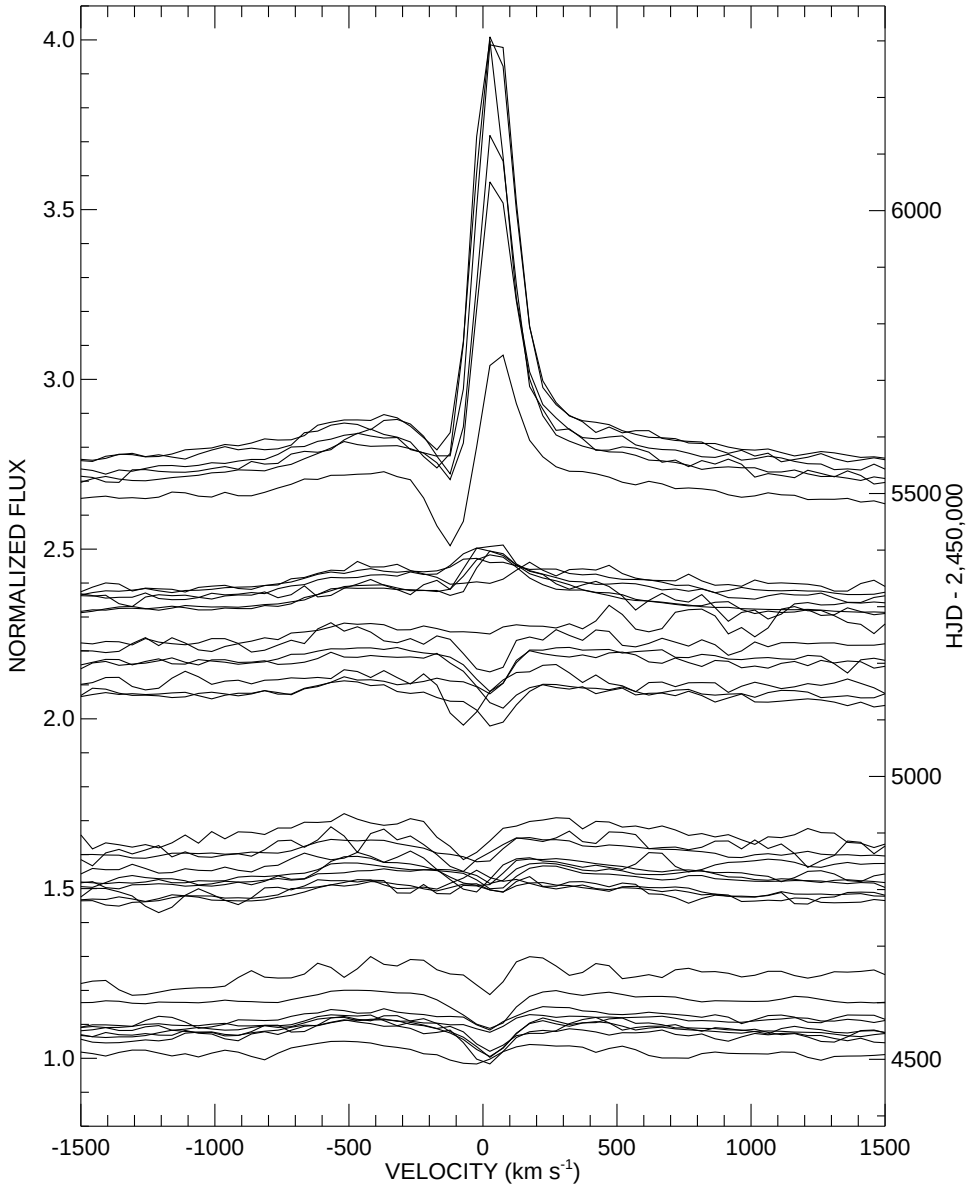

Figure 6.33 Observed line spectra of the He I 6678 profiles of AG Carinae from the CTIO 1.5 m telescope and R-C spectrograph.

6.4.8 Wra 751

Wra 751 (V432 Carinae) is a bona fide "strong active" Galactic LBV that was discovered to be an LBV candidate by Hu et al. (1990). In the discovery paper, it was found that the star has a similar spectrum to the hot LBVs ($T_{\rm eff} \approx 30,000$ K) and should have had an initial mass of at least 50 $M_{\odot}$. It is located in the Carina spiral arm with AG Car and HR Car at a distance of approximately 6 kpc. This LBV still resides in its birth cluster (Pasquali et al. 2006). The birth cluster contains several O and B stars that have been classified from spectroscopy. The cluster has an average extinction of $A_v \simeq 6.1$ magnitudes, and the earliest O supergiant is an O8 I star, implying that the cluster is at least 4 Myr old. The presence of O8 I stars supports that the initial mass of Wra 751 of at least 50 $M_{\odot}$ suggested by Hu et al. (1990) is realistic, as O8 I stars likely have a mass between between 30 and 50 $M_{\odot}$.

While spectroscopic investigations of this star are sparse, there is an excellent photometric discussion by Sterken et al. (2008). They demonstrated that the star varied by about a full magnitude in V (between 10.5 and 11.5) between 1985 and 2007 (see Fig. 6.36). The derived effective temperatures based on the multi-filter photometry imply that the star varies from $T_{\rm eff} = 10^{3.9}$ to $10^{4.5}$K, a range larger than found for the well studied LBV AG Carinae. An early study of the optical and ultraviolet spectrum (de Winter et al. 1992) found that the spectrum matched that of AG Car and HR Car at optical minimum (hot state), resembling an Of/WN9 star.

The beginning of the observations in the survey correspond to the optically bright state, and the Hα profile briefly began to brighten. However, this was a short maximum that was soon followed by a monotonic decline for the remainder of the observing seasons. The star probably had begin to cool towards its minimum temperature by the end of the 3 year campaign.

Figures 6.34 and 6.35 show the dynamical representation and the line plot of the Hα

profile, respectively. The observations show that while the photometry of Sterken et al. (2008) show a maximum in $\sim$ 2007, the Hα profile briefly recovered from this bright state, but then continued to brighten and the Hα profile faded during the course of these observations (2008–2010). It is now likely in an optically brighter state. The star is an extremely interesting strong-active LBV.

In Figure 6.36, we show the equivalent width of the Hα profile. There is strong variability present, which is seen as brightening and subsequent fading as discussed with Figures 6.34 and 6.35. The downward trend warrants additional observations as the star has covered very bright and very dim states in the recent observational record.

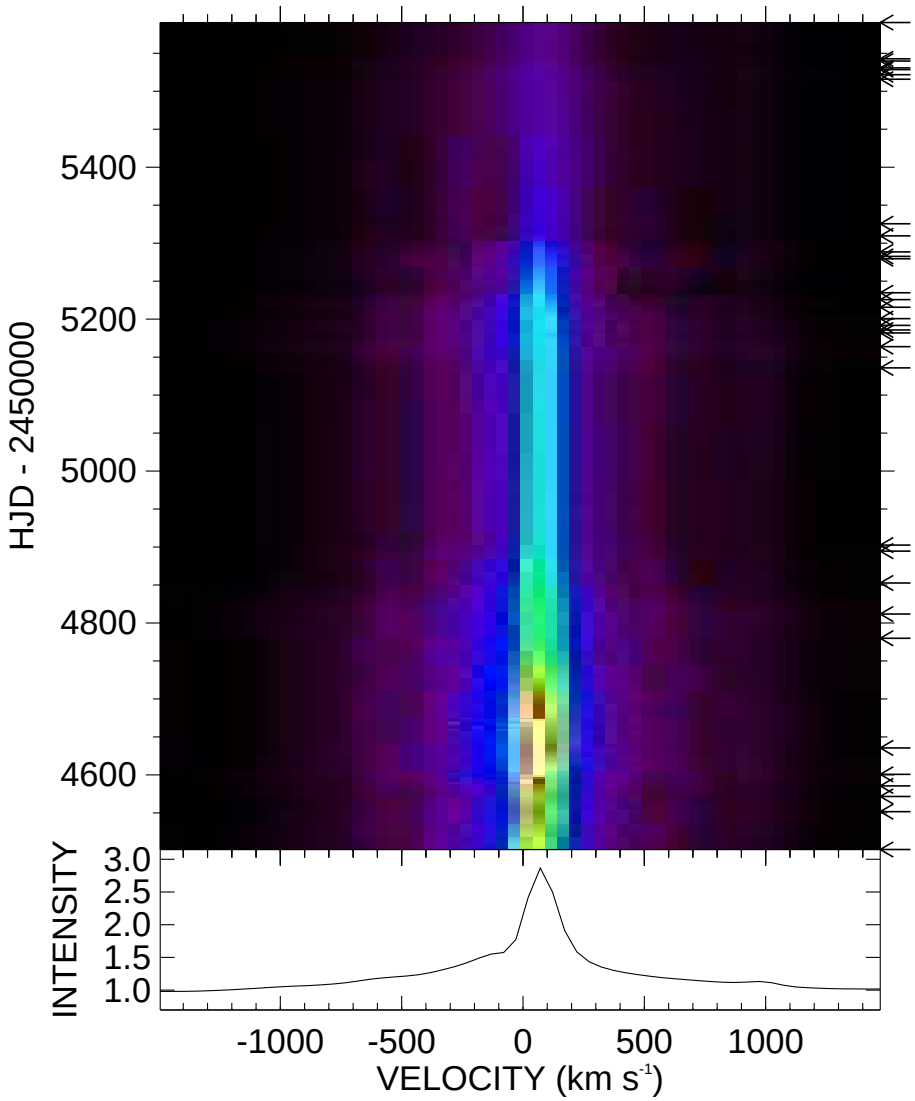

Figure 6.34 Dynamical spectrum of the Hα profile of Wra 751 during the survey. Note the local maximum and then monotonic decline in the profile strength. Color version available in electronic edition.

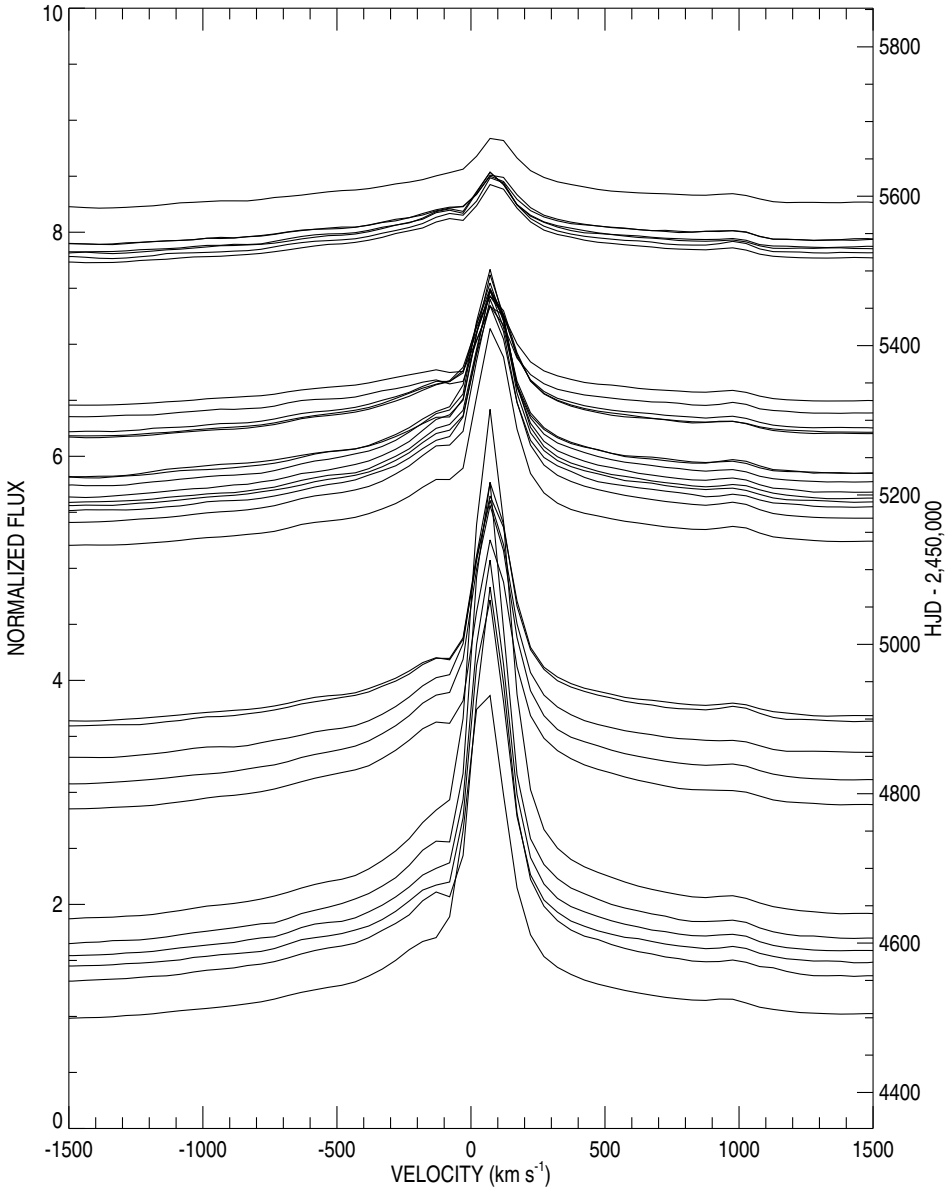

Figure 6.35 Hα profiles of Wra 751 during the survey.

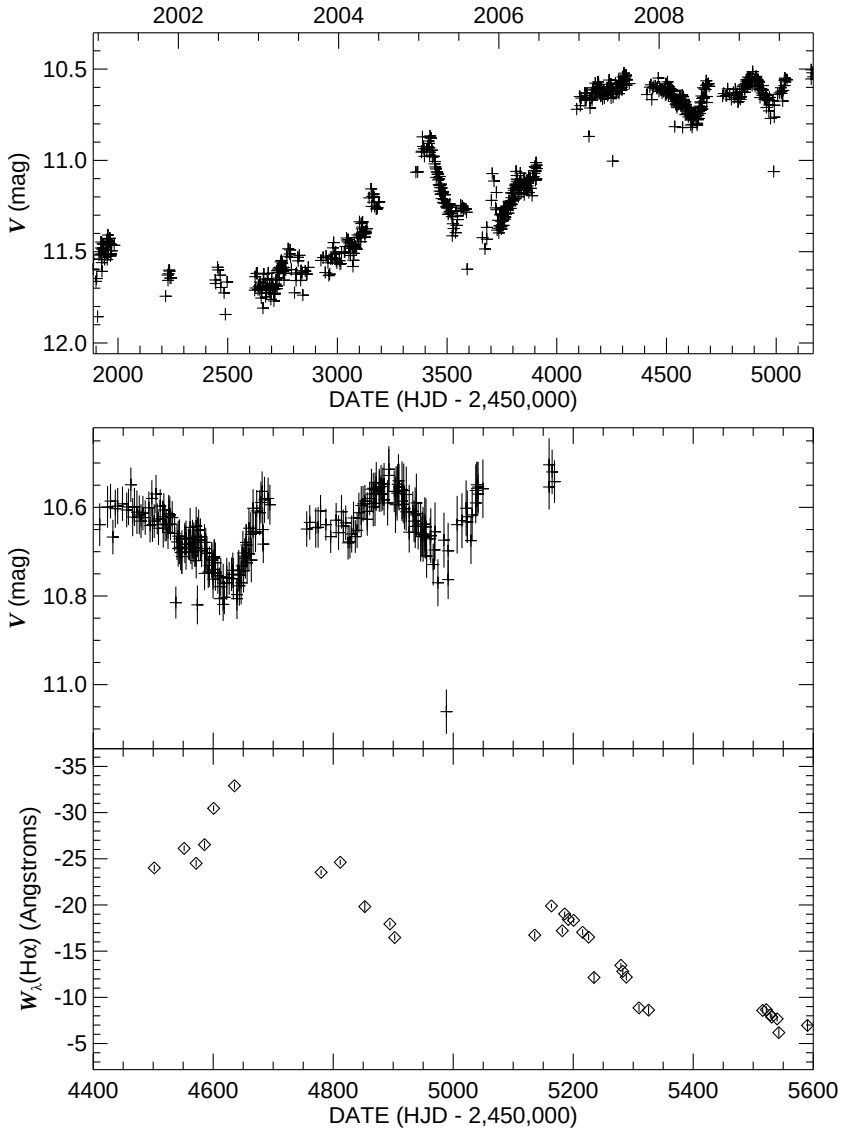

Figure 6.36 Photometry and Hα equivalent width variability of Wra 751. The top panel shows a historical V-band light curve, as observed by the All Sky Automated Survey (Pojmanski 2002), while the bottom two panels show the photometry and Hα equivalent width behavior during the course of the survey.

6.4.9 ζ^1 Sco

ζ^1 Scorpii is a Galactic hypergiant (B1.5Ia+) that is a suspected LBV candidate based on analysis of the light curve (Sterken et al. 1997a). This analysis shows that the star has a long $\sim 2,000$ day variability cycle, consistent with a short S Dor phase (i.e., $\lesssim 10$ years). Archival measurements dating back through the eighteenth century show that the star has varied by two magnitudes in V. Furthermore, the star varied in color over time. Gould (1879) described the color as "not red" when the star was faintest, consistent with typical S Doradus type behavior.

An in depth model of the star was made by Crowther et al. (2006) along with results for 24 other Galactic O and B supergiants. Most of these stars are not LBVs, but are "normal" hot supergiants. The terminal velocity of the wind of ζ^1 Sco is the lowest observed in the sample, with $v_\infty = 390$ km s^{-1}. The derived mass loss rate, $\dot{M} = 6 \times 10^{-6} M_\odot \mathrm{yr}^{-1}$ was the highest of the sample. Furthermore, the [N/C] abundance ratio was the highest in the sample (+2.05) in comparison with the normal supergiants that have values between +0.8 and +1.1. Clearly, this supports the idea that the star is a different stage of evolution than normal hot supergiants due to the vastly different wind parameters.

The variability of the spectrum of ζ^1 Sco was first noted by Jaschek & Jaschek (1973). Sterken & Wolf (1978), Wolf et al. (1994), and Rivinius et al. (1994) showed that the variable Hα profile can be explained by a variable mass loss rate, namely an underlying value of $\dot{M} = 0.8 \times 10^{-5} M_\odot$ yr^{-1} with episodic increases up to a factor of 2. Stahl et al. (1995) show that the Fe III λ 5156 profile has a variable absorption component, which they suggested could be used to examine the lower wind region.

The spectral variability was further explored by Rivinius et al. (1997). In this study, DAC-like features were seen in the Fe III 5156 line, and the acceleration of this component could be compared to velocities of similar narrow features in the lines Fe III 5127, He I 6678,

He I 5876, and Hα. When all velocities of propagating absorptions were compared, Rivinius et al. derived a β-type law exponent of 2.5 for these components with $v_\infty = 370$ km s^{-1}. The recurrence time for this feature is about 24 days, but the variability of emission components has a timescale of 15 days.

Our Hα observations are shown in Figures 6.37 and 6.38. The strength of the P Cygni absorption changes with time becoming stronger than normal at three or more epochs. The equivalent widths are shown in Figure 6.39. The profile strength is variable, but is reminiscent of hot supergiants (Kaufer et al. 1996; Richardson et al. 2011c) over these time scales, where sparse data show little or no obvious trend. The variations may occur on timescales shorter than the typical observational cadence we achieved in our survey.

The He I profiles are nearly static throughout our observations and show that the star is somewhat stable over these time scales. However, it should be stressed that the He I lines examined by Rivinius et al. (1997) did show variability on short time scales. It is likely that the longer time scales examined in the present study of ζ^1 Sco will hide the variability of the He I lines.

There is a need for time intensive spectroscopy of this star in order to examine the importance and presence of DAC-like features in the wind over long time scales. The presence of these features in so many lines (Rivinius et al. 1997) would allow an observational analysis of the long term behavior of the wind velocity law in order to fully characterize the long-term changes present in the stellar wind.

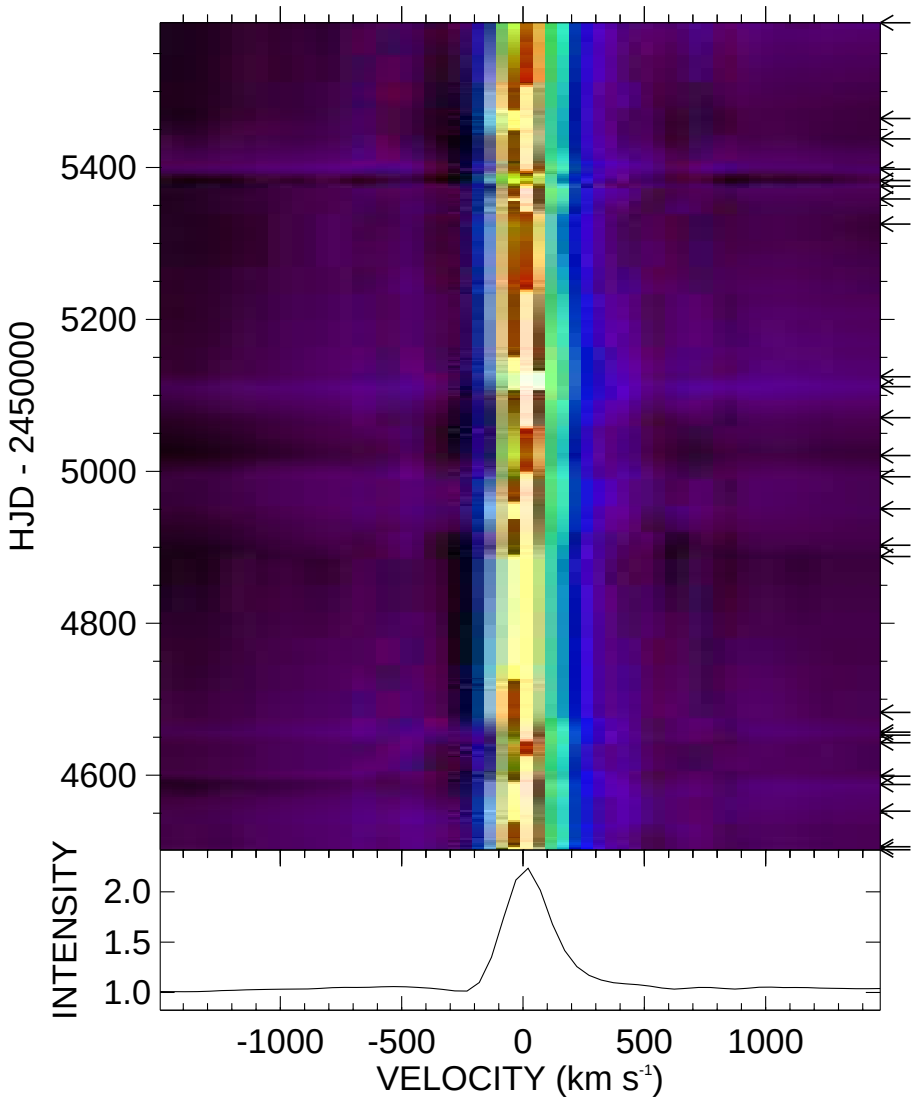

Figure 6.37 Dynamical spectrum of Hα profiles of ζ^1 Sco. Color version available in electronic edition.

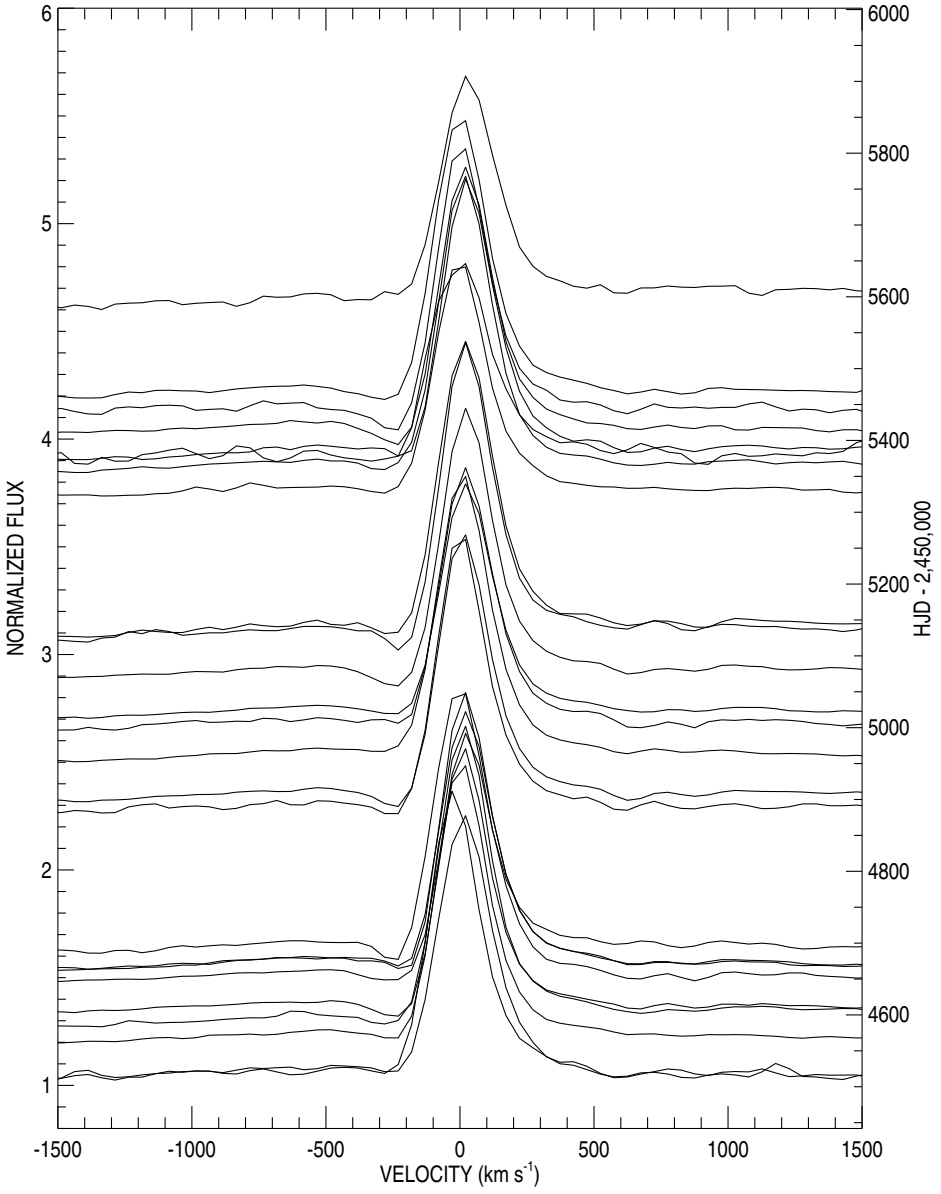

Figure 6.38 Hα profiles of ζ^1 Sco.

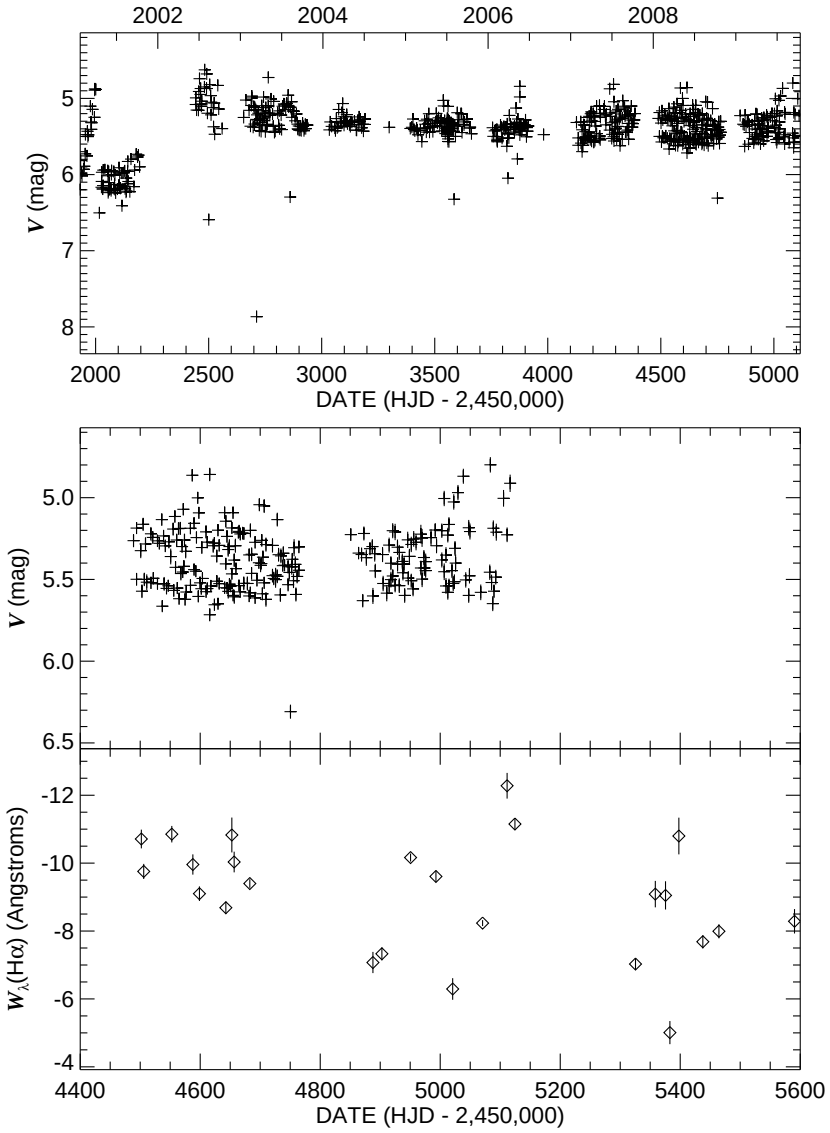

Figure 6.39 Photometry and Hα equivalent width variability of ζ^1 Scorpii. The top panel shows a historical V-band light curve, as observed by the All Sky Automated Survey (Pojmanski 2002), while the bottom two panels show the photometry and Hα equivalent width behavior during the course of the survey.

6.4.10 HD 160529

HD 160529 is classified as an A-type hypergiant (roughly an A9), but the star was observed to vary by 0.5 magnitudes between 1983 and 1991, while changing its spectral appearance to a late B hypergiant (B8 or B9) or supergiant (Sterken et al. 1991). According to the ASAS data, the star varied by ~ 1.2 mag in 2002, but this was early data from the All Sky Automated Survey, and the star is near the bright limit for the telescope. Subsequent ASAS data show similar variabilty to that discussed in Sterken et al. (1991). Comparisons of this star were made to R 110 and R 40, and it is suspected that the star is at the low luminosity end of the LBV variability strip. The star is more luminous than a typical supergiant, but less luminous than a typical LBV. Therefore, this target is extremely important to our understanding of stars of this luminosity. The star may have previously gone through a red supergiant phase, and may have a mass of only 13 $M_{\odot}$ (Sterken et al. 1991).

The spectrum of HD 160529 has been examined in a few key studies. The first major study (Wolf et al. 1974) showed a variable radial velocity of metallic absorption lines. They attributed the P Cygni type profile for Hα and Hβ profiles as due to a chromospheric effect in the atmosphere, which also was used to explain the high radial velocity for the Ca II K line. A modern study of the spectral variability was done by Stahl et al. (2003). They found that the mass loss rate varied between 7×10^{-6} and $1 \times 10^{-5} M_{\odot}$ yr^{-1}, nearly independent of the visual magnitude (and temperature) of the star. They found evidence of radial velocity variability in several metallic lines, but they argued that was caused by line profile changes and not binary orbital motion.

The Hα profile shown in Wolf et al. (1974) is similar to the P Cygni type profiles that we observed in some of our observations. This is weaker than even the weakest Hα P Cygni type emission observed by Stahl et al. (2003), where the peak emission was up to seven times stronger than the continuum, similar to that shown in the study by Sterken et al. (1991).

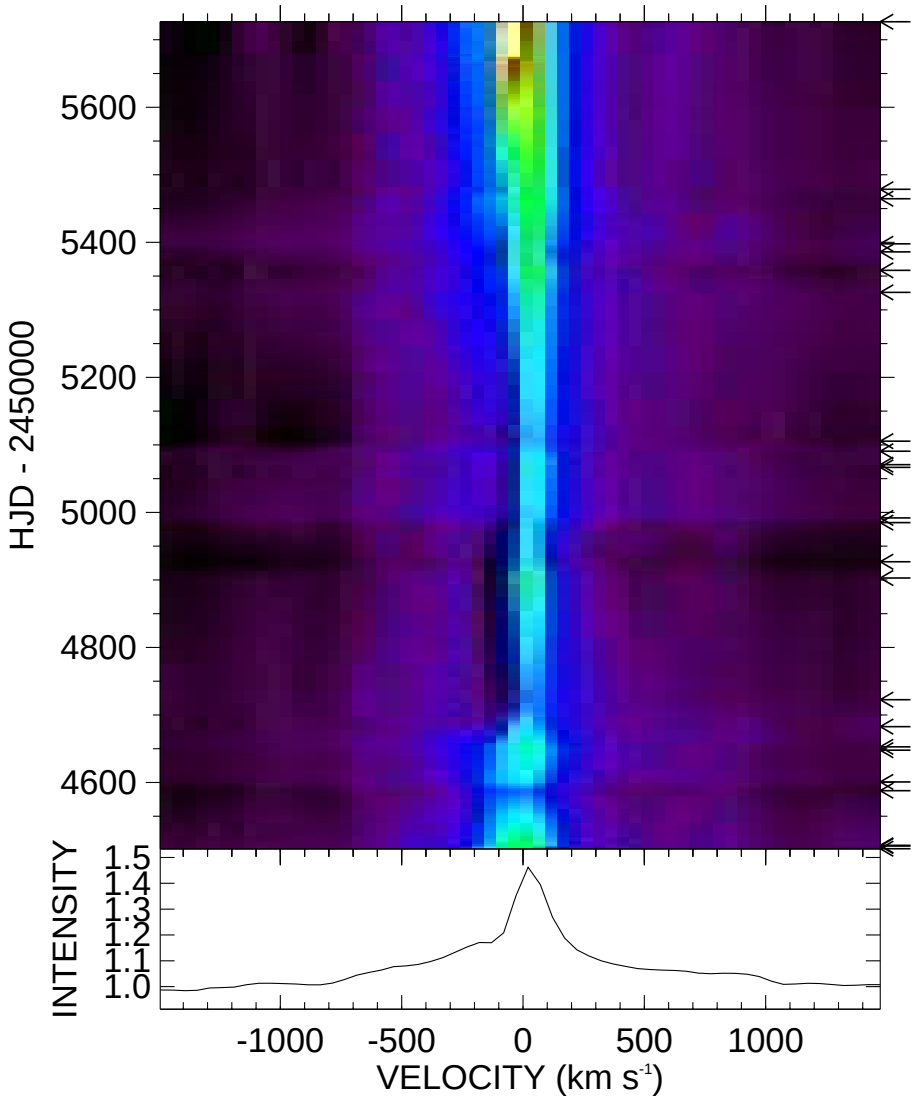

Figure 6.40 Dynamical spectrum of Hα profiles of HD 160529. Color version available in electronic edition.

Our Hα spectra are shown in Figures 6.40 and 6.41.

As seen in Figures 6.40 and 6.41, the Hα profile decreased in strength and then began increasing during the observed epochs. The equivalent width variations are shown in Figure 6.42. A strong P Cygni absorption appears for an extended period of time in the middle

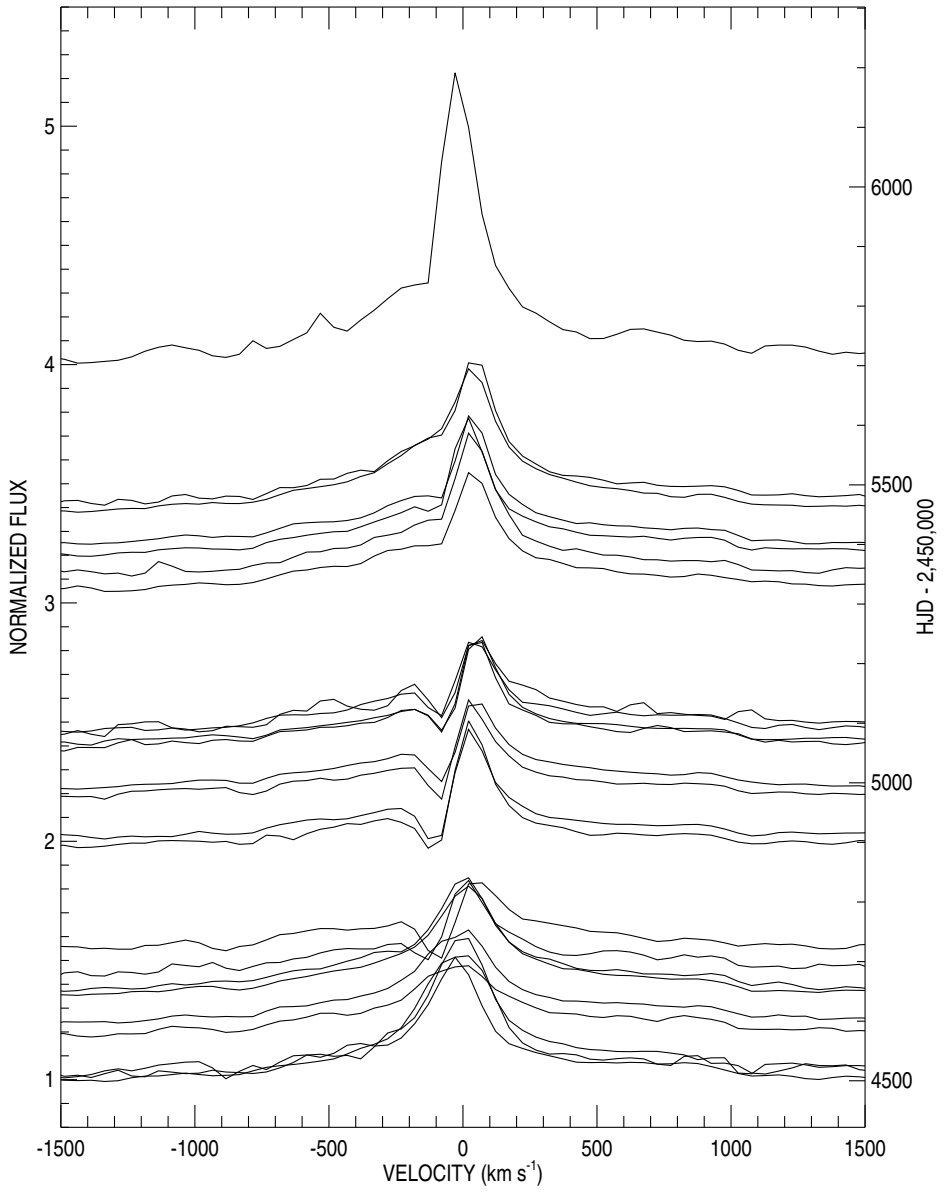

Figure 6.41 Line plots of Hα profiles of HD 160529. The final spectrum (top) was obtained at HLCO.

of our time series (Fig. 6.40 and 6.41), which causes some of the decrease observed in the strength of the profile. The strongest Hα is observed in the last observed spectrum, which was obtained at HLCO. The changes in profile morphology and line strength are further evidence that the star is a "strong-active" LBV, even with its low luminosity.

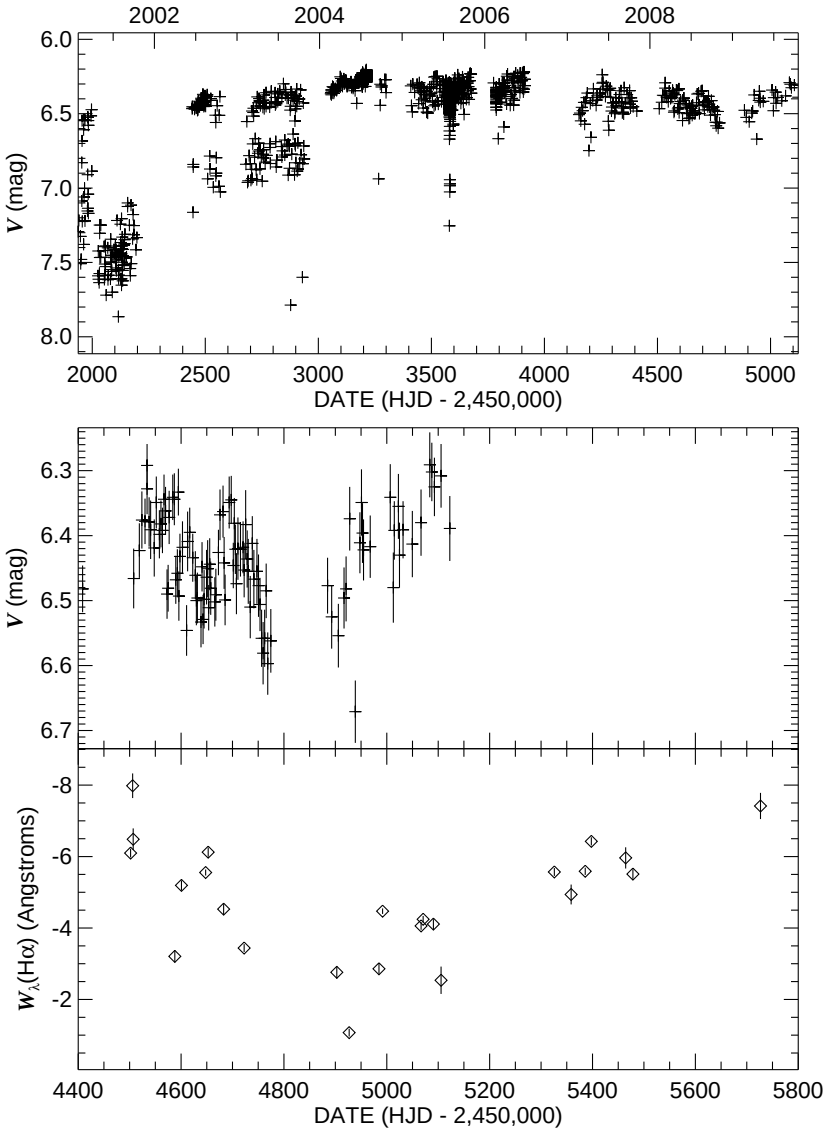

Figure 6.42 Photometry and Hα equivalent width variability of HD 160529. The top panel shows a historical V-band light curve, as observed by the All Sky Automated Survey (Pojmanski 2002), while the bottom two panels show the photometry and Hα equivalent width behavior during the course of the survey.

6.4.11 HD 168607

Chentsov (1980) proposed that HD 168607 was an LBV based upon spectra that showed that the Hα emission line had electron scattering wings that extended to $\pm$2000 km s^{-1}. In addition the spectrum showed that the P Cygni absorption lines varied in radial velocity, as a function of ionization, indicating an expanding wind. The spectrum was shown to be different than that of any other late B supergiant. For example, there are several Fe II emission lines in the red region of the spectrum shown in Chentsov (1980). The spectrum of HD 168607 was also described by Chentsov & Musaev (1996). Their observed spectrum was similar to other late B supergiants, but with stronger emission lines, and no reported Fe II emission. Our data show no indication of these Fe II emission lines, verifying the long term variability trends typical of LBVs. Photometry of HD 168607 confirms that the flux variations are consistent with the LBV classification (van Genderen et al. 1992; Sterken et al. 1999). The mass loss rate ($\dot{M} = 2.2 \times 10^{-6} M_{\odot}$ yr^{-1}) was derived by Leitherer et al. (1995) from radio measurements.

Figures 6.43 and 6.44 show the Hα profiles of HD 168607. Our observations of HD 168607 show that the Hα profile is generally weakening throughout our time series and that the profile has a pure emission profile at the very beginning and end of the time series. However, in the middle of the observations, the profile transitioned to a P Cygni profile (See Figures 6.43 and 6.44).

The Hα equivalent width variations of the profile are shown in Figure 6.45. This variability confirms that the star is a bona fide LBV, as suspected in the literature. However, this star is unusual in another way. It lies near M17, which is an open cluster with a surrounding nebula. There is another star of nearly the same color and brightness that lies only $\sim$ 1 arcminute away. This star, HD 168625[2] (Section 6.4.12), is another suspected LBV, making

[2]Anthony F.J. Moffat (Université de Montreal) is arranging a high precision photometric campaign on both HD 168607 and HD 168625 using the MOST satellite.

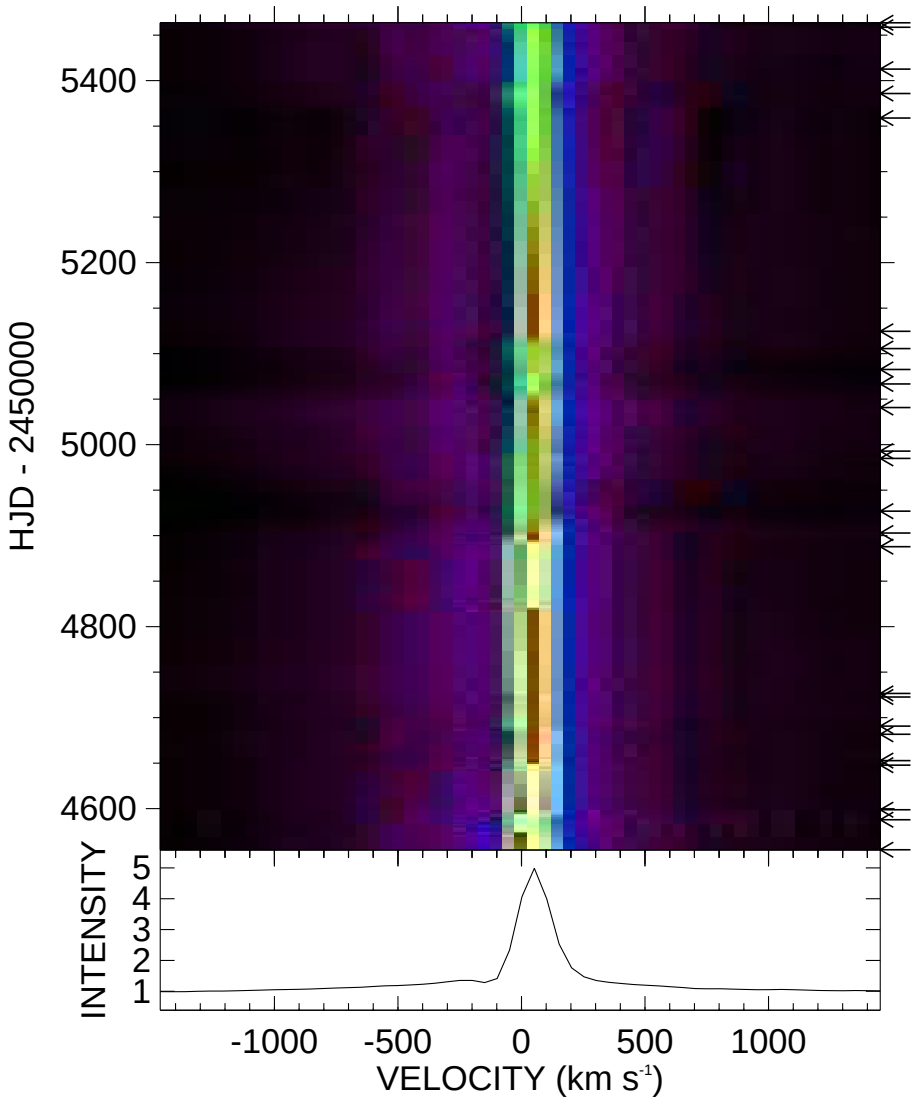

Figure 6.43 Dynamical representation of the Hα profile of HD 168607. Color version available in electronic edition.

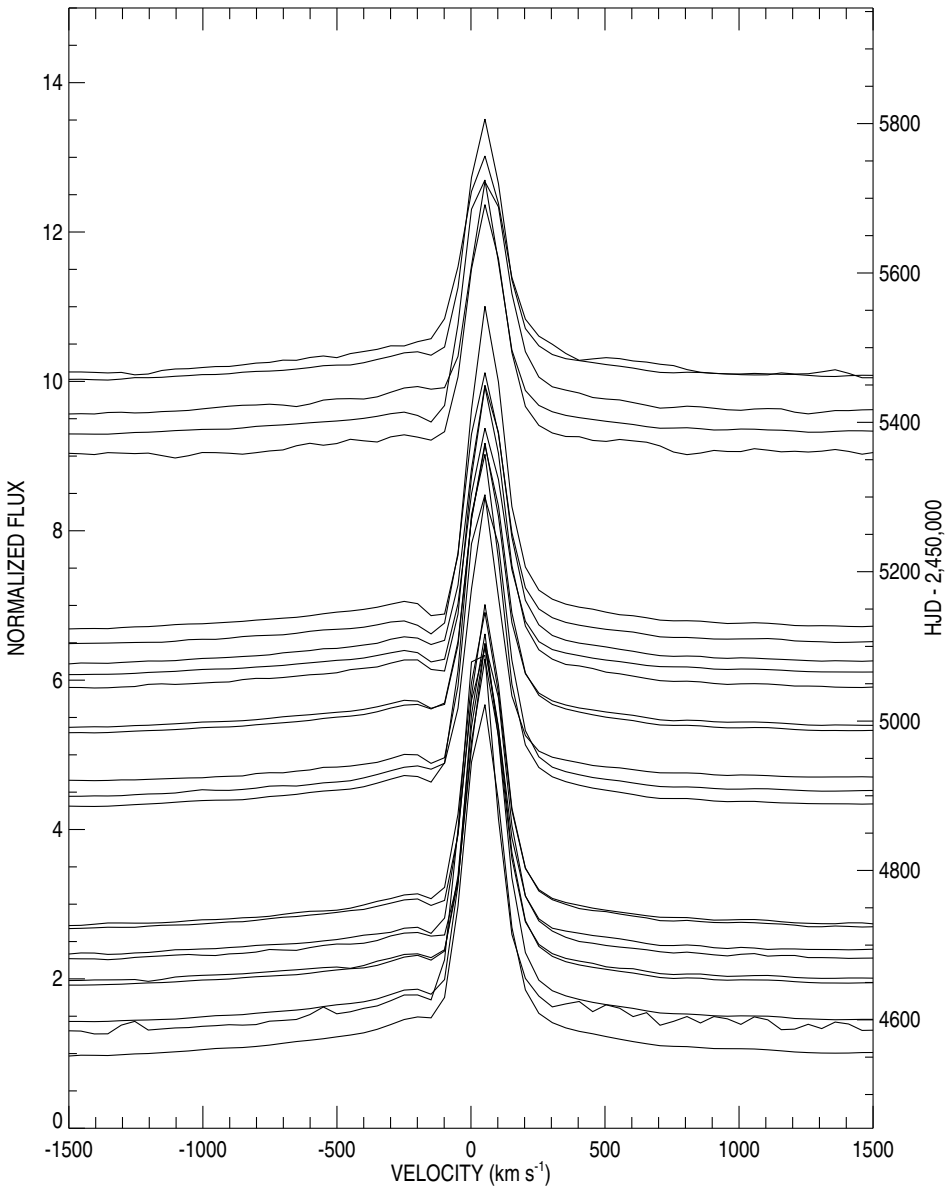

Figure 6.44 Line plots of the Hα profile of HD 168607.

this the closest LBV pair in the sky (Chentsov & Gorda 2004). However, the projected distance between these stars is large and implies that a binary orbit would take thousands of years.

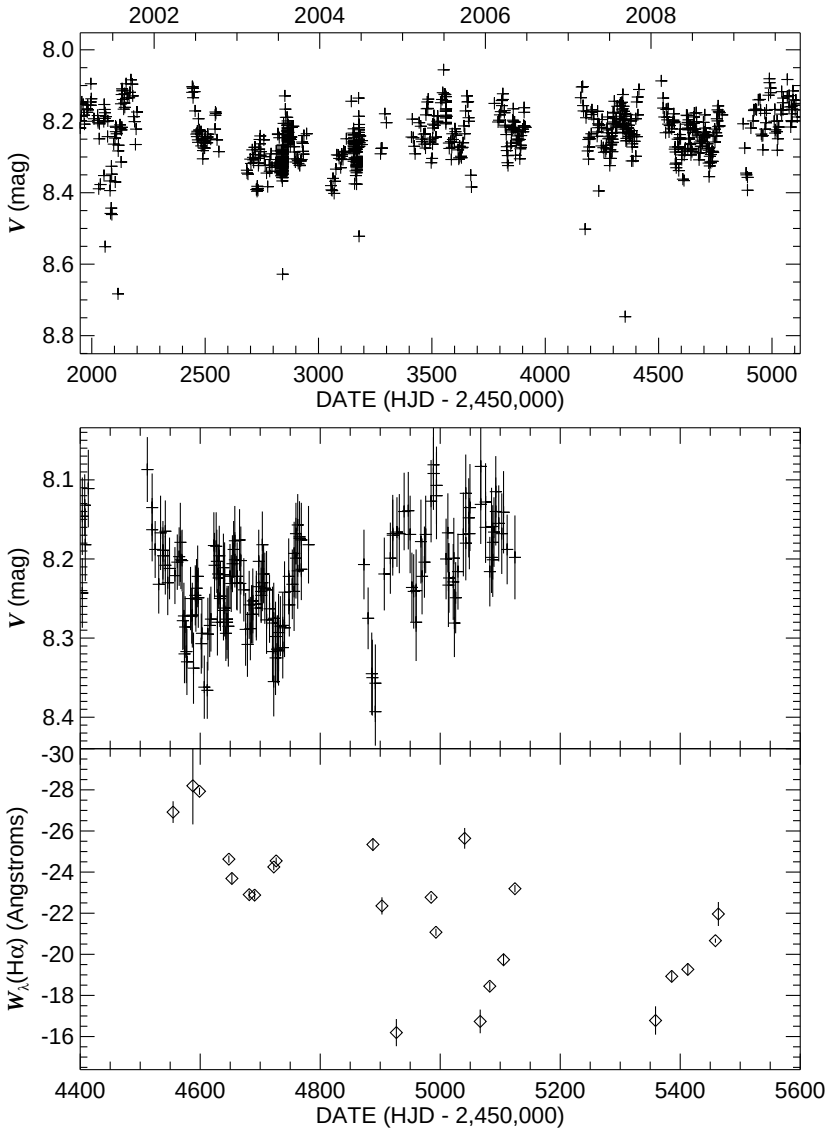

Figure 6.45 Photometry and Hα equivalent width variability of HD 168607. The top panel shows a historical V-band light curve, as observed by the All Sky Automated Survey (Pojmanski 2002), while the bottom two panels show the photometry and Hα equivalent width behavior during the course of the survey.

6.4.12 HD 168625

HD 168625 is often examined in the same studies as HD 168607, due to their spatial closeness in the sky. However, the star has remained classified as an LBV candidate only because the long-term LBV variability has never been observed. Despite more than 25 years of available photometry (van Genderen et al. 1992; Sterken et al. 1999), this star has not shown the S Doradus-phases or the changes typical of LBVs. It has, however, shown the typical α Cygni variations, which are attributed to pulsations of the photospheres for hot supergiants. Our observations show that the Hα profile is the weakest (on average) of all the observed Galactic LBVs in our survey (Fig. 6.1).

HD 168625 is an interesting target for another reason. Smith (2007) found a bipolar ring nebula surrounding the star that appears morphologically similar to the nebulosity that now reflects the light echo of SN 1987A in the LMC. The unusual supernova in the LMC taught us that blue supergiants are potential supernova progenitors and that a star does not need to necessarily go through a red supergiant phase in the late stages of massive star evolution.

Our observations of the Hα profile of HD 168625 (Fig. 6.46 and 6.47) show a very weak profile that changes between a P Cygni type appearance and pure emission (at our spectral resolution). The strength of the profile does not vary much, and the minor changes in strength are more due to the changes in the P Cygni absorption. In the red wing of the profile, the C II absorption doublet is consistently present. This feature has only been seen in one other LBV in this work, P Cygni (Chapter 2), but in the spectrum of P Cygni the features are P Cygni profiles, and are so weak in comparison to Hα that they were excluded from the Hα analysis. The equivalent width measurements (Figure 6.48) included this feature, but the strength of the C II doublet is nearly constant and has little affect on the variability observed.

The changes in the strength of Hα for HD 168625 show no clear pattern in this dataset.

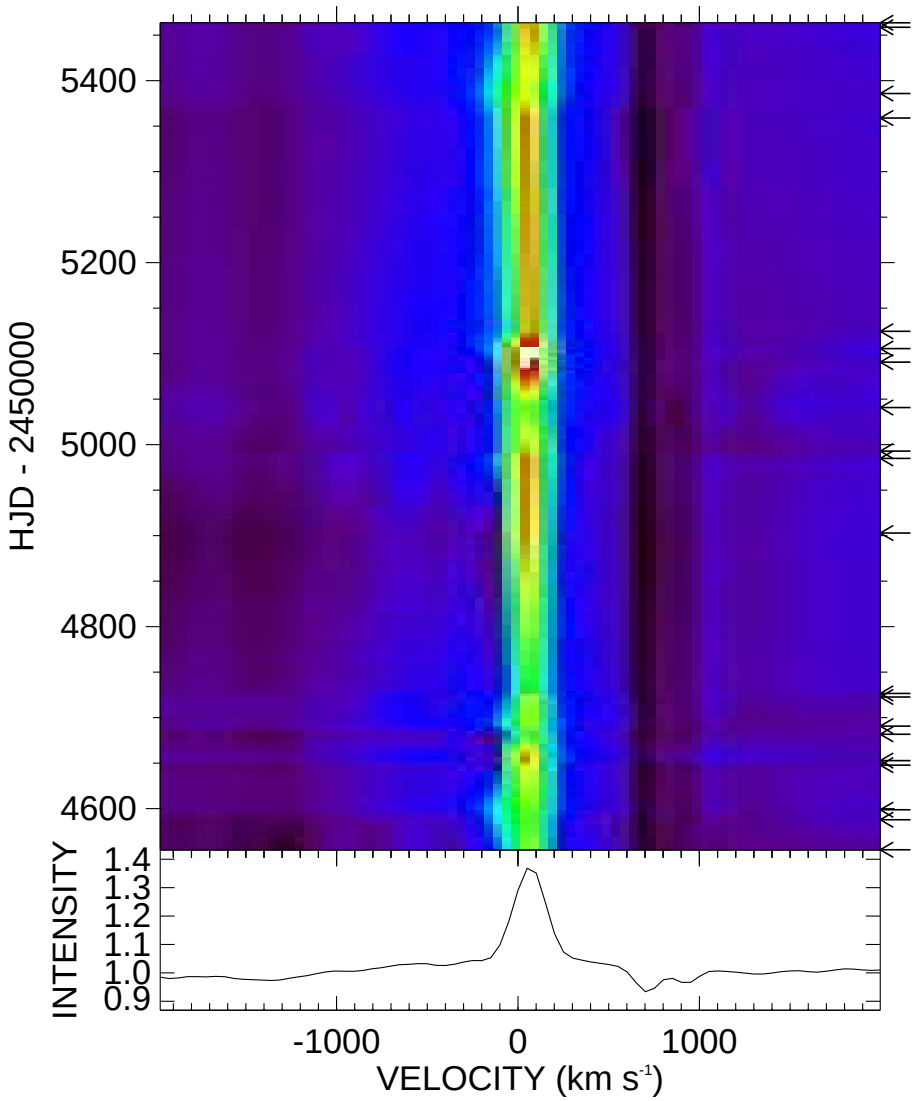

Figure 6.46 Dynamical representation of the Hα profile of HD 168625. Color version available in electronic edition.

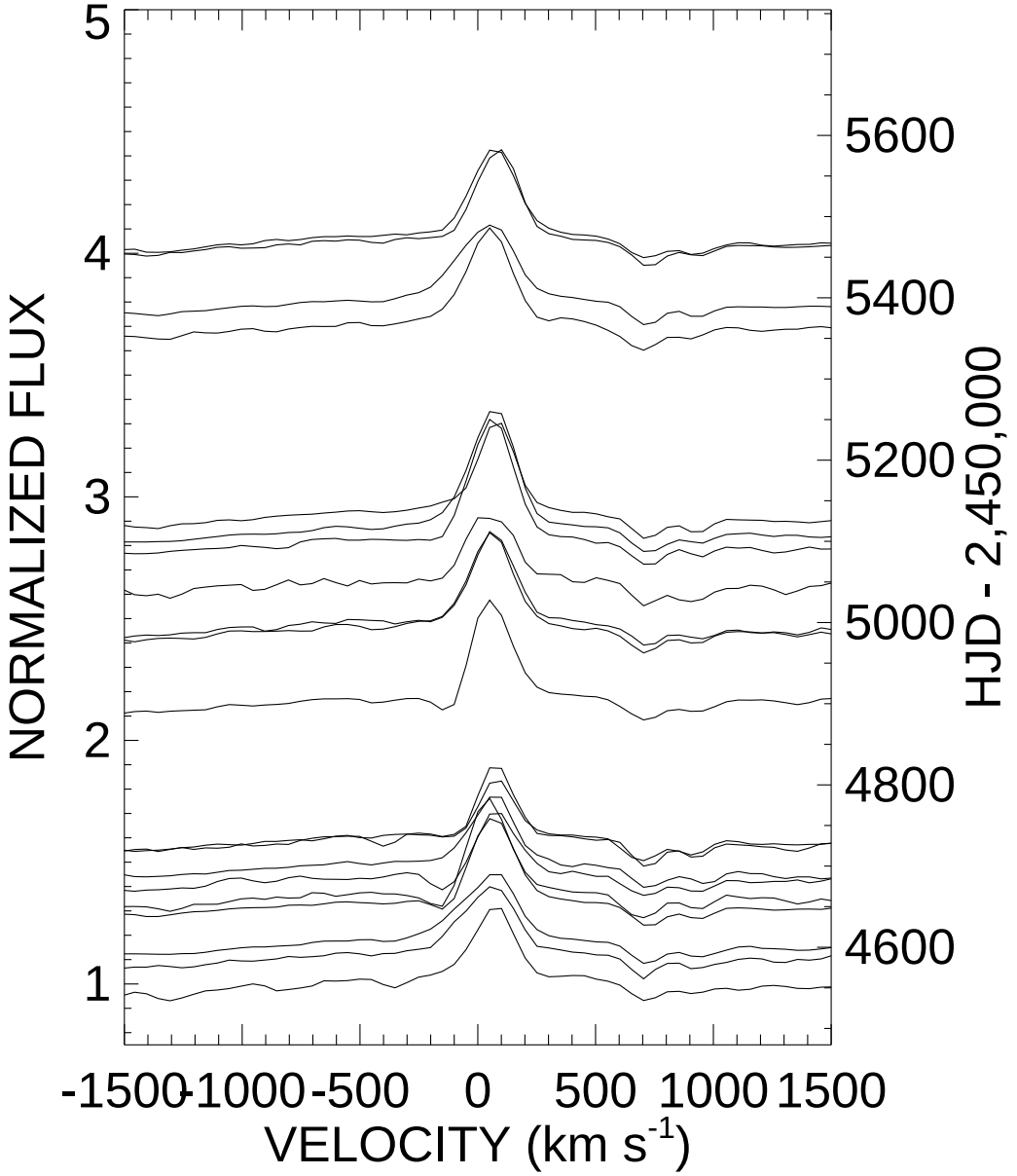

Figure 6.47 Line plots of the Hα profile of HD 168625.

This is similar to other variability studies of this star (van Genderen et al. 1992; Sterken et al. 1999). These data cannot confirm the LBV nature of HD 168625, but the stellar variability is different in that there are no obvious long-term trends, than that of the nearby HD 168607, whose LBV nature is secure.

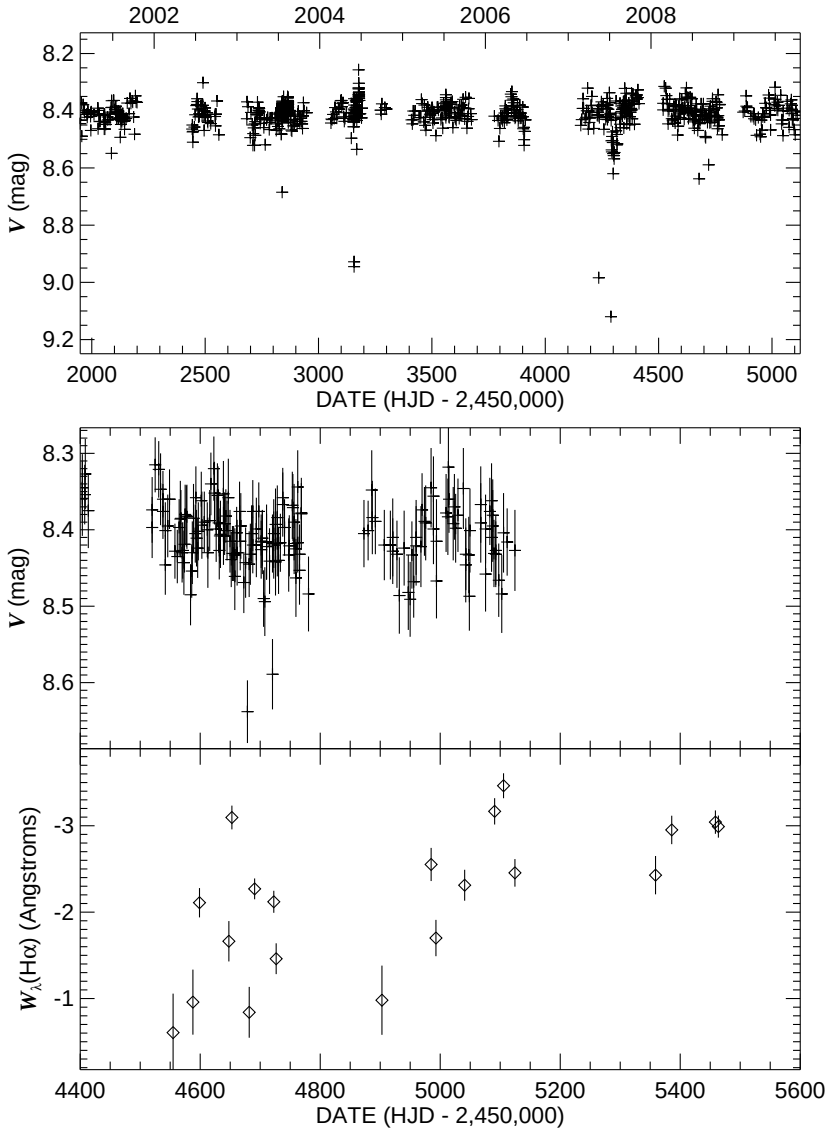

Figure 6.48 Photometry and Hα equivalent width variability of HD 168625. The top panel shows a historical V-band light curve, as observed by the All Sky Automated Survey (Pojmanski 2002), while the bottom two panels show the photometry and Hα equivalent width behavior during the course of the survey.

6.4.13 V452 Sct = AS 314

AS 314 is a candidate LBV that was analyzed by Miroshnichenko et al. (2000). The star has been classified as an A type supergiant and as a Be star (Venn et al. 1998). It was also considered a Be star in the photometric analysis of Kozok (1985). The best analysis is the recent work of Miroshnichenko et al. (2000) who find that the Hα line is a narrow P Cygni type profile. They also found that the star had a variable V magnitude, with an amplitude of 0.25 mag over the course of their observations.

The star has a relatively high galactic latitude of $-3.^{\circ}6$, and when compared to other stars of similar spectral type, Chentsov et al. (2003) speculate that this could be a runaway star or a low-mass post-AGB star (based on spectral similarity to the post-AGB star LS 3591). The radial velocity of AS 314 is ≈ -55 km s^{-1}, while the nearby ($< 4^{\circ}$ difference in galactic longitude) LBVs HD 168607 and HD 168625 have a velocity near +10 km s^{-1} (Chentsov et al. 2003).

Our observations of the Hα profile span three years, but this target was removed from the program for one year due to limited telescope time in the 2008B and 2009A observing semesters at CTIO. The Hα profiles are shown in Figures 6.49 and 6.50. The profile was fairly constant, although the last observed profiles had a P Cygni absorption, and the profile appeared as a pure emission profile in early observations (at this spectral resolution).

The equivalent width of Hα varied by less than a factor of two over the course of the survey (Fig. 6.51). This suggests that if the star is an LBV, it belongs to the "weak-active" subcategory of LBVs. The He I lines are too weak to analyze.

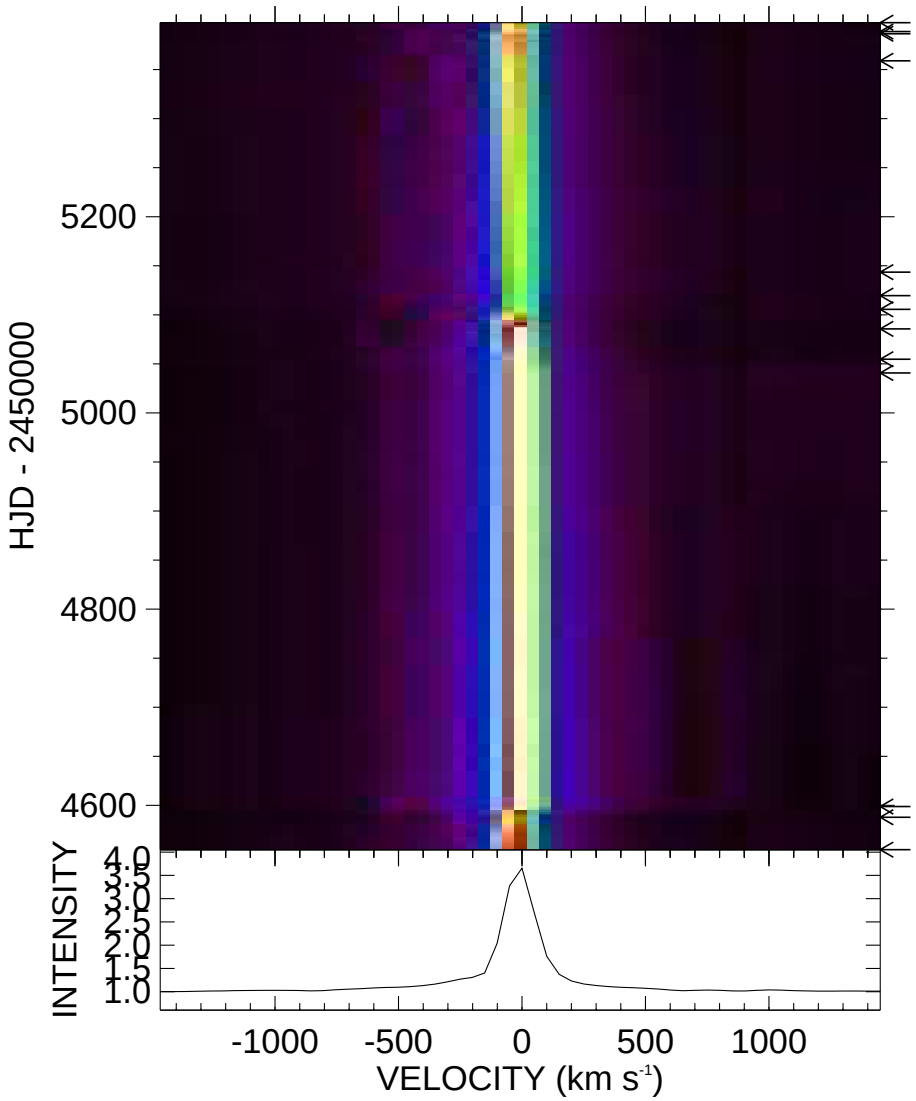

Figure 6.49 Dynamical representation of the observed Hα profiles of AS 314 from the CTIO 1.5 m telescope and R-C spectrograph. Color version available in electronic edition.

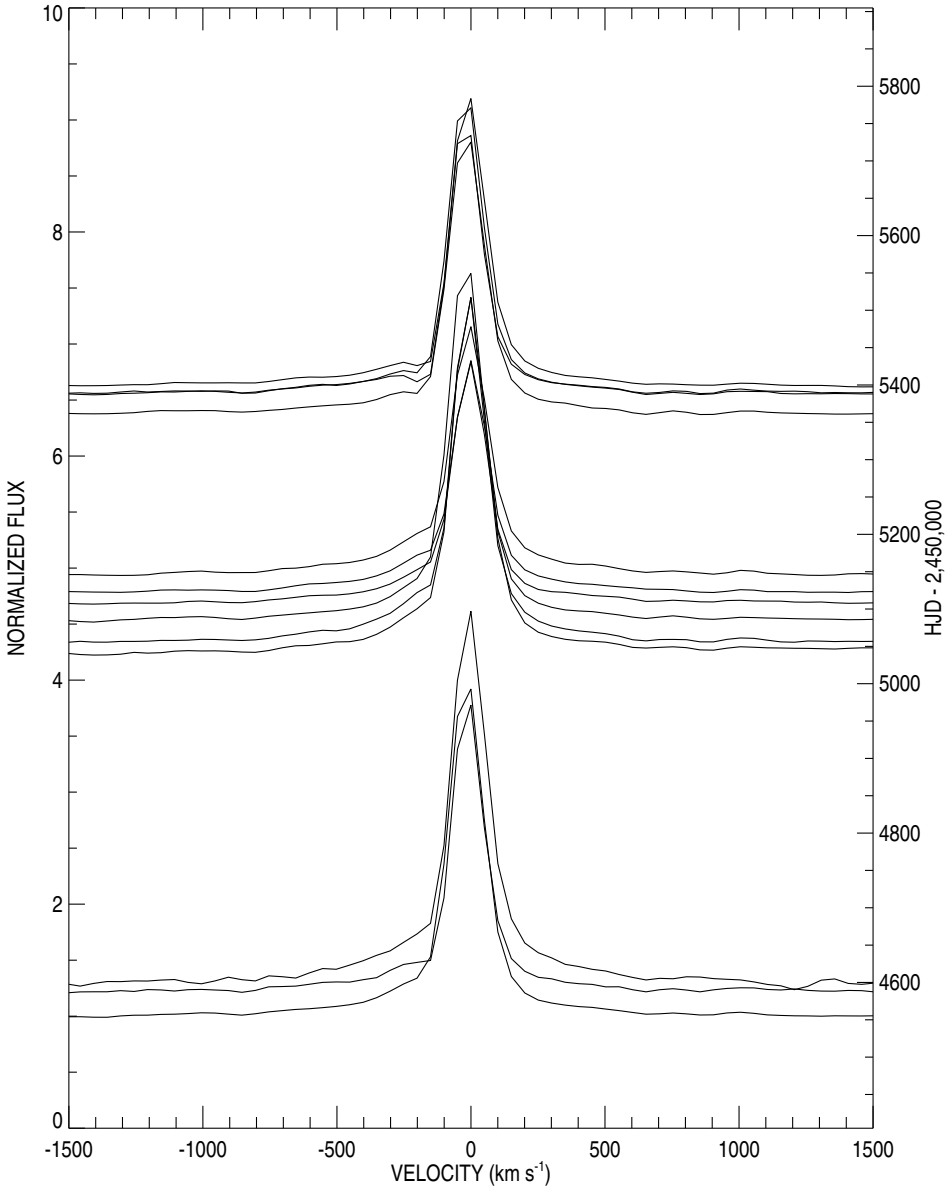

Figure 6.50 Line plots of the observed Hα profiles of AS 314 from the CTIO 1.5 m telescope and R-C spectrograph.

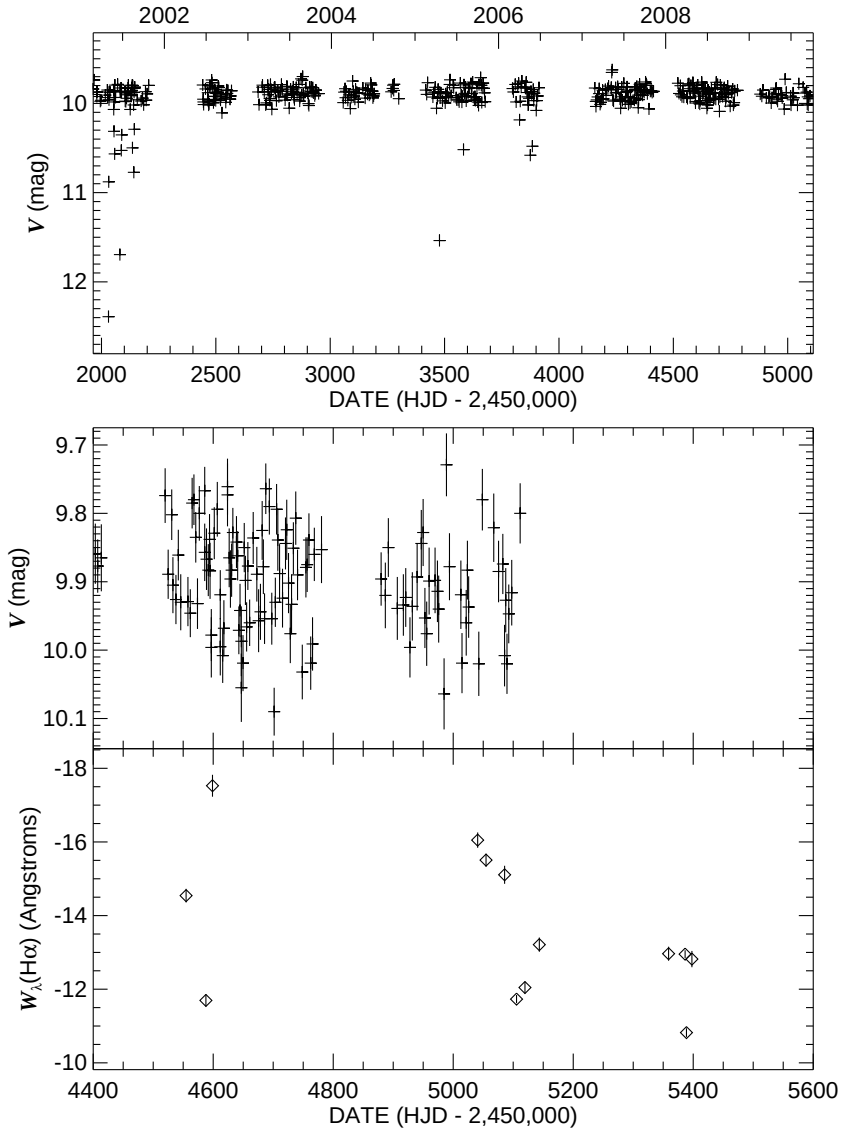

Figure 6.51 Photometry and Hα equivalent width variability of AS 314. The top panel shows a historical V-band light curve, as observed by the All Sky Automated Survey (Pojmanski 2002), while the bottom two panels show the photometry and Hα equivalent width behavior during the course of the survey.

6.5 STARS CROSSING THE BISTABILITY JUMP

The vast range of observed temperatures for LBVs implies that they are great laboratories for observing how a star crosses the so-called bistability jump (that occurs near $T_{\rm eff} = 21,000$ K). This is a physical consequence of a change in stellar temperature and wind ionization (Fe IV $\leftrightarrow$ Fe III) that in turn causes a change in the ratio of the wind terminal velocity to the escape velocity (Vink et al. 2000; Groh & Vink 2011). The changes in the stellar photospheric ionization cause the line-driven wind to have different amounts of driving force on either side of this point. For stars on the hot side of the bistability jump (near spectral type B1, Vink et al. (2000)), the terminal velocity is on order of

$$v_\infty \simeq 2.6 v_{\rm esc}.$$

When the star is cooler, the terminal velocity follows

$$v_\infty \simeq 1.3 v_{\rm esc}.$$

Some LBVs experience temperature variations that cross this jump. For example, R 127 has remarkable changes in its spectrum near the end of our campaign, where the He I lines went from nearly unobservable to extremely strong emission on a short time scale (Fig. 6.23). This was also seen with AG Car (Fig. 6.33). Further analysis of the light curve and with modeling of the spectra could prove that these stars crossed this temperature. Such confirmation would allow for these He I lines to be used as a probe of the stellar properties.

The P Cygni absorption component of wind lines such as Hα and Hβ are sometimes observed to have double absorption components for LBVs near the bistability jump (Groh & Vink 2011). Groh & Vink propose that the bi-stability jump and the abrupt changes in the stellar wind associated with the stellar effective temperature crossing this boundary

cause these two components to relate to the terminal velocity observed on either side of the bi-stability jump due to longer flow times in the winds of these stars compared to other hot star winds.

6.6 ON THE VARIABILITY OF THE POPULATION

Several questions remain to be answered in the field of LBV winds. The first question to ask is related to the luminosities of these stars. What minimum luminosity must a star have to be a *luminous* blue variable? HD 168607 and HD 168625 present interesting cases that may help answer that question. They are both in the same cluster, and so have similar ages and luminosities (Chentsov & Gorda 2004). The slightly brighter (and hence, more luminous) star HD 168607 meets the LBV criteria both from my work and others (van Genderen et al. 1992; Sterken et al. 1999), while these same studies do not show that large amplitude variability exists for the star HD 168625. Indeed, HD 168625 is the least variabile star observed in our sample. HD 168625 is 0.2 magnitudes fainter in V (from the SIMBAD database). Could this be a transitionary region in the HR Diagram, where the stars more luminous than HD 168625 are subject to the instability(ies) that cause the S Doradus phases and the typical behavior of the LBVs?

The second major question raised in this study is that of the types of variability observed: why are some stars largely variable with others nearly constant? We show in Table 6.3 the mean, minimum, and maximum equivalent width of the Hα profile for each target star. We also show a quantity, E/I, that represents the standard deviation of the equivalent widths divided by the mean of the associated errors in the equivalent width. If this quantity is near unity, the star is not variable, while a large number represents large variability. S Dor shows the largest variability, while HD 168625 shows the least. Further, all of our data have comparable S/N, which is the largest source of error in the measurement of the equivalent widths, implying that I is nearly constant across our sample.

Table 6.3 Hα Equivalent Width Summary

LBV	Mean(W_λ(Hα))	Max(W_λ(Hα))	Min(W_λ(Hα))	E/I
R 40	-6.90	-2.95	-10.11	10.6
R 85	-12.13	-8.87	-15.65	8.8
S Dor	-186.14	-51.17	-434.34	234.5
R 110	-20.92	-15.80	-25.81	11.3
R 127	-95.67	-64.35	-153.43	30.5
HR Car	-73.68	-58.98	-91.72	15.8
AG Car	-72.04	-49.58	-117.07	39.8
Wra 751	-16.63	-6.18	-32.91	20.3
ζ^1 Sco	-9.06	-5.01	-12.28	6.3
HD 160529	-4.84	-1.07	-7.98	9.5
HD 168607	-22.29	-16.19	-28.20	9.2
HD 168625	-2.16	-0.61	-3.46	4.5
AS 314	-13.61	-10.82	-17.53	10.8
P Cygni	-83.8	-67.8	-103.0	17.3

It is interesting to compare the mean equivalent width with the derived quantity E/I. This is plotted in Figure 6.52. There is a trend that emerges from this comparison, that can be fit with the relation

$$\log(E/I) = (0.365 \pm 0.18) + (0.61 \pm 0.13) \times \log(-W_\lambda).$$

All observed stars follow this relationship and trend. There is scatter, which is likely from intrinsic differences in the actual variability of these stars. This trend is also true for both "strong-active" and "weak-active" members of the LBV class, implying that there is no major difference between these differently classified LBVs.

Recently, Clark et al. (2012) presented a study of blue hypergiants, and found that the LBV candidates such as ζ^1 Sco, are typical blue hypergiants that have activity more like typical hot supergiants but are more luminous than the hot supergiants. These authors

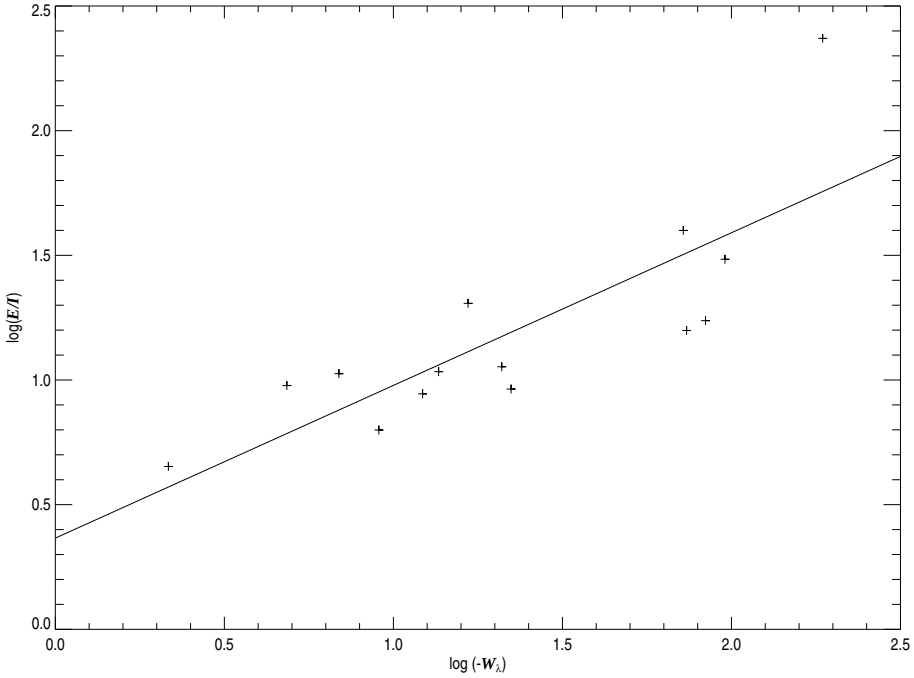

Figure 6.52 W_λ compared to E/I for our sample stars. The best fit of these data is shown overplotted.

suggest that the following type of post-main sequence evolution happens for massive stars.

$$\sim 60 - 120 M_\odot : \text{OIa} \rightarrow \text{OIaf}^+ \rightarrow \text{WNL} + \text{abs} \rightarrow \text{WN7}.$$

$$\sim 30 - 60 M_\odot : \text{O/BIa} \rightarrow \text{WN9} \leftrightharpoons \text{LBV} \rightarrow \text{WN8} \rightarrow \text{WN/C}.$$

$$\sim 30 - 40 M_\odot : \text{O} \rightarrow \text{OBIa} \rightarrow \text{BlueHG} \rightarrow \text{WN} \rightarrow \text{WC}.$$

This evolutionary scenario leads to the possibility that blue hypergiants co-habitate the upper HR diagram and that the candidate LBVs may actually be hypergiants and vice versa. This implies that three populations of stars lie in the same region of the H-R diagram: LBVs, BHGs, and the B[e] stars (e.g., Miroshnichenko 2006). The B[e] stars are stars of spectral type B that show forbidden line emission. If ζ^1 Scorpii is a BHG and not an LBV, then

the fact that it follows the E/I vs. $-W_\lambda$ relationship may indicate that both types of stars follow similar trends. If that is true, more stars need to be placed on this plot, so that a cutoff value for these measurements can be made for distinction.

This variability criterion may be able to be further exploited in the future. A few spectra of an object ($\sim$ 2 yr^{-1} for three years) may be able to totally qualify if an object experiences LBV-type instabilities, as the emerging definition of an LBV is based upon the S Doradus phases (either long and/or short), and the giant eruptions are no longer required for membership in this class of object. This could be achieved with large telescopes, despite large over-subscriptions. Then, the LBV-type stars can be observed to answer the physical questions related to their driving mechanisms. Further, quantification of a variability relationship with spectral lines in the NIR would allow for all candidate LBVs that are highly attenuated in the Galactic plane to be confirmed.

6.7 FUTURE WORK – WHICH LBVS ARE THE BEST TO OBSERVE AND WHY?

There is much variety in the LBV class, which implies that there may be multiple physical processes that drive the variability. In this dissertation, we have been mainly interested in the driving mechanisms for the long term trends seen in LBVs. The ultimate questions are:

- What causes the long term variability that can change the spectral type (and temperature) of the LBVs?
- How do the S Doradus phases relate to the giant eruptions, or are they related at all?

In order to answer either of these questions, there are several observational challenges in the future. The relationship between eruptions and SD-phases can only be explored if we have more observations of eruptions, i.e., for example, LBV eruptions observed in other galaxies that are detected through modern supernovae surveys.

Theoretical studies of LBVs are sparse, but some accomplishments should be highlighted. It has been thought that LBVs may have pseudo-photospheres in their winds induced by a dramatic increase in the star's mass loss rate. de Koter et al. (1996) demonstrated that the pseudo-photosphere is not a valid hypothesis, and that the underlying changes in radius and temperature must be caused below the stellar atmosphere. Furthermore, Stothers (2002) predicted that the difference between LBVs and the purely radiatively unstable WR stars is that the LBVs suffer a dynamical instability that causes secular changes in mass loss. Abolmasov (2011) showed that the variability amplitude of LBVs follows a power law when analyzed over multiple timescales. In addition, the flux variations are correlated for decades, which is longer than a "refreshment rate" for a pseudo-photosphere. This all implies that the driving mechanisms are in the stellar interiors, which are difficult to study when no atmospheric lines are present in the observed spectrum to probe the pulsational properties of the photosphere.

Photometric surveys such as the All Sky Automated Survey (Pojmanski 2002) or the planned Large Synoptic Survey Telescope[3] (LSST) will be crucial for monitoring bright and faint targets, respectively. These surveys will find candidate LBVs that are variable in the stochastic, large amplitude fashion. However, the light curves of LBVs such as P Cygni (which do not vary by more than a few tenths of magnitudes) may be missed entirely because the light curves such as those of HR Car or AG Car (Fig. 6.26 and 6.31) are more spectacular and easily found than those of stars such as P Cygni (Fig 2.2).

Spectroscopy of the confirmed and new candidate stars will be necessary to determine if the stars are really LBVs. Suspected candidates such as HDE 326823 (Chapter 5) may not prove to be bona fide LBVs when variability studies are performed. The most important targets for understanding the driving mechanisms for the long term variability are the targets that display the largest amplitudes in $\triangle T_{\rm eff}$ (= color variation, $\triangle(B-V)$), hence $\triangle V$.

[3]http://www.lsst.org

Therefore, the new stars found with these surveys will enlighten us on the LBV physics by providing probes for stars at very different effective temperatures, as well as an idea of how these stars change through this process.

Bright stars are also crucial. Small telescope time is often simpler to obtain, and long term projects will be more difficult with large (> 4 m class) telescopes due the demands of the entire astronomical community. Therefore, spectroscopic studies such as those done on P Cygni (Chapter 2) or η Carinae (Chapter 4) will allow more specific investigations of wind processes. The echelle spectroscopy of P Cygni (Chapter 2) also includes the transition of He I 5876, which can be analyzed for wind properties closer to the star once additional calibrations are performed[4]. Telescopes of the 0.5–1.5 m class will easily be able to study such processes.

S Doradus and R 127 stand out in the LMC with their remarkable variability. We have upcoming HST time to study the current ultraviolet portion of the spectrum of S Dor, which is being accompanied by optical monitoring at CTIO (both spectra with the RC Spectrograph, as well as the echelle spectrograph) and by amateur astronomers. R 127 continues to be studied by Nolan Walborn and his collaborators.

The SMC has few LBVs. The two most notable (perhaps only) SMC LBVs are HD 5980 and R 40. Both are certainly LBVs, but the HD 5980 system is extremely unusual. It is a binary with a short 19 d period (Koenigsberger et al. 2010). The secondary star is a Wolf Rayet star, and the system has strong interactions as the winds collide. There was a short outburst like a great eruption in the last 15 years, but the time period for the outburst was short. Indeed, Koenigsberger et al. (2010) believe that the close orbit prohibits the large optically thick wind atmosphere of the LBV-like star from developing, so that both stars appear as Wolf Rayet stars. The other star, R 40, offers clues to the physics of radiation driven winds at extremely low metallicity.

[4]Issues with wavelength calibration need to be fixed first, which is currently underway

Our own Galaxy may offer many exquisite examples of LBVs to study, but we are limited by the Galactic Plane. Interstellar extinction blocks many of these stars from our sight. LSST may overcome some of this by probing the faint optical stars of our Galaxy, but it is unknown how many of these systems may be discovered. Indeed, Shara et al. (2009) and Shara et al. (2011) have found 113 new Wolf-Rayet stars. LBVs reside in a similar color-color space as these WR stars, and such surveys may discover tens or hundreds of new LBVs. The six brightest LBVs without strong binary effects that warrant long-term studies with photometry, low and high resolution spectroscopy, and potentially interferometry are P Cygni, HR Carinae, AG Carinae, WRA 751, HD 160529, and HD 168607. Only P Cygni and perhaps HD 168607 are easily observed by northern observers, meaning that instrumentation and monitoring will require the help of southern observers.

Binary stars offer probes into the physics of the LBVs in different ways. They can change the ionization balance, cause Roche lobe overflow, and create tidally focused winds. The two most important members of this class are η Carinae and HD 5980. However, other stars such as R 81 (HDE 269128, Tubbesing et al. 2002) and MWC 314 (Lobel et al. 2011) may also provide insights into the interactions between an LBV and a companion. However, the LBV nature of both HD 269128 and MWC 314 remains to be fully established.

7
FUTURE WORK

The work started in this dissertation allows for numerous future studies with these massive, windy stars. Here I will outline some of the potential projects.

7.1 SPECTROSCOPY OF MASSIVE STELLAR WINDS AT HARD LABOR CREEK OBSERVATORY

A number of new instruments have been installed at Georgia State University's Hard Labor Creek Observatory (HLCO) in recent years. This included two new telescopes and new instrumentation for these telescopes. Note that the 24 inch PlaneWave Telescope will be installed in the near future. The 20 inch RC Optical Systems telescope[1] was commissioned with an LHIRES III Spectrograph[2]. I led an investigation with GSU undergraduate student Emily Aldoretta during the summer of 2011 to determine the limitations of this instrument. Naturally, I chose to examine some massive stars with winds. In Figure 7.1, I show four spectra of LBVs that were also included in the variability studies earlier in this dissertation. The quality of the spectra shows promise for future studies. Long-term studies of the Hα profile of the LBVs HD 160529 and HDE 316285 will be easily accomplished given sufficient observational effort.

In addition, we obtained spectra of three Wolf Rayet (WR) stars in the constellation Cygnus during this commissioning time. These spectra are shown in Figure 7.2. The emission line profiles in WR spectra show temporal variations that are probably the result of clumping in their winds (Lefèvre et al. 2005). Campaigns that involve multiple telescopes across the globe are needed to make long, uninterrupted time series observations and to determine the extent of clumping. Plans for such campaigns are underway (Thomas Eversberg, private comm.) for stars such as WR 137. HLCO will be an ideal location for such studies, because

[1] http://www.chara.gsu.edu/HLCO/RC20/
[2] http://astrosurf.com/thizy/lhires3/index-en.html

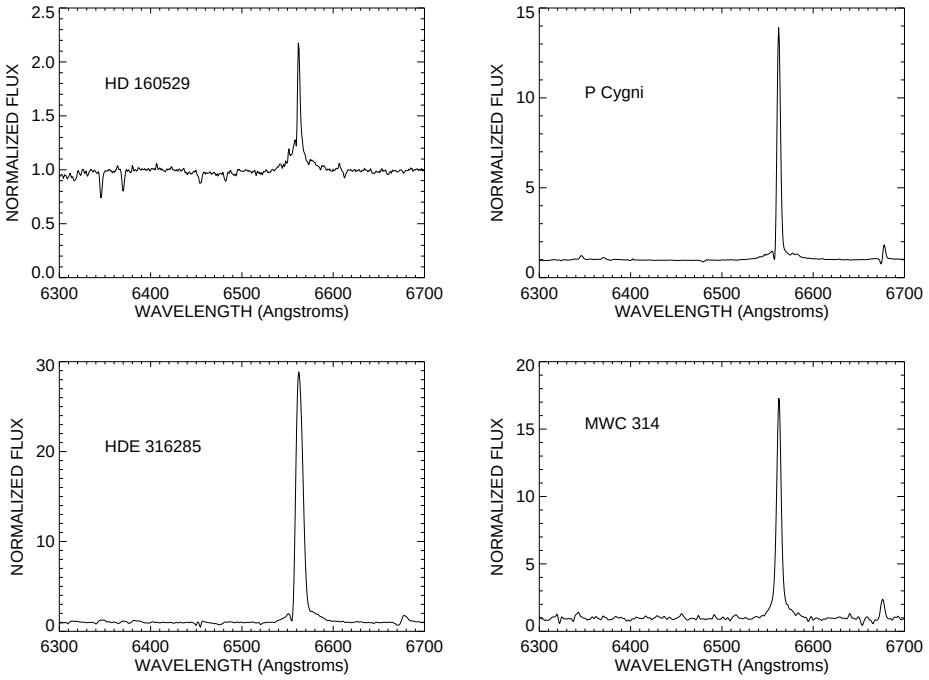

Figure 7.1 Four example spectra of LBVs from HLCO. These data were obtained with a 600 grooves mm^{-1} yielding a resolution of $R \sim 3000$. The fainter two stars, HDE 316285 and MWC 314, were smoothed over 2 and 3 pixels for clarity.

many contributors to such campaigns are amateur astronomers in Europe, and the physical location of HLCO would allow for much more temporal coverage.

It is notable that the spectrum of WR 140 is of extremely high quality. This star system consists of a massive WR and O star, and is a prototype for the class of colliding wind binaries. The orbit was recently determined interferometrically (Monnier et al. 2011), which yields masses of $M_{\rm WR} = 14.9 M_{\odot}$ and $M_{\rm O} = 35.9 M_{\odot}$, and this result shows how much mass must be lost for a massive star to lose its H envelope and become a WR star. In addition, the highly eccentric orbit allows observers to probe changes in the wind-wind collision zone (Fahed et al. 2011). The spectrum of WR 140 (Fig. 7.2 and 7.3) shows that with a modest 20 minute exposure time, we can detect evidence of the WR star (strong emission lines) and the O star companion (absorption lines).

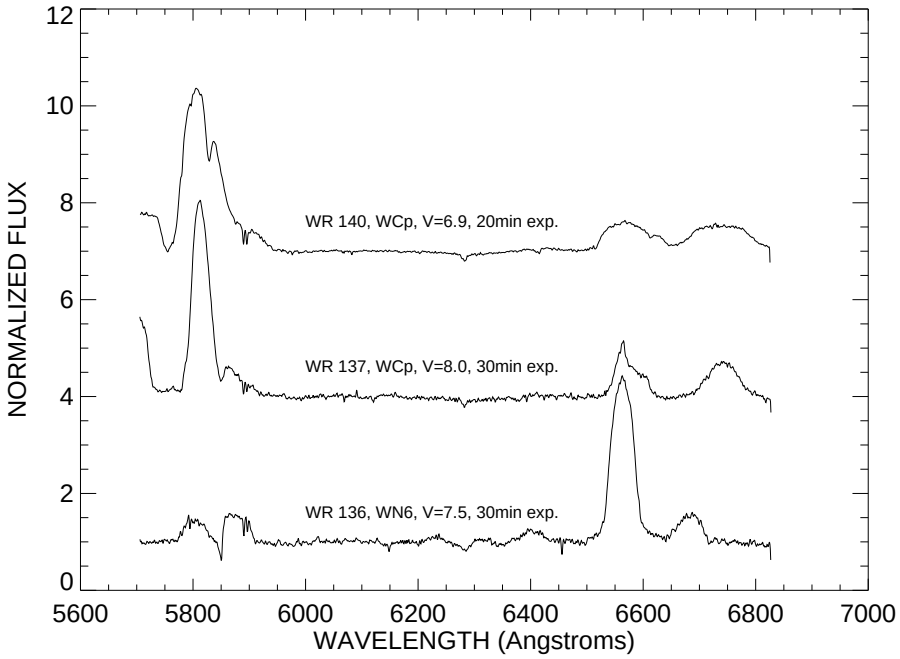

Figure 7.2 Three example spectra of WR stars from HLCO. These data were obtained with a 600 grooves mm^{-1} grating ($R \sim 3000$). Exposure times, V magnitudes, and spectral types from SIMBAD are given.

These spectra show that HLCO will be able to contribute to stellar wind observations both through long-term monitoring and intensive short-term monitoring campaigns. There is great potential here for many undergraduate research projects and components of future graduate student theses and dissertations.

7.2 INTERFEROMETRIC WORK

Chapter 3 detailed some of the interferometric work started during the course of this dissertation. P Cygni remains an ideal target for interferometric imaging, particularly in conjunction with near-contemporaneous NIR spectrophotometry, to determine if the circumstellar environment changes.

Other important targets for stellar wind studies are the bright, hot supergiants in Orion

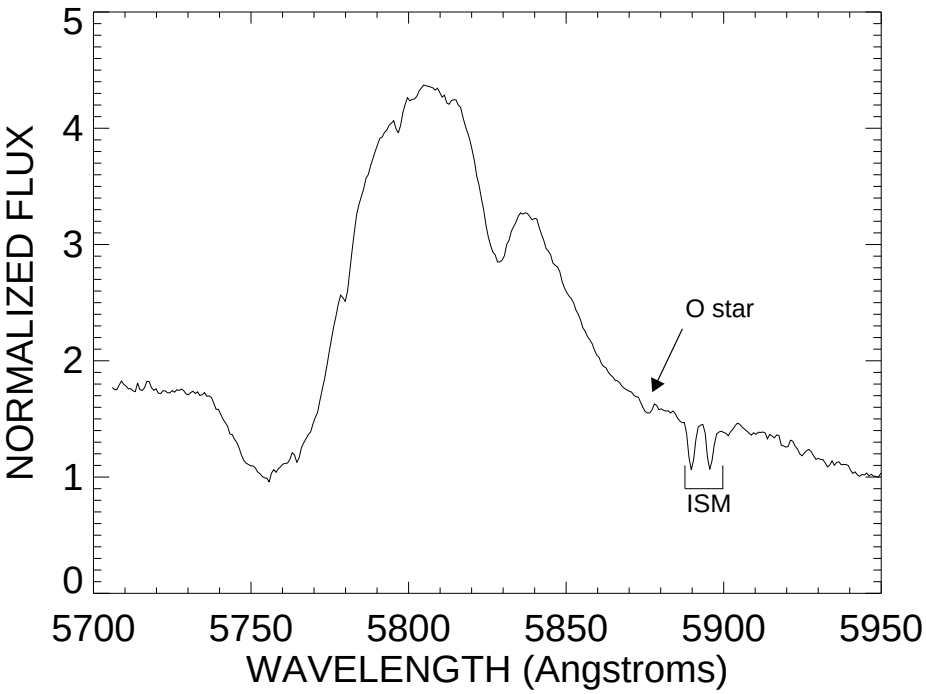

Figure 7.3 A zoom in on the C IV $\lambda\lambda$ 5802, 5812 and He I λ 5876 emission complex in the spectrum of WR 140, obtained at HLCO. Three narrow absorption features are present, including one from the O star, and two from the interstellar Na D doublet (marked ISM).

(Rigel, ϵ Ori, ζ Ori A, and κ Ori). A preliminary analysis of the interferometric diameters and spectrophotometry has already shown that the wind of ϵ Orionis has nearly the same temperature as the stellar photosphere. Such observations can help place constraints on stellar wind theory and the extent of wind clumping.

I began an interferometric survey of O and B star diameters with the CHARA Array and the new combiner PAVO. The stellar diameters are small (typically $\lesssim$ 0.5 mas), so their measurement was only possible thanks to the sensitivity of PAVO and the improved angular resolution in the red portion of the optical spectrum (0.6–0.85 μm). Unfortunately, the full reduction of these data has not yet been completed. Many of these observations were obtained with three telescopes simultaneously. The instrumental polarization features are not fully calibrated out in the pipeline yet, but the pipeline is now beginning to make

excellent measurements of the squared visibilities with two telescope data.

P Cygni and the Orion supergiants are ideal targets for PAVO. The wavelength channels would allow for a direct measurement of the emitting region size across that portion of the spectrum. In late 2011, PAVO data were collected on P Cygni with optical choppers in the beam to allow better flux measurements from the beams. This should allow for excellent calibration, but the addition of these choppers also means that the reduction has not been done yet because further software is needed.

Many of these projects suffered from bad weather during my runs with the CHARA Array. After my first PAVO run (with three good nights), I obtained less than five more nights total spread across six observing runs when the weather and seeing conditions allowed me to obtain data. These data are awaiting a fully functional reduction pipeline to complete this work. The instrument specialists at the University of Sydney are continually building and improving the reduction pipeline, which should be completed in the near future.

7.3 LUMINOUS BLUE VARIABLES

With the advent of major cosmological surveys searching for supernovae, the pre-supernova properties and circumstellar environments of LBVs are becoming extremely crucial to the understanding of core collapse supernovae. The in-depth study of P Cygni, presented in Chapter 2, presents a long term probe into the changes that are happening with this star. The Hα line studied in this dissertation is only one optical line transition, and more clues to the physical changes can be found by studying more transitions. The camera at Ritter Observatory also records the Na D complex (both emission and absorption components) and He I λ 5876 line that provide clues about the wind at different physical radii. Once some wavelength calibration issues with this region are resolved, we can begin a study of these lines to sample the wind at different radii. The discovery of Hα DACs is new, and their properties are different from those in other stars and wind lines. Do DACs exist in the Hα

profile of other LBVs?

The enigmatic binary η Carinae will be a mystery for a long time, but continued monitoring of this "prototypical" object will reveal the true cause(s) of its variability. It seems to have major changes approximately every 50 years – a great eruption in 1840s; second eruption 1890s; first spectroscopic events (where the high excitation lines fade near periastron) in the 1940s (see Humphreys & Koppelman 2005); and the start of a mass-loss rate decrease in the 1990s (see Mehner 2011). Detailed high spectral and temporal resolution studies are important to our understanding, but such work can only be done with queue scheduling on small telescopes. Larger ground and space based telescopes are in too high demand to observe this object with sufficient cadence.

It is necessary to consider the entire *population* in addition to detailed studies on *individual members* of the class. This is difficult. Many Galactic LBVs are highly attenuated by dust in the Galactic Plane due to their large distances. While the optical study (Chapter 6) is an excellent start, an observational bridge needs to be built to understand the whole population, through combined multi-wavelength observations.

High resolution, multi-epoch spectroscopy of these stars will be the best option for determining their multiplicity. While I have collected some data with high angular resolution techniques with the Fine Guidance Sensors on the Hubble Space Telescope, these data are difficult to use detect all binaries, because the FGS is only sensitive to bright LBVs with wide and bright companions. We have confirmed through spectroscopy that HD 5980, HD 269128, MWC 314, and η Carinae are binaries. How much does a companion influence the evolution of these stars? Are companions responsible for great eruptions, as suggested by Smith & Frew (2010) for η Car, or do they only further complicate our understanding of the population? Surveys, such as the All Sky Automated Survey and the Large Synoptic Survey Telescope (coming soon) will provide high quality light curves for most of the LBV population. Spectroscopic studies accompanying these forthcoming data will be necessary

to determine the fundamental stellar properties and to understand how these objects enrich the interstellar medium through winds and eruptions. Such studies may even provide the necessary clues for understanding the physics of the eruptions and variable winds.

The next several years will be exciting for the research of LBVs. LSST will be able to study the optical variability of highly attenuated LBVs across the southern Galactic plane, allowing a much more detailed optical photometric survey of LBVs than previously accomplished. The H-R Diagram will be updated with the upcoming Gaia mission, which will accurately determine distances (and luminosities) for the bright LBVs, such as those studied in the survey mentioned in Chapter 6.

References

Abolmasov, P. 2011, New A, 16, 421

Balan, A., Tycner, C., Zavala, R. T., Benson, J. A., Hutter, D. J., & Templeton, M. 2010, AJ

Bond, H. E., & Landolt, A. U. 1970, PASP, 82, 313

Borges Fernandes, M., de Araújo, F. X., Bastos Pereira, C., & Codina Landaberry, S. J. 2001, ApJS, 136, 747

Castor, J. I., Abbott, D. C., & Klein, R. I. 1975, ApJ, 195, 157

Chentsov, E. L. 1980, Soviet Astronomy Letters, 6, 199

Chentsov, E. L., Ermakov, S. V., Klochkova, V. G., Panchuk, V. E., Bjorkman, K. S., & Miroshnichenko, A. S. 2003, A&A, 397, 1035

Chentsov, E. L., & Gorda, E. S. 2004, Astronomy Letters, 30, 461

Chentsov, E. L., & Musaev, F. A. 1996, Astronomy Letters, 22, 589

Cioni, M.-R. L. 2009, A&A, 506, 1137

Clark, J. S., Larionov, V. M., & Arkharov, A. 2005, A&A, 435, 239

Clark, J. S., Najarro, F., Negueruela, I., Ritchie, B. W., Urbaneja, M. A., & Howarth, I. D. 2012, ArXiv e-prints

Clemens, D. P., Sarcia, D., Grabau, A., Tollestrup, E. V., Buie, M. W., Dunham, E., & Taylor, B. 2007, PASP

Corcoran, M. F. 2005, AJ, 129, 2018

Cranmer, S., & Owocki, S. 1996, ApJ

Crowther, P. A., Lennon, D. J., & Walborn, N. R. 2006, A&A, 446, 279

Crowther, P. A., & Willis, A. J. 1994, in Evolution of Massive Stars, ed. D. Vanbeveren, W. van Rensbergen, & C. De Loore, 85–103

Damineli, A., et al. 2008a, MNRAS, 384, 1649

——. 2008b, MNRAS, 386, 2330

Damineli, A., Kaufer, A., Wolf, B., Stahl, O., Lopes, D. F., & de Araújo, F. X. 2000, ApJ, 528, L101

Damineli, A., Stahl, O., Kaufer, A., Wolf, B., Quast, G., & Lopes, D. F. 1998, A&AS, 133, 299

Damineli, A., et al. 2009, IAU Circ., 9011, 1

Daminelli, A., Conti, P. S., & Lopes, D. F. 1997, New Astronomy, 2, 107

Davidson, K., & Humphreys, R. M. 1997, ARA&A, 35, 1

Davidson, K., et al. 2005, AJ, 129, 900

de Groot, M. 1990, in Properties of Hot Luminous Stars (ASP Conf. Ser. 7), ed. C. D. Garmany (San Francisco: ASP)

de Groot, M., & Lamers, H. J. G. L. M. 1992, Nature

de Groot, M., Sterken, C., & van Genderen, A. M. 2001, A&A

de Koter, A., Lamers, H. J. G. L. M., & Schmutz, W. 1996, A&A, 306, 501

de Winter, D., Perez, M. R., Hu, J. Y., & The, P. S. 1992, A&A, 257, 632

Dessart, L. 2004, A&A

Drissen, L., Crowther, P. A., Smith, L. J., Robert, C., & Roy, J., a. D. J. 2001, ApJ

Eggleton, P. P. 1983, ApJ, 268, 368

Fahed, R., et al. 2011, MNRAS, 418, 2

Feast, M. W., Thackeray, A. D., & Wesselink, A. J. 1960a, MNRAS

——. 1960b, MNRAS, 121, 337

Ferland, G. J. 1980, PASP, 92, 596

Fernández Lajús, E., et al. 2010, New Astronomy, 15, 108

Fernández Lajús, E., Gamen, R., Schwartz, M., Salerno, N., Llinares, C., Fariña, C., a. A. R., & Niemela, V. 2003, IBVS, 5477, 1

Foellmi, C., et al. 2008, RMxAA, 44, 3

Friend, D. B., & Castor, J. I. 1982, ApJ, 261, 293

Fullerton, A. W., Massa, D. L., & Prinja, R. K. 2006, ApJ, 637, 1025

Fullerton, A. W., & Owocki, S. P. 1992, Nonisotropic and Variable Outflows from Stars (ASP Conf. Ser. 22), ed. L. Drissen, C. Leitherer, & A. Nota (San Francisco: ASP)

Gaviola, E. 1953, ApJ, 118, 234

Gies, D. R., et al. 2007, ApJ, 654, 527

Gies, D. R., & Bolton, C. T. 1986, ApJ, 304, 371

Gould, B. A. 1879, Resultados del Observatorio Nacional Argentino, 1, D1

Groh, J. H., et al. 2009a, ApJ, 705, L25

Groh, J. H., Hillier, D. J., & Damineli, A. 2006, ApJ, 638, L33

——. 2011, ApJ, 736, 46

Groh, J. H., Hillier, D. J., Damineli, A., Whitelock, P. A., Marang, F., & Rossi, C. 2009b, ApJ, 698, 1698

Groh, J. H., & Vink, J. S. 2011, A&A, 531, L10

Grundstrom, E. D., Gies, D. R., Hillwig, T. C., McSwain, M. V., Smith, N., Gehrz, R. D., Stahl, O., & Kaufer, A. 2007, ApJ, 667, 505

Gull, T. R., et al. 2009, MNRAS, 396, 1308

Gull, T. R., Vieira Kober, G., & Nielson, K. E. 2006, ApJS, 163, 173

Heydari-Malayeri, M., Rauw, G., Esslinger, O., & Beuzit, J.-L. 1997, A&A, 322, 554

Hillier, D. J., & Allen, D. A. 1992, A&A, 262, 153

Hillier, D. J., Davidson, K., Ishibashi, K., & Gull, T. 2001, ApJ, 553, 837

Hillier, D. J., & Miller, D. L. 1999, ApJ, 519, 354

Howarth, I. D., Siebert, K. W., Hussain, G. A. J., & Prinja, R. K. 1997, MNRAS, 284, 265

Howarth, I. D., et al. 2007, MNRAS, 381, 433

Howell, S. B., Walter, F. M., Harrison, T. E., & Huber, M. E. 2006, ApJ, 652, 709

Hu, J. Y., de Winter, D., The, P. S., & Perez, M. R. 1990, A&A, 227, L17

Hubble, E., & Sandage, A. 1953, ApJ, 118, 353

Humphreys, R. M., & Davidson, K. 1994, PASP, 106, 1025

Humphreys, R. M., Davidson, K., & Smith, N. 2002, "Exotic Stars as Challenges to Evolution" (ASP Conf. Vol. 279), ed. C. A. Tout & W. Van Hamme (San Francisco: ASP), 79

Humphreys, R. M., Lamers, H. J. G. L. M., Hoekzema, N., & Cassatella, A. 1989, A&A, 218, L17

Iping, R. C., Sonneborn, G., Gull, T. R., Massa, D. L., & Hillier, D. J. 2005, ApJ, 633, L37

Ireland, M. J., Monnier, J. D., & Thureau, N. 2006, in Society of Photo-Optical Instrumentation Engineers (SPIE) Conference Series, Vol. 6268, Society of Photo-Optical Instrumentation Engineers (SPIE) Conference Series

Ishibashi, K., et al. 2003, ApJ, 125, 3222

Israelian, G., & de Groot, M. 1999, Space Sci. Rev., 90, 493

Israelian, G., de Groot, M., Parker, J. W., & Sterken, C. 1996, MNRAS, 283, 119

Jaschek, M., & Jaschek, C. 1973, PASP, 85, 127

Johansson, S., Gull, T. R., Hartman, H., & Letokhov, V. 2005, A&A

Kaper, L., et al. 1997, A&A, 327, 281

Kaper, L., Henrichs, H. F., Nichols, J. S., & Telting, J. H. 1999, A&A, 344, 231

Kashi, A. 2010, MNRAS, 405, 1924

Kaufer, A., Stahl, O., Wolf, B., Gaeng, T., Gummersbach, C. A., Kovacs, J., Mandel, H., & Szeifert, T. 1996, A&A, 305, 887

Koenigsberger, G., Auer, L. H., Georgiev, L., & Guinan, E. 1998a, ApJ, 496, 934

Koenigsberger, G., Georgiev, L., Hillier, D. J., Morrell, N., Barba, R., & Gamen, R. 2010, AJ, 139, 2600

Koenigsberger, G., Pena, M., Schmutz, W., & Ayala, S. 1998b, ApJ, 499, 889

Koenigsberger, G., Shore, S., Guinan, E., & Auer, L. 1996, 5, 92

Kolka, I. 1998, in Cyclical Variability in Stellar Winds, ed. L. Kaper & A. W. Fullerton, 111

Kozok, J. R. 1985, A&AS, 61, 387

Lamers, H. J. G. L. M., & Cassinelli, J. P. 1999, Introduction to Stellar Winds (Cambridge, UK: Cambridge University Press)

Lamers, H. J. G. L. M., & de Groot, M. J. H. 1992, A&A, 257, 153

Lamers, H. J. G. L. M., Korevaar, P., & Cassatella, A. 1985, A&A, 149, 29

Langer, N., Hamann, W.-R., Lennon, M., Najarro, F., Pauldrach, A. W. A., & Puls, J. 1994, A&A, 290, 819

Lanz, T., & Hubeny, I. 2007, ApJS, 169, 83

Lawson, P. R., ed. 2000, Principles of Long Baseline Stellar Interferometry

Lefèvre, L., et al. 2005, MNRAS, 360, 141

Leitherer, C., Appenzeller, I., Klare, G., Lamers, H. J. G. L. M., Stahl, O., Waters, L. B. F. M., & Wolf, B. 1985, A&A, 153, 168

Leitherer, C., Chapman, J. M., & Koribalski, B. 1995, ApJ, 450, 289

Lépine, S., & Moffat, A. F. J. 2008, AJ, 136, 548

Lépine, S., Moffat, A. F. J., & Henriksen, R. N. 1996, ApJ, 466, 392

Lobel, A., & Blomme, R. 2008, ApJ, 678, 408

Lobel, A., et al. 2011, ArXiv e-prints

Lopes, D. F., Damineli Neto, A., & de Freitas Pacheco, J. A. 1992, A&A, 261, 482

Luud, L. S. 1967, Soviet Ast., 11, 211

Machado, M. A. D., de Araújo, F. X., Pereira, C. B., & Fernandes, M. B. 2002, A&A, 387, 151

Madura, T., Owocki, S., Gull, T., Okazaki, A., & Smith, N. 2010, in IAU XXVII General Assembly Joint Discussion 13: Eta Carinae in the Context of the Most Massive Stars, ed. A. Damineli et al.

Manfroid, J., et al. 1995, A&AS, 109, 329

Marcolino, W. L. F., de Araújo, F. X., Lorenz-Martins, S., & Fernandes, M. B. 2007, AJ, 133, 489

Markova, N. 1986, A&A, 162, L3

——. 1993, Ap&SS, 201, 61

——. 2000, A&AS, 144, 391

Markova, N., Morrison, N., Kolka, I., & Markov, H. 2001, A&A, 376, 898

Markova, N., & Puls, J. 2008, A&A, 478, 823

Markova, N., Puls, J., Scuderi, S., & Markov, H. 2005, A&A, 440, 1133

Martins, F., Schaerer, D., & Hillier, D. J. 2005, A&A, 436, 1049

Massey, P. 2000, PASP, 112, 144

Massey, P., Conti, P. S., & Niemela, V. S. 1981, ApJ, 246, 145

Massey, P., McNeill, R. T., Olsen, K. A. G., Hodge, P. W., Blaha, C., Jacoby, G. H., Smith, R. C., & Strong, S. B. 2007, AJ, 134, 2474

Melnick, J., Ruiz, M. T., & Maza, J. 1982, A&A, 111, 375

Meynet, G., & Maeder, A. 2003, A&A, 404, 975

Michelson, A. A., & Pease, F. G. 1921, ApJ, 53, 249

Miroshnichenko, A. S. 2006, in Astronomical Society of the Pacific Conference Series, Vol. 355, Stars with the B[e] Phenomenon, ed. M. Kraus & A. S. Miroshnichenko, 13

Miroshnichenko, A. S., Chentsov, E. L., & Klochkova, V. G. 2000, A&AS, 144, 379

Moffat, A. F. J., et al. 1998, ApJ, 497, 896

Monnier, J. D., et al. 2011, ApJ, 742, L1

——. 2007, Science, 317, 342

Morbey, C. L., & Brosterhus, E. B. 1974, PASP, 86, 455

Morrison, N. D., Knauth, D. C., Mulliss, C. L., & Lee, W. 1997, PASP, 109, 676

Muratorio, G., Rossi, C., & Friedjung, M. 2008, A&A, 487, 637

Najarro, F. 2001, in Astronomical Society of the Pacific Conference Series, Vol. 233, P Cygni 2000: 400 Years of Progress, ed. M. de Groot & C. Sterken, 133

Najarro, F., Hillier, D. J., & Stahl, O. 1997, A&A, 326, 1117

Nazarenko, V. V., & Glazunova, L. V. 2006, Astronomy Reports, 50, 369

Nielsen, K. E., Corcoran, M. F., Gull, T. R., Hillier, D. J., Hamaguchi, K., Ivarsson, S., & Lindler, D. J. 2007, ApJ, 660, 669

Nielsen, K. E., Kober, G. V., Weis, K., Gull, T. R., Stahl, O., & Bomans, D. J. 2009a, ApJS, 181, 473

——. 2009b, ApJS, 181, 473

Niemela, V. S., Barba, R. H., Morrell, N. I., & Corti, M. 1997, in Astronomical Society of the Pacific Conference Series, Vol. 120, Luminous Blue Variables: Massive Stars in Transition, ed. A. Nota & H. Lamers, 222

North, J. R., Tuthill, P. G., Tango, W. J., & Davis, J. 2007, MNRAS, 377, 415

Nota, A., Leitherer, C., Clampin, M., Greenfield, P., & Golimowski, D. A. 1992, ApJ, 398, 621

Okazaki, A. T., Owocki, S. P., Russell, C. M. P., & Corcoran, M. F. 2008, MNRAS, 388, L39

Parkin, E. R., Pittard, J. M., Corcoran, M. F., Hamaguchi, K., & Stevens, I. R. 2009, MNRAS, 394, 1758

Pasquali, A., Comerón, F., & Nota, A. 2006, A&A, 448, 589

Pauldrach, A. W. A., & Puls, J. 1990, A&A, 237, 409

Percy, J. R., Evans, T. D. K., Henry, G. W., & Mattei, J. A. 2001, in Astronomical Society of the Pacific Conference Series, Vol. 233, P Cygni 2000: 400 Years of Progress, ed. M. de Groot & C. Sterken, 31

Percy, J. R., et al. 1988, A&A, 191, 248

Percy, J. R., & Welch, D. L. 1983, PASP, 95, 491

Perrier, C., Breysacher, J., & Rauw, G. 2009, A&A, 503, 963

Petriella, A., Paron, S., & Giacani, E. 2011, ArXiv e-prints

Pichardo, B., Sparke, L. S., & Aguilar, L. A. 2008, MNRAS, 391, 815

Pittard, J. M., & Corcoran, M. F. 2002, A&A, 383, 636

Pojmanski, G. 2002, Acta Astron., 52, 397

Pojmanski, G., & Maciejewski, G. 2004, Acta Astron., 54, 153

Porter, J. M., & Rivinius, T. 2003, PASP, 115, 1153

Prinja, R. K., Massa, D., & Fullerton, A. W. 2002, A&A, 388, 587

Puls, J., et al. 1996, A&A, 305, 171

Puls, J., Vink, J. S., & Najarro, F. 2008, A&A Rev., 16, 209

Rayner, J. T., Toomey, D. W., Onaka, P. M., Denault, A. J., Stahlberger, W. E., Vacca, W. D., Cushing, M. C., & Wang, S. 2003, PASP, 115, 362

Richardson, N. D., & Gies, D. R. 2010, The Astronomer's Telegram, 2560, 1

Richardson, N. D., Gies, D. R., Henry, T. J., Fernández-Lajús, E., & Okazaki, A. T. 2010, AJ, 139, 1534

Richardson, N. D., Gies, D. R., & Williams, S. J. 2011a, AJ, 142, 201

Richardson, N. D., Morrison, N. D., Gies, D. R., Markova, N., Hesselbach, E. N., & Percy, J. R. 2011b, AJ, 141, 120

Richardson, N. D., Morrison, N. D., Kryukova, E. A., & Adelman, S. J. 2011c, AJ, 141, 17

Rivinius, T., et al. 1997, A&A, 318, 819

Rivinius, T., Wolf, B., Kaufer, A., & Stahl, O. 1994, in Astronomische Gesellschaft Abstract Series, Vol. 10, Astronomische Gesellschaft Abstract Series, ed. G. Klare, 155

Roberts, D. H., Lehar, J., & Dreher, J. W. 1987, AJ, 93, 968

Runacres, M. C., & Owocki, S. P. 2002, A&A, 381, 1015

Sanduleak, N. 1970, Contributions from the Cerro Tololo Inter-American Observatory, 89

Scargle, J. D. 1982, ApJ, 263, 835

Schaefer, G. H., et al. 2010, AJ, 140, 1838

Shafter, A. W., Szkody, P., & Thorstensen, J. R. 1986, ApJ, 308, 765

Shara, M. M., Faherty, J. K., Zurek, D., Moffat, A. F. J., Gerke, J., Doyon, R., Artigau, E., & Drissen, L. 2011, ArXiv e-prints

Shara, M. M., et al. 2009, AJ, 138, 402

Shore, S. N., & Brown, D. N. 1990, ApJ, 365, 665

Shore, S. N., Brown, D. N., Bopp, B. W., Robinson, C. R., Sanduleak, N., & Feldman, P. D. 1990, ApJS, 73, 461

Smith, N. 2004, MNRAS, 351, L15

——. 2005, MNRAS, 357, 1330

——. 2007, AJ, 133, 1034

Smith, N., Davidson, K., Gull, T. R., Ishibashi, K., & Hillier, D. J. 2003, ApJ, 586, 432

Smith, N., & Frew, D. J. 2011, MNRAS

Smith, N., Li, W., Silverman, J. M., Ganeshalingam, M., & Filippenko, A. V. 2011, MNRAS, 415, 773

Smith, N., & Owocki, S. P. 2006, ApJ, 645, L45

Stahl, O. 1990, in Reviews in Modern Astronomy, Vol. 3, Reviews in Modern Astronomy, ed. G. Klare, 286–296

Stahl, O., Gäng, T., Sterken, C., Kaufer, A., Rivinius, T., Szeifert, T., & Wolf, B. 2003, A&A, 400, 279

Stahl, O., et al. 1995, Journal of Astronomical Data, 1, 3

Stahl, O., Weis, K., Bomans, D. J., Davidson, K., Gull, T. R., & Humphreys, R. M. 2005, A&A, 435, 303

Stahl, O., Wolf, B., Klare, G., Juettner, A., & Cassatella, A. 1990, A&A, 228, 379

Stahl, O., Wolf, B., Leitherer, C., & de Groot, M. 1985, A&AS, 61, 237

Stahl, O., Wolf, B., Leitherer, C., Zickgraf, F.-J., Krautter, J., & de Groot, M. 1984, A&A, 140, 459

Sterken, C., Arentoft, T., Duerbeck, H. W., & Brogt, E. 1999, A&A, 349, 532

Sterken, C., & Breysacher, J. 1997, A&A, 328, 269

Sterken, C., de Groot, M., & van Genderen, A. M. 1997a, A&A, 326, 640

——. 1998, A&A, 333, 565

Sterken, C., Gosset, E., Juttner, A., Stahl, O., Wolf, B., & Axer, M. 1991, A&A, 247, 383

Sterken, C., et al. 1993, A&AS, 102, 79

Sterken, C., Stahl, O., Wolf, B., Szeifert, T., & Jones, A. 1995, A&A, 303, 766

Sterken, C., van Genderen, A. M., & de Groot, M. 1997b, in Astronomical Society of the Pacific Conference Series, Vol. 120, Luminous Blue Variables: Massive Stars in Transition, ed. A. Nota & H. Lamers, 35

Sterken, C., van Genderen, A. M., Plummer, A., & Jones, A. F. 2008, A&A, 484, 463

Sterken, C., & Wolf, B. 1978, A&A, 70, 641

Stothers, R. B. 2002, ApJ, 568, 312

Szeifert, T., Kaufer, A., Crowther, P. A., Stahl, O., & Sterken, C. 2003, in IAU Symposium, Vol. 212, A Massive Star Odyssey: From Main Sequence to Supernova, ed. K. van der Hucht, A. Herrero, & C. Esteban, 243

Szeifert, T., Stahl, O., Wolf, B., Zickgraf, F.-J., Bouchet, P., & Klare, G. 1993, A&A, 280, 508

Tarasov, A. E. 2000, in Astronomical Society of the Pacific Conference Series, Vol. 214, IAU Colloq. 175: The Be Phenomenon in Early-Type Stars, ed. M. A. Smith, H. F. Henrichs, & J. Fabregat, 644

ten Brummelaar, T. A., et al. 2005, ApJ, 628, 453

Touhami, Y., et al. 2010, PASP, 122, 379

Townsend, R. H. D., & Owocki, S. P. 2005, MNRAS, 357, 251

Tubbesing, S., et al. 2002, A&A, 389, 931

Tuthill, P., ten Brummelaar, T., Ireland, M., Ridgway, S., McAlister, H., & Turner, N. 2006, in "Advances in Stellar Interferometry. Edited by Monnier, Scholler, & Danchi. Proceedings of the SPIE"

Ud-Doula, A., Owocki, S. P., & Townsend, R. H. D. 2009, MNRAS, 392, 1022

Umana, G., Buemi, C. S., Trigilio, C., Leto, P., & Hora, J. L. 2010, ApJ, 718, 1036

Vacca, W. D., Cushing, M. C., & Rayner, J. T. 2003, PASP, 115, 389

van Genderen, A. M. 2001, A&A, 366, 508

van Genderen, A. M., de Groot, M., & Sterken, C. 1997, A&AS, 124, 517

van Genderen, A. M., Sterken, C., & Allen, W. H. 2003, A&A, 405, 1057

van Genderen, A. M., Sterken, C., & de Groot, M. 1998, A&A, 337, 393

van Genderen, A. M., et al. 1990, A&AS, 82, 189

——. 1992, A&A, 264, 88

Venn, K. A., Smartt, S. J., Lennon, D. J., & Dufton, P. L. 1998, A&A, 334, 987

Vink, J. S., de Koter, A., & Lamers, H. J. G. L. M. 2000, in Astronomical Society of the Pacific Conference Series, Vol. 204, Thermal and Ionization Aspects of Flows from Hot Stars, ed. H. Lamers & A. Sapar, 427

Wachter, S., Mauerhan, J. C., Van Dyk, S. D., Hoard, D. W., Kafka, S., & Morris, P. W. 2010, AJ, 139, 2330

Walborn, N. R., & Fitzpatrick, E. L. 2000, PASP, 112, 50

Walborn, N. R., et al. 2008, ApJ, 683, L33

Waters, L. B. F. M., & Wesselius, P. R. 1986, A&A, 155, 104

Weis, K. 2011, in IAU Symposium, Vol. 272, IAU Symposium, ed. C. Neiner, G. Wade, G. Meynet, & G. Peters, 372–377

Weis, K., Stahl, O., Bomans, D. J., Davidson, K., Gull, T. R., & Humphreys, R. M. 2005, AJ, 129, 1694

Whitelock, P. A., Feast, M. W., Marang, F., & Breedt, E. 2004, MNRAS, 352, 447

Williams, S. J., Gies, D. R., Matson, R. A., & Huang, W. 2009, ApJ, 696, L137

Wisse, P. N. J., & Wisse, M. 1971, A&A, 12, 149

Wolf, B., Campusano, L., & Sterken, C. 1974, A&A, 36, 87

Wolf, B., Kaufer, A., Rivinius, T., & Stahl, O. 1994, in Astronomische Gesellschaft Abstract Series, Vol. 10, Astronomische Gesellschaft Abstract Series, ed. G. Klare, 40

Zhao, M., et al. 2008, ApJ, 684, L95

Zucker, S. 2003, MNRAS, 342, 1291

Appendices

A
HLCO SPECTROSCOPY REDUCTION

A.1 INTRODUCTION

The general reductions for spectroscopy obtained at HLCO are outlined here. These procedures are done with IRAF, and assume a general working knowledge of reductions.

After starting IRAF (`cl`) in an xgterminal, call up the following packages: `noao, imred, ccdred, kpnoslit`. The basic reductions will include the subtraction of a bias frame, dark current, and then flat fielding the spectra. Cosmic ray removal is left to final clean up of the spectra. A general script is available for download[1] that will perform the first tasks. To run this script, you must define it with IRAF using the call sequence `task reduce=reduce.cl`. Then, typing `reduce` from the command line will perform these operations on all images in the directory, assuming you have the following lists of images, given in Table A.1.

A.2 EXTRACTING THE SPECTRA AND WAVELENGTH CALIBRATION

You will extract spectra using the `apall` procedure in the `kpnoslit` package. Basic parameters can be found in a more detailed document[2]. After the interactive features are completed, the procedure `apsum` is used on the comparison lamps in order to extract the same region as the spectra that were extracted. These extracted comparison lamps are then identified using known line identifications and wavelengths with the task `identify`.

[1] http://www.chara.gsu.edu/∼richardson/reduce.cl
[2] http://www.chara.gsu.edu/∼richardson/reduction_manual_HLCO.pdf

Table A.1 Reduction lists for HLCO

File name	lists all of ...
zero.lst	bias frames
dark.lst	dark frames
flat.lst	flat fields
in.lst	spectra and comps

In order to apply the wavelength solution to the data, the `hedit` task can be used to add a value to the header called REFSPEC1 (and REFSPEC2 if two comps are being used). The value for this header keyword should be the filename of the comp lamp(s) identified. Also use hedit to set the right ascension (RA), declination (DEC), and epoch of the coordinates of your target (EPOCH). The DATE-OBS keyword is correct, but you will also need the universal time (part of the DATE-OBS keyword) added to the header.

With all of these additions, you can run the task `observatory` to set the location as HLCO (latitude:33.671185; longitude:83.593984). With the observatory set, you can run the task `rvcorrect` in the `astutil` package in order to set the heliocentric julian date (HJD) and the header keyword VHELIO, which is the projected radial velocity of the Earth in the line of sight of your target.

Normalization or flux calibration is left to the users for their own methods (either IDL or IRAF) as well as any additional calibrations, including telluric line removal. In general, this procedure that has been outlined, will leave your data in a state ready for analysis.

B
MEASUREMENTS

This appendix is designed to tabulate measurements made from the spectroscopic and interferometric observations shown throughout this thesis. In particular, long tables will be placed here.

Table B.1: Hα Measurements of P Cygni, 1993 – 2007

HJD −2,400,000 (d) (1)	W_λ (net) (Å) (2)	V (mag) (3)	W_λ (corr) (Å) (4)	I_p (norm.) (5)	FWHM (km s^{-1}) (6)	$\triangle V_r$ (km s^{-1}) (7)	V_r (min) (km s^{-1}) (8)	V_r (DAC) (km s^{-1}) (9)	W_λ (DAC) (Å) (10)
49512.730	89.8	4.79	90.6	21.1	169.8	+0.3	−203.3	−151.1	0.61
49544.770	91.5	4.81	90.7	20.7	177.4	−2.5	−203.4	−159.6	0.48
49572.755	76.3	4.72	82.1	18.3	183.6	−0.8	−203.7	−156.2	0.59
49579.717	78.1	4.74	82.5	17.9	177.4	−0.5	−204.7	−154.4	0.52
49594.692	80.2	4.81	79.5	17.3	182.0	−1.0	−205.0	−156.9	0.57
49599.701	83.1	4.83	80.8	17.2	179.0	−1.5	−205.6	−157.7	0.47
49613.687	83.0	4.86	78.5	17.9	175.9	−4.3	−206.5	−162.2	0.37
49615.743	84.5	4.86	80.0	18.1	179.0	−5.0	−206.2	−167.3	0.31
49628.561	83.4	4.85	79.6	17.5	186.6	−5.9	−206.4	...	...
49629.640	79.7	4.85	76.1	16.9	188.2	−6.1	−206.7	...	...
49638.584	80.1	4.82	78.6	16.7	192.7	−7.5	−206.5	...	...
49664.618	75.1	4.83	73.1	14.6	200.4	−3.7	−206.5	...	...
50003.651	67.2	4.78	68.4	14.0	189.7	−7.4	−209.7	...	...
50013.574	70.8	4.77	72.8	14.5	192.7	−7.9	−210.8	...	...
50045.460	77.5	4.84	74.7	15.2	191.2	−4.4	−210.7	...	...
50074.495	72.2	...	...	...	195.8	−4.9	−211.7	...	...
50268.843	66.4	4.75	69.5	14.0	186.6	−6.6	−215.3	...	...
50321.633	69.3	4.71	75.3	15.7	174.4	−1.4	−212.3	...	...
50604.817	77.4	4.82	76.0	15.5	182.0	−0.5	−212.6	...	...
50609.794	75.5	4.82	74.1	15.8	174.4	−1.0	−213.0	...	...
50614.794	79.5	4.82	78.0	16.7	179.0	−0.8	−212.0	...	...
50626.794	81.2	4.82	79.7	17.4	180.5	−2.2	−212.5	...	...
50631.737	73.7	4.82	72.4	15.8	182.0	−2.5	−212.8	...	...
50649.843	78.4	...	...	...	188.2	−2.7	−211.6	...	...
50674.708	71.5	4.78	72.8	15.4	192.7	−1.5	−210.9	−126.4	0.11
50684.641	70.7	4.78	72.0	14.5	189.7	−3.6	−211.1	−128.1	0.05
50717.689	68.2	4.75	71.4	16.6	174.4	−4.5	−211.4	...	...
50765.545	75.0	...	...	...	185.1	−0.4	−211.0	−142.3	0.16
50999.782	81.0	4.70	88.8	20.9	160.6	+0.1	−210.7	−146.5	0.32
51044.769	82.4	4.76	85.5	19.2	163.7	−2.7	−211.1	−144.4	0.55
51055.623	81.2	4.74	85.8	19.6	165.2	−2.4	−209.8	−145.9	0.50
51062.680	74.7	4.72	80.4	18.4	165.2	−1.9	−209.0	−148.5	0.50
51079.602	77.8	4.72	83.7	18.3	166.7	+0.8	−208.0	−145.9	0.56
51097.522	79.2	4.75	82.9	18.3	165.2	+2.1	−208.3	−142.8	0.71
51110.586	82.0	4.76	85.1	19.3	163.7	+0.5	−207.9	−142.0	0.73
51336.757	83.4	4.85	79.6	16.5	192.7	−5.3	−206.5	...	...
51338.791	86.2	4.87	80.8	16.6	194.3	−5.8	−207.8	...	...
51348.808	85.8	4.89	79.0	16.3	194.3	−3.1	−207.0	...	...
51364.768	76.1	4.83	74.0	15.1	194.3	−1.6	−207.0	−162.9	0.05
51390.752	72.2	4.82	70.9	14.5	192.7	−1.2	−205.6	−163.2	0.07
51392.778	74.7	4.82	73.3	14.5	195.8	−1.6	−207.0	−163.1	0.27
51406.744	69.7	4.74	73.7	14.4	192.7	+0.0	−204.8	−157.3	0.38
51411.784	70.0	4.72	75.4	15.5	185.1	−2.6	−204.7	−162.9	0.32
51425.618	70.0	4.74	74.0	14.8	185.1	−2.6	−203.7	−163.0	0.61
51436.675	73.8	4.78	75.2	15.2	180.5	−1.2	−203.4	−162.0	0.50
51445.630	76.3	4.82	74.9	15.2	185.1	+0.3	−203.7	−160.4	0.52
51767.661	84.0	4.78	85.6	19.9	154.5	+3.9	−207.5	−141.7	0.51
51794.670	79.5	4.74	84.0	19.4	156.0	+3.3	−206.5	−142.8	0.49
51806.567	80.8	4.76	83.8	19.4	156.0	+1.2	−208.5	−139.9	0.91
51814.620	68.2	4.76	70.8	17.4	160.6	+1.7	−209.7	−123.5	0.97
51817.658	82.5	4.75	86.4	19.4	156.0	+2.0	−207.0	−142.0	0.87
51839.556	77.6	4.71	84.3	20.2	162.1	+0.5	−207.5	−141.5	0.69
51854.489	78.5	4.73	83.7	19.1	159.1	+0.1	−205.8	−144.2	0.98
51865.490	72.2	4.71	78.4	18.2	154.5	+0.1	−205.6	−144.8	0.95
52029.826	91.1	4.77	93.7	22.8	143.8	+6.5	−206.2	−137.2	1.06
52069.810	95.2	4.75	99.7	23.9	149.9	+6.0	−203.3	−139.8	1.07
52103.753	87.8	4.68	98.1	22.7	157.6	+3.4	−200.0	−145.1	0.82
52115.730	90.3	4.72	97.2	21.9	156.0	+1.9	−199.7	−145.7	0.83
52128.677	85.7	4.70	94.0	21.7	151.4	+2.6	−199.5	−145.4	1.03
52135.638	83.7	4.71	90.9	21.1	146.9	+2.4	−200.8	−142.3	0.99
52150.688	86.9	4.74	91.8	21.6	140.7	+2.6	−200.8	−143.2	1.03
52151.618	86.8	4.74	91.7	21.1	145.3	+3.5	−200.6	−142.6	0.93
52154.542	85.9	4.74	90.8	21.1	145.3	+3.0	−201.1	−143.2	0.96
52158.587	86.3	4.74	91.2	21.3	143.8	+3.2	−201.0	−142.6	0.97
52163.578	85.7	4.75	89.7	21.1	142.3	+3.6	−201.1	−141.4	0.97
52165.550	87.4	4.75	91.5	21.4	142.3	+4.3	−200.9	−142.3	0.96
52168.595	86.7	4.78	88.3	20.6	137.7	+4.6	−200.7	−139.8	0.94
52169.558	87.7	4.79	88.5	20.8	137.7	+4.0	−201.7	−141.6	0.97
52173.616	88.0	4.79	88.8	21.0	139.2	+4.7	−200.9	−141.2	0.92
52182.549	91.2	4.80	91.2	21.7	136.1	+4.2	−201.1	−140.1	0.94
52184.554	90.3	4.80	90.3	21.7	136.1	+5.1	−199.9	−140.9	0.97
52186.594	92.2	4.80	92.2	22.3	136.1	+4.9	−200.1	−140.2	0.91
52192.594	94.6	4.79	95.5	22.5	136.1	+4.2	−200.8	−140.5	0.96
52200.512	94.9	4.79	95.8	23.4	137.7	+4.2	−200.9	−138.4	0.93
52203.478	96.6	4.79	97.5	23.3	140.7	+3.8	−201.1	−138.7	0.91
52214.476	95.8	4.80	95.8	23.5	140.7	+3.1	−201.4	−136.9	0.86

Continued on next page

Table B.1 – continued from previous page

HJD −2,400,000 (d) (1)	W_λ (net) (Å) (2)	V (mag) (3)	W_λ (corr) (Å) (4)	I_p (norm.) (5)	FWHM (km s^{-1}) (6)	$\triangle V_r$ (km s^{-1}) (7)	V_r (min) (km s^{-1}) (8)	V_r (DAC) (km s^{-1}) (9)	W_λ (DAC) (Å) (10)
52217.596	97.2	4.80	97.2	23.4	146.9	+2.6	−200.7	−137.3	0.85
52220.481	94.5	4.80	94.5	23.2	145.3	+2.9	−200.5	−137.3	0.81
52221.510	96.8	4.79	97.7	24.1	143.8	+2.5	−200.6	−136.9	0.79
52224.476	96.1	4.79	97.0	23.9	148.4	+3.8	−198.7	−138.1	0.81
52225.464	95.8	4.79	96.7	24.3	145.3	+3.4	−198.7	−138.1	0.80
52226.462	93.8	4.79	94.7	23.3	146.9	+3.4	−198.8	−139.5	0.86
52236.465	94.5	4.78	96.3	23.7	148.4	+3.5	−198.1	−139.6	0.85
52263.477	98.0	...	...	...	159.1	+3.3	−198.0	−139.4	0.89
52390.821	89.2	...	...	...	145.3	+4.5	−196.6	−141.9	0.87
52391.857	87.7	...	...	...	151.4	+4.5	−197.0	−140.5	0.78
52399.803	90.8	...	...	...	154.5	+3.9	−196.5	−138.7	0.92
52404.875	89.2	...	...	...	154.5	+3.2	−198.0	−138.2	0.91
52413.831	92.5	...	...	...	157.6	+2.4	−196.4	−141.4	0.84
52416.779	90.6	...	...	...	159.1	+1.4	−197.3	−140.2	0.84
52421.800	94.9	...	...	...	163.7	+0.7	−196.8	−140.4	0.93
52426.786	92.0	...	...	...	163.7	+1.1	−196.2	−140.8	0.89
52441.792	83.8	...	...	...	165.2	+1.6	−194.6	−145.1	0.88
52442.776	81.3	...	...	...	162.1	+2.3	−192.2	−143.7	0.91
52450.756	81.9	...	...	...	163.7	+1.6	−194.6	−145.2	1.10
52456.691	79.7	...	...	...	159.1	+1.8	−193.2	−145.8	1.09
52460.804	83.3	4.71	90.5	19.7	165.2	+2.0	−192.2	−146.1	1.11
52462.751	83.1	4.71	90.3	19.6	163.7	+1.0	−193.9	−146.1	1.17
52564.557	95.7	4.72	103.0	23.8	163.7	+8.0	−181.4	−146.4	1.16
52568.508	92.9	4.74	98.2	22.9	159.1	−3.3	−192.9	−137.8	1.10
52570.487	93.9	4.75	98.3	23.1	160.6	−1.0	−191.2	−148.0	1.00
52570.522	95.8	4.75	100.3	23.4	157.6	−1.4	−191.4	−148.1	1.16
52579.490	91.8	4.78	93.5	22.0	163.7	−1.3	−191.4	−147.9	0.82
52584.499	95.4	4.81	94.5	22.1	163.7	+0.7	−190.0	−147.1	0.85
52588.491	95.7	4.81	94.8	22.6	163.7	+0.4	−190.0	−146.2	0.88
52592.504	94.2	4.81	93.3	22.0	165.2	−1.4	−191.5	−138.4	0.77
52780.814	82.9	...	...	...	157.6	+2.2	−195.0	−146.0	0.82
52781.812	81.3	...	...	...	153.0	+1.9	−194.3	−146.2	1.13
52806.774	81.9	4.80	81.9	18.7	159.1	+0.0	−195.7	−146.0	1.01
52812.789	86.1	4.78	87.7	19.9	159.1	−0.7	−196.7	−146.1	1.08
52813.748	87.6	4.78	89.2	20.1	160.6	−3.4	−201.0	−144.1	1.12
52815.647	88.4	4.78	90.0	20.6	159.1	+1.1	−195.5	−146.4	1.12
52834.754	85.5	4.78	87.1	19.7	163.7	+4.2	−193.5	−147.9	1.07
52837.646	83.0	4.78	84.5	19.1	163.7	−0.4	−196.8	−146.8	1.09
52845.679	86.8	4.77	89.2	20.1	166.7	−5.9	−204.6	−145.5	1.02
52850.628	84.3	4.77	86.7	19.6	163.7	+2.2	−194.8	−149.1	1.13
52871.608	87.8	4.78	89.4	20.3	162.1	−1.0	−197.2	−148.7	1.07
52875.607	87.5	4.77	90.0	20.4	163.7	−0.9	−197.3	−149.3	1.10
52876.683	87.2	4.77	89.6	20.6	162.1	−2.3	−197.2	−148.5	0.95
52899.677	81.9	4.77	84.2	18.6	171.3	−3.5	−195.7	−149.2	0.90
52906.649	82.9	4.79	83.7	18.6	171.3	−5.2	−196.8	−150.4	0.96
52921.570	82.2	4.77	84.5	18.9	169.8	−0.8	−192.9	−151.0	1.07
52929.570	79.2	4.77	81.4	17.9	169.8	+3.5	−187.8	−152.6	1.04
53164.826	68.6	4.77	70.5	15.0	169.8	−10.4	−208.9	−142.6	1.01
53187.777	79.0	4.78	80.5	16.5	175.9	−7.3	−204.8	−158.9	0.98
53189.727	77.9	4.77	80.1	16.6	172.9	−4.6	−206.5	−156.5	1.13
53223.686	76.3	4.72	82.1	16.9	180.5	−3.6	−205.1	−156.2	0.77
53240.676	78.8	4.78	80.3	16.8	177.4	−8.3	−207.7	−162.2	0.88
53258.635	75.1	4.77	77.2	15.9	175.9	−4.2	−206.0	−162.6	0.97
53269.540	77.1	4.74	81.5	16.6	179.0	−3.1	−204.8	−160.2	0.94
53282.531	73.1	4.73	78.0	16.2	171.3	−3.9	−205.7	−157.6	0.70
53323.501	74.9	4.74	79.2	17.4	165.2	−9.3	−209.9	−154.7	0.76
53499.871	78.8	4.74	83.3	18.4	165.2	−5.4	−206.7	...	...
53516.855	81.0	4.74	85.6	18.2	168.3	−10.1	−210.3	−151.1	0.89
53544.699	81.9	4.75	85.8	19.1	166.7	−2.9	−203.8	−154.2	0.59
53545.746	79.7	4.75	83.5	19.0	159.1	+1.8	−202.5	−153.8	0.82
53559.761	80.0	4.73	85.3	19.5	157.6	−2.6	−207.8	...	...
53623.728	85.0	4.81	84.2	18.8	174.4	−1.0	−203.3	...	...
53644.603	82.7	4.84	79.7	17.2	186.6	−6.8	−210.1	−155.2	−0.18
53658.533	79.8	4.80	79.8	16.8	188.2	−3.3	−205.9	−161.1	0.24
53686.551	72.1	4.75	75.5	15.5	192.7	−6.2	−206.6	−157.9	0.70
53892.814	77.1	4.82	75.7	16.2	165.2	−4.2	−208.5	...	...
53902.819	80.2	4.82	78.7	17.0	169.8	−2.8	−207.6	...	...
53912.775	76.3	4.77	78.4	16.2	174.4	−3.7	−207.2	...	...
53917.754	79.4	4.74	83.9	17.4	179.0	−3.5	−206.4	−156.0	0.33
53924.778	79.5	4.77	81.7	17.1	180.5	+1.0	−204.1	−158.4	0.42
53933.735	75.9	4.78	77.3	15.9	175.9	−4.4	−204.8	−156.6	0.55
54003.601	70.8	4.74	74.8	15.4	179.0	−2.0	−205.2	...	...
54273.799	76.1	4.80	76.1	18.0	160.6	+1.2	−203.9	...	...
54294.753	78.7	4.79	79.4	18.5	172.9	+1.8	−203.6	...	...
54297.757	75.6	4.72	81.4	18.9	175.9	+0.8	−204.1	...	...
54303.682	72.8	4.72	78.4	18.2	175.9	+0.6	−203.8	−152.6	0.72
54340.686	67.6	4.70	74.1	18.8	157.6	−0.1	−203.2	−150.6	0.72
54348.647	68.1	4.73	72.6	18.7	156.0	−0.7	−203.6	−150.2	0.81
54361.632	70.2	4.76	72.8	18.8	156.0	+0.3	−203.0	−149.8	0.87
54372.584	64.2	4.74	67.8	17.5	156.0	+2.6	−202.0	−149.3	0.84
54402.551	68.7	4.73	73.3	19.7	149.9	+3.5	−202.4	−147.5	0.88
54403.527	68.4	4.73	73.0	19.8	149.9	+3.1	−202.7	−147.1	0.99

Table B.2: Hα Measurements of η Carinae During the 2009.0 Event

Date HJD - 2,450,000	**Orbital Phase**	**Spectrograph**	W_λ **(Hα)** (Å)	$W_{\lambda,corr}$ **(Hα)** (Å)	V_b **km s^{-1}**
4779.8615	11.969	R-C	−678	...	...
4784.8577	11.972	echelle	−650	−650	−18.1
4786.8458	11.972	R-C	−640	−635	...
4801.7878	11.980	R-C	−599	−611	...
4803.7731	11.981	R-C	−629	−645	...
4814.8012	11.986	R-C	−639	−652	...
4818.8060	11.988	echelle	−535	−551	−26.6
4819.8108	11.989	echelle	−550	−569	−24.4
4821.8520	11.990	echelle	−561	−584	−23.4
4824.7536	11.991	echelle	−561	−589	−27.1
4829.7838	11.994	echelle	−545	−576	−27.5
4831.7530	11.995	echelle	−518	−559	−28.3
4836.7315	11.997	echelle	−483	−526	−27.3
4836.7444	11.997	echelle	−498	−542	−25.8
4838.7496	11.998	echelle	−481	−529	−25.8
4840.7721	11.999	echelle	−447	−496	−24.7
4841.7684	12.000	echelle	−449	−501	−24.3
4842.7673	12.000	echelle	−428	−477	−23.8
4843.7668	12.001	echelle	−436	−491	−23.7
4844.7694	12.001	echelle	−439	−494	−22.5
4845.7581	12.002	echelle	−438	−490	−24.2
4846.7611	12.002	echelle	−447	−500	−20.7
4847.7971	12.003	echelle	−429	−471	−19.9
4848.7348	12.003	echelle	−424	−463	−16.6
4849.7148	12.004	echelle	−435	−470	−19.5
4850.7272	12.004	echelle	−435	−464	−18.8
4851.7129	12.005	echelle	−434	−456	−17.6
4852.7313	12.005	echelle	−468	−486	−17.6
4853.7222	12.006	echelle	−437	−447	−17.6
4854.7335	12.006	echelle	−466	−475	−16.1
4855.7283	12.007	echelle	−459	−458	−16.0
4857.7714	12.008	echelle	−472	−463	−16.0
4858.7605	12.008	echelle	−471	−463	−16.0
4859.7681	12.009	echelle	−463	−455	−16.4
4861.7205	12.010	echelle	−474	−468	−16.6
4862.7332	12.010	echelle	−480	−470	−18.2
4863.7529	12.011	echelle	−488	−479	−19.1
4865.7026	12.011	echelle	−464	−459	−19.9
4866.7104	12.012	echelle	−474	−472	−20.2
4867.7011	12.012	echelle	−454	−453	−21.9
4875.6456	12.016	echelle	−455	−472	−22.3
4879.6545	12.018	echelle	−455	−477	−23.3
4880.6719	12.019	echelle	−440	−461	−21.6
4881.6680	12.019	echelle	−457	−483	−22.1
4883.5776	12.020	R-C	−429	−462	...
4897.5556	12.027	R-C	−398	−462	...
4902.5327	12.030	R-C	−406	−471	...
4926.5314	12.042	R-C	−414	−475	...
4938.4690	12.047	R-C	−453	−526	...
5032.5139	12.094	R-C	−445	−588	...

Table B.3: Hα Measurements of LBVs

Target	HJD	W_λ (Å)	$\sigma(W_\lambda)(\AA)$
HD 6884	4501.5391	-9.14	0.24
HD 6884	4600.9215	-9.32	0.11
HD 6884	4650.8722	-8.39	0.09
HD 6884	4652.8333	-9.91	0.24
HD 6884	4658.8140	-9.11	0.33
HD 6884	4682.8211	-9.04	0.11
HD 6884	4721.6843	-8.60	0.20

Continued on next page

Table B.3 – continued from previous page

Target	HJD	W_λ	$\sigma(W_\lambda)$
HD 6884	4742.6444	-7.40	0.23
HD 6884	4752.5917	-9.62	0.12
HD 6884	4779.5559	-8.99	0.10
HD 6884	4786.5806	-10.11	0.43
HD 6884	4801.5347	-8.26	0.09
HD 6884	4814.5473	-8.31	0.12
HD 6884	4838.5398	-6.15	0.26
HD 6884	4850.5417	-5.30	0.35
HD 6884	4871.5714	-6.28	0.19
HD 6884	4991.8701	-7.87	0.15
HD 6884	4992.9105	-8.28	0.11
HD 6884	5024.8796	-8.24	0.08
HD 6884	5030.8683	-7.61	0.12
HD 6884	5038.8723	-6.21	0.22
HD 6884	5049.8192	-6.97	0.12
HD 6884	5066.7396	-6.88	0.11
HD 6884	5085.7096	-6.31	0.17
HD 6884	5100.6902	-7.39	0.15
HD 6884	5111.6506	-7.34	0.16
HD 6884	5222.5869	-3.89	0.63
HD 6884	5247.5279	-5.06	0.30
HD 6884	5375.5024	-3.50	0.11
HD 6884	5382.5021	-2.95	0.28
HD 6884	5388.8203	-3.53	0.12
HD 6884	5397.8402	-4.11	0.35
HD 6884	5429.8850	-4.88	0.12
HD 6884	5463.5016	-5.16	0.08
HD 6884	5465.7655	-5.34	0.15
HD 6884	5487.7316	-4.78	0.21
HD 6884	5528.4991	-5.01	0.08
R 85	4501.6930	-15.30	0.22
R 85	4544.5743	-12.29	0.19
R 85	4563.5187	-11.74	0.28
R 85	4589.4873	-11.92	0.16
R 85	4687.8489	-12.13	0.18
R 85	4722.7959	-13.74	0.13
R 85	4744.7649	-12.30	0.12
R 85	4786.6489	-11.44	0.19
R 85	4801.6363	-13.86	0.14
R 85	4803.5917	-13.36	0.12
R 85	4838.6762	-10.27	0.24
R 85	4850.6294	-8.96	0.31
R 85	4861.6098	-8.96	0.34
R 85	4871.5878	-8.87	0.34
R 85	5040.8902	-12.70	0.14
R 85	5054.8398	-11.17	0.24
R 85	5085.7747	-11.82	0.16
R 85	5105.7255	-12.21	0.11

Continued on next page

Table B.3 – continued from previous page

Target	HJD	W_λ	$\sigma(W_\lambda)$
R 85	5185.5620	-11.68	0.18
R 85	5249.5672	-11.44	0.16
R 85	5265.5726	-12.54	0.16
R 85	5282.5558	-12.81	0.21
R 85	5288.5266	-12.22	0.14
R 85	5388.5004	-12.11	0.13
R 85	5433.8529	-12.57	0.14
R 85	5458.8465	-13.54	0.15
R 85	5513.7912	-15.65	0.15
S Dor	4501.6332	-51.36	0.49
S Dor	4541.6093	-51.17	0.11
S Dor	4554.5644	-55.58	0.07
S Dor	4571.5090	-57.30	0.09
S Dor	4576.5157	-53.08	0.17
S Dor	4687.8640	-70.96	0.32
S Dor	4697.8028	-74.10	0.13
S Dor	4721.8048	-72.40	0.28
S Dor	4752.7057	-70.22	0.46
S Dor	4786.6632	-80.68	0.26
S Dor	4801.6518	-72.46	0.14
S Dor	4803.6068	-72.48	0.41
S Dor	4841.7110	-80.10	0.25
S Dor	4852.6257	-79.68	0.20
S Dor	4871.6047	-75.00	0.53
S Dor	5046.8433	-89.95	0.57
S Dor	5090.7794	-111.05	0.27
S Dor	5105.7439	-118.94	0.11
S Dor	5124.6453	-122.07	0.21
S Dor	5135.6163	-124.86	0.30
S Dor	5143.6725	-121.03	0.51
S Dor	5185.5764	-150.24	0.10
S Dor	5232.6003	-167.77	0.35
S Dor	5247.5677	-197.93	0.23
S Dor	5279.5623	-225.90	0.59
S Dor	5282.5489	-235.05	0.59
S Dor	5288.5055	-223.28	0.15
S Dor	5382.9639	-392.84	2.74
S Dor	5309.4928	-267.65	0.36
S Dor	5315.4894	-263.46	0.65
S Dor	5324.5000	-278.64	0.79
S Dor	5412.8857	-333.07	1.28
S Dor	5432.8455	-361.56	0.41
S Dor	5450.8703	-411.72	2.35
S Dor	5464.8973	-375.83	0.95
S Dor	5480.8763	-420.21	1.02
S Dor	5487.8528	-391.40	0.98
S Dor	5521.7336	-434.34	1.25
S Dor	5528.4999	-424.13	1.39

Continued on next page

Table B.3 – continued from previous page

Target	HJD	W_λ	$\sigma(W_\lambda)$
R 110	4544.5887	-22.21	0.23
R 110	4563.5346	-20.36	0.33
R 110	4589.5058	-22.49	0.24
R 110	4687.8720	-19.16	0.50
R 110	4697.8145	-24.57	0.21
R 110	4715.9093	-19.58	0.20
R 110	4725.7800	-22.62	0.34
R 110	4744.7827	-18.75	0.19
R 110	4786.6774	-21.25	0.28
R 110	4801.6632	-23.94	0.22
R 110	4803.6137	-24.21	0.14
R 110	4848.6471	-17.37	0.47
R 110	4861.6337	-17.64	0.24
R 110	4876.5766	-21.24	0.31
R 110	5046.8497	-22.22	0.23
R 110	5070.8231	-22.52	0.13
R 110	5090.7923	-25.81	0.13
R 110	5105.7598	-22.91	0.12
R 110	5124.6658	-22.67	0.18
R 110	5135.6281	-24.97	0.17
R 110	5249.5781	-17.93	0.26
R 110	5288.5387	-17.30	0.36
R 110	5309.5121	-16.07	0.31
R 110	5315.5038	-15.80	0.36
R 110	5432.8492	-20.25	0.17
R 110	5458.9016	-19.96	0.17
R 127	5046.9058	-88.16	0.46
R 127	5054.9364	-91.12	0.50
R 127	5070.8432	-90.08	0.54
R 127	5085.7907	-82.82	0.46
R 127	5100.7739	-74.39	0.63
R 127	5111.5001	-74.68	0.94
R 127	5124.7550	-70.39	0.47
R 127	5185.5848	-64.35	0.46
R 127	5232.6203	-67.45	1.09
R 127	5247.5286	-74.66	0.92
R 127	5279.5791	-98.31	0.70
R 127	5282.5667	-85.07	0.69
R 127	5288.5523	-85.84	0.84
R 127	5309.5225	-99.52	0.58
R 127	5315.5143	-99.87	0.82
R 127	5325.4835	-109.67	0.72
R 127	5412.8944	-88.98	0.53
R 127	5432.9214	-112.39	0.87
R 127	5450.5003	-85.19	0.61
R 127	5464.9031	-109.93	0.95
R 127	5480.8871	-86.68	0.79
R 127	5501.7708	-125.97	1.10

Continued on next page

Table B.3 – continued from previous page

Target	HJD	W_λ	$\sigma(W_\lambda)$
R 127	5521.7404	-142.07	1.40
R 127	5530.4998	-153.43	1.99
R 127	5550.7056	-130.84	0.90
HR Car	4501.7709	-63.88	0.89
HR Car	4524.6337	-71.67	0.58
HR Car	4539.5753	-74.93	0.54
HR Car	4554.6001	-72.36	0.62
HR Car	4571.5389	-82.31	0.50
HR Car	4576.5265	-79.23	0.56
HR Car	4600.6925	-88.65	0.66
HR Car	4635.4432	-85.46	0.56
HR Car	4752.8664	-83.10	0.76
HR Car	4779.8566	-87.49	0.55
HR Car	4786.8523	-88.92	0.70
HR Car	4801.7969	-89.48	0.57
HR Car	4803.8497	-87.26	0.68
HR Car	4814.7965	-91.72	0.64
HR Car	4838.6912	-88.99	0.69
HR Car	4852.6376	-88.33	0.64
HR Car	4871.6395	-80.68	0.60
HR Car	4879.5620	-79.56	0.77
HR Car	5124.8720	-72.10	0.64
HR Car	5135.8401	-67.67	0.67
HR Car	5163.7535	-71.21	0.69
HR Car	5188.8506	-62.26	0.71
HR Car	5200.6839	-64.75	0.61
HR Car	5215.6662	-67.13	0.64
HR Car	5234.5342	-58.98	1.02
HR Car	5249.6357	-67.97	0.55
HR Car	5279.5961	-69.16	0.49
HR Car	5282.6428	-65.66	0.59
HR Car	5288.6139	-61.89	0.72
HR Car	5309.6322	-64.59	0.72
HR Car	5315.5309	-59.04	0.71
HR Car	5325.5225	-68.90	0.53
HR Car	5478.4972	-64.92	0.71
HR Car	5501.4980	-70.25	0.64
HR Car	5515.8139	-69.39	0.94
HR Car	5521.8023	-64.23	0.60
HR Car	5528.7677	-65.57	0.55
HR Car	5545.4988	-60.24	0.54
AG Car	4501.7665	-103.17	0.39
AG Car	4524.6299	-93.57	1.21
AG Car	4527.6592	-91.38	0.65
AG Car	4539.5711	-82.87	0.22
AG Car	4545.6196	-84.85	0.35
AG Car	4571.5364	-75.09	0.31
AG Car	4576.5030	-68.38	1.33

Continued on next page

Table B.3 – continued from previous page

Target	HJD	W_λ	$\sigma(W_\lambda)$
AG Car	4598.7084	-70.98	0.11
AG Car	4635.4514	-70.43	0.29
AG Car	4773.8676	-69.68	0.35
AG Car	4779.8640	-63.01	0.12
AG Car	4786.8568	-59.83	0.36
AG Car	4801.7914	-58.68	0.40
AG Car	4803.7750	-58.40	0.14
AG Car	4814.8042	-58.70	0.19
AG Car	4838.6943	-52.88	0.21
AG Car	4852.6422	-55.80	0.20
AG Car	4871.6448	-51.80	0.31
AG Car	4879.5664	-52.94	0.33
AG Car	5124.8760	-64.84	0.58
AG Car	5135.8434	-55.20	0.25
AG Car	5163.7640	-55.44	0.39
AG Car	5188.8532	-56.36	0.37
AG Car	5200.6884	-49.58	0.14
AG Car	5215.6689	-55.10	0.48
AG Car	5249.6230	-60.30	0.38
AG Car	5279.5920	-73.86	0.55
AG Car	5282.6403	-74.27	0.47
AG Car	5288.6112	-76.47	0.82
AG Car	5309.5030	-70.62	0.30
AG Car	5315.5246	-67.93	0.45
AG Car	5325.5200	-62.03	0.36
AG Car	5479.8979	-74.73	0.46
AG Car	5515.8200	-89.72	0.54
AG Car	5521.8193	-92.62	0.56
AG Car	5530.4978	-105.95	0.54
AG Car	5539.8568	-112.88	0.98
AG Car	5542.7204	-117.07	1.06
Wra 751	4501.7792	-24.01	0.34
Wra 751	4551.5877	-26.13	0.32
Wra 751	4571.5601	-24.51	0.37
Wra 751	4585.4881	-26.53	0.41
Wra 751	4600.7020	-30.45	0.32
Wra 751	4635.4727	-32.91	0.36
Wra 751	4779.8666	-23.54	0.28
Wra 751	4811.7665	-24.62	0.29
Wra 751	4852.6491	-19.83	0.53
Wra 751	4894.5612	-17.95	0.28
Wra 751	4902.5367	-16.48	0.34
Wra 751	5135.8462	-16.75	0.39
Wra 751	5163.7686	-19.90	0.24
Wra 751	5181.8462	-17.21	0.35
Wra 751	5185.7381	-19.03	0.27
Wra 751	5191.7960	-18.44	0.27
Wra 751	5200.6934	-18.34	0.30

Continued on next page

Table B.3 – continued from previous page

Target	HJD	W_λ	$\sigma(W_\lambda)$
Wra 751	5215.6711	-17.05	0.32
Wra 751	5225.7135	-16.52	0.34
Wra 751	5234.7041	-12.15	0.54
Wra 751	5279.5030	-13.46	0.25
Wra 751	5282.6468	-12.81	0.36
Wra 751	5288.5030	-12.18	0.36
Wra 751	5309.6385	-8.86	0.43
Wra 751	5325.5376	-8.62	0.48
Wra 751	5515.8255	-8.58	0.31
Wra 751	5521.8229	-8.67	0.37
Wra 751	5528.4976	-8.11	0.35
Wra 751	5530.7922	-7.87	0.35
Wra 751	5539.8207	-7.67	0.29
Wra 751	5542.7235	-6.18	0.49
Wra 751	5590.5006	-6.96	0.61
ζ^1 Sco	4501.8621	-10.71	0.28
ζ^1 Sco	4505.8716	-9.76	0.22
ζ^1 Sco	4552.6888	-10.85	0.24
ζ^1 Sco	4587.7812	-9.96	0.30
ζ^1 Sco	4598.7546	-9.10	0.22
ζ^1 Sco	4642.7700	-8.69	0.19
ζ^1 Sco	4652.7491	-10.83	0.51
ζ^1 Sco	4656.6388	-10.03	0.30
ζ^1 Sco	4682.7134	-9.40	0.13
ζ^1 Sco	4887.8790	-7.07	0.31
ζ^1 Sco	4902.7607	-7.33	0.19
ζ^1 Sco	4950.6118	-10.16	0.12
ζ^1 Sco	4992.8570	-9.61	0.16
ζ^1 Sco	5020.7989	-6.29	0.32
ζ^1 Sco	5070.6490	-8.23	0.09
ζ^1 Sco	5111.5272	-12.28	0.38
ζ^1 Sco	5124.5118	-11.15	0.16
ζ^1 Sco	5325.5048	-7.03	0.17
ζ^1 Sco	5358.5260	-9.09	0.39
ζ^1 Sco	5375.5052	-9.05	0.42
ζ^1 Sco	5382.8169	-5.01	0.34
ζ^1 Sco	5397.7616	-10.80	0.54
ζ^1 Sco	5437.6604	-7.68	0.20
ζ^1 Sco	5464.4963	-7.99	0.21
ζ^1 Sco	5590.4967	-8.29	0.36
HD 160529	4501.8864	-6.10	0.12
HD 160529	4505.8925	-7.98	0.34
HD 160529	4506.8993	-6.48	0.29
HD 160529	4587.8659	-3.21	0.18
HD 160529	4600.8060	-5.19	0.13

Continued on next page

Table B.3 – continued from previous page

Target	HJD	W_λ	$\sigma(W_\lambda)$
HD 160529	4647.7938	-5.55	0.09
HD 160529	4652.7772	-6.12	0.13
HD 160529	4682.7254	-4.53	0.14
HD 160529	4722.6350	-3.44	0.12
HD 160529	4902.8633	-2.76	0.15
HD 160529	4926.9046	-1.07	0.10
HD 160529	4984.8673	-2.86	0.14
HD 160529	4991.8194	-4.47	0.08
HD 160529	5066.6733	-4.06	0.11
HD 160529	5070.6660	-4.24	0.10
HD 160529	5090.6366	-4.11	0.14
HD 160529	5105.5140	-2.54	0.38
HD 160529	5325.8678	-5.57	0.11
HD 160529	5358.5057	-4.94	0.30
HD 160529	5385.8380	-5.59	0.11
HD 160529	5397.7746	-6.43	0.12
HD 160529	5464.5225	-5.96	0.30
HD 160529	5478.5307	-5.51	0.13
HD 160529	5726.6824	-7.42	0.34
HD 168607	4554.8128	-26.92	0.52
HD 168607	4587.7915	-28.20	1.76
HD 168607	4598.7795	-27.93	0.17
HD 168607	4647.7975	-24.63	0.17
HD 168607	4652.7808	-23.69	0.25
HD 168607	4681.7247	-22.90	0.18
HD 168607	4690.7126	-22.88	0.19
HD 168607	4722.6490	-24.25	0.15
HD 168607	4726.6060	-24.55	0.17
HD 168607	4887.8818	-25.34	0.31
HD 168607	4902.8539	-22.35	0.43
HD 168607	4926.8952	-16.19	0.69
HD 168607	4984.8744	-22.77	0.14
HD 168607	4992.8667	-21.07	0.16
HD 168607	5040.7367	-25.64	0.51
HD 168607	5066.6769	-16.73	0.56
HD 168607	5082.6045	-18.45	0.24
HD 168607	5105.5734	-19.74	0.28
HD 168607	5124.5366	-23.19	0.18
HD 168607	5358.9042	-16.78	0.65
HD 168607	5385.8503	-18.93	0.24
HD 168607	5412.6571	-19.27	0.28
HD 168607	5458.6356	-20.66	0.11
HD 168607	5463.5846	-21.96	0.58
HD 168625	4554.8169	-0.61	0.43
HD 168625	4587.8051	-0.96	0.36
HD 168625	4598.7831	-2.11	0.14
HD 168625	4647.8020	-1.66	0.16
HD 168625	4652.7854	-3.10	0.14

Continued on next page

Table B.3 – continued from previous page

Target	HJD	W_λ	$\sigma(W_\lambda)$
HD 168625	4681.7310	-0.84	0.25
HD 168625	4690.7167	-2.27	0.17
HD 168625	4722.6522	-2.12	0.13
HD 168625	4726.6106	-1.46	0.15
HD 168625	4902.8580	-0.98	0.31
HD 168625	4984.8778	-2.55	0.18
HD 168625	4992.8706	-1.70	0.18
HD 168625	5040.7405	-2.31	0.19
HD 168625	5090.6552	-3.17	0.15
HD 168625	5105.5770	-3.46	0.13
HD 168625	5124.5402	-2.45	0.16
HD 168625	5358.9081	-2.43	0.15
HD 168625	5385.8562	-2.95	0.18
HD 168625	5458.6405	-3.04	0.13
HD 168625	5463.5903	-2.99	0.10
AS 314	4554.8206	-14.54	0.18
AS 314	4587.8682	-11.70	0.17
AS 314	4598.7881	-17.53	0.30
AS 314	5040.7486	-16.05	0.21
AS 314	5054.7463	-15.51	0.18
AS 314	5085.6436	-15.11	0.24
AS 314	5105.5833	-11.73	0.11
AS 314	5119.5552	-12.05	0.16
AS 314	5143.4982	-13.21	0.19
AS 314	5358.9131	-12.96	0.19
AS 314	5386.5057	-12.95	0.11
AS 314	5388.7872	-10.82	0.12
AS 314	5397.7989	-12.82	0.22

Table B.4: H-band Interferometric Measurements of P Cygni

Baseline	λ	V^2	$\sigma(V^2)$	u	v
(m)	(μm)			(m)	(m)
237.55	1.746	0.360	0.015	143.50	189.31
237.55	1.715	0.332	0.016	143.50	189.31
237.55	1.682	0.318	0.015	143.50	189.31
237.55	1.648	0.354	0.016	143.50	189.31
237.55	1.613	0.338	0.018	143.50	189.31
237.55	1.577	0.327	0.018	143.50	189.31
237.55	1.541	0.306	0.016	143.50	189.31
237.55	1.506	0.287	0.020	143.50	189.31
241.41	1.746	0.358	0.043	−64.49	232.64
241.41	1.715	0.325	0.045	−64.49	232.64
241.41	1.682	0.309	0.046	−64.49	232.64
241.41	1.648	0.349	0.053	−64.49	232.64
241.41	1.613	0.332	0.053	−64.49	232.64
241.41	1.577	0.332	0.053	−64.49	232.64
241.41	1.541	0.326	0.047	−64.49	232.64
241.41	1.506	0.302	0.032	−64.49	232.64
177.40	1.746	0.460	0.033	7.53	177.24
177.40	1.715	0.451	0.037	7.53	177.24

Continued on next page

Table B.4 – continued from previous page

Baseline (m)	λ (μm)	V^2	$\sigma(V^2)$	u (m)	v (m)
177.40	1.682	0.439	0.025	7.53	177.24
177.40	1.648	0.488	0.026	7.53	177.24
177.40	1.613	0.471	0.026	7.53	177.24
177.40	1.577	0.458	0.026	7.53	177.24
177.40	1.541	0.432	0.034	7.53	177.24
177.40	1.506	0.416	0.035	7.53	177.24
212.42	1.746	0.455	0.017	−207.95	43.33
212.42	1.715	0.420	0.019	−207.95	43.33
212.42	1.682	0.399	0.019	−207.95	43.33
212.42	1.648	0.431	0.024	−207.95	43.33
212.42	1.613	0.415	0.022	−207.95	43.33
212.42	1.577	0.405	0.025	−207.95	43.33
212.42	1.541	0.401	0.021	−207.95	43.33
212.42	1.506	0.394	0.026	−207.95	43.33
136.52	1.746	0.626	0.041	−135.98	−12.06
136.52	1.715	0.605	0.042	−135.98	−12.06
136.52	1.682	0.586	0.037	−135.98	−12.06
136.52	1.648	0.619	0.041	−135.98	−12.06
136.52	1.613	0.606	0.046	−135.98	−12.06
136.52	1.577	0.602	0.040	−135.98	−12.06
136.52	1.541	0.596	0.044	−135.98	−12.06
136.52	1.506	0.592	0.043	−135.98	−12.06
90.826	1.746	0.748	0.028	71.97	−55.40
90.826	1.715	0.714	0.036	71.97	−55.40
90.826	1.682	0.699	0.041	71.97	−55.40
90.826	1.648	0.720	0.054	71.97	−55.40
90.826	1.613	0.709	0.058	71.97	−55.40
90.826	1.577	0.707	0.065	71.97	−55.40
90.826	1.541	0.706	0.070	71.97	−55.40
90.826	1.506	0.723	0.070	71.97	−55.40
240.59	1.746	0.360	0.015	136.83	197.89
240.59	1.715	0.331	0.015	136.83	197.89
240.59	1.682	0.311	0.012	136.83	197.89
240.59	1.648	0.348	0.015	136.83	197.89
240.59	1.613	0.341	0.014	136.83	197.89
240.59	1.577	0.326	0.016	136.83	197.89
240.59	1.541	0.307	0.020	136.83	197.89
240.59	1.506	0.281	0.019	136.83	197.89
242.83	1.746	0.380	0.028	−83.21	228.13
242.83	1.715	0.335	0.022	−83.21	228.13
242.83	1.682	0.324	0.020	−83.21	228.13
242.83	1.648	0.349	0.018	−83.21	228.13
242.83	1.613	0.338	0.018	−83.21	228.13
242.83	1.577	0.342	0.019	−83.21	228.13
242.83	1.541	0.331	0.022	−83.21	228.13
242.83	1.506	0.308	0.023	−83.21	228.13
177.40	1.746	0.474	0.025	−3.67	177.36
177.40	1.715	0.454	0.021	−3.67	177.36
177.40	1.682	0.439	0.017	−3.67	177.36
177.40	1.648	0.485	0.016	−3.67	177.36
177.40	1.613	0.474	0.019	−3.67	177.36
177.40	1.577	0.461	0.023	−3.67	177.36
177.40	1.541	0.434	0.032	−3.67	177.36
177.40	1.506	0.410	0.033	−3.67	177.36
222.15	1.746	0.434	0.019	−220.09	30.21
222.15	1.715	0.395	0.020	−220.09	30.21
222.15	1.682	0.374	0.017	−220.09	30.21
222.15	1.648	0.397	0.016	−220.09	30.21
222.15	1.613	0.382	0.016	−220.09	30.21
222.15	1.577	0.377	0.021	−220.09	30.21
222.15	1.541	0.363	0.019	−220.09	30.21
222.15	1.506	0.350	0.019	−220.09	30.21
142.01	1.746	0.619	0.016	−140.52	−20.53
142.01	1.715	0.584	0.017	−140.52	−20.53
142.01	1.682	0.559	0.017	−140.52	−20.53
142.01	1.648	0.589	0.020	−140.52	−20.53
142.01	1.613	0.583	0.021	−140.52	−20.53
142.01	1.577	0.579	0.021	−140.52	−20.53
142.01	1.541	0.573	0.026	−140.52	−20.53
142.01	1.506	0.578	0.023	−140.52	−20.53
94.360	1.746	0.769	0.030	79.53	−50.77
94.360	1.715	0.718	0.036	79.53	−50.77
94.360	1.682	0.714	0.032	79.53	−50.77

Continued on next page

Table B.4 – continued from previous page

Baseline	λ	V^2	$\sigma(V^2)$	u	v
(m)	(μm)			(m)	(m)
94.360	1.648	0.727	0.037	79.53	−50.77
94.360	1.613	0.726	0.037	79.53	−50.77
94.360	1.577	0.735	0.049	79.53	−50.77
94.360	1.541	0.723	0.048	79.53	−50.77
94.360	1.506	0.718	0.050	79.53	−50.77

C
SPECTRAL ATLASES FOR LBVS OBSERVED AT CTIO IN THE RANGE OF 5700–6800Å

This atlas displays the average spectrum for each LBV discussed here and includes line identifications on the top axis. Diffuse Interstellar Bands (DIBs) or other interstellar lines are marked with vertical lines below the continuum. Unmarked absorption lines are likely interstellar in origin.

Line identifications come from Nielsen et al. (2009a) for η Carinae and other high mass-loss rate objects and from Chentsov et al. (2003) for the low mass loss rate objects. The two most unusual objects in this LBV zoo (from their spectral appearance) have separate spectral atlases published in the literature. Namely, identifications for HD 5980 come from Heydari-Malayeri et al. (1997) and identifications for HDE 326823 come from Borges Fernandes et al. (2001).

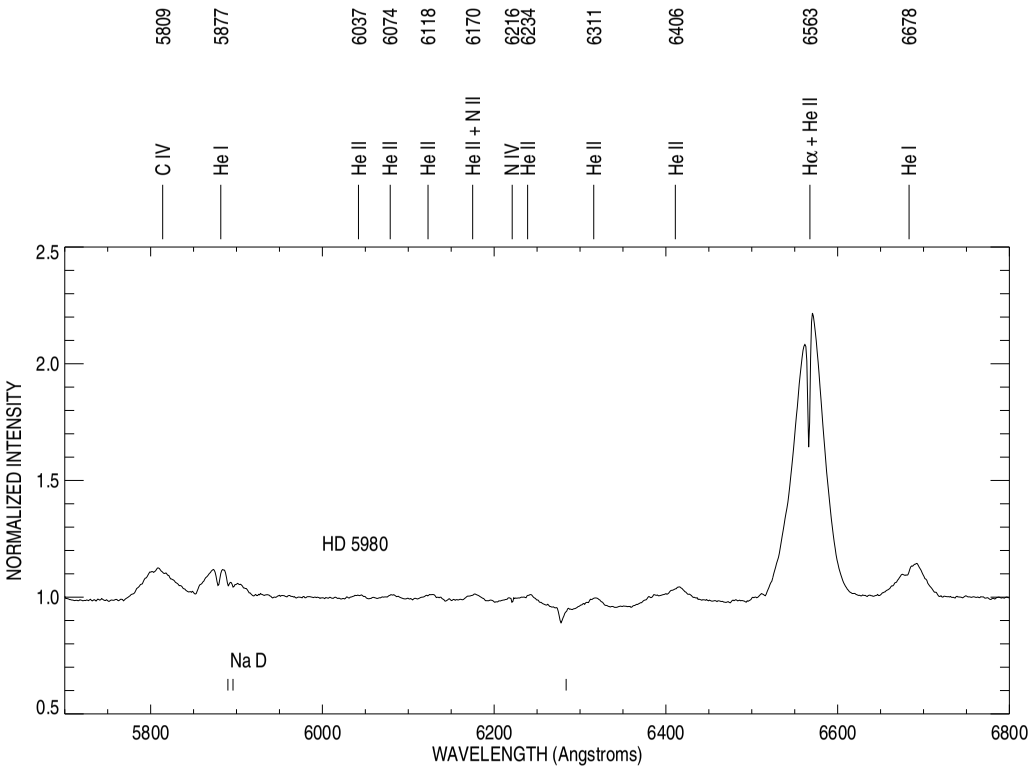

Figure C.1 Line identifications for HD 5980.

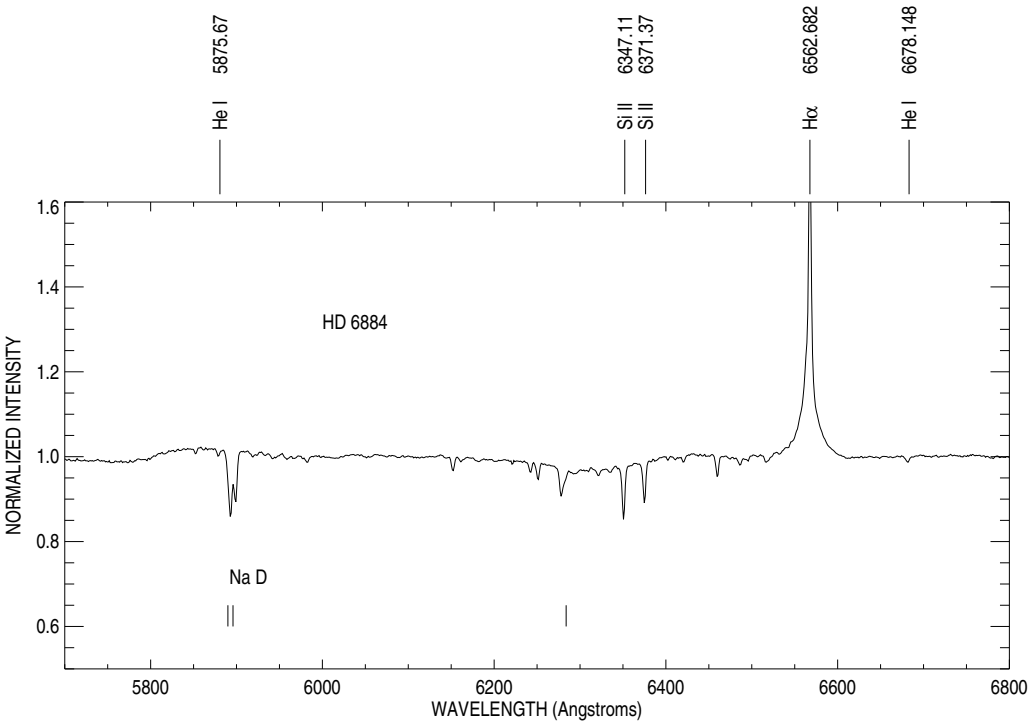

Figure C.2 Line identifications for HD 6884.

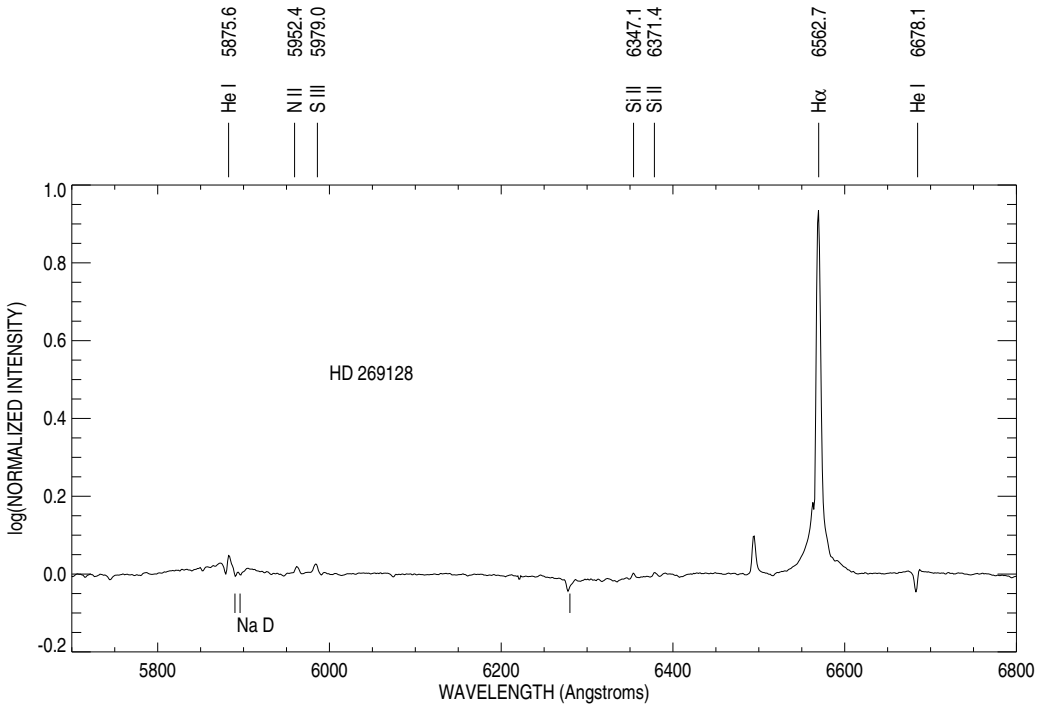

Figure C.3 Line identifications for HD 269128.

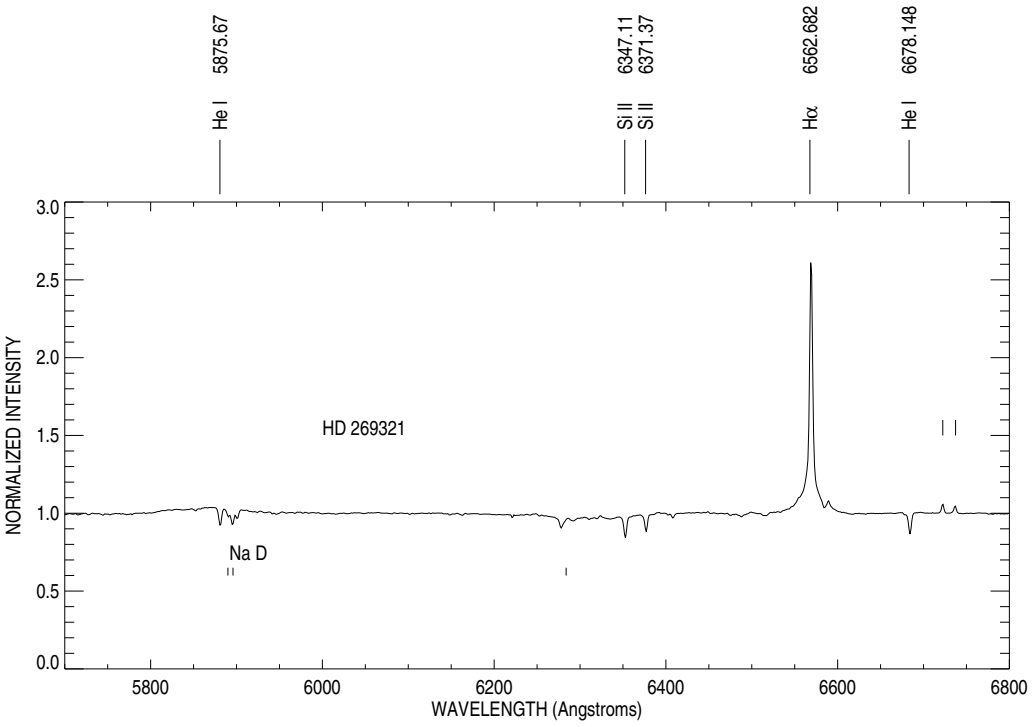

Figure C.4 Line identifications for HD 269321.

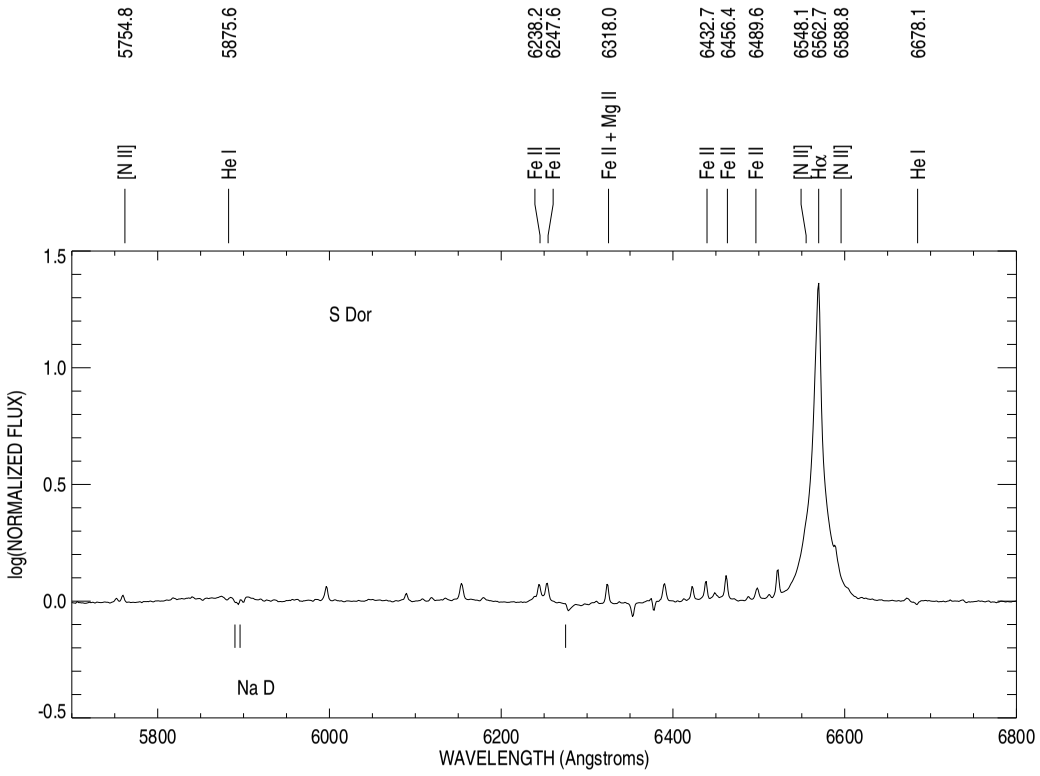

Figure C.5 Line identifications for S Doradus.

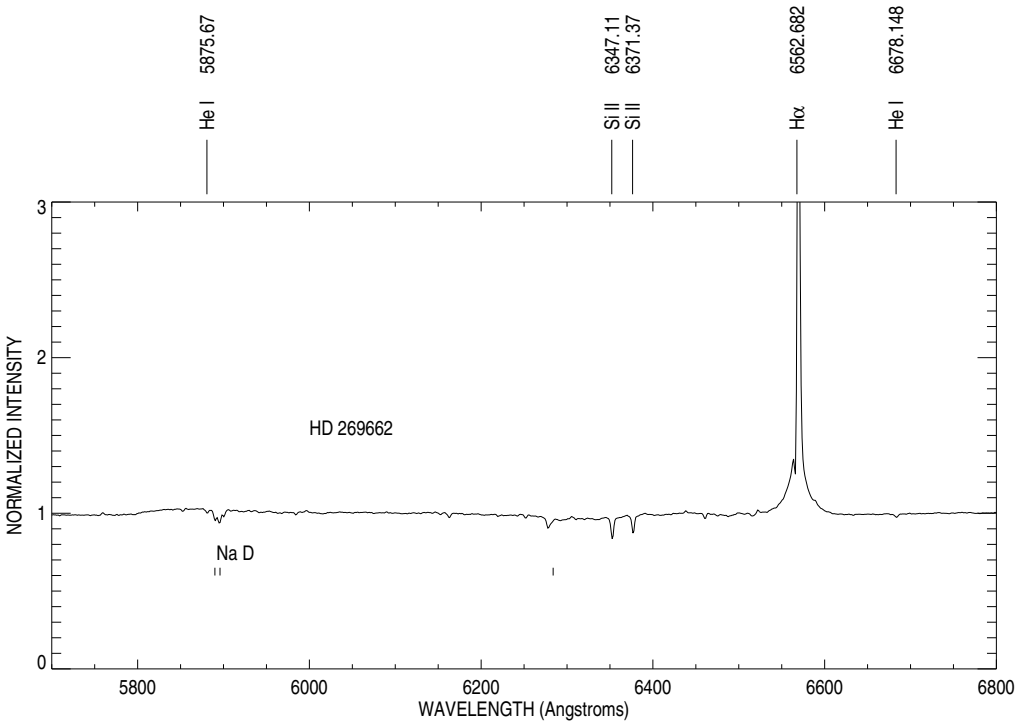

Figure C.6 Line identifications for HD 269662.

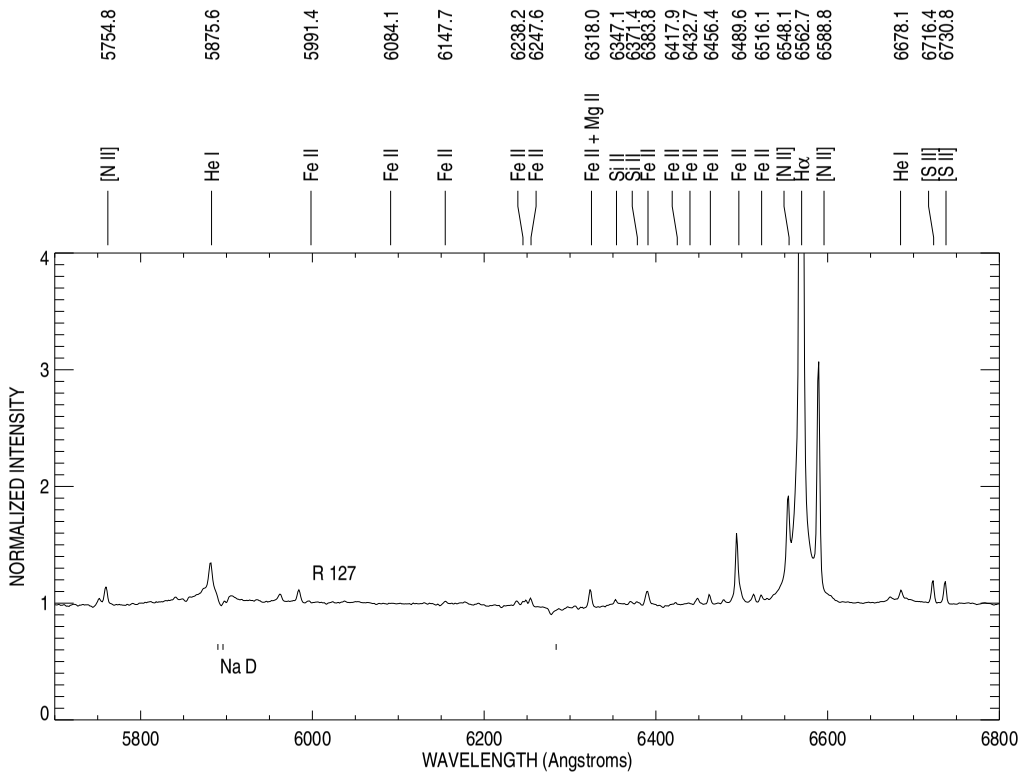

Figure C.7 Line identifications for R 127.

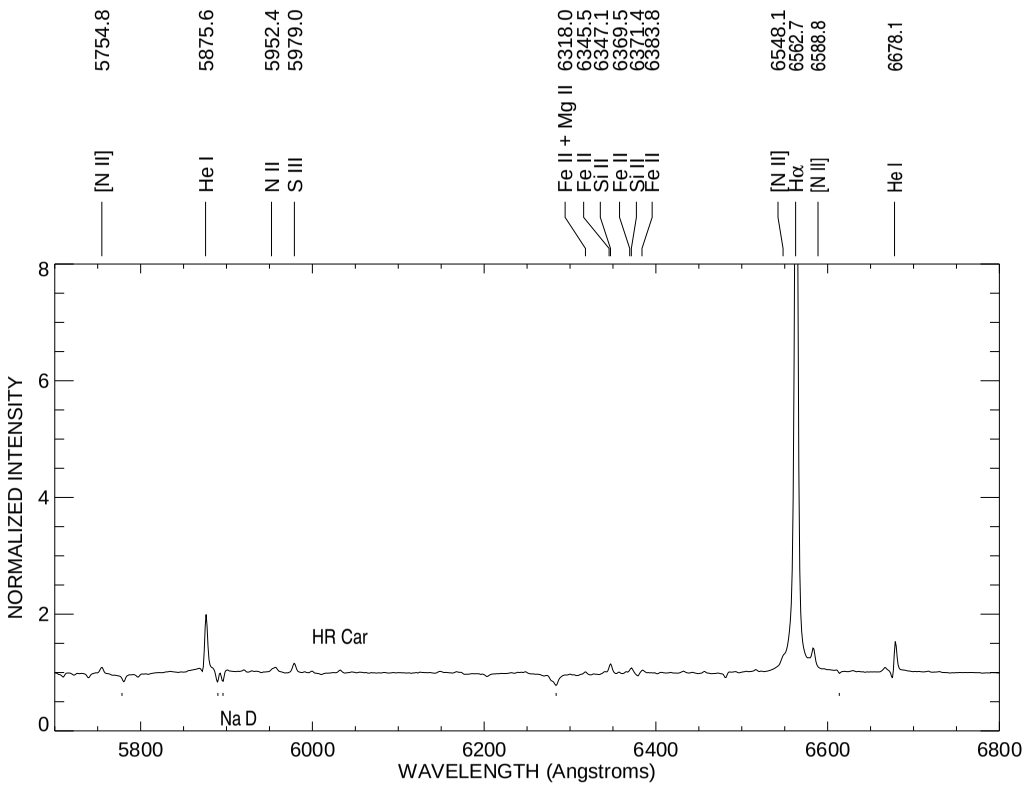

Figure C.8 Line identifications for HR Car.

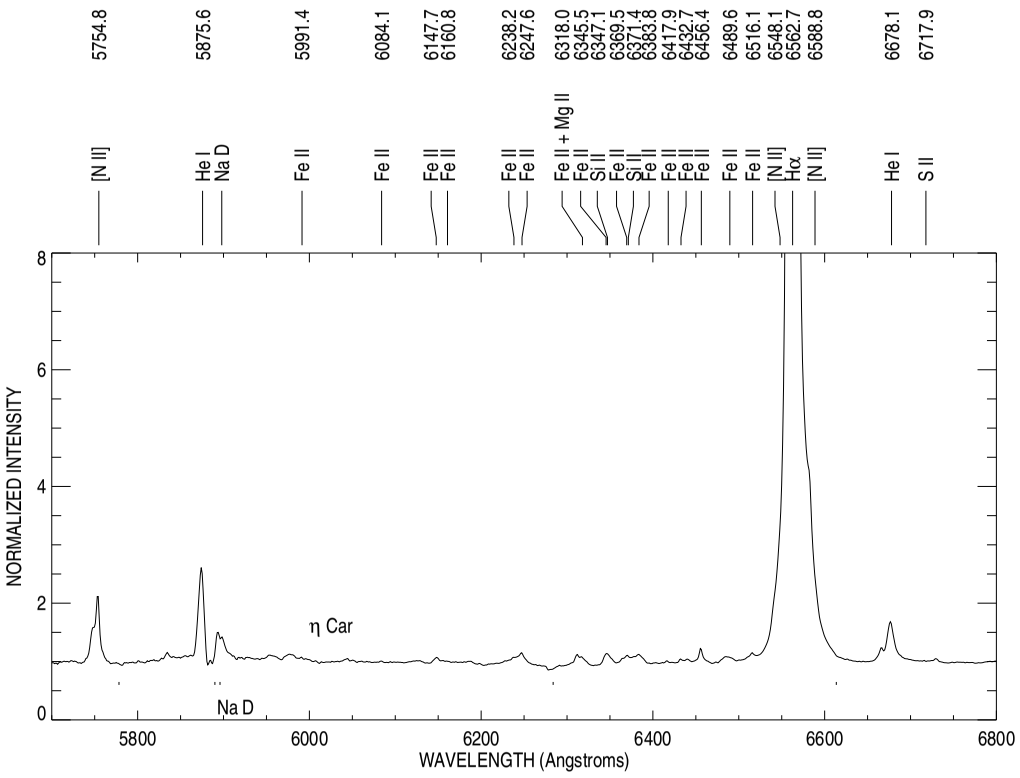

Figure C.9 Line identifications for η Car.

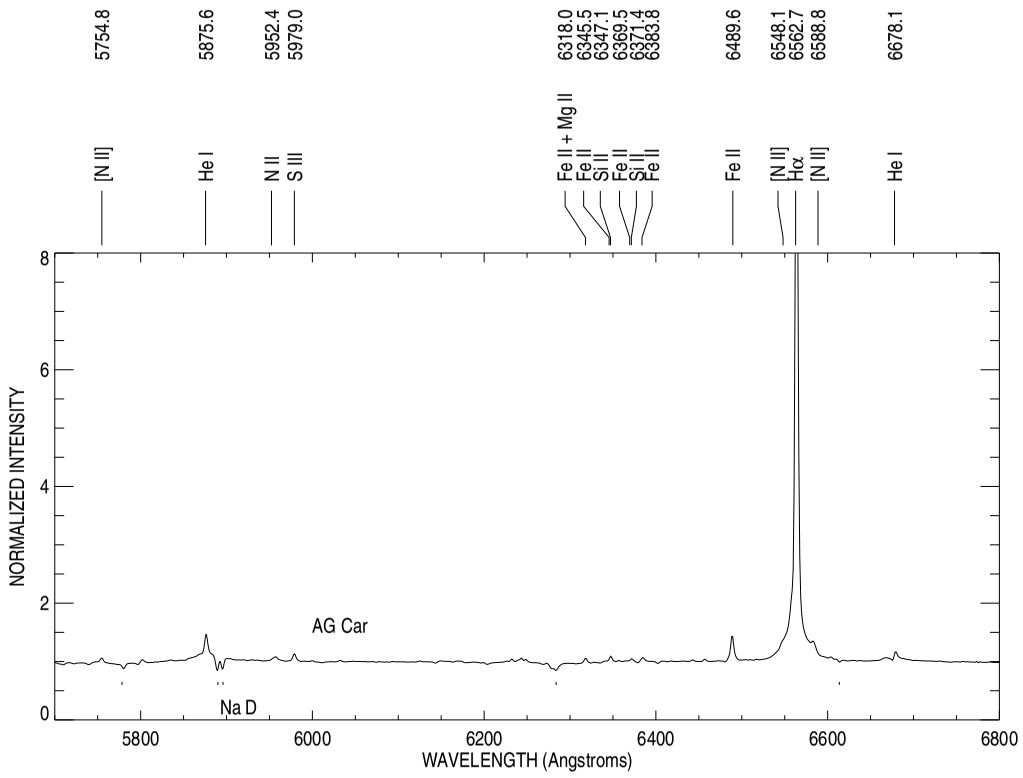

Figure C.10 Line identifications for AG Car.

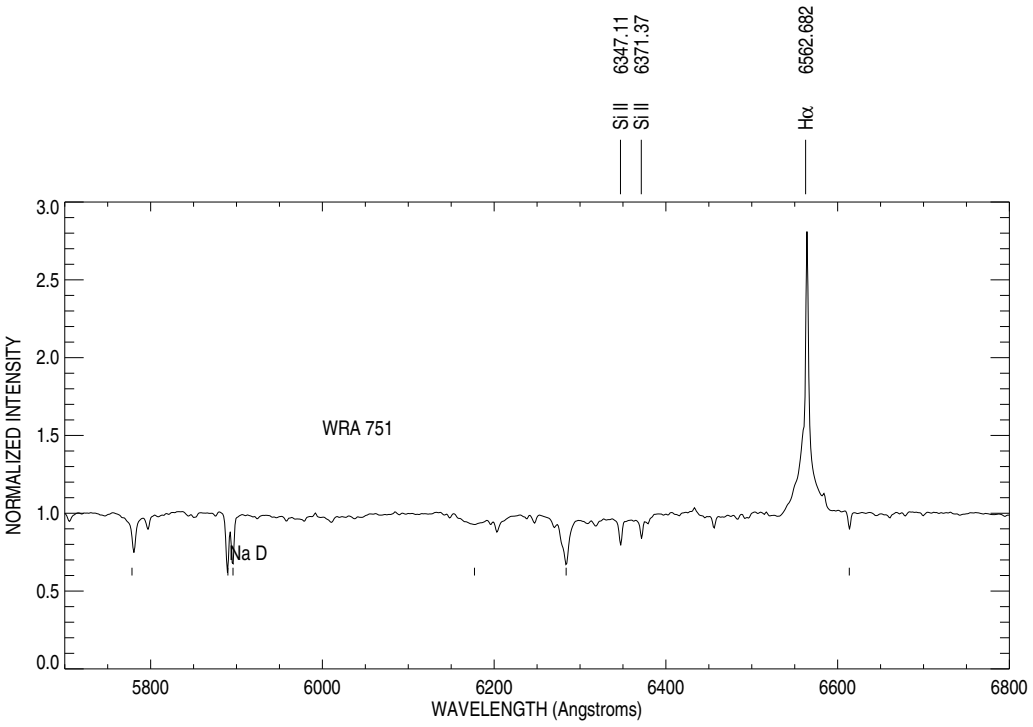

Figure C.11 Line identifications for V432 Car.

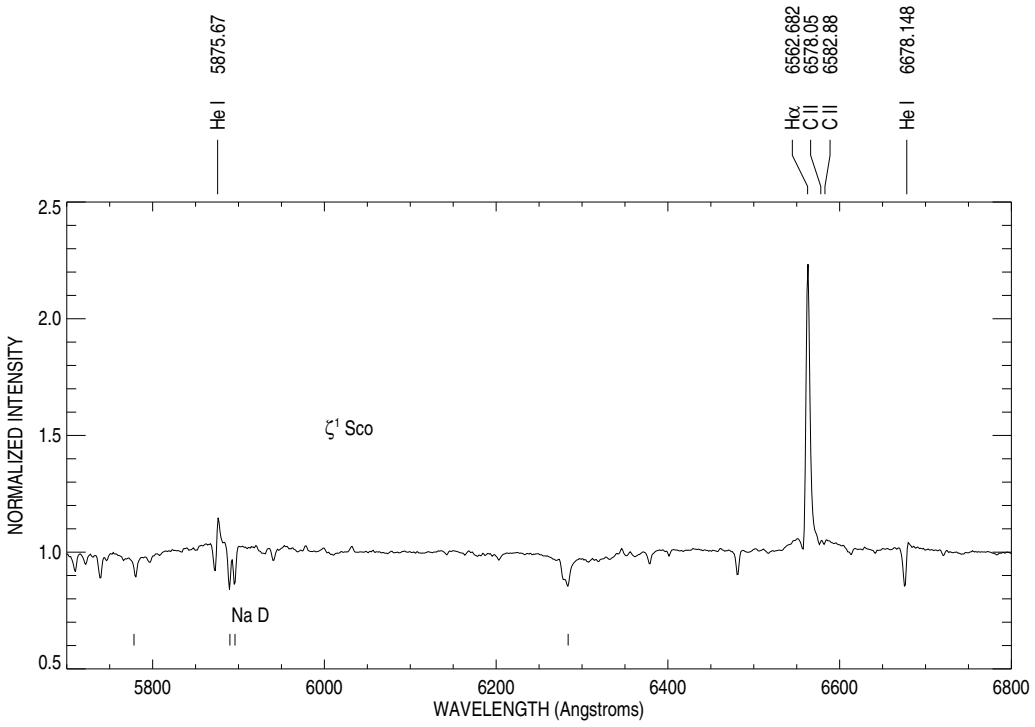

Figure C.12 Line identifications for ζ^1 Scorpii.

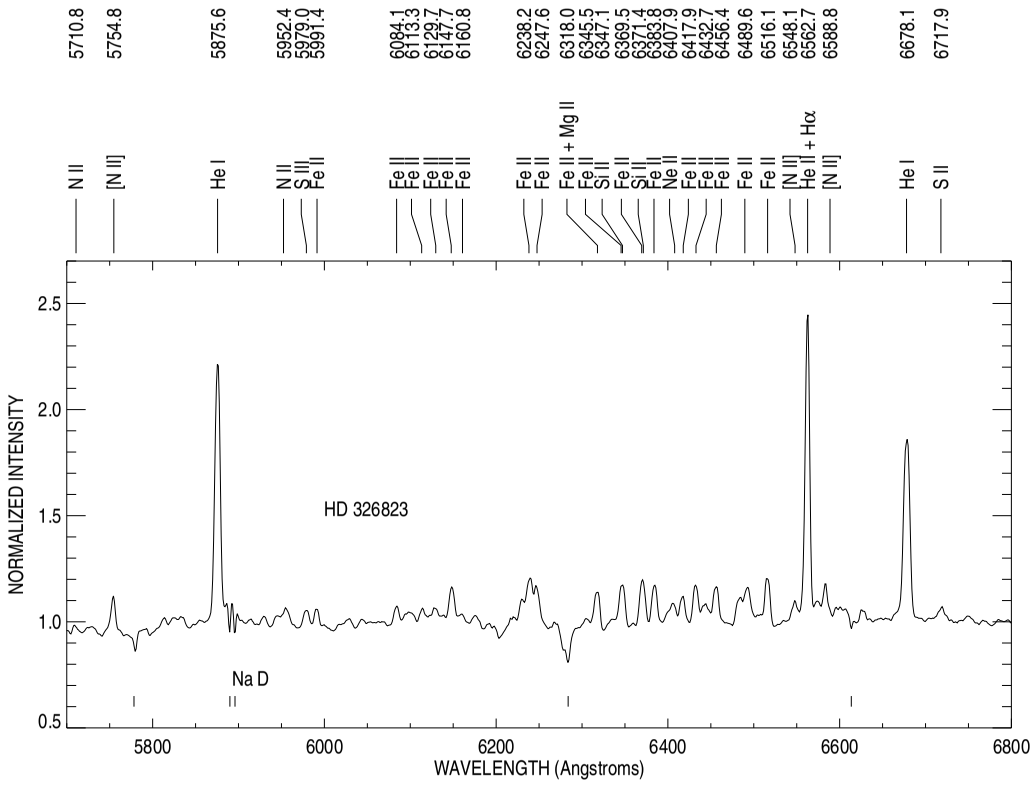

Figure C.13 Line identifications for HD 326823.

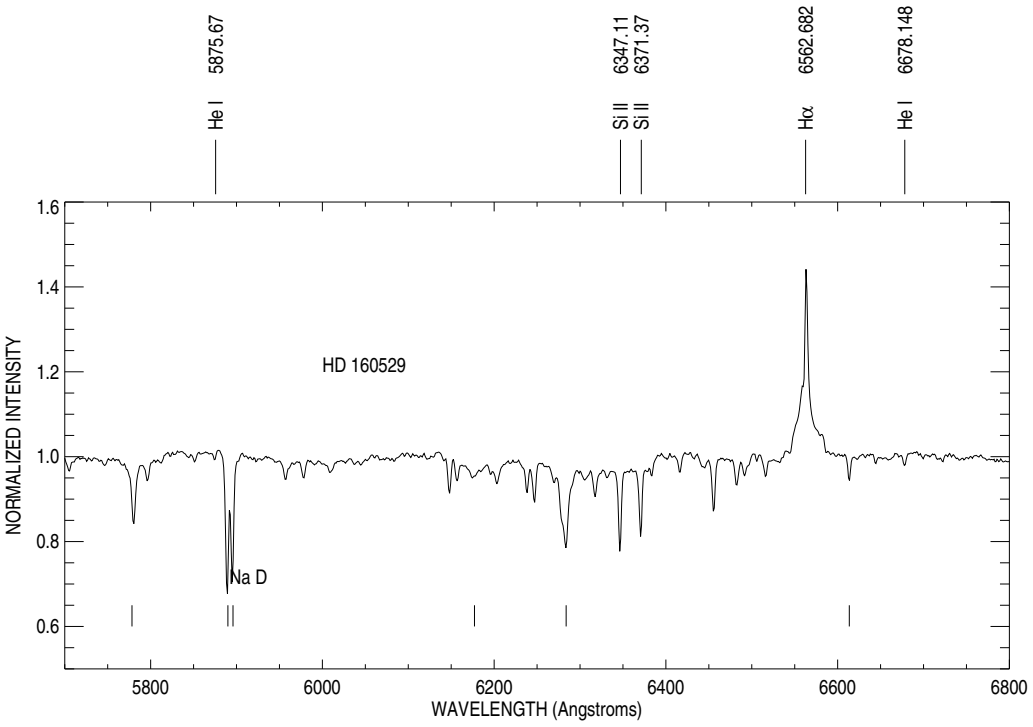

Figure C.14 Line identifications for HD 160529.

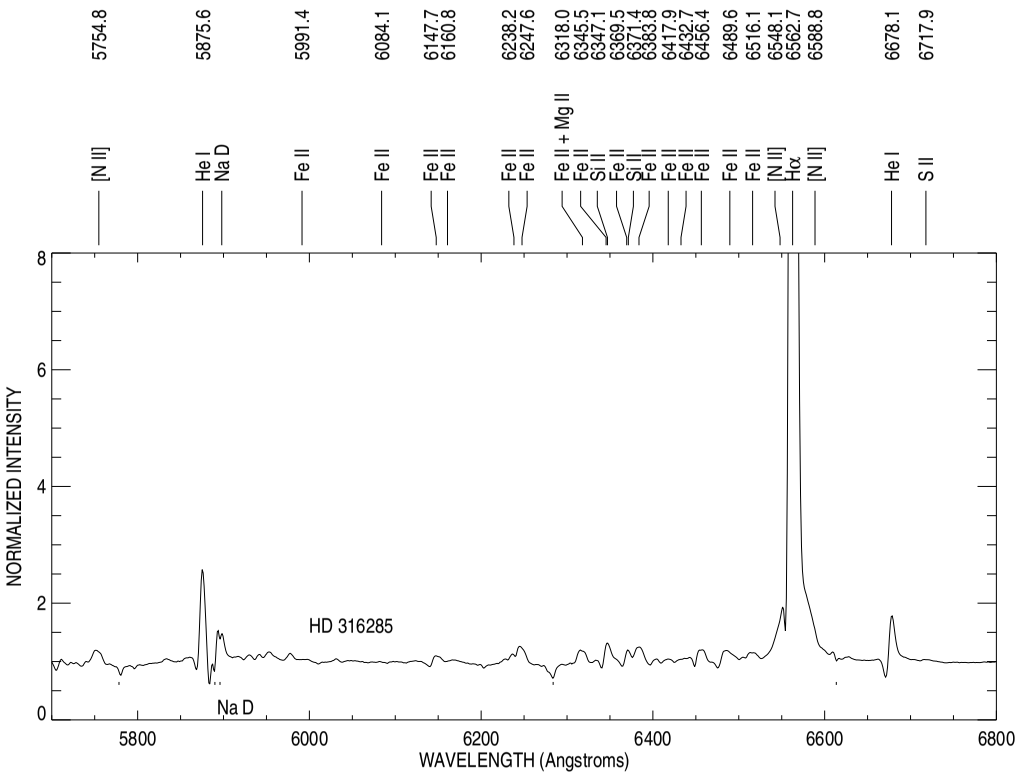

Figure C.15 Line identifications for HD 316285.

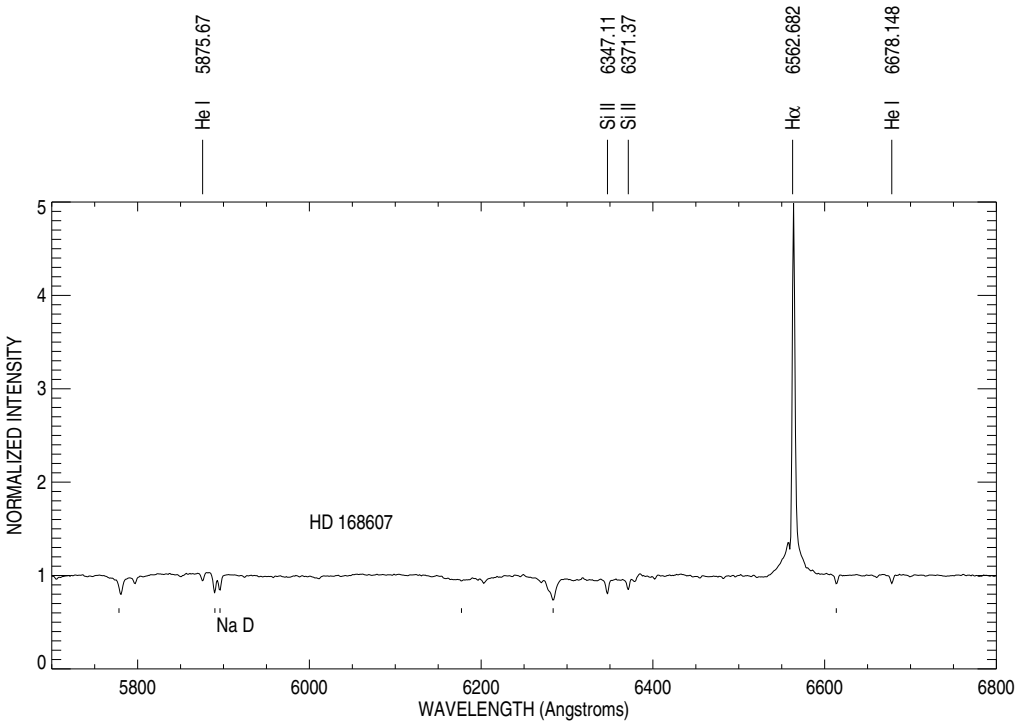

Figure C.16 Line identifications for HD 168607.

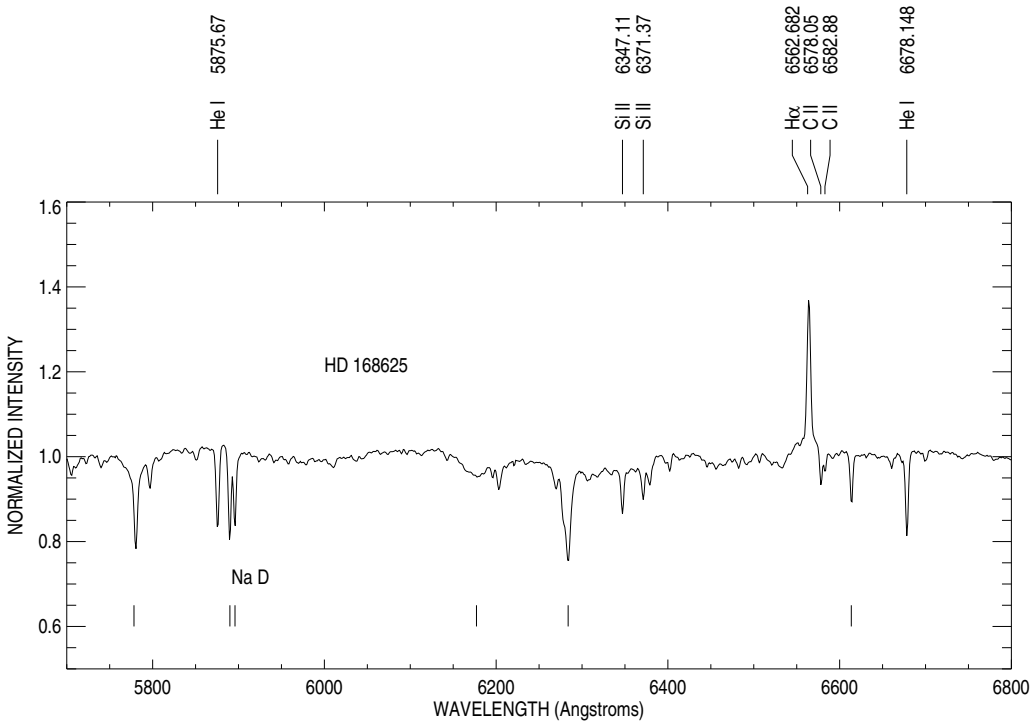

Figure C.17 Line identifications for HD 168625.

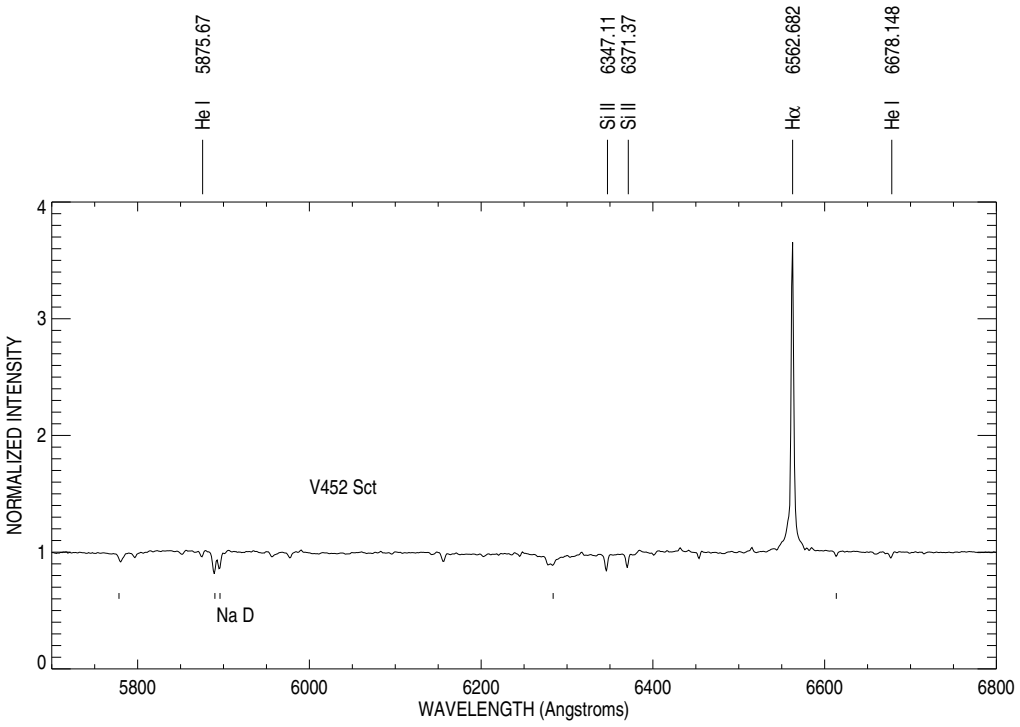

Figure C.18 Line identifications for V452 Sct.

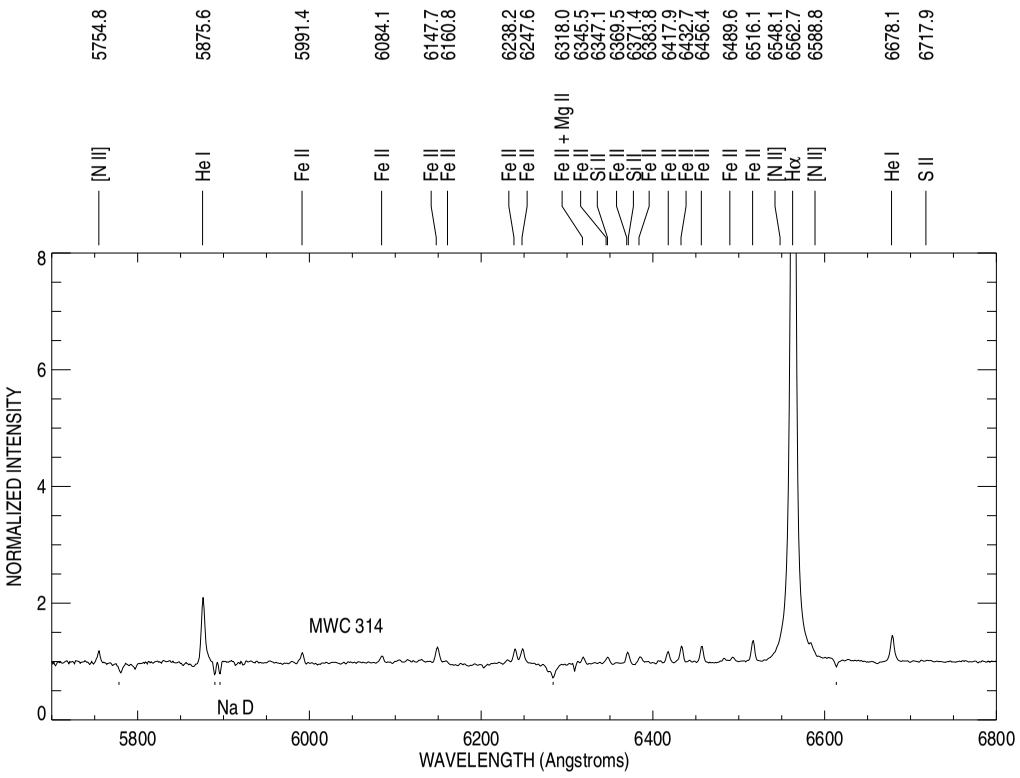

Figure C.19 Line identifications for MWC 314.